
Quantum Simulation of Fermionic Models in Superconducting Circuits

Laura García-Álvarez

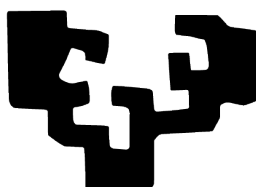
Supervised by

Prof. Enrique Solano

and

Prof. Íñigo Egusquiza

eman ta zabal zazu



Departamento de Química Física
y
Departamento de Física Teórica e Historia de la Ciencia
Facultad de Ciencia y Tecnología
Universidad del País Vasco

June 2017

This document is a PhD thesis developed during the period from October 2013 to June 2017 at QUTIS (Quantum Technologies for Information Science) group, led by Prof. Enrique Solano. This work was funded by the University of the Basque Country with a PhD fellowship.

©2017 by Laura García-Álvarez. All rights reserved.

An electronic version of this thesis can be found at www.qutisgroup.com

Bilbao, June 2017

This document was generated with the 2015 L^AT_EX distribution.

The L^AT_EX template is adapted from a [template](#) by Iagoba Apellaniz.

The bibliographic style was created by Sofia Martinez Garaot.

To my family

Ya está incorporado a una comunidad de la que, a pesar de todo, forma parte y de la que no podrá deshacerse con facilidad. Al entrar allí, la ciudad – con una de sus conciencias más agudas – de él ha tomado nota: existe.

Luis Martín-Santos, Tiempo de silencio

Contents

Abstract	i
Resumen	iii
Acknowledgements	ix
List of Publications	xiii
List of Figures	xvi
Abbreviations and conventions	xvii
1 Introduction	1
1.1 What you will find in this Thesis	6
2 Digital Quantum Simulation of Fermions with Qubits	9
2.1 Encoding of fermions in qubits and quantum gates in superconducting circuits	11
2.1.1 CZ_ϕ gates with capacitive couplings	12
2.1.2 XY gates with resonators	12
2.1.3 Collective gates with resonators	13
2.2 Quantum algorithms for variations of the Fermi-Hubbard model	14
2.2.1 Asymmetric Hubbard model	16
2.2.2 Numerical analysis of the errors	19

2.3	An implementation in superconducting circuits	25
2.3.1	Implementing the Hubbard model with gates	26
2.3.2	Verifying operator anticommutativity	27
2.3.3	Simulations with two fermionic modes	28
2.3.4	Simulations with three and four fermionic modes	30
2.3.5	Time-varying interactions	33
2.4	Hybrid digital quantum-classical simulation of fermions	35
2.4.1	Quantum simulator based on two-site DMFT	37
2.4.2	Two-site DMFT protocol	38
2.4.3	Quantum algorithm for the SIAM model with superconducting circuits	40
2.4.4	Quantum gate decomposition of the time-evolution operator . . .	41
2.4.5	Results	43
3	Digital Quantum Simulation of Minimal AdS/CFT	51
3.1	The holographic model	53
3.1.1	SYK models	53
3.2	Algorithm for quantum simulation of SYK models	54
3.2.1	Protocol for correlation measurements	56
3.2.2	Protocols for time inversion	57
3.2.3	Protocol for state initialization	57
3.3	Implementation in quantum platforms	57
3.3.1	Trapped ions	58
3.3.2	Superconducting circuits	60
3.4	Gate count comparison per Trotter step	60
3.5	Criteria for simulated time	62
3.6	Implementation details for $n = 4$ complex fermions	64
4	Digital–Analog Quantum Simulations of QFT	71
4.1	Quantum field theory model	72
4.2	Encoding of fermions in qubits	72
4.3	Superconducting circuit model	74
4.4	Simulation of spatial degrees of freedom	75
4.5	Sequence of quantum operations	77
4.6	Encoding of information	77
5	DAQS of Quantum Chemistry and Biology	79
5.1	Simulation of electronic Hamiltonians	80
5.2	Simulation of environmental effects	86
6	Conclusions	91
	Appendices	95

A	Details of the experiment in superconducting circuits	97
A.1	Experimental details and state fidelity	97
A.2	Trotter step pulse sequences	98
A.2.1	Pulse sequences and gate counts	98
A.2.2	Initialization	98
A.3	Quantum process tomography	99
A.4	Randomized benchmarking and the two-mode Trotter step	100
A.5	Digital error	101
A.6	Minimizing leakage of the CZ_ϕ gate	102
B	Hubbard model in infinite dimensions and DMFT	105
C	Interferometry for the impurity Green function	109
C.1	Definitions	109
C.2	Jordan–Wigner transformation	110
C.3	Measurement protocol	110
D	Details on the holographic models	113
D.1	SYK models	113
D.1.1	Details on Majorana models	114
D.1.2	Details on spinless complex fermion models	115
E	Details on the quantum algorithm for SYK	117
E.1	Construction of spin interaction terms for the quantum algorithm	117
E.1.1	Details on Majorana models	117
E.1.2	Details on spinless complex fermion models	119
E.2	Details on the protocols of the quantum algorithm	122
E.2.1	Protocol for correlation measurements	122
E.2.2	Protocol for time inversion	122
E.2.3	Protocol for state initialization	123
E.2.4	Details on Mølmer–Sørensen gates	124
F	Details on the QFT model	125
F.1	Discretization and comoving modes	126
F.2	Hamiltonian in the Schrödinger picture	127
G	Details on the DAQS for QFT	129
G.1	Details on the superconducting circuit model	129
G.2	Higher dimensions and scalability issues	132
	Bibliography	135

Abstract

One of the obstacles we encounter in our path to acquire knowledge about the universe is the computational complexity of the required mathematical models. Among these, fermionic models constitute one of the most challenging problems, with the intractable sign problem arising from its anticommutativity. We find fermions at the core of the description of nature, and their study is crucial in many areas, from condensed matter physics and high-energy physics to quantum gravity. The understanding of fermionic models would illuminate the principles underlying important phenomena, such as the Mott metal-insulator transition, high-temperature superconductivity, colossal magnetoresistance, or scrambling of information in black holes.

The development of the theory of quantum mechanics one hundred years ago has entailed a scientific and technological revolution, resulting in devices relying on quantum effects, as the laser, atomic clocks, or the transistor. With the growing control over quantum systems, we are paving the way for a second quantum revolution, in which we actively create quantum states and manipulate them, harnessing quantum phenomena as entanglement and superposition. Among the new applications, quantum computation and quantum simulation are candidates to overcome the limits of classical computers.

The development of quantum technologies has not yet provided the expected quantum supremacy, but constant advances in quantum platforms enable us to study scientific problems. Among the variety of quantum platforms, superconducting circuits are a cutting-edge technology in terms of control, design versatility, and scalability. We explore the possibilities of current and near-future technology, conceiving superconducting circuits as computational devices with potential resources beyond

qubits. In that regard, we propose to harness distinctive features of superconducting circuits in order to simulate models of quantum field theory. Thus, we consider the continuum complexity in the quantum field theory description of an open transmission line to capture the continuum complexity of bosonic modes in quantum fields with a complexity-simulating-complexity paradigm.

This Thesis embraces different methods for quantum simulation of fermionic models, and a report of an implementation in superconducting circuits of one of those quantum simulation proposals. We begin with the usual digital encoding of information into qubits, proper to universal quantum computing, to then shift the paradigm towards hybrid techniques in which we consider not only the qubits as the carriers of information, but also other elements in the quantum platforms whose degrees of freedom are potential resources for storage and computation. With an eye on the complexity-simulating-complexity concept, we propose quantum digital-analog approaches and classical-quantum protocols to enhance the possibilities of superconducting circuits in the simulation of fermions, fermionic models in condensed-matter, quantum gravity, quantum field theory, and quantum chemistry. The narrower purpose quantum simulators with analog information encoding are promising candidates for the simulation of complex problems in realistic current devices.

Resumen

En esta Tesis, aunamos diferentes paradigmas de computación para maximizar las posibilidades de las tecnologías cuánticas actuales en el desarrollo de la ciencia. Comprendemos el universo a través de modelos con los que identificamos simetrías y patrones en los fenómenos que observamos. El conocimiento humano no sólo está limitado por nuestra capacidad de observar la naturaleza, de la que extraemos información imperfecta e incompleta, sino que también depende de nuestra capacidad de modelización, desarrollo matemático y computación. Los procedimientos para desarrollar modelos y obtener resultados engloban las derivaciones matemáticas y el uso de máquinas para simulaciones artificiales y cálculos.

En 1936, Alan Turing formalizó la idea de calcular y dió la noción abstracta de lo que es un algoritmo, revolucionando la ciencia y dando lugar al ordenador digital actual. Su modelo matemático se conoce como máquina de Turing y nos ayuda a investigar si los problemas son tratables y a clasificarlos según su complejidad. La exploración teórica de los límites de la computación es un hito inevitable en el estudio de los límites del conocimiento, tan importante como la exploración de los límites de las representaciones matemáticas, el desarrollo de la lógica matemática o la filosofía. El campo que estudia los problemas según su dificultad se conoce como teoría de complejidad. Es natural estudiar los límites de la computación de acuerdo a los recursos de que disponemos. En este sentido, es razonable considerar como intratables aquellos problemas para los que conocemos un algoritmo, pero éste tardaría más que la edad del universo en dar una solución. Las posibilidades de resolver un problema de forma eficiente están limitadas por nuestra capacidad de almacenar información, la energía y el tiempo que llevaría. De esta forma, se pueden

diferenciar clases de complejidad de acuerdo a la tasa de crecimiento de los recursos necesarios respecto al tamaño del problema, es decir, los datos iniciales necesarios. La ciencia se enfrenta a problemas computacionalmente complejos, entre los que cabe destacar la resolución de modelos fermiónicos.

Un pilar fundamental en el entendimiento de la naturaleza es la descripción de los constituyentes básicos de la materia. De las observaciones y experimentos a diferentes escalas inferimos que estos constituyentes básicos, y sus composiciones, se pueden clasificar según su espín en dos grupos: fermiones si su número de espín es semientero, y bosones si es entero. Esta profunda restricción de la naturaleza se recoge en el teorema de espín-estadística, y atribuye una antisimetría en la función de onda cuántica que describe a los fermiones. Estas particulares características conllevan una serie de dificultades en la simulación numérica de fermiones, que se vuelve intratable incluso para modelos fermiónicos simplificados. En este sentido, las técnicas de diagonalización exacta están limitadas por el número de estados, que crece exponencialmente con el tamaño del sistema. En modelos de una dimensión espacial, es posible prescindir de ciertos estados de tal forma que se pueden calcular ciertas propiedades de estos sistemas con técnicas del grupo de renormalización de la matriz densidad. Para modelos en más dimensiones, estas técnicas fallan debido a la complejidad creciente de los modelos. Las técnicas de Monte Carlo cuánticas tampoco son efectivas en la simulación de fermiones, debido al problema de signo que surge de su antisimetría. Este problema numérico es un obstáculo en el estudio de fermiones fuertemente correlacionados. Resolver este tipo de modelos fermiónicos es la base para entender los principios que rigen el comportamiento de los materiales cuánticos complejos e implicaría un avance tecnológico inmediato, relacionado con fenómenos tan relevantes como la transición metal-aislante de Mott, la superconductividad a altas temperaturas y la magnetorresistencia colosal.

Las simulaciones constituyen otro de los diferentes métodos que el ser humano ha venido usando a lo largo de la historia para extraer información de modelos sobre sistemas y fenómenos físicos. Una simulación es una reproducción de un modelo en un sistema físico controlable, imitando sus características y fenómenos. Fue Richard Feynman quien conjeturó en 1982 que los problemas de la mecánica cuántica no serían tratables por un ordenador clásico, y sugirió la simulación de sistemas cuánticos con otros sistemas cuánticos, lo que supondría una fuente de poder computacional sin precedentes. De esta forma, las nociones de complejidad computacional en la teoría clásica y su relación con los límites del conocimiento se enfrentan a un nuevo paradigma de procesamiento de información basado en efectos cuánticos. La teoría de la mecánica cuántica lleva con nosotros casi cien años, y ha traído consigo una profunda transformación en la concepción que tenemos del universo. El desarrollo de esta nueva teoría y de las leyes físicas que gobiernan los comportamientos a escala microscópica ha supuesto a su vez una revolución tecnológica, con avances tan importantes como el láser, los relojes atómicos, la resonancia magnética nuclear, o el transistor. La idea de simulación cuántica propuesta por Feynman se incluye en lo que se conoce como segunda revolución cuántica, junto a otras aplicaciones como la metrología cuántica, los sensores cuánticos, la comunicación cuántica y la

computación cuántica. Todas ellas tienen en común el uso de efectos cuánticos no explotados hasta ahora, como la superposición cuántica, el entrelazamiento y el efecto túnel. El ordenador cuántico aprovecha estas propiedades para codificar y procesar la información en bits cuánticos, también llamados qubits. Con la tecnología actual se han alcanzado procesadores cuánticos que contienen del orden de una decena de qubits controlables individualmente, mientras que teóricamente se predice que los ordenadores cuánticos con 50 qubits serían ya capaces de ejecutar cálculos fuera del alcance de cualquier ordenador convencional.

Tanto la computación como la simulación cuánticas requieren un alto control de las plataformas cuánticas. En las dos últimas décadas se han propuesto diferentes arquitecturas físicas como candidatas a procesadores de información cuántica. Entre ellas podemos destacar iones atrapados, átomos ultrafríos, puntos cuánticos, sistemas fotónicos, redes ópticas y circuitos superconductores, entre otros. Las plataformas superconductoras se encuentran entre las más desarrolladas en términos de control coherente, la versatilidad de los diseños y su escalabilidad. Estos sistemas macroscópicos se aprovechan de la superconductividad, es decir, el fenómeno de diamagnetismo perfecto y resistividad nula que aparece en ciertos materiales a bajas temperaturas. En la fase superconductora, el sistema se representa con una función de onda coherente que describe al sistema completo colectivamente y lo caracteriza con una fase única. Esta coherencia cuántica permite que variables macroscópicas del sistema, como corrientes y voltajes, exhiban comportamientos cuánticos.

En esta Tesis conciliamos estos diferentes paradigmas computacionales con el objetivo de cruzar la frontera de lo que se considera calculable. Convencidos de que el progreso científico se fundamenta en el diálogo entre teoría y experimentos, nos subordinamos a lo implementable en la tecnología actual para nuestras propuestas de simulaciones híbridas, clásico-cuánticas y cuánticas digital-analógicas, y analizamos cómo se podrían extender en tecnologías futuras. Exploramos las posibilidades de las plataformas cuánticas, y en particular de los circuitos superconductores, en la simulación de modelos intratables clásicamente. Los métodos de cálculo propuestos se basan inicialmente en la codificación y procesamiento de información propios de la computación cuántica, enriqueciéndose posteriormente al aprovechar las características de los circuitos superconductores como recursos cuánticos para el procesamiento de información.

Proponemos un método de simulación cuántica digital eficiente para modelos de fermiones. El protocolo se basa en la traducción de las interacciones fermiónicas a un lenguaje de qubits a través de la transformación de Jordan-Wigner, que relaciona grados de libertad fermiónicos con sistemas de dos niveles. La complejidad de los modelos fermiónicos se recoge secuencialmente en la simulación, donde cada paso digital introduce un tipo de interacción diferente a través de puertas lógicas definidas para conjuntos de qubits. El resultado final recoge la evolución completa del sistema simulado aproximada con cierto error digital. Esta propuesta, estudiada para modelos fermiónicos de Hubbard con acoplos entre primeros y segundos vecinos, ha sido llevada a cabo experimentalmente en una colaboración con el grupo de John M. Martinis en Google/Universidad de California, Santa Barbara. El experimento,

pionero en simulación cuántica digital de fermiones, incluía más de 300 puertas lógicas cuánticas. Las fidelidades de los resultados sugieren que el método es escalable eficientemente para sistemas mayores y modelos más complejos, lo que hace viables simulaciones más elaboradas en tecnologías futuras.

Nuestro siguiente paso consiste en la combinación de estas simulaciones cuánticas digitales con algoritmos clásicos para explotar las posibilidades de simulación cuántica actual. En particular, la combinación del método anterior con algoritmos basados en la teoría dinámica de campo medio nos permite reproducir, con el estado del arte de las tecnologías cuánticas, sistemas fermiónicos en el límite termodinámico, donde el número de qubits no restringe el número de fermiones simulables. Con un procesador de tan sólo 5 qubits se puede emplear esta técnica híbrida para simular fermiones fuertemente correlacionados, y reproducir cualitativamente fenómenos como la transición de Mott de metal a aislante.

Fermiones interaccionando entre todos ellos con acoplos aleatorios y no locales constituyen un desafío mayor dentro de este conjunto de modelos ya intratables clásicamente. Estas interacciones no locales aparecen en teorías de gravitación cuántica, como el modelo de Sachdev-Ye-Kitaev, que conecta gravedad y teoría de campos a través de una dualidad holográfica. Una comprensión de la física de este modelo podría arrojar luz sobre aspectos no resueltos en el campo de la cosmología y la cuántica, como la paradoja de la pérdida de información en agujeros negros. En esta tesis desarrollamos un algoritmo que utiliza recursos polinomiales para la simulación cuántica digital de este tipo de modelos. Nuestro protocolo incluye métodos para extraer información sobre fenómenos no perturbativos y fuera del equilibrio, como la propagación y mezcla de la información en un sistema. Esta propuesta abre una nueva ruta entre teorías de materia condensada, gravedad cuántica e información cuántica. Con ella buscamos comparar y acercar fenómenos exóticos de procesamiento de información en la naturaleza con procesamientos de información en plataformas cuánticas controlables.

Un paradigma distinto de computación respecto a la teoría de Turing de computación clásica y la teoría de computación cuántica es aquel que considera almacenamiento y procesamiento de información analógico. La diferencia fundamental estriba en que en este tratamiento analógico de la información nos encontramos con variables continuas en lugar de discretas. Vamos más allá de las teorías computacionales clásica y cuántica actuales, y sugerimos utilizar recursos físicos descritos por la teoría cuántica de campos abriendo un nuevo camino en el procesamiento de información. Esta teoría está en la base de la descripción de los fenómenos naturales, ya que aún los principios de la física cuántica, el concepto de campo y la relatividad especial. Su formulación viene dada en términos de un número infinito y continuo de grados de libertad, lo que otorgaría unas propiedades diferentes a los procesadores que almacenaran y transformaran información de acuerdo a estas leyes físicas. En los circuitos superconductores hay elementos que se describen por medio de esta teoría cuántica de campos, y en esta tesis proponemos su uso para la simulación de modelos de teoría cuántica de campos, que están más allá de la mecánica cuántica y son difíciles de resolver computacionalmente. Proponemos una simulación cuántica

digital-analógica en circuitos superconductores de dispersión fermión-fermión mediada por un continuo de modos bosónicos. Esta plataforma cuántica contiene de forma natural un acoplo fuerte entre qubits superconductores y un continuo de modos electromagnéticos de las líneas de transmisión abiertas. Conciliamos el método digital desarrollado en la primera parte de la tesis, para la simulación eficiente de fermiones con qubits, con la codificación analógica en las líneas de transmisión de la complejidad del continuo de los modos bosónicos de la teoría de campos que buscamos simular. Este concepto de *complejidad simulando complejidad* cobra protagonismo como idea central de nuestros esfuerzos en simulaciones cuánticas eficientes y escalables de teorías cuánticas de campos. Una consecuencia de este nuevo paradigma de computación es el desarrollo tecnológico de plataformas cuánticas en otras direcciones antes descartadas, no sólo persiguiendo la escalabilidad y controlabilidad de los qubits, sino desarrollando el control de las características físicas de cada una de ellas.

La parte final está dedicada a la combinación de las técnicas de computación anteriores para resolver problemas complejos de química cuántica y aspectos cuánticos de procesos biológicos. Así, hibridamos algoritmos clásicos y protocolos de simulación cuántica digital-analógica para reproducir fenómenos de transporte electrónico en biomoléculas. Se propone usar la metodología eficiente en el cálculo de modelos fermiónicos, desarrollada en la primera parte de la tesis, junto con algoritmos clásicos, para resolver la estructura electrónica de moléculas. Además, consideramos la reproducción de interacciones entre sistemas biológicos y su entorno con simuladores cuánticos digitales-analógicos, en los que proponemos usar la complejidad bosónica de las líneas de transmisión para imitar efectos disipativos y de transporte.

En conclusión, esta tesis engloba técnicas para la simulación cuántica de modelos complejos. Establecemos un diálogo entre la teoría de información cuántica y gravedad cuántica, materia condensada, física de altas energías, y biología y química cuánticas a través de protocolos de simulación cuántica de fermiones, holografía, teoría cuántica de campos y química cuántica. Con nuestros esfuerzos pretendemos influenciar en la forma en que se utilizan las plataformas cuánticas actuales en computación, aprovechando sus recursos más allá de la codificación discreta de la información. La naturaleza es en sí misma un procesador de información, y es necesario explorar experimental y teóricamente cómo los sistemas físicos almacenan y operan con esta información para explorar los límites de la computación y superar las posibilidades actuales.

Acknowledgements

As any simulation, the task of conveying my gratitude and thoughts through few lines is not only impossible, but also entails the continuous mutation of the information originally contained. Because, as any written piece, it lives and changes, and different interpretations of the same words at different times by different readers are not only inevitable, but desirable. I encourage you, reader, to recognize yourself in these lines as an active character who had played a role in the creation of this Thesis, and who is playing a role in its posterior evolution.

I am still too close to this Thesis to have an unaltered global perspective of these four years. Revisiting such period and my identity evolution is an exhausting, painful and rewarding task. Looking back, I barely recognize myself while I think that the essentials remain the same. This has been mostly a period of destruction and reconstruction. The emptying of previous ideas and desires, the fallen purposes and beliefs, the self-examination, the reconciliation with the contradictions, and the consequent self-reinvention are not performed in solitude. People around me have unconsciously leading roles in my life. I want to thank all of them, who had changed me profoundly, and whom I wish I have influenced back.

Firstly, I want to deeply thank my supervisors, Prof. Enrique Solano and Prof. Íñigo Egusquiza, who have always scientifically supported and encouraged me. Prof. Enrique Solano has extended his mentoring labor beyond science, and I appreciate that he shares not only his scientific knowledge, but also other kind of wisdom, that embracing experiences and opinions. He is interested in basically any discipline where the human being can be considered an artist, and from him I have learned the importance of aesthetics in our work as artists. He has been able to conciliate my

interests into the pursue for scientific knowledge, persuading me to consider us not only physicists, but also writers. Prof. Íñigo Egusquiza is one of the most fair and generous people I have ever met. He is always willing to help, listen, and discuss with us the youngest students. I have enjoyed working side by side with him, which has almost gotten me to follow his twisted sense of humor. Especially, I have enjoyed our passionate and elaborated discussions about feminism, linguistics, literature, music, and philosophy, and also those meandering and byzantine discussions stemming from the first ones, which push us to document our arguments with confronting references.

I am aware that I am privileged. Throughout this PhD period, I have had the opportunity to participate in several scientific activities, which have been crucial for my maturation as a researcher. I have been in contact with top-level experimental groups and scientists, and I consider those interactions and collaborations as the most important elements for the development of this Thesis. Usually, one tends to forget the first causes enabling that interactions, but in this case, I met Prof. Göran Wendin in the very first workshop I attended, in Benasque, and later on in many initiatives he organizes. I want to thank him, as coordinator of the SCALEQIT project, for creating such enriching scientific environment which has allowed me to discuss physics around the world. I am grateful to all scientists with whom I have discussed physics, who have taught me more than any book. I would like to mention some of them. I thank Prof. John M. Martinis, and all the members of the experimental group he leads in Santa Barbara, especially Dr. Rami Barends, for all the fruitful discussions. This collaboration was possible thanks to Prof. Michael Geller, whom I met in the mentioned workshop in Benasque, and whom I want to thank for the interesting scientific exchanges we shared there. I feel very grateful to the group of Prof. Rudolf Gross at the Walther-Meissner-Institute in Munich, and especially to my closest collaborators Dr. Alex Baust and Dr. Frank Deppe. Thanks to all of them for our scientific interchanges in my many visits there, their warmth, and the invitations for their Friday barbecues. I have had the pleasure to collaborate with the group of Prof. Dieter Jaksch, at the University of Oxford, and I want to thank them, and in particular Juha M. Kreula for our interesting discussions. I thank deeply Prof. Julian Sonner for inviting me to Geneva, for his patience and kindness, and for being always willing to discuss and teach about the mysteries of quantum gravity. I want to thank as well Prof. Adolfo del Campo, for our collaboration and all our continuous scientific interactions. With all my visits I have broadened my mind, but I want to highlight the one to Waterloo, for the nice scientific environment I could enjoy. For that, I want to thank Prof. Chris Wilson for his invitation and support, and Dr. Pol Forn-Díaz for being such a nice host. My first contact with Dr. Pol Forn-Díaz began long before I actually met him, through his PhD thesis, which was one of my references when I had any doubt about superconducting circuits. Nowadays, I feel grateful for counting with him among my collaborators. I want to thank Dr. Carlos Sabín, who is one of my role models in the scientific career, for our collaborations, for his sense of humor, and for our bar conversations, which I invoke from time to time if I need a guide. Many thanks to Prof. William D. Oliver and his group, at MIT, for our collaboration. In particular, warm thanks to Dr. Dan Campbell for

everything I have learned from him since we start our scientific discussion in Bilbao, which continues up today via our weekly meetings.

This Thesis has been developed at the QUTIS research group in the University of the Basque Country. I want to thank all the QUTISers, the former and present members, who have accompanied me daily in my scientific and personal growth these four years, for the friendly environment and the daily conversations. Inevitably, I have to begin with Dr. Guillermo Romero, who has babysat me in my first steps into this world, during the first years of my research activity. Warm thanks for all I have learned from him, for his friendship, his really infinite patience, and his generosity. Some members have contributed significantly to this Thesis, and I would like to dedicate special words to my closest collaborators. I thank Dr. Lucas Lamata for his support and his huge dedication to science. His immediate disposition when needed has been indeed one of the key ingredients for our work to thrive. I would like to thank as well Dr. Simone Felicetti, former officemate, not only for his (my) desk, but also for our later scientific collaboration. Next, I want to thank a present officemate, Dr. Enrique Rico, for our scientific collaboration, and for our everyday conversations about society, gender, and politics. I really appreciate his sense of humor and open-minded character. Lastly, I would like to thank Dr. Urtzi Las Heras, who started with me this journey and has become a friend, for our collaborations.

I am fortunate, and I would like to mention every single person to whom I feel grateful. However, I will not try this Herculean task of naming all the PhD students, academic staff, and close friends I want to thank. It would not be the first time one forgets a name in this important section, and I'd rather not run the risk of failing. At the University, I have managed to be surrounded by a large growing heterogeneous group of nice people, which I classify one way or another, depending on the day, in overlapping sets. I would like to thank the group of students and friends in the theoretical physics department, in my own department, in the condensed matter department, my bio-friends, and the Basque speakers, although they are included in the previous sets. I thank also the C group, a set almost overlapping with all the previous ones too. Their friendship extends beyond the academic world, to the personal life. I believe that, from this period on, I will treasure some lasting relationships. And they could mutate, but they will remain over time. Outside the University, I want to thank my closest friends, who always support me, although almost all are abroad, and my flatmates, who enrich my life everyday.

I want to thank all of them, because they especially have had leading roles in my life, and have left their marks. The transcendental conversations, the daily companionship, and the shared moments are elementary blocks in who I am today.

And above all, I would like to thank my family. For their unconditional and immutable love and support in this world of fluctuations. My parents and my siblings have taught me more than anyone, not with speeches, but with their daily acts. Of them I try to learn the empathy, the loyalty, the perseverance and the forgiveness.

List of Publications

This thesis is based on the following publications and preprints:

Chapter 2: Digital Quantum Simulation of Fermions with Qubits

1. U. Las Heras, L. García-Álvarez, A. Mezzacapo, E. Solano, and L. Lamata, *Fermionic models with superconducting circuits*, [EPJ Quantum Technology](#) **2**, 8 (2015).
2. R. Barends, L. Lamata, J. Kelly, L. García-Álvarez, A. G. Fowler, A. Megrant, E. Jeffrey, T. C. White, D. Sank, J. Y. Mutus, B. Campbell, Y. Chen, Z. Chen, B. Chiaro, A. Dunsworth, I.-C. Hoi, C. Neill, P. J. J. O'Malley, C. Quintana, P. Roushan, A. Vainsencher, J. Wenner, E. Solano. and J. M. Martinis *Digital quantum simulation of fermionic models with a superconducting circuit*, [Nature Communications](#) **6**, 7654 (2015).
3. J. M. Kreula, L. García-Álvarez, L. Lamata, S. R. Clark, E. Solano, and D. Jaksch, *Few-qubit quantum-classical simulation of strongly correlated lattice fermions*, [EPJ Quantum Technology](#) **3**, 11 (2016).

Chapter 3: Digital Quantum Simulation of Minimal AdS/CFT

4. L. García-Álvarez, I. L. Egusquiza, L. Lamata, A. del Campo, J. Sonner, and E. Solano, *Digital quantum simulation of minimal AdS/CFT*, [arXiv:1607.08560](#) (2016).

Chapter 4: Digital–Analog Quantum Simulations of QFT

5. L. García-Álvarez, J. Casanova, A. Mezzacapo, I. L. Egusquiza, L. Lamata, G. Romero, and E. Solano,
Fermion-fermion scattering in quantum field theory with superconducting circuits,
[Physical Review Letters **114**, 070502 \(2015\)](#).

Chapter 5: DAQS of Quantum Chemistry and Biology

6. L. García-Álvarez, U. Las Heras, A. Mezzacapo, M. Sanz, E. Solano, and L. Lamata,
Quantum chemistry and charge transport in biomolecules with superconducting circuits,
[Scientific Reports **6**, 27836 \(2016\)](#).

Other publications not included in this thesis:

7. U. Las Heras, L. García-Álvarez, A. Mezzacapo, E. Solano, and L. Lamata,
Quantum simulation of spin chains coupled to bosonic modes with superconducting circuits,
[Chapter in R. S. Anderssen et al. \(eds.\), Mathematics for Industry 11 \(Springer Japan, 2015\)](#).
8. A. Baust, E. Hoffmann, M. Haeberlein, M. J. Schwarz, P. Eder, J. Goetz, F. Wulschner, E. Xie, L. Zhong, F. Quijandría, D. Zueco, J.-J. García Ripoll, L. García-Álvarez, G. Romero, E. Solano, K. G. Fedorov, E. P. Menzel, F. Deppe, A. Marx, and R. Gross
Ultrastrong coupling in two-resonator circuit QED,
[Physical Review B **93**, 214501 \(2016\)](#).
9. L. García-Álvarez, S. Felicetti, E. Rico, E. Solano, and C. Sabín,
Entanglement of superconducting qubits via acceleration radiation,
[Scientific Reports **7**, 657 \(2017\)](#).

List of Figures

2.1	Probability P for each state $ ij\rangle$ in the Hubbard model with two fermionic modes	20
2.2	Fidelities for the two-mode Fermi-Hubbard model	21
2.3	Probability P for each state $ ijk\rangle$ in the Hubbard model with three fermionic modes	22
2.4	Sequence of qubit gates for simulating nonlocal fermionic interactions	23
2.5	Collective gates with resonators	24
2.6	Fermionic model with nearest and next-nearest neighbor interactions in a grid	25
2.7	Model and device	26
2.8	Gate construction	28
2.9	QPT of operator anticommutation	29
2.10	Simulation of two fermionic modes	30
2.11	Fermionic model with three modes	31
2.12	Fermionic model with four modes	32
2.13	Simulations with time-varying interactions	34
2.14	DMFT	38
2.15	Nonlinear hybrid quantum-classical scheme	39
2.16	Quantum gates for one Trotter step	42
2.17	Reordering of quantum gates	43
2.18	Time-evolution of the state fidelity	44
2.19	Impurity Green function in the time domain	45

2.20	The retarded impurity Green function and self-energy in the frequency domain	46
2.21	Spectral functions in the metallic and insulating phases	48
2.22	Quasiparticle weight as a function of interaction U	49
3.1	Engineering many-body interactions in trapped-ion qubits	59
3.2	Engineering many-body interactions in superconducting circuits	61
3.3	Digital fidelities of the quantum simulation	64
3.4	Total lower bounds of the state fidelity in trapped ions	65
3.5	Total lower bounds of the state fidelity in superconducting circuits	66
4.1	Circuit QED schematic representation and operation sequence for simulating two-qubit gates coupled to the continuum of bosonic modes in a single Trotter step	73
4.2	Extension to N fermionic modes	76
5.1	Sequence of gates in a single Trotter step of the digital quantum simulation of the electronic Hamiltonian for the H_2 molecule	83
5.2	Digital quantum simulation of electronic Hamiltonian	84
5.3	Total upper bound of errors in digital quantum simulation of electronic Hamiltonian	85
5.4	Scheme of the cQED setup and digital-analog protocol	88
A.1	Pulse sequences in the experiment	98
A.2	Initialization gate sequence	99
A.3	Randomized benchmarking	100
A.4	Digital error for the time-independent simulation	101
A.5	Digital error for the time-dependent simulation	102
A.6	Minimizing leakage of the CZ_ϕ gate	103
C.1	Quantum network to measure contributions to the Green function	111
G.1	Tunable transmon qubit coupled to resonator and transmission line	130

Abbreviations and conventions

We use the following abbreviations throughout the thesis

DMRG Density Matrix Renormalization Group

DMFT Dynamical Mean-Field Theory

QMC Quantum Monte Carlo

NMR Nuclear Magnetic Resonance

AQC Adiabatic Quantum Computation

QFT Quantum Field Theory

JW Jordan–Wigner

cQED Circuit Quantum ElectroDynamics

SYK Sachdev-Ye-Kitaev

CZ_ϕ Controlled- Z_ϕ

AHM Asymmetric Hubbard Model

QPT Quantum Process Tomography

SIAM Single-Impurity Anderson Model
QCD Quantum Chromodynamics
OTO(C) Out-of-Time-Order(-Correlator)
AdS Anti-de-Sitter
CFT Conformal Field Theory
NAdS2 Near-*AdS2*
MS Mølmer-Sørensen
CPW CoPlanar Waveguide
DAQS Digital-Analog Quantum Simulation
CI Configuration Interaction

We set the reduced Planck constant $\hbar = 1$ throughout the thesis. Additionally, the speed of light c is set to 1 in chapter 4 and the corresponding appendix F.

1 Introduction

QUESTIONS regarding the limitation of human knowledge thread through all history of science and philosophy. Our understanding of nature is given in terms of models that capture certain essentials of our restricted perception as observers of the universe. Thus, our knowledge is limited in first place by the accessible data that we can acquire from observations and experiments, and secondly, by our ability to model and handle the mathematical abstract representations of the accessible nature. A model is an idealization that brings together the main aspects of an actual or devised system while disregarding secondary elements. Successful models illuminate the principles that underlie the key observations, and predict unobserved behaviors under new conditions. Therefore, the boundaries of knowledge are set by our ability to produce good quality models, and the possibilities of extracting results from the model development. Since antiquity, we have used different methods for exploring the models we create. For instance, with simulations we imitate in another controllable system the characteristics and behaviors of a model, which represents either a physical or abstract system or process. We can use those accessible and controllable systems to reproduce the evolution over time of such real or invented systems in order to gain insight into their functioning, and predict phenomena in alternative conditions. In general, the procedures of solving the equations that resulted from model development embrace both analytical mathematical derivations, and the use

of physical machines for artificial reproduction and calculation. Evidences indicate that algorithms and computing technologies exist since the beginning of History. We could mention the abacus as an ancient representative technology for numerical computing, or Babylonian methods for factorization and finding square roots as some of the earliest mathematical recipes for calculation.

In 1936, Alan Turing developed an abstract notion of what is an algorithm and formalized the idea of computing [1]. He represented all processes of computation themselves in a universal mathematical model known as Turing machine, capable of reproducing efficiently any given algorithmic process. This disgregation of the concept of calculation and the physical computing machine itself is the seminal idea at the foundations of the theory of computation, which predates the modern digital computer. In the study of the limits of knowledge, exploring the limits of computability is an inevitable step, as important as the exploration of the limits of mathematical representations [2], the development of mathematical logic or philosophy. The theoretical exploration of computability constitutes an upper boundary, which is followed by a classification in terms of the hardness of the problems, a field known as computational complexity theory [3]. It is natural to study the limits of computation attending to the resources that we can avail ourselves of in practice in order to solve problems. For instance, we can consider as intractable those problems for which an algorithm exists, but take longer than the age of the universe to produce an answer. Our possibilities of efficiently extracting results are limited by our storage, energy and time capabilities, and we can differentiate complexity classes according to the rate of growth of the required resources as the input data for characterizing the problem increase. Among the plethora of complexity classes, we identify easy problems as those belonging to the complexity class P, that is, those for which an algorithm can be performed in a time that rises polynomially with the size of the input. However, scientific research faces the challenge of solving more demanding problems in the development of models describing nature. In particular, there is no efficient algorithm hitherto to solve certain problems included in the complexity class NP, for which, on the contrary, a proposed solution can be checked in polynomial time. One of the largest challenges in different fields of research is the simulation of fermionic models, since there one comes up against these computationally hard problems.

A fundamental pillar in the description of nature is the search of the basic constituents of matter. Our many observations at different scales have taught us that we can classify fundamental and composite particles according to their spin quantum number in two types. Particles with integer spin are called bosons, and obey Bose-Einstein statistics; and those with half-integer spin are called fermions, and obey Fermi-Dirac statistics. This profound restriction of nature is condensed in the spin-statistics theorem. It determines the description of fermions via wavefunctions that are antisymmetric under exchange of identical particles, and results in the Pauli exclusion principle, which states that two or more identical fermions cannot exist in the same quantum state. These features entail challenges and difficulties in classical numerical methods, which fail to simulate even simplified toy models of many-particle fermionic systems. In this respect, exact diagonalization techniques are severely lim-

ited by the number of states, which grow exponentially with the system size. This number of states can be truncated in a controlled way for computing the desired properties of the systems via tensor network methods and the Density Matrix Renormalization Group (DMRG) [4, 5, 6, 7, 8]. However, these well-established approaches face computational challenges beyond one spatial dimensional systems. Along these lines, dynamical mean-field theory (DMFT) [9] is another powerful technique capable of capturing some features of interacting fermions, though it still deals with a fermionic quantum many-body problem. It consists in reducing the complexity of the initial fermionic model while imposing a self-consistency condition which guarantees that the properties of the reduced model are those of the former one. Quantum Monte Carlo methods (QMC) [10, 11] are ineffective for fermions due to the sign problem. This numerical problem refers to the difficulty of integrating over a highly oscillatory function with a large number of variables, and has been demonstrated to be NP-hard [12]. In general, the kind of Hamiltonians for which sign-problem free QMC simulations cannot be applied are called nonstoquastic Hamiltonians. Strategies for solving efficiently nonstoquastic Hamiltonians, and in particular fermionic models are worthwhile in many areas, such as nuclear physics, particle physics, and condensed matter physics. In fact, the understanding of strongly correlated fermions would shed light into the principles that rule the behavior of complex quantum materials and structures. Such theoretical advances would also imply immediate technological development, involving phenomena as important as the Mott metal-insulator transition [13, 14], high-temperature superconductivity [15, 16], and colossal magnetoresistance [17].

The challenge of simulating fermions is included in the challenge of simulating general quantum mechanical systems. In quantum physics, the mathematical description of a process requires, in principle, computational resources growing exponentially with system size, as the dimensionality of the Hilbert space increases. This first obstacle in the storage of the input data of the quantum mechanical problem was identified by Richard Feynman, who proposed the simulation of quantum physics with a device which itself is quantum mechanical [18], thus providing us with an unparalleled computational resource. Hence, the notions of hardness in classical complexity theory and their relation with the limits of achievable knowledge must be confronted with this new view of information processing based on quantum effects.

The theory of quantum mechanics gradually arose a century ago, and has entailed a profound revision of our understanding of nature, which has resulted in turn in ground-breaking technologies, such as the laser, the atomic clock, the nuclear magnetic resonance (NMR), and the transistor. The application of the physical laws of the quantum theory with these staggering results is called the first quantum revolution. Nowadays, with growing control over previously untapped quantum effects, which now play a key role, we are paving the way for a second quantum revolution. This embraces applications such as quantum metrology, quantum sensing, quantum communication, quantum simulation, and quantum computing [19]. The theoretical and experimental development of these last two technologies are crucial to pursue the study of nature, and to overcome the present limits of science. Theoretically,

a quantum computer based on quantum bits, or qubits, harnessing properties like quantum superposition, entanglement, and tunneling is able to simulate quantum many-body systems and to perform factorization efficiently [20], which is a known NP problem. It still remains uncertain whether we could build a quantum computer capable of performing a computational task beyond the possibilities of any known algorithm running on classical devices. This *quantum supremacy* has been predicted for fifty-qubit computers [21].

At the same time, a parallel and partially overlapping road for solving mathematical models has been followed by quantum simulations, which consists in the intentional reproduction of the properties of a quantum system in another controllable quantum system. This complementary approach offers means to tackle intractable models and to solve open questions in areas where progress is impeded by the computing limits. A quantum simulation protocol involves the initialization of the system, its controlled evolution, and its final measurement. According to the processing of information, the protocols are classified in two kinds, digital and analog. In digital quantum simulations, the unitary evolution of quantum systems is decomposed and mimicked sequentially in a discrete number of steps [22], which allows the implementation of unnatural dynamics for the quantum simulator at the cost of introducing errors. On the other hand, analog quantum simulations reproduce straightforwardly the dynamics of a given simulated model in the simulating quantum platform, reproducing qualitatively the behavior of the system under study.

Both quantum computing and quantum simulation demand highly controllable quantum platforms for the implementation of simulation protocols. Over the last two decades, different physical architectures have been proposed as quantum information processors, including trapped ions, ultracold atoms, quantum dots, photonic systems, optical networks, and superconducting circuits, among others. The latter is one of the most advanced, reaching a significant level of maturity in terms of coherent control, design versatility, and scalability [23]. This macroscopic solid state system harnesses superconductivity, i.e., the phenomenon of perfect diamagnetism and zero resistivity that characterizes certain materials at very low temperatures. In the superconducting phase, the system is collectively described by a coherent many-body wavefunction with a unique phase, which enables macroscopic variables, such as currents or voltages, to exhibit quantum behavior. The experimental progress in superconducting circuits has made possible the demonstration of both digital and analog quantum simulations.

In this Thesis, we merge different computational paradigms in order to maximize the possibilities of current technology and near-future technology in the pursue of knowledge. With that purpose, we analyze the mathematical models describing nature, and realize that they can be classified in discrete or continuous according to the nature of their variables. A discrete model describes the objects of the system as a discrete set, whereas a continuous model represents the system via continuous variables and functions. This classification is also applicable to models of computability, and, in particular, discrete predominates in the field. After all, the Turing machine is a universal model for all methods of algorithmic computation,

in which both the information about the systems and the operations performed are codified by discrete variables. Turing broadened the scope of his universal model of computation for studying the nature of the human brain, and considered all mental operations as computable processes. At this point, both kind of models, continuum and discrete, became confronted, since he considered the brain as a physical machine characterized by continuous variables. He distinguished between digital and continuous machines [24], and favored discrete computation over analog simulators, arguing that the continuity is not relevant for the function of computation. Even further, he aimed to effectively imitate continuous chaotic phenomena with a discrete system and random choices.

However, most scientific problems have mathematical formulations in the continuum. We consider that the relation between computability and mathematical logic with the physical world and continuous systems needs to be explored theoretically and practically. With the development of quantum mechanics, we have exploited new laws of physics in order to improve computational performance, but the concept of universal quantum computation remains with a discrete structure. The information is encoded digitally into qubits, and its processing is performed through algorithms in a discrete sequence of quantum gates. We contemplate nature itself as a computer, and explore how physical systems store and process information. In principle, the components of quantum platforms are optimized towards universal quantum computing, and thus described in terms of qubits or two-level systems. Along with this usual approach, we analyze the actual resources of quantum platforms, and consider the natural description of the elements in order to propose distinct processors of information. In the arena of quantum technologies, quantum simulators offer possibilities to take advantage straightforwardly of other quantum-mechanical degrees of freedom, which would encode similar degrees of freedom of the simulated quantum system. Quantum annealers, such as the D-Wave processors, and the approach of adiabatic quantum computation (AQC) constitute as well a different paradigm of computation, closest to quantum simulators. In these kind of devices, for which the speedup over classical processors is still unclear, the computation can be reduced to a single gate, ruled by a time-dependent Hamiltonian. The efficiency in their performance has been related with the Hamiltonian complexity, and particularly with nonstoquastic Hamiltonians [25], like those of fermionic models.

With current approaches and their means in mind, we propose to harness device properties beyond quantum mechanics, and we consider the quantum field theory (QFT) description of superconducting elements in order to store and process information. This theory is at the core of the description of nature, since it merges the principles of quantum mechanics, the concept of field, and special relativity, and among its distinct features we encounter the formulation in terms of an infinite and continuum number of degrees of freedom. This continuum in QFT is a unique feature that sets these kind of information processors apart from the Turing model of computation with discrete storage and algorithmic treatment of information. We merge two-paradigms of computation in order to solve QFT models involving fermions in what we term digital-analog quantum simulations. On one hand, we consider discrete

storage of fermionic degrees of freedom in qubits, and continuous encoding of bosonic degrees of freedom in superconducting transmission lines described with QFT. On the other hand, the information is processed digitally in a sequential method, with analog operations based on unitary evolutions described by a continuum of variables. Both storage and processing harness the continuous description of physical systems in order to challenge the current limits of computation.

We contemplate QFT as a general resource for computation, and thus we pursue future mathematical and technological advances in order to encode any computational problem in an ideal device ruled by these laws. Current state-of-the-art of superconducting circuits already provides experiments of scattering of propagating photons in an open transmission line coupled to qubits [26], which is described by QFT. Describing the transport of n -photon Fock states of light has been demonstrated to be computationally hard [27], and we could consider this kind of devices as the processors for solving similar hard problems. Advances in physics and experiments influence the fundamentals of information theory, with simulations being the first link between both worlds. In turn, nature can be deeper understood in terms of information and computational power, and studying the resources of physical systems could help knowledge evolve in unforeseen directions.

In this vein, the study of scrambling of information in physical systems constitutes a key aspect towards the understanding of nature. This phenomenon consists in the spreading of quantum information, initially localized in a subsystem, across a larger system [28, 29]. This notion connects information theory with physical systems and quantum gravity, and enables us to explore computationally the bounds of the scrambling time and whether black holes are the fastest scramblers of information [30]. The fundamentals of physics shed light on the feasibility of simulations, and the consideration of any system as capable of storing and processing information induces revisions and insights into the logic of information and computation.

1.1 What you will find in this Thesis

The road to explore the limits of knowledge and push away the boundaries of computability goes by the conciliation of different computation paradigms implementable in current technologies. In this light, we propose hybrid quantum-classical and quantum digital-analog simulations for fermionic models, which are hard to compute in classical devices due to their description in terms of nonstoquastic Hamiltonians. We discuss the benchmarking and scaling of the simulations in realistic quantum platforms, in the conviction that the advance of science comes through the dialogue between theory and experiments. This Thesis is structured in six chapters, including this introduction and a concluding chapter, and is devoted to the description of quantum simulation protocols which grow in sophistication as we merge different

approaches of computation.

In chapter 2, we provide a method for the efficient quantum simulation of fermionic systems with superconducting circuits. The protocol is based in the suitable use of Jordan–Wigner (JW) mapping, digital decomposition of the evolution, and multi-qubit gates. We study the cases of 1D and 2D Fermi-Hubbard models, involving couplings with nearest and next-nearest neighbors, and the scalability and possible implementation of the method in current technology. In this chapter, we will also report on the consequent experimental demonstration of the proposed digital quantum simulation, which was carried out, in collaboration with us, by the group of John M. Martinis at Google/University of California, Santa Barbara. Finally, we study the combination of feasible digital quantum simulation of fermions with DMFT classical algorithms, thus extending the range of simulatable systems in few-qubit devices.

In chapter 3, we propose the digital quantum simulation of a minimal AdS/CFT model in controllable quantum platforms. We consider the Sachdev-Ye-Kitaev (SYK) model describing interacting Majorana fermions with randomly distributed all-to-all couplings, encoding nonlocal fermionic operators onto qubits to efficiently implement their dynamics via digital techniques. Moreover, we also give a method for probing non-equilibrium dynamics and the scrambling of information. Finally, this approach serves as a protocol for reproducing a simplified low-dimensional model of quantum gravity in trapped ions and superconducting circuits, with the aim to address the gap between exotic information processing in nature and controllable computations.

In chapter 4, we merge digital and analog quantum simulation paradigms, by considering the QFT description of physical nature as a resource in a new path of information processing. We propose a digital-analog quantum simulation of fermion-fermion scattering mediated by a continuum of bosonic modes within a circuit quantum electrodynamics (cQED) scenario. This quantum technology naturally provides strong coupling of superconducting qubits with a continuum of electromagnetic modes in an open transmission line. In this way, we consider the previous protocol for efficiently simulating fermions with qubits, while we consider the continuum complexity of a QFT description of the open transmission line to simulate the continuum complexity of bosonic modes in other QFT. Here, the complexity-simulating-complexity concept becomes a leading paradigm in our effort towards scalable quantum simulations of QFT.

In chapter 5, we introduce the hybridization of quantum digital-analog simulations with classical algorithms for the simulation of quantum chemistry and quantum aspects of biological processes. We propose an efficient protocol for digital quantum simulation of quantum chemistry problems and enhanced digital-analog quantum simulation of transport phenomena in biomolecules with superconducting circuits. Along these lines, we optimally digitize fermionic models of molecular structure with single-qubit and two-qubit gates, by means of the efficient techniques considered in previous chapters. Furthermore, the simulation of the system-environment interactions of biomolecules is addressed with digital-analog approach, in which we introduce analogically bosonic degrees of freedom. Finally, we consider gate-truncated quantum algorithms to allow the study of environmental effects.

Digital Quantum Simulation of Fermions with Qubits

SIMULATING quantum physics with a device which is itself quantum mechanical, a notion Richard Feynman originated [18], is one of the most promising research fields in quantum information, allowing the possibility of solving problems exponentially faster than classical computers.

The key to quantum simulation is mapping a model Hamiltonian onto a physical system. When the physical system natively mimics the model, the mapping can be direct and simulations can be performed using analog techniques. In those cases in which analog quantum simulation is hard or impossible, one may decompose the simulated quantum dynamics in terms of discrete quantum gates through a technique known as digital quantum simulation [22, 31, 32]. It allows the construction of arbitrary interactions, and holds the promise that it can be implemented on an error-corrected quantum computer, but at the cost of many gates. This application of quantum information simulating nature leads to the simulation of fermionic models, since fermions are ubiquitous in nature, appearing in condensed matter systems, chemistry, and high-energy physics.

The universal quantum simulation of fermionic systems is daunting due to their particle statistics [33], and Feynman left as an open question whether it could be done, because of the need for physically implementing nonlocal control. Quantum

simulation of fermionic models is highly desirable, as computing the properties of interacting particles is classically difficult. Classical numerical methods have limited ability to study even significantly simplified toy models of strongly correlated fermions. For instance, exact diagonalization faces exponential scaling with system size, while QMC methods [10, 11] are often crippled by the fermionic sign problem [12], arising from anticommutation. Tensor network methods [4, 5, 6, 7, 8] are powerful in one spatial dimension where they track strong correlations accurately. However, in higher dimensional systems, correlations tend to grow more quickly with system size, making these methods computationally challenging.

Using highly controllable quantum devices to study other quantum systems offers a means to tackle strongly correlated fermion models that are intractable on classical computers. This is vital for understanding complex quantum materials [34] with strong electronic correlations that exhibit a plethora of exciting physical phenomena of immediate technological interest. Examples of such effects include the Mott metal-insulator transition [13, 14], colossal magnetoresistance [17], and high-temperature superconductivity [15, 16].

Thus far, quantum simulation of fermionic models has been mostly restricted to the analogue paradigm, especially with ultracold atoms in optical lattices [35, 36, 37]. Digital simulation approaches can be regarded as a demanding task for any platform, because they require complex sequences of logic gates, especially for nonlocal control, which hinge on carefully constructed interactions between subsets of qubits in a larger system.

In this chapter, we present a method for encoding the simulation of fermionic systems for arbitrary spatial dimensions, long range or short range couplings, and highly nonlinear interactions in qubits. Our method consists in mapping a set of N fermionic modes to N spin operators via the JW transformation [38]. Then, we make use of the Trotter expansion [22, 31, 32] to decompose the unitary evolution of the simulated system in a sequence of quantum gates. For the efficient simulation of fermions in near-future technology, we consider not only purely quantum techniques, but also the hybrid combination of quantum and classical simulations [39, 40].

We focus on a suitable quantum platform and we propose an optimal architecture for the implementation of the model. In particular, we consider superconducting circuits as a candidate platform, although, e.g., trapped ions [41, 42, 43, 44] could also be considered. Superconducting circuits [23] is one of the most advanced quantum technologies in terms of coherent control and scalability aspects. Several analog quantum simulations have been proposed in this quantum platform, e.g., spin models [45], quantum phase transitions [46], spin glasses [47], disordered systems [48], metamaterials [49], time symmetry breaking [50], topological order [51], atomic physics [52], open systems [53], dynamical gauge theories [54], and fermionic models in one dimension [55], among others. Furthermore, digital quantum simulations have been recently proposed for superconducting circuits [56, 57] and two pioneering experiments have been performed [58, 59].

For our purpose, we differentiate two kinds of superconducting setups, those employing pairwise capacitive qubit interactions [60], and the ones employing mi-

crowave resonators to generate nonlocal coupling between the qubits [61]. This way, the many-body interactions [62] of the sequenced evolution are implemented either with a sequence of capacitive two-qubit gates or by fast multiqubit gates mediated by resonators [63]. Our method allows the implementation of highly nonlinear and long-range interactions employing only polynomial resources, which makes it suitable for simulating complex physical problems intractable for classical computers. To this extent, we analyze the simulation of the Fermi-Hubbard model with different superconducting architectures, considering couplings with nearest neighbors and next-nearest neighbors in two-dimensional fermionic lattices.

This chapter is composed of four sections. In section 2.1, we explain the method for decomposing a fermionic dynamics via digital techniques, and we give a description of different proposals for implementing quantum gates for fermions in superconducting circuits, either with pairwise capacitive couplings or via resonators. We consider these tools in the next part, section 2.2, in which we introduce quantum algorithms for the simulation of the Fermi-Hubbard model. In section 2.3, we report on the first experimental realization of a quantum digital simulation of fermionic models with a superconducting quantum circuit, performed by the group of John M. Martinis at Google/University of California, Santa Barbara, in collaboration with us. Finally, in section 2.4, we propose a possible implementation of a proof-of-principle example of an hybrid quantum-classical simulation of strongly correlated fermion models in the thermodynamic limit.

2.1 Encoding of fermions in qubits and quantum gates in superconducting circuits

We consider a method for the efficient quantum simulation of fermionic systems with superconducting circuits, which consists in the suitable use of JW mapping, Trotter decomposition, and multiqubit gates. The JW transformation maps fermionic creation and annihilation operators onto tensor products of spin operators. When the fermionic lattice is two or three-dimensional, it is possible that local fermionic interactions are mapped onto nonlocal spin ones. The JW mapping reads

$$\begin{aligned} b_k^\dagger &= \sigma_k^+ \sigma_{k-1}^z \sigma_{k-2}^z \cdots \sigma_2^z \sigma_1^z, \\ b_k &= (b_k^\dagger)^\dagger, \end{aligned} \tag{2.1}$$

in which $b_k(b_k^\dagger)$ are the fermionic annihilation and creation operators and σ_i^α are the spin operators of the i th site, being σ^α for $\alpha = x, y, z$ the Pauli matrices and $\sigma^+ = (\sigma^x + i\sigma^y)/2$.

Often, the simulating system cannot provide in a simple manner the dynamical structure of the simulated systems. Therefore, one may feel compelled to use digital

methods for implementing unnatural interactions in the controllable system, based on the decomposition of the exact unitary evolution into a sequence of discrete gates [22]. That is, one can use the Trotter formula [31] in order to obtain a polynomial sequence of efficiently implementable gates. The Trotter formula is an approximation of the unitary evolution e^{-iHt} , where H is the simulated Hamiltonian, consisting of M quantum gates $e^{-iH_i t}$ that fulfill the condition $H = \sum_i^M H_i$, with H_i the natural interaction terms of the controllable system. The Trotter expansion can be written as

$$e^{-iHt} \simeq \left(e^{-iH_1 t/l} \dots e^{-iH_M t/l} \right)^l + \sum_{i < j} \frac{[H_i, H_j] t^2}{2l}. \quad (2.2)$$

Here, $e^{-iH_i t}$ are the gates that can be implemented in the controllable system and l is the total number of Trotter steps. By shortening the execution times of the gates and applying the protocol repeatedly, the digitized unitary evolution becomes more accurate. As can be seen in Eq. (2.2), the error estimate in this approximation scales with t^2/l , in such a way that the longer the simulated time is, the more digital steps we need to apply in order to get good fidelities.

We now consider how the JW transformed fermionic models can be implemented in an experimental arrangement based on superconducting circuits. We present two alternative approaches, the first with qubits, and the second with qubits and a transmission line resonator. The first approach involves qubits with nearest-neighbor pairwise couplings, and, in particular, one can obtain the Controlled- Z_ϕ (CZ_ϕ) gate via a capacitive coupling of nearest-neighbor transmon qubits. These CZ_ϕ gates have been implemented with high fidelities of above 99% for a variant of transmon qubits called Xmon qubits [60]. The second approach couples the qubits with a transmission line resonator, introducing multiqubit interactions in a single step. For the case of two qubits, this method leads to the so-called XY gate.

2.1.1 CZ_ϕ gates with capacitive couplings

To perform the CZ_ϕ gate, one qubit is kept at a fixed frequency while the other carries out an adiabatic trajectory near an appropriate resonance of the two-qubit states. By varying the amplitude of this trajectory one can tune the conditional phase ϕ . The unitary for the CZ_ϕ is given by

$$CZ_\phi = \begin{pmatrix} 1 & 0 & 0 & 0 \\ 0 & 1 & 0 & 0 \\ 0 & 0 & 1 & 0 \\ 0 & 0 & 0 & e^{i\phi} \end{pmatrix}. \quad (2.3)$$

2.1.2 XY gates with resonators

The basic Hamiltonian coupling a set of qubits to the resonator has the form of a detuned Jaynes-Cummings model. Both qubits are kept at the same frequency, and the resonator has zero excitations. By adiabatically eliminating the resonator one

obtains, when the resonator is in the vacuum state, the well-known XY model for a pair of qubits l and m as

$$H_{XY} = \frac{g_l g_m}{2\Delta} (\sigma_l^x \sigma_m^x + \sigma_l^y \sigma_m^y). \quad (2.4)$$

Here, Δ is the detuning between the qubit level-spacing and the resonator mode, g_l is the coupling constant between qubit l and the resonator, and σ^x and σ^y are Pauli operators. The XY gate is universal for quantum computation and simulation in combination with single-qubit gates, and is the natural interaction customarily employed in superconducting circuits.

2.1.3 Collective gates with resonators

Quantum simulations of fermionic and bosonic models, as well as quantum chemistry problems, have been recently proposed in trapped ions [44, 64, 65, 66]. In these proposals, the use of nonlocal interactions via a quantum bus, together with digital expansion techniques, which have been implemented in recent ion-trap experimental setups [67, 68], allows us to retrieve arbitrary fermionic dynamics. Most current superconducting circuit setups are composed of superconducting qubits and transmission line resonators [23]. A resonator is a useful tool with several applications such as single-qubit rotations, two-qubit gates between distant spins, and dispersive qubit readout [69]. In this section, we analyze how a resonator permits the efficient reproduction of the dynamics of 2D and 3D fermionic systems.

Recently, the engineering of fast multiqubit interactions with tunable couplings between transmon qubit and a resonator has been proposed [63]. These many-body interactions support the realization of multipartite entanglement [70], topological codes [71], and as we show below, simulation of fermionic systems. Employing two multiqubit gates and a single-qubit rotation, the unitary evolution associated with a tensor product of spin operators can be constructed,

$$U = U_{S_z^2} U_{\sigma^y}(\phi) U_{S_z^2}^\dagger = \exp(i\phi \sigma_1^y \sigma_2^z \sigma_3^z \dots \sigma_k^z), \quad (2.5)$$

where $U_{S_z^2} = \exp(-i\pi/4 \sum_{i < j} \sigma_i^z \sigma_j^z)$ and $U_{\sigma^y}(\phi) = \exp[-i\phi' \sigma_1^{y(x)}]$ for odd(even) k . The phase ϕ' also depends on the number of qubits, i.e., $\phi' = \phi$ for $k = 4n + 1$, $\phi' = -\phi$ for $k = 4n - 1$, $\phi' = -\phi$ for $k = 4n - 2$, and $\phi' = \phi$ for $k = 4n$, where n is a positive integer. Making use of this unitary evolution and introducing single-qubit rotations, it is possible to generate any tensor product of Pauli matrices during a controlled phase that is given in terms of ϕ .

2.2 Quantum algorithms for variations of the Fermi-Hubbard model

In this section, we apply our method to the paradigmatic cases of 1D and 2D Fermi-Hubbard models, involving couplings with nearest and next-nearest neighbors. Although we focus on models with a restricted number of fermionic modes, for the sake of clarity, these techniques are straightforwardly extendable to arbitrary number of fermionic modes in two and three spatial dimensions. These cases are in general mapped into multiqubit gates that can be always polynomially decomposed into sets of two-qubit gates, as shown below in Eq. (2.5). In the last part of section 2.1, we focus on another cQED platform that uses resonators instead of direct qubit couplings to mediate the interactions.

The Fermi-Hubbard dynamics is a condensed matter model describing traveling electrons in a lattice. The model captures the competition between the kinetic energy of the electrons, discretized in a lattice and encoded in a hopping term, with their Coulomb interaction that is expressed by a nonlinear term. We begin by considering a small lattice realizable with current technology. We consider the Fermi-Hubbard-like model for three spinless fermions with open boundary conditions,

$$H = -h \left(b_1^\dagger b_2 + b_2^\dagger b_1 + b_2^\dagger b_3 + b_3^\dagger b_2 \right) + U \left(b_1^\dagger b_1 b_2^\dagger b_2 + b_2^\dagger b_2 b_3^\dagger b_3 \right). \quad (2.6)$$

Here, b_m^\dagger and b_m are fermionic creation and annihilation operators for the site m .

We will use the JW transformation in our derivation to encode the fermionic operators into tensor products of Pauli matrices. We will show below that the latter may be efficiently implemented in superconducting circuits. The JW mapping reads,

$$\begin{aligned} b_1^\dagger &= \sigma_1^+, & b_2^\dagger &= \sigma_2^+ \sigma_1^z, \\ b_3^\dagger &= \sigma_3^+ \sigma_2^z \sigma_1^z. \end{aligned} \quad (2.7)$$

Thus, we rewrite the Hamiltonian in Eq. (2.6) in terms of spin-1/2 operators,

$$H = \frac{h}{2} (\sigma_2^x \sigma_1^x + \sigma_2^y \sigma_1^y + \sigma_3^x \sigma_2^x + \sigma_3^y \sigma_2^y) + \frac{U}{4} (\sigma_3^z \sigma_2^z + \sigma_2^z \sigma_1^z + \sigma_3^z + 2\sigma_2^z + \sigma_1^z). \quad (2.8)$$

Here, the different interactions can be simulated via digital techniques using a specific sequence of gates. We will first consider the associated Hamiltonian evolution in terms of $\exp(-i\phi\sigma_\ell^z\sigma_m^z)$ interactions between pairs of qubits ℓ and m . These can be implemented in small steps of CZ_ϕ gates, where an average single-qubit gate and two-qubit gate fidelities of 99.92% and up to 99.4%, respectively, have been recently achieved [60]. One can then use the following relations,

$$\begin{aligned} \sigma_\ell^x \sigma_m^x &= R_y^{(\ell)} \left(\frac{\pi}{2} \right) R_y^{(m)} \left(\frac{\pi}{2} \right) \sigma_\ell^z \sigma_m^z R_y^{(\ell)} \left(-\frac{\pi}{2} \right) R_y^{(m)} \left(-\frac{\pi}{2} \right), \\ \sigma_\ell^y \sigma_m^y &= R_x^{(\ell)} \left(-\frac{\pi}{2} \right) R_x^{(m)} \left(-\frac{\pi}{2} \right) \sigma_\ell^z \sigma_m^z R_x^{(\ell)} \left(\frac{\pi}{2} \right) R_x^{(m)} \left(\frac{\pi}{2} \right), \end{aligned} \quad (2.9)$$

in which $R_j^{(s)}(\theta) = \exp(-i\frac{\theta}{2}\sigma_s^j)$ denote local rotations along the j th axis of the Bloch sphere acting on qubit s . We also consider the compact notation $R_\alpha^{(\ell m \dots s)}(\phi) = R_\alpha^{(\ell)}(\phi)R_\alpha^{(m)}(\phi) \dots R_\alpha^{(s)}(\phi)$ for local rotations in different qubits.

The evolution operator associated with the Hamiltonian in Eq. (2.8) can be expressed in terms of $\exp(-i\phi\sigma_\ell^z\sigma_m^z)$ interactions. Moreover, the operators may be rearranged in a more suitable way in order to optimize the number of gates and eliminate global phases,

$$e^{-iHt} \approx \left[R_y^{(23)}\left(\frac{\pi}{2}\right) e^{-i\frac{\hbar}{2}\sigma_2^z\sigma_3^z\frac{t}{n}} R_y^{(23)}\left(-\frac{\pi}{2}\right) R_y^{(12)}\left(\frac{\pi}{2}\right) e^{-i\frac{\hbar}{2}\sigma_1^z\sigma_2^z\frac{t}{n}} R_y^{(12)}\left(-\frac{\pi}{2}\right) \right. \\ \times R_x^{(23)}\left(-\frac{\pi}{2}\right) e^{-i\frac{\hbar}{2}\sigma_2^z\sigma_3^z\frac{t}{n}} R_x^{(23)}\left(\frac{\pi}{2}\right) R_x^{(12)}\left(-\frac{\pi}{2}\right) e^{-i\frac{\hbar}{2}\sigma_1^z\sigma_2^z\frac{t}{n}} R_x^{(12)}\left(\frac{\pi}{2}\right) \\ \left. \times e^{-i\frac{U}{4}\sigma_2^z\sigma_3^z\frac{t}{n}} e^{-i\frac{U}{2}\sigma_2^z\frac{t}{n}} e^{-i\frac{U}{4}\sigma_3^z\frac{t}{n}} e^{-i\frac{U}{4}\sigma_1^z\sigma_2^z\frac{t}{n}} e^{-i\frac{U}{4}\sigma_1^z\frac{t}{n}} \right]^n. \quad (2.10)$$

If we consider that rotations applied on qubit s follow $R_j^{(s)}(\alpha)R_j^{(s)}(\beta) = R_j^{(s)}(\alpha + \beta)$, the sequence of gates for one Trotter step in the digital simulation of the Hubbard model with three qubits is shown in Table 2.1. There, gates A and B are two-qubit gates written in terms of $\exp(-i\phi\sigma_\ell^z\sigma_m^z)$ interactions, $A = \exp(-i\frac{\hbar}{2}\sigma_\ell^z\sigma_m^z\frac{t}{n})$ and $B = \exp(-i\frac{U}{4}\sigma_\ell^z\sigma_m^z\frac{t}{n})$. Z_1 and Z_2 are single-qubit phases, $Z_1 = \exp(-i\frac{U}{4}\sigma_\ell^z\frac{t}{n})$ and $Z_2 = \exp(-i\frac{U}{2}\sigma_\ell^z\frac{t}{n})$, while X_α and Y_α are rotations along the x and y axis, respectively.

The $\exp(-i\phi\sigma_\ell^z\sigma_m^z)$ interaction can be implemented in small steps with optimized CZ_ϕ gates, since

$$\exp\left(-i\frac{\phi}{2}\sigma_\ell^z\sigma_m^z\right) = \begin{pmatrix} 1 & 0 & 0 & 0 \\ 0 & e^{i\phi} & 0 & 0 \\ 0 & 0 & e^{i\phi} & 0 \\ 0 & 0 & 0 & 1 \end{pmatrix}, \quad (2.11)$$

where we have dropped constant terms. Quantum circuits for simulating these gates are shown in Tables 2.2 and 2.3. In the Tables, X and Y are π pulses.

Table 2.1: Sequence of gates for one Trotter step of Hamiltonian in Eq. (2.6).

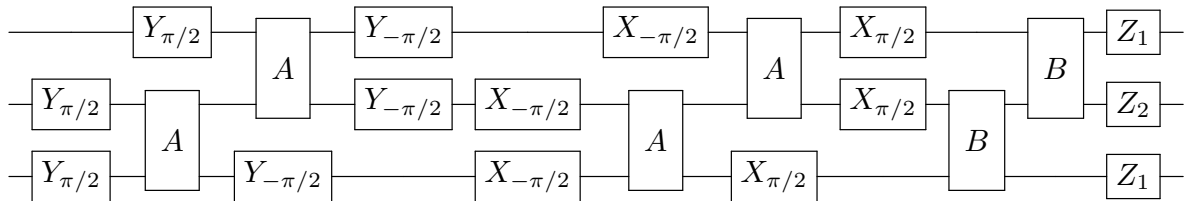
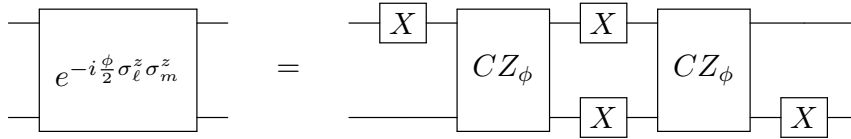
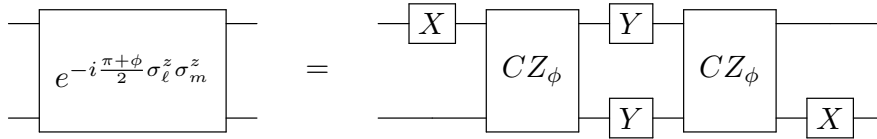


Table 2.2: Two-qubit gates in terms of the optimized CZ_ϕ gate and X π pulses.

 Table 2.3: Two-qubit gates in terms of the optimized CZ_ϕ gate and Y π pulses.


2.2.1 Asymmetric Hubbard model

Here, we include the analysis of the fermionic asymmetric Hubbard model (AHM) for 4 qubits employed in section 2.3.4. Firstly, we present the model in terms of spin operators via the JW transformation, and describe different limits of the model. Secondly, we analyze the digital quantum simulation in terms of Trotter steps involving the optimized gates CZ_ϕ .

The AHM is a variation of the Hubbard model that describes anisotropic fermionic systems. Here, we are going to consider this model for two different fermionic species, that could represent spins, interacting with each other by the Coulomb term, and two lattice sites. The operators for this model have two indices, A_{ij} , where i and j indicate the site position and kind of particle, respectively. Since the fermions might have different masses, we have no reason to assume that the hopping terms will be the same. We can write the Hamiltonian for two sites, x and y , and two kinds of fermions, 1 and 2, as

$$\begin{aligned}
 H = & -V_1 \left(b_{x1}^\dagger b_{y1} + b_{y1}^\dagger b_{x1} \right) - V_2 \left(b_{x2}^\dagger b_{y2} + b_{y2}^\dagger b_{x2} \right) \\
 & + U_x b_{x1}^\dagger b_{x1} b_{x2}^\dagger b_{x2} + U_y b_{y1}^\dagger b_{y1} b_{y2}^\dagger b_{y2},
 \end{aligned} \tag{2.12}$$

in which b_{mi}^\dagger and b_{mi} are fermionic creation and annihilation operators of the kind of particle i for the site m . For the sake of simplicity, in section 2.3.4 we use $b_1^\dagger, b_2^\dagger, b_3^\dagger, b_4^\dagger$, for $b_{x1}^\dagger, b_{y1}^\dagger, b_{y2}^\dagger, b_{x2}^\dagger$.

The JW transformation will be used in our derivation to relate the fermionic and antifermionic operators with tensor products of Pauli matrices, which are operators that we can simulate in the superconducting circuit setup. In this case, we consider

the relations

$$\begin{aligned} b_{x1}^\dagger &= \sigma_1^+, & b_{y1}^\dagger &= \sigma_2^+ \sigma_1^z, \\ b_{y2}^\dagger &= \sigma_3^+ \sigma_2^z \sigma_1^z, & b_{x2}^\dagger &= \sigma_4^+ \sigma_3^z \sigma_2^z \sigma_1^z. \end{aligned} \quad (2.13)$$

Then, Hamiltonian in Eq. (2.12) is rewritten in terms of spin-1/2 operators as

$$\begin{aligned} H &= \frac{V_1}{2} (\sigma_2^x \sigma_1^x + \sigma_2^y \sigma_1^y) + \frac{V_2}{2} (\sigma_4^x \sigma_3^x + \sigma_4^y \sigma_3^y) \\ &+ \frac{U_x}{4} (\sigma_4^z \sigma_1^z + \sigma_1^z + \sigma_4^z) + \frac{U_y}{4} (\sigma_3^z \sigma_2^z + \sigma_2^z + \sigma_3^z), \end{aligned} \quad (2.14)$$

where the different interactions can be simulated via digital techniques in terms of single-qubit and CZ_ϕ gates.

We consider the digital quantum simulation of the dynamics of Hamiltonian in Eq. (2.14). As explained previously in section 2.1, the Trotter expansion consists of dividing the time t into n time intervals of length t/n , and applying sequentially the evolution operator of each term of the Hamiltonian for each time interval. In this case the evolution operators are associated with the different summands of the Hamiltonian.

In order to describe the digital simulation in terms of Trotter steps involving the optimized gates CZ_ϕ , we will first consider the Hamiltonian in terms of $\exp(-i\phi\sigma_\ell^z\sigma_m^z/2)$ interactions. We take into account the relations in Eq. (2.9).

The evolution operator associated with Hamiltonian in Eq. (2.14) in terms of $\exp(-i\phi\sigma_\ell^z\sigma_m^z/2)$ interactions is

$$\begin{aligned} e^{-iHt} &\approx \prod_k \left(e^{-iH_k \frac{t}{n}} \right)^n \\ &\approx \left[R_y^{(12)} \left(\frac{\pi}{2} \right) e^{-i\frac{V_1}{2}\sigma_2^z\sigma_1^z\frac{t}{n}} R_y^{(12)} \left(-\frac{\pi}{2} \right) R_x^{(12)} \left(-\frac{\pi}{2} \right) e^{-i\frac{V_1}{2}\sigma_2^z\sigma_1^z\frac{t}{n}} R_x^{(12)} \left(\frac{\pi}{2} \right) \right. \\ &\quad \times R_y^{(34)} \left(\frac{\pi}{2} \right) e^{-i\frac{V_2}{2}\sigma_4^z\sigma_3^z\frac{t}{n}} R_y^{(34)} \left(-\frac{\pi}{2} \right) R_x^{(34)} \left(-\frac{\pi}{2} \right) e^{-i\frac{V_2}{2}\sigma_4^z\sigma_3^z\frac{t}{n}} R_x^{(34)} \left(\frac{\pi}{2} \right) \\ &\quad \left. \times e^{-i\frac{U_x}{4}\sigma_4^z\sigma_1^z\frac{t}{n}} e^{-i\frac{U_x}{4}\sigma_1^z\frac{t}{n}} e^{-i\frac{U_x}{4}\sigma_4^z\frac{t}{n}} e^{-i\frac{U_y}{4}\sigma_3^z\sigma_2^z\frac{t}{n}} e^{-i\frac{U_y}{4}\sigma_2^z\frac{t}{n}} e^{-i\frac{U_y}{4}\sigma_3^z\frac{t}{n}} \right]^n. \end{aligned} \quad (2.15)$$

Note that, in principle, the ordering of the gates inside a Trotter step does not have a sizable effect as far as there are enough Trotter steps. Here, the number of Trotter steps is limited, n approximately ≤ 10 , and different orderings will have different results. The different values in the orderings differ in a $O(1)$ constant, while the global digital error depends on the number of Trotter steps n as $1/n$. The difference in errors due to different orderings does not depend on n .

If we consider the Trotter error, the fidelity could increase with an optimal ordering where we group terms of the Hamiltonian that commute with each other. Nevertheless, from the experimental point of view, the operators can be rearranged in a more suitable way in order to optimize the number of gates and eliminate global phases. Hence, we must look for the optimal ordering by considering both aspects.

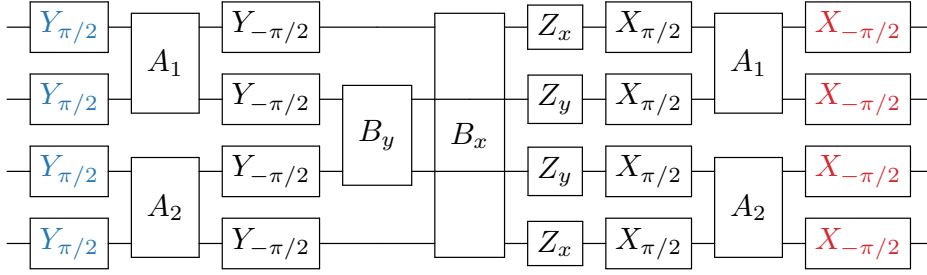
2.2 Quantum algorithms for variations of the Fermi-Hubbard model

Here, we simply rearrange the operators in order to optimize the number of gates. If we consider that $R_j^{(s)}(\alpha) + R_j^{(s)}(\beta) = R_j^{(s)}(\alpha + \beta)$ for a qubit s , then

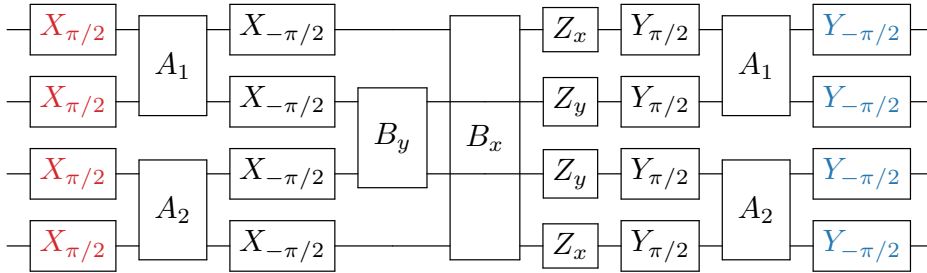
$$\begin{aligned}
 e^{-iHt} \approx & \prod_{i=1}^{n/2} \left[R_y^{(1234)}\left(\frac{\pi}{2}\right) e^{-i\frac{V_1}{2}\sigma_2^z\sigma_1^z\frac{t}{n}} e^{-i\frac{V_2}{2}\sigma_4^z\sigma_3^z\frac{t}{n}} R_y^{(1234)}\left(-\frac{\pi}{2}\right) \right. \\
 & \times e^{-i\frac{U_x}{4}\sigma_4^z\sigma_1^z\frac{t}{n}} e^{-i\frac{U_x}{4}\sigma_1^z\frac{t}{n}} e^{-i\frac{U_x}{4}\sigma_4^z\frac{t}{n}} e^{-i\frac{U_y}{4}\sigma_3^z\sigma_2^z\frac{t}{n}} e^{-i\frac{U_y}{4}\sigma_2^z\frac{t}{n}} e^{-i\frac{U_y}{4}\sigma_3^z\frac{t}{n}} \\
 & \times \left. R_x^{(1234)}\left(-\frac{\pi}{2}\right) e^{-i\frac{V_1}{2}\sigma_2^z\sigma_1^z\frac{t}{n}} e^{-i\frac{V_2}{2}\sigma_4^z\sigma_3^z\frac{t}{n}} R_x^{(1234)}\left(\frac{\pi}{2}\right) \right]_{2i-1} \\
 & \times \left[R_x^{(1234)}\left(-\frac{\pi}{2}\right) e^{-i\frac{V_1}{2}\sigma_2^z\sigma_1^z\frac{t}{n}} e^{-i\frac{V_2}{2}\sigma_4^z\sigma_3^z\frac{t}{n}} R_x^{(1234)}\left(\frac{\pi}{2}\right) \right. \\
 & \times e^{-i\frac{U_x}{4}\sigma_4^z\sigma_1^z\frac{t}{n}} e^{-i\frac{U_x}{4}\sigma_1^z\frac{t}{n}} e^{-i\frac{U_x}{4}\sigma_4^z\frac{t}{n}} e^{-i\frac{U_y}{4}\sigma_3^z\sigma_2^z\frac{t}{n}} e^{-i\frac{U_y}{4}\sigma_2^z\frac{t}{n}} e^{-i\frac{U_y}{4}\sigma_3^z\frac{t}{n}} \\
 & \times \left. R_y^{(1234)}\left(\frac{\pi}{2}\right) e^{-i\frac{V_1}{2}\sigma_2^z\sigma_1^z\frac{t}{n}} e^{-i\frac{V_2}{2}\sigma_4^z\sigma_3^z\frac{t}{n}} R_y^{(1234)}\left(-\frac{\pi}{2}\right) R_y^{(1)}\left(-\frac{\pi}{2}\right) \right]_{2i}. \quad (2.16)
 \end{aligned}$$

This decomposition between even and odd Trotter steps is suitable in order to simplify rotations in x and y , and, therefore, avoid higher number of gates.

The sequence of gates for one odd Trotter step in the digital simulation of the Hubbard model with four qubits is

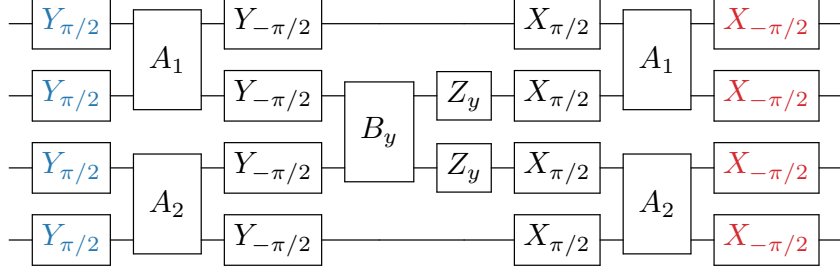


And for one even Trotter step,

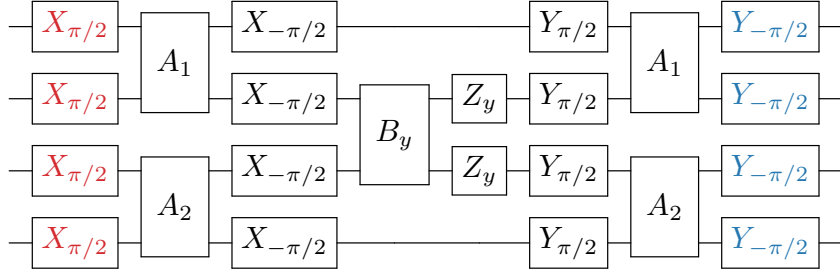


The gates A_i and B_j are two-qubit gates in terms of the $\exp[-i(\phi/2)\sigma_\ell^z\sigma_m^z]$ interactions, $A_i = \exp(i\frac{V_i}{2}\sigma_\ell^z\sigma_m^z\frac{t}{n})$ and $B_j = \exp(-i\frac{U_j}{4}\sigma_\ell^z\sigma_m^z\frac{t}{n})$. The Z_i gates are single-qubit rotations $Z_i = \exp(-i\frac{U_i}{4}\sigma^z\frac{t}{n})$, and X_α and Y_α are rotations along the x and y axis, respectively.

In order to avoid the gate B_x between the first and the fourth qubit, we can consider a particular case of the AHM, with $U_x = 0$. In this case, the circuit is the same but without the B_x and the Z_x gates. That is, for one odd Trotter step,



And for one even Trotter step,



It is important to note that, for $n = 2$ Trotter steps, the red gates cancel each other, and we reduce the number of gates that should be applied. For $n > 2$, the blue gates also cancel each other except in the beginning and in the end of the quantum simulation. The relation among the values of the parameters in the numerical simulations and the values of the phases in the gates is the following

$$A_1 = \exp(-i \frac{V_1}{2} \sigma_\ell^z \sigma_m^z \frac{t}{n}) \quad \rightarrow \quad \Phi_{A_1} = \frac{V_1}{2} \frac{t}{n}$$

$$A_2 = \exp(-i \frac{V_2}{2} \sigma_\ell^z \sigma_m^z \frac{t}{n}) \quad \rightarrow \quad \Phi_{A_2} = \frac{V_2}{2} \frac{t}{n}$$

$$B_y = \exp(-i \frac{U_y}{4} \sigma_\ell^z \sigma_m^z \frac{t}{n}) \quad \rightarrow \quad \Phi_{B_y} = \frac{U_y}{4} \frac{t}{n}$$

$$Z_y = \exp(-i \frac{U_y}{4} \sigma^z \frac{t}{n}) \quad \rightarrow \quad \Phi_2 = \frac{U_y}{4} \frac{t}{n} .$$

In summary, the fermionic AHM with two excitations, one for each kind of fermion, has been analysed and expressed in terms of simulatable spin operators. We have considered the digital quantum simulation in terms of Trotter steps involving the optimized gates CZ_ϕ . This is the four-mode system experimentally simulated in section 2.3.4.

2.2.2 Numerical analysis of the errors

Here, we present numerical simulations for specific values of model parameters, that is, the time t , the hopping coefficient h , and nonlinear coupling U . We compute

numerically the results for the proposed model with three fermionic modes, as well as the equivalent one with two fermionic modes, for the sake of completeness. In Figs. 2.1 and 2.3, we show the results of the Fermi-Hubbard model with two and three fermionic modes, respectively, for $n = 4$ and $n = 10$ Trotter steps. As shown below, the achieved fidelities can be large at the end of each digital protocol.

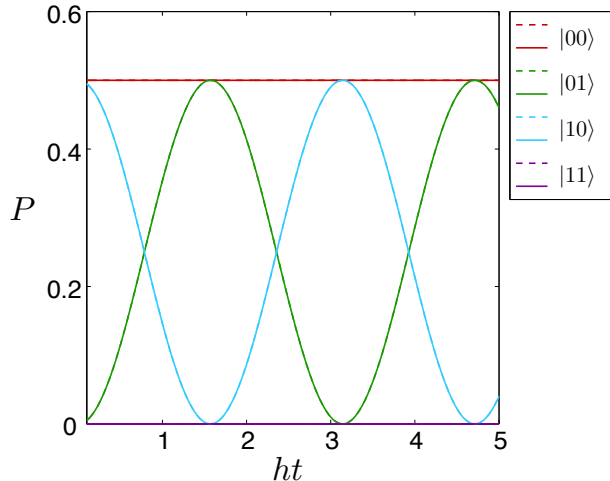


Figure 2.1: **Probability P for each state $|ij\rangle$ in the Hubbard model with two fermionic modes.** We obtain the same dynamics for hopping $h = 1$, and values of the potential $U = 1$ and $U = 0.5$. We also consider in both cases different number of Trotter steps, $n = 4$ and $n = 10$, and observe the same result with no Trotter error. The initial state is in all cases $(|00\rangle + |10\rangle)/\sqrt{2}$. Dashed lines refer to numerical solutions without Trotter approximation, and solid lines to numerical solutions with Trotter approximation. The absence of Trotter error comes from the fact that the second term in the Trotter expansion in Eq. (2.2), i.e., the term proportional to the sum of commutators, is zero for this specific model, allowing us to perform the simulation in a single Trotter step.

In Fig. 2.2, we plot the fidelities of the digitally-evolved state with respect to the ideal dynamics associated with Eq. (2.6), where $\theta \equiv Ut$, for $n = 4$ Trotter steps. The fidelities are defined as $F = |\langle \Psi_T | \Psi \rangle|^2$, with $|\Psi\rangle$ and $|\Psi_T\rangle$ the states evolved under the exact unitary evolution and the digital one, respectively. Fidelities well above 90% can be achieved for a large fraction of the considered period.

Summarizing, we have analyzed the digital quantum simulation of the Fermi-Hubbard model with three fermionic modes in terms of simulatable spin operators with nearest neighbor interactions. Furthermore, we have considered the digital steps involving optimized gates CZ_ϕ .

In Fig. 2.4, we show how to implement the i th-site hopping terms of a system made of N fermionic sites onto N superconducting qubits coupled to a quantum bus. Notice that local interactions between nearest and next-nearest neighbors in the square lattice involve several qubits in the experimental setup.

In order to benchmark our protocol with a specific example, we consider the Hamiltonian of the Fermi-Hubbard model with both nearest and next-nearest neigh-

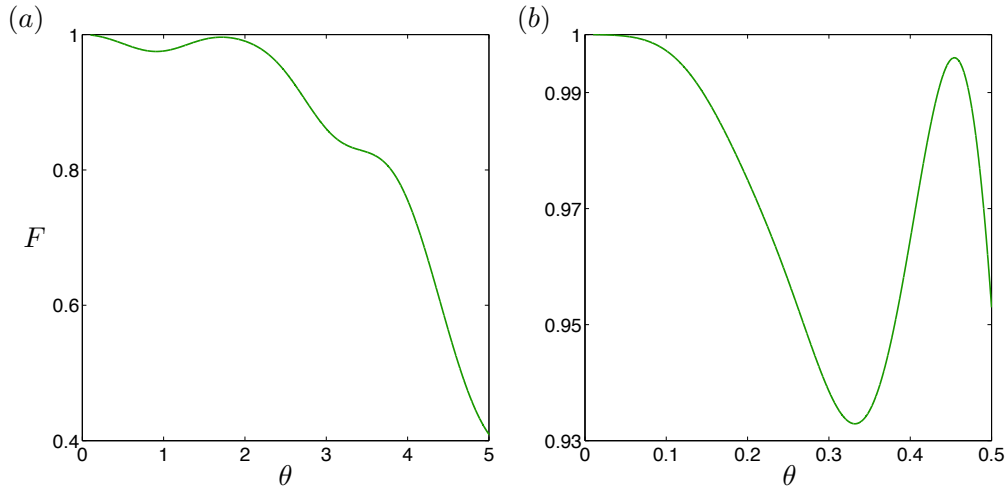


Figure 2.2: **Fidelities for the two-mode Fermi-Hubbard model.** We show the fidelities obtained for the dynamics of Eq. (2.6), where $\theta \equiv Ut$, for $n = 4$ Trotter steps. The physical parameters used are hopping $h = 1$, together with (a) $U = 1$, and (b) $U = 0.5$. The initial state is in both cases $(|011\rangle + |101\rangle)/\sqrt{2}$.

bor couplings,

$$\begin{aligned}
 H = & \sum_{\langle i,j \rangle} \left[-h(b_i^\dagger b_j + b_j^\dagger b_i) + U \left(n_i - \frac{1}{2} \right) \left(n_j - \frac{1}{2} \right) \right] \\
 & + \sum_{\langle\langle i,j \rangle\rangle} \left[-h'(b_i^\dagger b_j + b_j^\dagger b_i) + U' \left(n_i - \frac{1}{2} \right) \left(n_j - \frac{1}{2} \right) \right]. \quad (2.17)
 \end{aligned}$$

where $\langle i, j \rangle$ ($\langle\langle i, j \rangle\rangle$) denote sum extended to nearest (next-nearest) neighbors, h (h') is the hopping parameter and U (U') is the interaction for nearest (next-nearest) neighbors. Here, b_i (b_i^\dagger) is the fermionic annihilation (creation) operator for site i , that satisfies the anticommutation relation $\{b_i, b_j^\dagger\} = \delta_{i,j}$, and $n_i = b_i^\dagger b_i$ is the fermionic number operator.

Employing the method introduced before, it is possible to simulate any fermionic dynamics. Let us analyze the interactions we need to simulate in a superconducting qubit platform considering a two-dimensional lattice of 4×4 sites. Taking as an example the 6th site in Fig. 2.5, the simulation of hopping terms with sites 5 and 7 requires only two-qubit gates, since they are nearest neighbors in the order chosen for the mapping. However, the simulation of hopping terms between sites 2 and 6 involves 5 superconducting qubits, $b_6^\dagger b_2 + b_2^\dagger b_6 = -(\sigma_2^x \sigma_3^z \sigma_4^z \sigma_5^z \sigma_6^x + \sigma_2^y \sigma_3^z \sigma_4^z \sigma_5^z \sigma_6^y)/2$. The same thing happens for next-nearest neighbor interactions, which are simulated employing multiqubit gates consisting of either 4 or 6 spin operators. On the other hand, interaction terms between qubits i and j can be implemented by evolving the system with a global interaction involving all the qubits with labels between i and j , decoupling the rest of the qubits from the resonator.

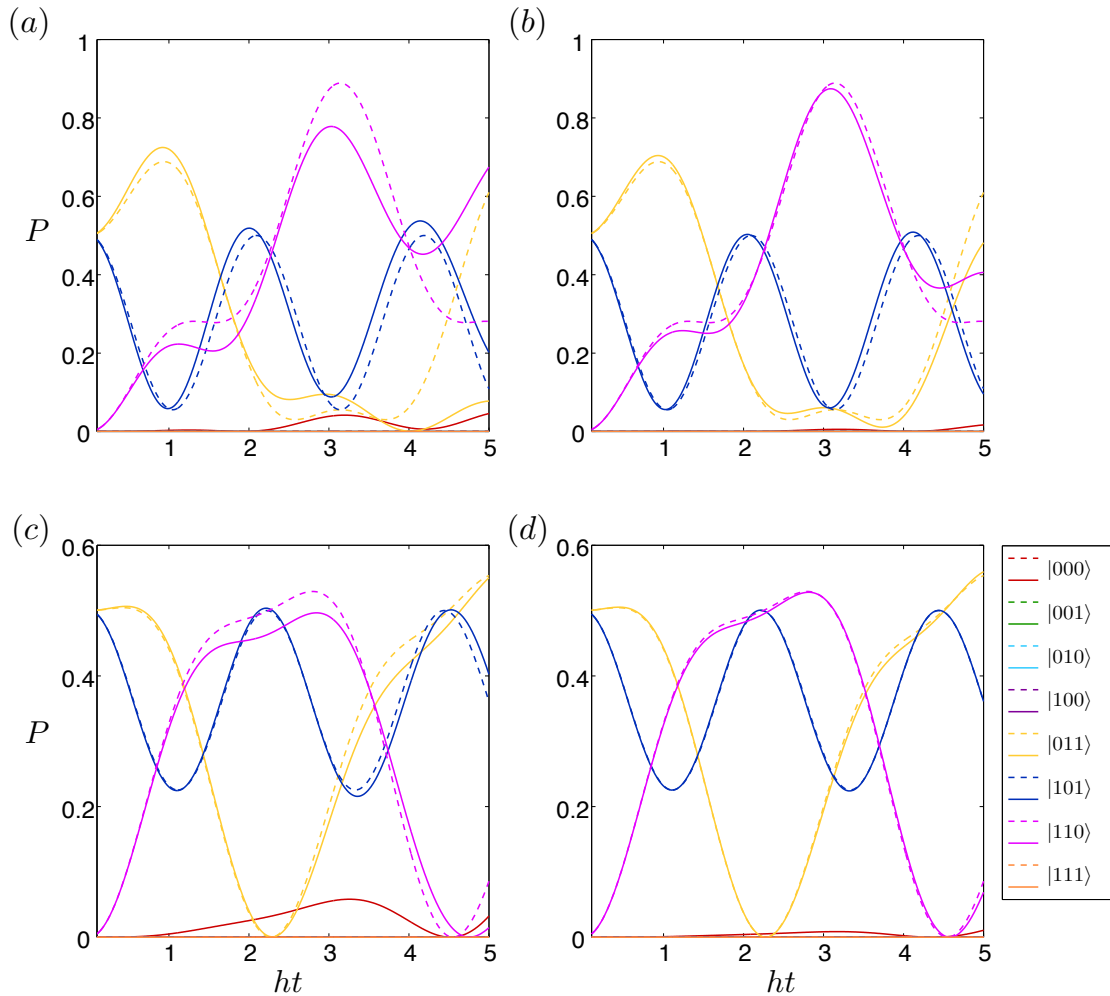


Figure 2.3: **Probability P for each state $|ijk\rangle$ in the Hubbard model with three fermionic modes.** The physical parameters used are hopping $h = 1$, together with (a) $U = 1$ and number of Trotter steps $n = 4$, (b) $U = 1$ and $n = 10$, (c) $U = 0.5$ and $n = 4$, and (d) $U = 0.5$ and $n = 10$. The initial state is in all cases $(|011\rangle + |101\rangle)/\sqrt{2}$. Dashed lines refer to numerical solutions without Trotter approximation, and solid lines to numerical solutions with Trotter approximation.

The number of gates needed for realizing this simulation depends linearly on the number of qubits. Assuming that N is the number of fermionic sites in a 2D square lattice, the number of hopping and interaction terms that we need to simulate is $2\sqrt{N}(\sqrt{N} - 1)$ for nearest neighbors and $2(\sqrt{N} - 1)^2$ for next-nearest neighbors. As can be seen in Fig. 2.4, every hopping term involving qubits with distant labels is made of 8 single-qubit rotations and 4 multiqubit gates. On the other hand, interaction terms can be simulated by applying just one multiqubit gate.

The superconducting setup that we are considering for this quantum simulation is composed of N transmon qubits coupled to a single resonator. In order to perform

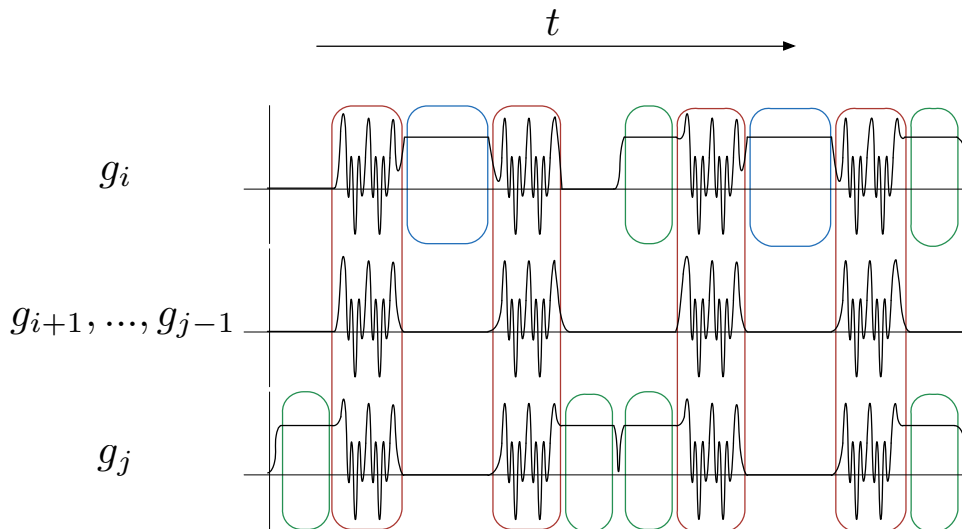


Figure 2.4: **Sequence of qubit gates for simulating nonlocal fermionic interactions.** We indicate the scheme of the magnitude of the couplings, g_l , of the superconducting qubits i, \dots, j with the transmission line resonator as a function of time for the simulation of fermionic hopping terms. This sketch shows how sequences of rotations and nonlocal multiqubit gates gives place to interactions of the form $b_i^\dagger b_j + b_j^\dagger b_i$, which can be written in terms of spin operators as $-(\sigma_i^x \sigma_{i+1}^z \dots \sigma_{j-1}^z \sigma_j^x + \sigma_i^y \sigma_{i+1}^z \dots \sigma_{j-1}^z \sigma_j^y)/2$. Multiqubit gates are marked with red color where all the couplings suffer a frequency modulation [63]. Single-qubit rotations are implemented by coupling a single qubit to the resonator. They are marked with green color for a phase of $\pi/4$ and with blue for a phase-dependent single-qubit rotation, $U_{\sigma^y}(\phi)$, where the phase ϕ is proportional to the simulated time evolution of the hopping term. Note that all the qubits between sites i and j play a role in this interaction in order to fulfill the JW mapping.

highly nonlocal interactions between two distant qubits, every qubit with label inside the interval spanned by them should interact with the same resonator. Coupling several qubits to just one resonator can be a difficult task wherever the number of simulated sites is large enough. Therefore, we propose an optimized architecture for the simulation of Fermi-Hubbard model with up to next-nearest neighbors in 2D. As shown in Fig. 2.5, we propose a setup with N superconducting circuits distributed in a square lattice [72]. Sequentially coupling two rows by a single transmission line resonator, one can reduce the number of qubits coupled to a single resonator. Nevertheless, all the interactions needed for satisfying the JW mapping can be simulated with this architecture. Furthermore, one can achieve a speedup of the protocol by performing interactions that involve different qubits in a parallel way, e.g., the interaction between qubits 2 and 3 and the one between qubits 5 and 9 can be performed simultaneously using resonators 1 and 2, respectively.

In order to benchmark our protocol, we study its efficiency by computing the error associated with a digital decomposition. To this extent, we analyze the occupation

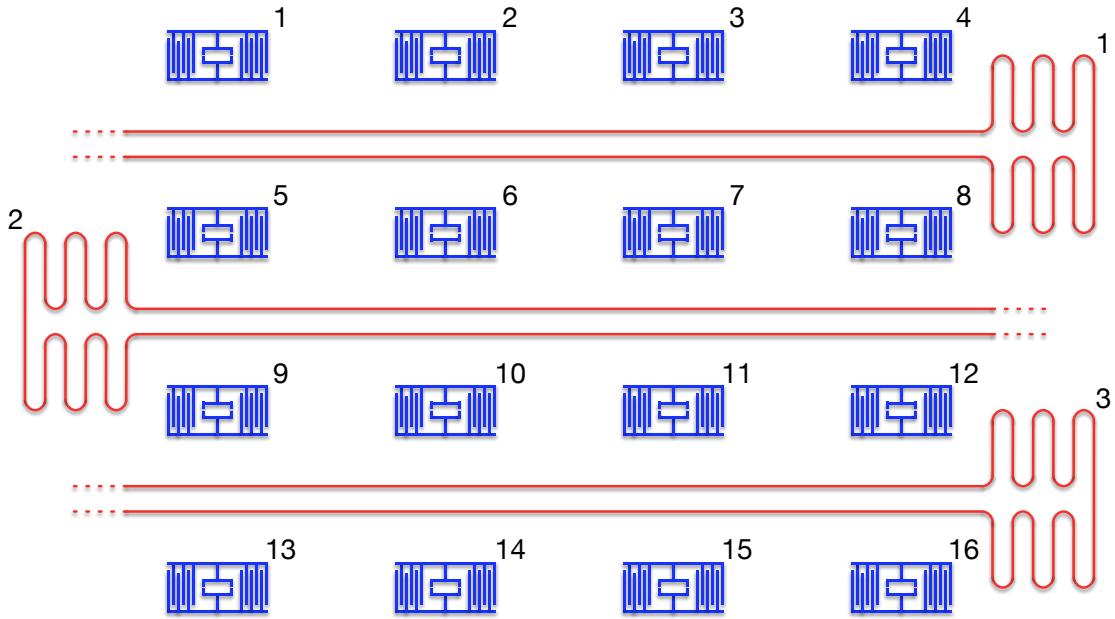


Figure 2.5: **Collective gates with resonators.** Architecture of superconducting qubits coupled to microwave resonators optimized for the simulation of a square lattice of 4×4 fermionic sites with Fermi-Hubbard interactions between nearest and next-nearest neighbors. By the use of resonators as quantum buses in the dispersive regime, several qubits are coupled allowing the implementation of single-qubit and multiqubit gates, which are necessary for the simulation of fermionic operators. Coupling two subsequent rows of superconducting qubits via a resonator provides all the interactions required for the simulation. In order to scale the system, one needs to couple two more qubits to every resonator for simulating one more column of sites, or make use of one more resonator for connecting another row. This scheme shows an optimized architecture for the simulation of fermionic models, and further resonators would be required for the read-out and single-control of the qubits.

of the fermionic sites in a 3×3 lattice. In Fig. 2.6, we show a plot of these populations considering a perfect unitary evolution of the Fermi-Hubbard model versus the evolution associated with the digital decomposition, where l is the number of Trotter steps. As l increases, the fidelity $F = |\langle \Psi_T | \Psi \rangle|^2$ improves, with $|\Psi\rangle$ and $|\Psi_T\rangle$ the states evolved under the exact unitary evolution and the digital one, respectively.

The application of our method for the digital quantum simulation of many-body fermionic systems requires polynomial resources, and can be implemented in realistic cQED setups, as the proposed architectures. Moreover, in this section, we have analyzed the efficiency of this method for the simulation of the Fermi-Hubbard model in 1D and 2D with different superconducting platforms. This work paves the way for the quantum simulation of complex fermionic dynamics in superconducting circuits.

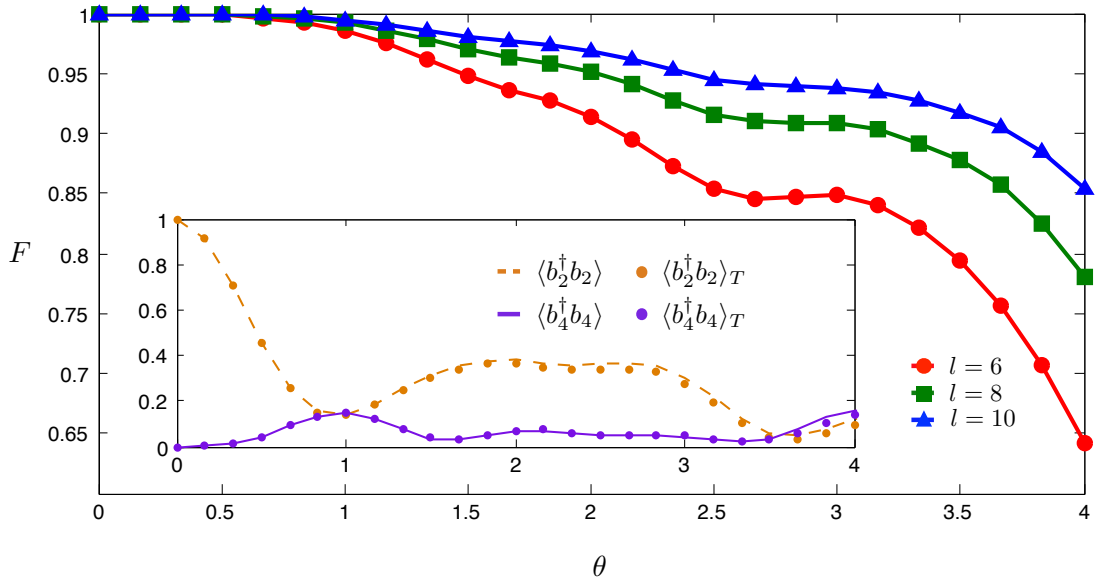


Figure 2.6: **Fermionic model with nearest and next-nearest neighbor interactions in a grid.** Simulation of a 2D lattice of 3×3 sites where the coupling ratios are: $U/t = 2$, $U/t' = 10$ and $U/U' = 5$. The principal plot shows the fidelity of the evolved state with digital methods for a phase of $\theta \equiv Ut = 4$ applying different numbers of Trotter steps, l . The inset shows the population of sites 2 and 4 with the initial state $|\Psi_I\rangle = b_2^\dagger|0\rangle$. The markers denote the digital evolution with 10 Trotter steps while the lines show the exact evolution.

2.3 An implementation in superconducting circuits

Here, we explore fermionic interactions with digital techniques [22] in a superconducting circuit. Focusing on the Hubbard model [73, 74] studied before, we perform time evolutions with constant interactions as well as a dynamic phase transition with up to four fermionic modes encoded in four qubits, using the JW transformation presented previously. The digital approach we implement here is universal and simulates fermions efficiently. The required number of gates scales only polynomially with the number of modes [74], even with physical nearest-neighbor qubit coupling only. Moreover, the model system is not limited to the dimensionality of the physical system, expanding our range of simulations of fermionic models to two and three spatial dimensions [74, 44]. We use in excess of 300 single-qubit and two-qubit gates, to implement fermionic models which require fully, yet separately tunable XX , YY , and ZZ interactions. We reach global fidelities which are limited by gate errors in an intuitive error model. These results are made possible by recent advances in architecture and control of superconducting qubits [60, 75, 76]. Our experiment is a critical

step on the path to creating an analog-digital quantum simulator – we foresee one using discrete fermionic modes combined with discrete [65] or continuous [77] bosonic modes, highlights the digital approach, and is a demonstration of digital quantum simulation in the solid state.

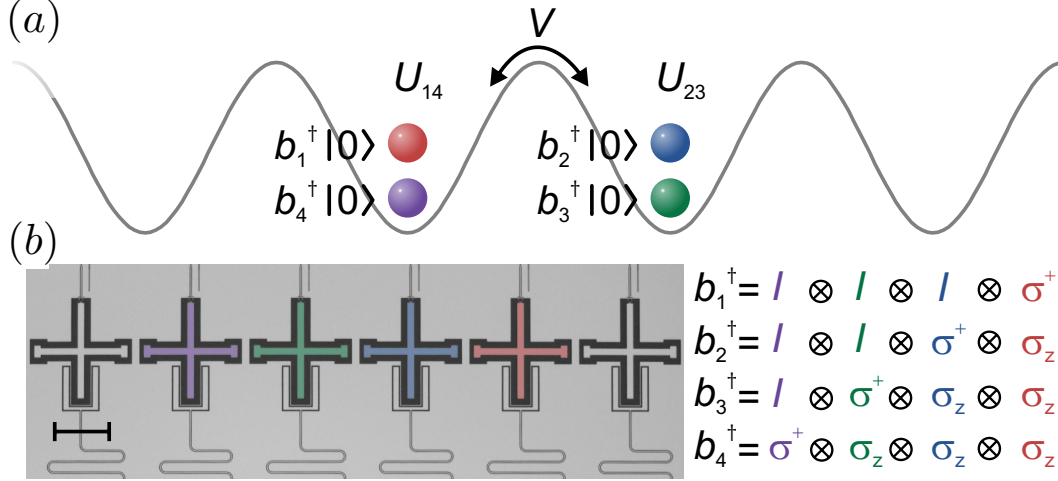


Figure 2.7: **Model and device.** (a) Hubbard model picture with two sites and four modes, with hopping strength V and on-site interactions U . The creation of one excitation from the ground state is shown for each mode. (b) Optical micrograph of the device. The scale bar (bottom left) denotes $200 \mu\text{m}$. The colored cross-shaped structures are the used Xmon transmon qubits. The construction of the fermionic operators for four modes is shown on the right. Colors highlight the corresponding sites, qubits, and operators.

2.3.1 Implementing the Hubbard model with gates

At low temperatures, whole classes of fermionic systems can be accurately described by the Hubbard model. Here, hopping strength V and repulsion strength U compete, see Fig. 2.7a, capturing the rich physics of many-body interactions such as insulating and conducting phases in metals [78, 79]. The generic Hubbard Hamiltonian is given by: $H = -V \sum_{\langle i,j \rangle} (b_i^\dagger b_j + b_j^\dagger b_i) + U \sum_{i=1}^N n_{i\uparrow} n_{i\downarrow}$, with b the fermionic annihilation operator, and i, j running over all adjacent lattice sites. The first term describes the hopping between sites and the last term the on-site repulsion. It is insightful to look at a fermionic two-mode example,

$$H = -V (b_1^\dagger b_2 + b_2^\dagger b_1) + U b_1^\dagger b_1 b_2^\dagger b_2. \quad (2.18)$$

We can express the fermionic operators in terms of Pauli and ladder operators using the JW transformation [38]: $b_1^\dagger = \sigma_1^+$ and $b_2^\dagger = \sigma_2^+ \sigma_1^z$, where the σ^z term ensures anticommutation. In essence, we use nonlocal control and map a local fermionic Hamiltonian to a local spin Hamiltonian. The qubits act as spins, and carry the

fermionic modes, see Fig. 2.7a-b. A fermionic mode is either occupied or unoccupied, and spinless – the spin degree of freedom is implemented here by using four modes to simulate two sites with two spins. We note that for higher spatial dimensions this approach is still viable, the only difference being that the local fermionic Hamiltonian now maps to a nonlocal spin Hamiltonian, which can be efficiently implemented as recently shown [74, 44]. Using the above transformation, the Hamiltonian becomes

$$H = \frac{V}{2} (\sigma_2^x \sigma_1^x + \sigma_2^y \sigma_1^y) + \frac{U}{4} (\sigma_2^z \sigma_1^z + \sigma_1^z + \sigma_2^z), \quad (2.19)$$

which can be implemented with separately tunable XX , YY , and ZZ interactions. Here, we use the convention of mapping an excited fermionic mode $|1\rangle$ (excited logical qubit) onto a qubit’s physical ground state $|g\rangle$, and a vacuum fermionic mode $|0\rangle$ (ground logical qubit) onto a qubit’s physical excited state $|e\rangle$.

The experiment uses a superconducting nine-qubit multipurpose processor, see Fig. 2.7b. Device details can be found in Ref. [80]. The qubits are cross-shaped structures [81] patterned out of an aluminium film on a sapphire substrate. They are arranged in a linear chain with nearest-neighbor coupling. Qubits are individually controlled, using microwave and frequency-detuning pulses (top), and readout is done through dispersive measurement (bottom) [52]. By frequency tuning of the qubits, interactions between adjacent pairs can be separately turned on and off. This system allows the implementation of nonlocal gates, as it has a high level of controllability, and is capable of performing high fidelity gates [60, 82]. Importantly, single- and two-qubit gate fidelities are maintained when scaling the system to larger numbers of qubits, as shown by the consistency of errors with the five qubit device [60].

The basic element used to generate all the interactions is a simple generalization of the CZ entangling gate, see Fig. 2.8a-b. We implement a state-dependent frequency pull by holding one qubit steady in frequency and bringing a second qubit close to the avoided level crossing of $|ee\rangle$ and $|gf\rangle$ using an adiabatic trajectory [83]. By tuning this trajectory, we can implement a tunable CZ_ϕ gate. During this operation, adjacent qubits are detuned away in frequency to minimize parasitic interactions. The practical range for ϕ is 0.5-4.0 rads; below this range parasitic ZZ interactions with other qubits become relevant, and above this range population starts to leak into higher energy levels¹. Using single-qubit gates and two-qubit entangling gates, we can implement the tunable ZZ interactions, as shown in Fig. 2.8c. In this gate construction, the π -pulses naturally suppress dephasing [84].

2.3.2 Verifying operator anticommutativity

First, we have experimentally verified that the encoded fermionic operators anticommute, see Fig. 2.9, by implementing the following anticommutation relation $\{b_1, b_2^\dagger\} + \{b_2, b_1^\dagger\} = 0$. The latter can be separated into two non-trivial Hermitian terms: $b_1 b_2^\dagger + b_2 b_1^\dagger$ (Fig. 2.9a) and $b_1^\dagger b_2 + b_2^\dagger b_1$ (Fig. 2.9b). Their associated unitary evolution, $U = \exp(-i\frac{\phi}{2}(b_1 b_2^\dagger + b_2 b_1^\dagger))$ for the first one, has been implemented using

¹See appendix A.6 and Refs. [60, 80] for further details.

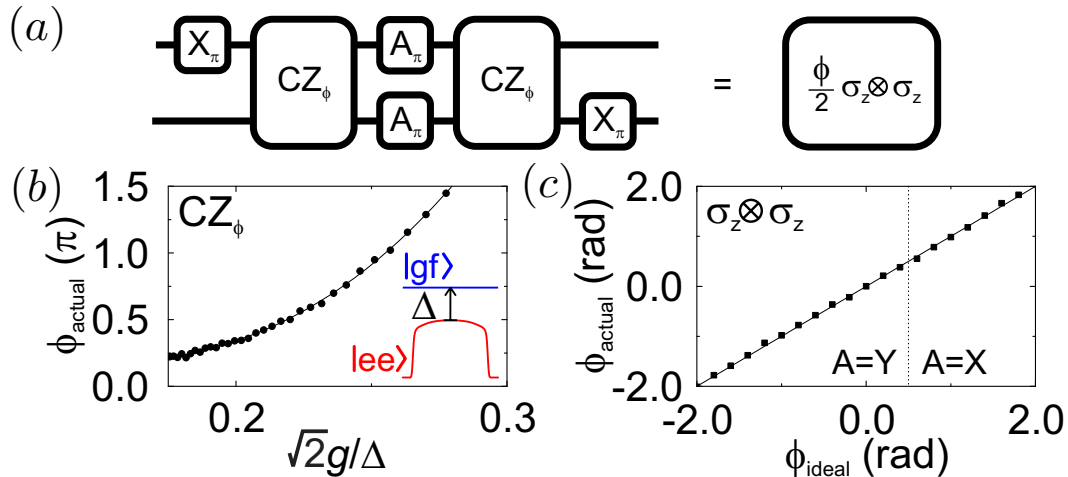


Figure 2.8: **Gate construction.** (a) Construction of the gate $U = \exp(-i\frac{\phi}{2}\sigma_l^z\sigma_m^z)$ from single-qubit rotations and the tunable CZ_ϕ entangling gate. To enable small and negative angles we include π pulses around the X-axis ($A=X$) or Y-axis ($A=Y$). The unitary diagonals are $(1 e^{i\phi} e^{i\phi} 1)$. (b) Tunable CZ_ϕ gate, implemented by moving $|ee\rangle$ (red) close to $|gf\rangle$ (blue). Coupling strength is $g/2\pi = 14$ MHz, pulse length is 55 ns, and typically $\Delta/2\pi = 0.7$ GHz when idling. (c) Measured versus desired phase of the full sequence, determined using quantum state tomography.

gates with strength $\phi = \pi$. We consider the standard representation of quantum process tomography (QPT) results via the process matrix χ [19]. The measured process matrices, χ , for these terms are determined using QPT, and constrained to be physical¹. We find that the processes are close to the ideal, with fidelities $\text{Tr}(\chi_{\text{ideal}}\chi) = 0.95, 0.96$. As the Hermitian terms sum up to zero, their unitary evolutions combine to the identity (Fig. 2.9c). We find that the sequence of both processes yields in fact the identity, as expected for anticommutation, with a fidelity of 0.91.

2.3.3 Simulations with two fermionic modes

We now discuss the simulation of fermionic models. We use the Trotter approximation described in section 2.1 to digitize the evolution of Hamiltonian $H = \sum_k H_k$: $U = \exp(-iHt) \simeq [\exp(-iH_1t/n)\exp(-iH_2t/n)\dots]^n$, with each part implemented using single- and two-qubit gates. We benchmark the simulation by comparing the experimental results to the exact digital outcome. Discretization unavoidably leads to deviations, and the digital errors can be quantified².

We start by visualizing the kinetic interactions between two fermionic modes. The construction of the Trotter step is shown in Fig. 2.10a, and directly follows from the Hamiltonian in Eq. (2.19). The step consists of the XX , YY , and ZZ terms,

¹See appendix A.3.

²For details on the estimated digital error see appendix A.5.

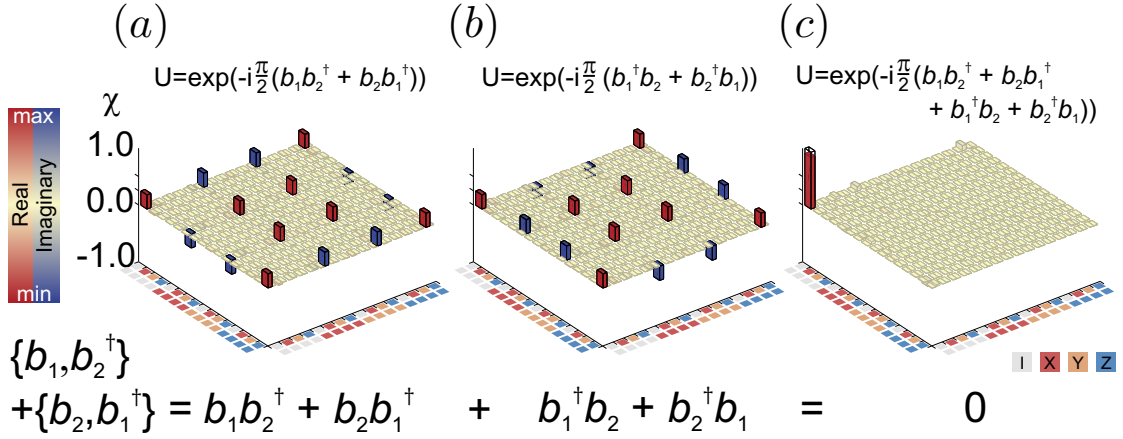


Figure 2.9: **QPT of operator anticommutation.** The process matrices are shown for the non-trivial Hermitian terms of the anticommutation relations. (a) Process matrix of the unitary $U = \exp(-i\frac{\pi}{2}[b_1b_2^\dagger + b_2b_1^\dagger])$. (b) Process matrix of the unitary $U = \exp(-i\frac{\pi}{2}[b_1^\dagger b_2 + b_2^\dagger b_1])$. (c) The sequence of both processes, $U = \exp(-i\frac{\pi}{2}[b_1b_2^\dagger + b_2b_1^\dagger + b_1^\dagger b_2 + b_2^\dagger b_1])$, yields the identity. The significant matrix elements, red for the real and blue for the imaginary elements, are close to the ideal (transparent).

constructed from ZZ terms and single-qubit rotations¹. We simulate the evolution during time Δt by setting $\phi_{xx} = \phi_{yy} = V\Delta t$ and $\phi_z = \phi_{zz} = U\Delta t/2$, and using $V = U = 1$. We evolve the system to a time of $T = 5.0$, and increase the number of steps, $\Delta t = T/n$, with $n = 1, \dots, 8$. The data show hallmark oscillations (Fig. 2.10b) indicating that the modes interact and exchange excitations. We find that the end state fidelity, taken at the same simulated time, decreases approximately linearly by 0.054 per step (Fig. 2.10c).

The above example shows that fermionic simulations, clearly capturing the dynamics arising from interactions, can be performed digitally using single-qubit gates and the tunable CZ_ϕ gate. Moreover, increasing the number of steps improves the time resolution, but at the price of increasing errors. A crucial result is that the per-step decrease in the end state fidelity is consistent with the gate fidelities. Using the typical values of $7.4 \cdot 10^{-3}$ entangling gate error and $8 \cdot 10^{-4}$ single-qubit gate error as previously determined for this platform [60], we arrive at an expected Trotter step process error of 0.07, considering the step consists of six entangling gates and 28 single-qubit gates, including X, Y rotations as well as idles. In addition, we have determined the Trotter step gate error in a separate interleaved randomized benchmarking experiment², and found a process error of 0.074, which is consistent with the observed per-step state error. We find that the process fidelity is thus a useful estimate, even though the simulation fidelity depends on the state and implemented model.

¹See appendix A.2 for the pulse sequence and gate count.

²See appendix A.4.

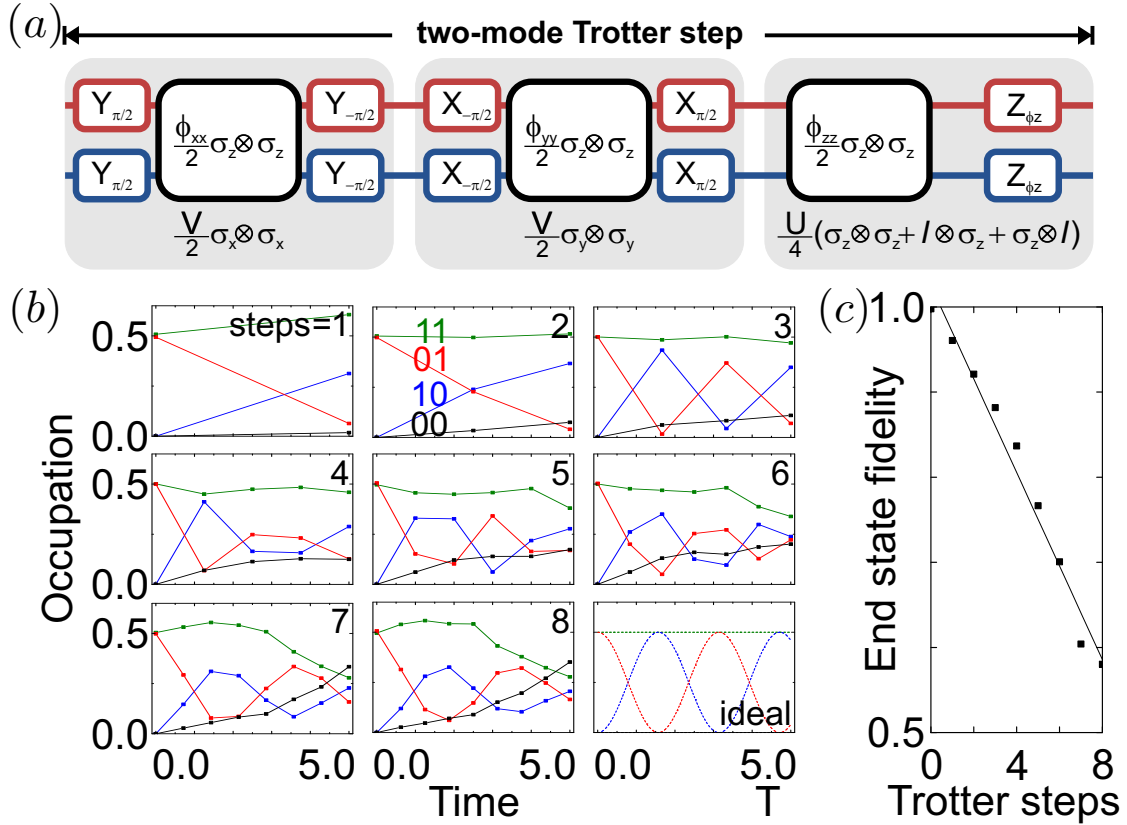


Figure 2.10: **Simulation of two fermionic modes.** (a) Construction of the two-mode Trotter step, showing the separate terms of the Hamiltonian in Eq. (2.19). (b) Occupation of the modes versus simulated time for $n = 1, \dots, 8$ steps. Color coding denotes the state probabilities. Input state is $(|01\rangle + |11\rangle)/\sqrt{2}$, and $V = U = 1$. The ideal dependence is shown in the bottom right. The final simulation time is $T = 5$. (c) The end-state fidelity decreases with step by 0.054, following a linear trend.

2.3.4 Simulations with three and four fermionic modes

Simulations of fermionic models with three and four modes are shown in Figs. 2.11 and 2.12. The three-mode Trotter step and its pulse-sequence are shown in Figs. 2.11a-b. An implementation of the YY gate is highlighted: the top qubit (red) is passive and detuned away, the middle qubit (blue) is tuned to an optimal frequency for the interaction, and the bottom qubit (green) performs the adiabatic trajectory. π -pulses on the passive qubit suppress dephasing and parasitic interactions. Fig. 2.11c shows the simulation results for $V = 1, U = 0$, hopping only, and $V = 1, U = 1$, with on-site repulsion. After initializing the system¹, the simulation data (closed symbols) follows the exact digital outcome (open symbols), accumulating a per-step error of 0.15, see Fig. 2.12c, and gradually populating other states (black symbols). The fidelity is

¹Input state generation is shown in appendix A.2.

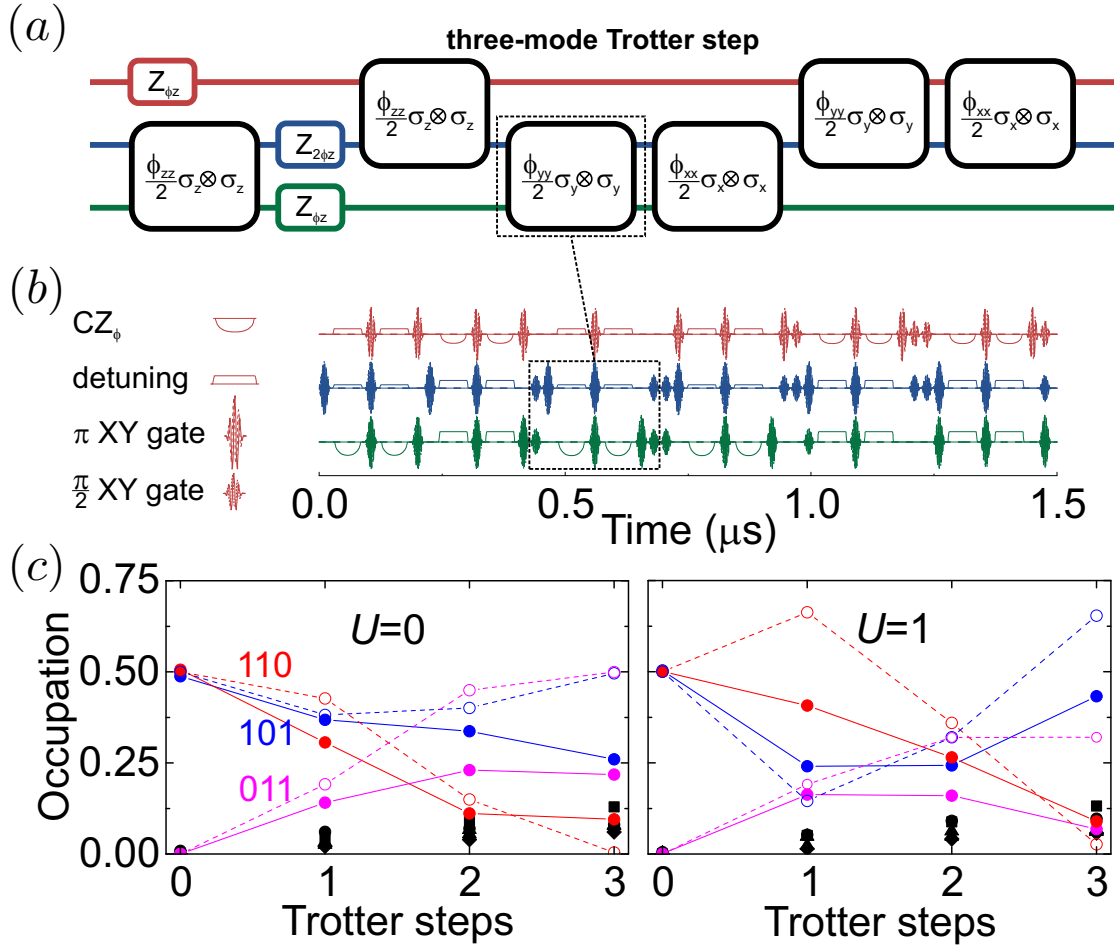


Figure 2.11: **Fermionic model with three modes.** (a) Three-mode Trotter step, with the Trotter step pulse-sequence in (b). The Trotter step consists of 12 entangling gates and 87 single-qubit gates. The YY interaction is highlighted (dashed). The amplitudes of the rotations are controlled by the values of V and U : $\frac{\phi_{xx}}{2} = \frac{\phi_{yy}}{2} = \frac{V}{2}\Delta t$, and $\frac{\phi_z}{2} = \frac{\phi_{zz}}{2} = \frac{U}{4}\Delta t$. (c) Simulation results for three modes with and without on-site interaction. Full symbols: experiment. Open symbols: ideal digitized. Black symbols: population of other states. Input state is $(|101\rangle + |110\rangle)/\sqrt{2}$, and $V = 1$.

the relevant figure of merit; the per-step error being the same for different model parameters indicates that the simulation outcomes are distinct.

For the four-mode experiment, we simulate an asymmetric variation on the Hubbard model. Here, the repulsive interaction is between the middle modes only (right well in Fig. 2.7a), while the hopping terms are kept equal. Asymmetric models are used in describing anisotropic fermionic systems [85]. In addition, the simulation can be optimized: gate count is reduced by the removal of interaction between the top and bottom modes, and the Trotter expansion can be rewritten in terms of odd and even steps such that the starting and ending single-qubit gates cancel, as discussed

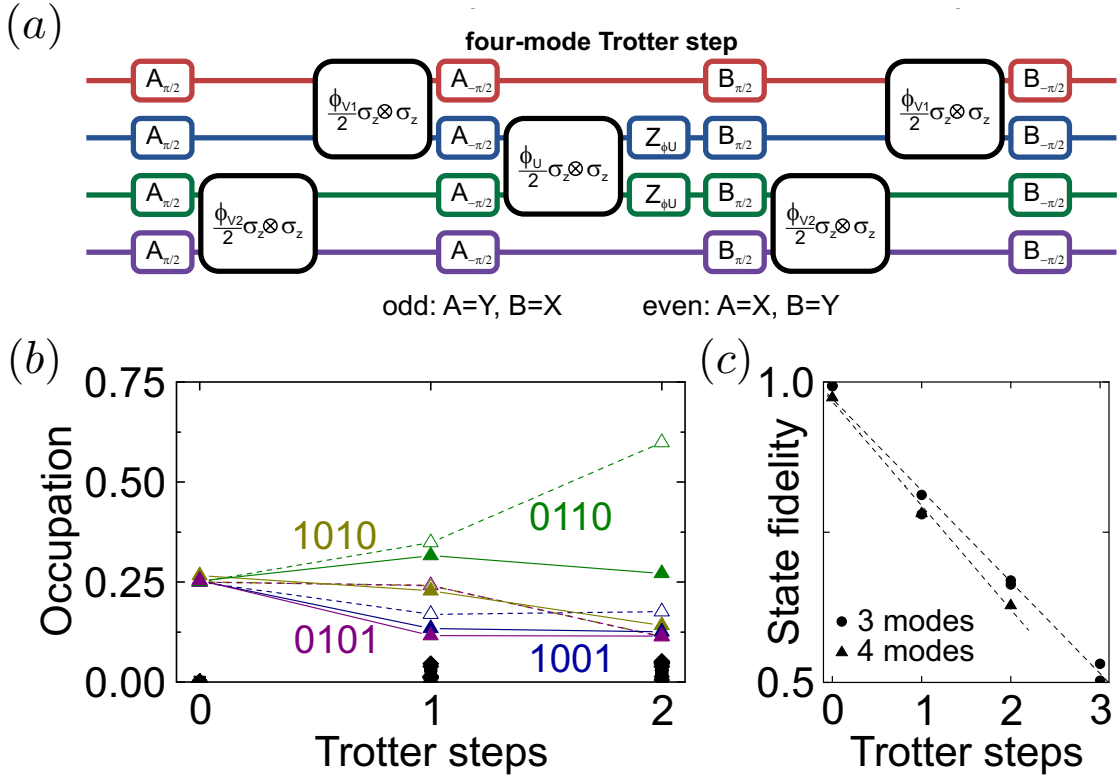


Figure 2.12: **Fermionic model with four modes.** (a) Construction of the four mode Trotter step. The amplitudes of the rotations are: $\frac{\phi_{V1}}{2} = \frac{V_1}{2} \Delta t$, $\frac{\phi_{V2}}{2} = \frac{V_2}{2} \Delta t$, and $\frac{\phi_U}{2} = \frac{U}{4} \Delta t$. (b) Four mode simulation results for $V_1 = V_2 = 1$, $U_{23} = 1$, and $U_{14} = 0$. Input state is $(|0101\rangle + |1001\rangle + |0110\rangle + |1010\rangle)/2$. (c) Fidelities versus Trotter step for the three mode simulation (dots) and the four mode simulation (triangles). Full symbols: experiment. Open symbols: ideal digitized. Black symbols: population of other states.

in section 2.2.1. The Trotter step is shown in Fig. 2.12a. The results are plotted in Fig. 2.12b. We find that the state fidelity decreases by 0.17 for the four mode simulation, see Fig. 2.12c.

The three- and four-mode experiments underline that fermionic models can be simulated digitally with large numbers of gates. The three-mode simulation uses in excess of 300 gates. We perform three Trotter steps, and per step we use 12 entangling gates, 53 microwave π and $\pi/2$ gates, 19 idle gates, and 3 single-qubit phase gates. For the non-participating qubit during the entangling operation, we use 12 frequency detuning gates where phases need to be accurately tracked. Using the above typical errors for gates, we arrive at an estimated process error of 0.16 for the three mode simulation, and an error of 0.15 for the four-mode simulation (per four-mode Trotter step, we use 10 entangling gates and 98 single-qubit gates). The process errors are close to the observed drop in state fidelity. The data are summarized in Table 2.4. Importantly, these results strongly suggest that the simulation errors scale with the number of gates, not qubits (modes), which is a crucial aspect of

scalably implementing models on our platform. Therefore, the appreciable drop in total fidelity is currently the optimal for any quantum platform considering the large number of gates that we have implemented in this experiment. Moreover, the precision achieved in our experiment allows us to observe the expected fermionic behavior at every Trotter step of the implemented protocol.

	two-mode	three-mode	four-mode
entangling CZ_ϕ gates	6	12	10
single-qubit gates	28	87	98
microwave π and $\pi/2$	20	53	56
idle	6	19	22
detuning	0	12	18
virtual phase	2	3	2
estimated Trotter step error	0.067	0.16	0.15
experimental Trotter step error	0.054	0.15	0.17

Table 2.4: **Gate counts for the two-, three-, and four-mode Trotter step.** We count idles as having the same duration as the microwave π and $\pi/2$ gates; this is the relevant approach for estimating total process fidelities. The gate counts are for a single Trotter step only, and exclude input state preparation. Estimated and experimental errors per Trotter step are tabulated at the bottom.

2.3.5 Time-varying interactions

We now address the simulation of fermionic systems with time-dependent interactions. In Fig. 2.13a, we show an experiment where we ramp the hopping term V from 0 to 1 while keeping the on-site repulsion U at 1; essentially changing the system from an insulating to a metallic phase. This transition is simulated for two modes using two Trotter steps, see inset, and with one step for three modes. For the latter case, we take the average of V over the relevant time domain. The data are shown in Figs. 2.13b-c, and clearly mirror the dynamics of the hopping term. At time smaller than 1.0, the system is frozen and the mode occupations are virtually unchanged, reflecting the insulating state. Interactions become visible when hopping is turned on, effectively melting the system, and follow the generic features of the exact digital outcome (dashed). The simulation fidelities lie around 0.9-0.95 for two modes and 0.7-0.8 for three modes, see Fig. 2.13d. These fidelities are around or somewhat below those for time evolution with constant interactions, presumably due to control errors related to parasitic qubit interactions, which also lead to the populating of other states (black symbols). The dynamic simulation highlights the possibilities of exploring parameter spaces and transitions with few steps.

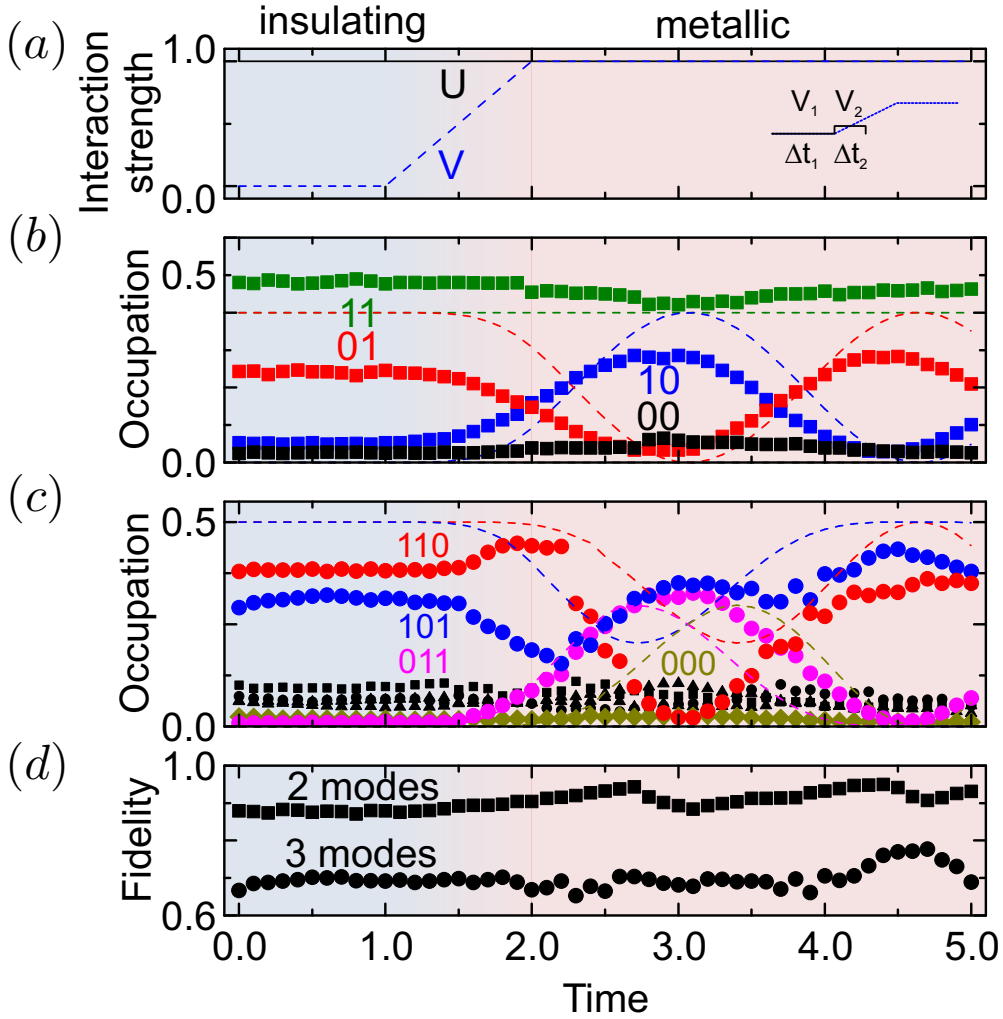


Figure 2.13: **Simulations with time-varying interactions.** (a) The system is changed from an insulating state (blue background) to a conducting phase (red background), by ramping the hopping term V from zero to one. Solid line: U , dashed line: V . Inset shows the choice of digitization on the ramp for the two-mode simulation. (b) Two-mode simulation showing dynamic behavior starting at the onset of the V ramp. Dashed lines denote the ideal digitized evolution. (c) Three mode simulation, showing non-trivial dynamics when the hopping term is nonzero. Dashed lines denote the ideal digitized evolution. Black symbols indicate the population of other states. (d) Simulation fidelities.

In this section, we have demonstrated the digital quantum simulation of fermionic models. Simulation fidelities are close to the expected values, and with improvements in gates and architecture, the construction of larger testbeds for fermionic systems appears viable. Moreover, a future implementation of quantum error correction in combination with these techniques will enable the efficient and scalable digital quantum simulation of fermionic models. Bosonic modes can be elegantly introduced by

adding linear resonators to the circuit, establishing a fermion-boson analog-digital system [65, 77] as a distinct paradigm for quantum simulation.

2.4 Hybrid digital quantum-classical simulation of fermions

In this section, we consider hybrid quantum-classical simulation of strongly correlated fermion models in the thermodynamic limit, and study a proof-of-principle example feasible with near-future technology. In a “two-site” DMFT approach we reduce the Hubbard model to an effective impurity model subject to self-consistency conditions. The resulting minimal two-site representation of the nonlinear hybrid setup involves four qubits implementing the impurity problem, plus an ancilla qubit on which all measurements are performed. We outline a possible implementation with superconducting circuits feasible with near-future technology.

A well-established approach to the study of strongly correlated fermionic lattice systems is DMFT [9]. It reduces the complexity of the original problem, e.g., the Hubbard model [73] *in the thermodynamic limit*, by mapping it onto a simpler impurity problem that is subject to a self-consistency condition relating its properties to those of the original model. Since an impurity problem is local, the mapping corresponds to neglecting spatial fluctuations. In the limit of infinite spatial dimensions this mapping is exact, but for finite dimensions it is an approximation. Nonetheless for lattice geometries with a large coordination number, self-consistently solving the impurity problem can yield an accurate approximate solution to the original Hubbard problem.

The ‘impurity’ itself consists of a single lattice site taken from the original problem, and so inherits on-site interactions from the Hubbard model. This impurity site is then immersed into a time-dependent, self-consistent mean-field with which it can dynamically exchange fermions. The mean-field thus attempts to model the rest of the lattice and by being dynamical can describe retardation phenomena. Overall the impurity problem can be represented by a Hamiltonian in which the interacting impurity site is coupled to a discrete set of non-interacting ‘bath’ sites. The bath sites represent the mean-field and if there is an infinite number of them then the self-consistency condition is guaranteed to be satisfied. However, in practical implementations only a finite number of bath sites are used, which restricts the frequency resolution of the bath so self-consistency condition can only be fulfilled approximately. Nevertheless, many strongly-correlated features, e.g., the Mott transition, are still captured correctly [9]. For a study of different bath discretization strategies in DMFT, see [86].

Although DMFT maps a Hubbard model to an impurity model this is still a non-trivial quantum many-body problem to solve because of the interactions at the impurity site. It is usually solved by classical numerical methods, e.g., specialized

versions of those used to tackle the original problem, which attempt to keep track of the quantum correlations between impurity and bath sites. Again this limits the number of bath sites that can be treated accurately. Here, we consider an alternative approach in which the impurity problem is solved with a quantum simulator, thus avoiding many issues that are inherent to the classical methods for fermions.

We consider a digital quantum simulator with a restricted number of qubits to describe fermionic models directly in the thermodynamic limit when the DMFT approach is adopted. We thus avoid direct implementation of the Hubbard model, which would suffer from severe finite size effects in quantum simulators with small number of qubits. This is the case for the experiments reported in quantum processors, in which the number of qubits is presently rather small. The constant effort to reach quantum supremacy boosts the improvement of the technology, and both approaches, the direct scalable implementation and the DMFT approach, complement each other.

To demonstrate this method we focus on the minimal incarnation of DMFT, the so-called “two-site” DMFT [87], where the impurity model consists of one impurity site and only one bath site, both with local Hilbert space dimension four, subjected to two specially chosen self-consistency conditions. Since two-site DMFT considers only the smallest possible impurity model, the approach cannot match the accuracy of full DMFT, but it can still give a *qualitatively* correct description of the infinite-dimensional Hubbard model, and its simplicity makes it a good starting point before advancing to more accurate schemes. For explicit details of two-site DMFT and its features compared to full DMFT we refer to Ref. [87].

The two-site system corresponds to four qubits, two for the impurity site and two for the bath site, while a fifth, ancillary qubit is used for measurements. This number of qubits is readily available in current digital quantum simulator platforms, with IBM having made a five-qubit quantum processor available to the public [88]. A nine-qubit processor has already been demonstrated in superconducting circuits [80, 58, 89], as reported in section 2.3. Trapped-ion technologies also provide us with digital quantum simulations involving up to six qubits [42, 90]. Being commensurate with current state-of-the-art technology is a further justification for studying this minimal model. Our scheme is readily generalizable to a larger number of qubits supporting more accurate simulations and potentially offering an exponential speed-up over classical Hamiltonian-based DMFT methods [40]. As presented in section 2.1, the number of multiqubit Mølmer–Sørensen (MS) gates scales only linearly with the number of bath sites, enabling efficient simulations [44, 65, 74, 40].

The self-consistency conditions are taken care of iteratively in a classical feedback loop, which thus completes the nonlinear, hybrid quantum-classical device we introduce. Dynamical mean-field simulations have already been proposed for such hybrid devices [39, 40]. Quantum gates similar to the ones needed in the two-site scheme have been used in demonstrating digital quantum simulation of fermionic models with superconducting circuits [74, 58]. We thus focus on superconducting circuits as a candidate platform, although, e.g., trapped ions [41, 42, 43, 44] could also be considered.

2.4.1 Quantum simulator based on two-site DMFT

In terms of the single-impurity Anderson model (SIAM), the smallest impurity problem involves one fermionic site corresponding to the impurity and only one fermionic site corresponding to the entire mean-field $\Delta(\omega)$ ¹. Since two qubits are needed to encode the local Hilbert space of a fermionic site, we only require four physical qubits to implement this representation in the lab. The SIAM Hamiltonian for only one bath site reads

$$H_{\text{SIAM}} = U n_{1\downarrow} n_{1\uparrow} - \mu \sum_{\sigma} n_{1\sigma} + \sum_{\sigma} \epsilon_c c_{2\sigma}^{\dagger} c_{2\sigma} + \sum_{\sigma} V \left(c_{1\sigma}^{\dagger} c_{2\sigma} + c_{2\sigma}^{\dagger} c_{1\sigma} \right). \quad (2.20)$$

Here, U is the Hubbard interaction at the impurity site 1, and μ is the chemical potential that controls the electron filling in the grand canonical ensemble. Furthermore, ϵ_c and V describe the on-site energy of the non-interacting bath site 2 and hybridization between the impurity and the bath site, respectively, and give the mean-field as

$$\Delta(\omega) = \frac{V^2}{\omega - \epsilon_c}. \quad (2.21)$$

See Fig. 2.14c for illustration of the two-site SIAM. The parameters ϵ_c and V are initially unknown and they need to be determined iteratively such that two self-consistency conditions are satisfied. For details of the derivation and motivation of these conditions we refer to Ref. [87].

The first condition is that the electron filling n_{imp} of the impurity site and the filling $n = \langle n_{j\downarrow} \rangle + \langle n_{j\uparrow} \rangle$ of the lattice model match, i.e.,

$$n_{\text{imp}} \equiv n. \quad (2.22)$$

The second self-consistency condition is given by

$$V^2 = \mathcal{Z} M_2^{(0)} = \mathcal{Z} \int_{-\infty}^{\infty} d\epsilon \epsilon^2 \rho_0(\epsilon) = \mathcal{Z} t^{*2}, \quad (2.23)$$

where quasiparticle weight reads

$$\mathcal{Z} = \left[1 - \frac{d\text{Re}[\Sigma_{\text{imp}}(\omega + i\eta)]}{d\omega} \Big|_{\omega=0} \right]^{-1}. \quad (2.24)$$

In Eq. (2.23), $M_2^{(0)}$ is the second moment of the non-interacting density of states, and the final equality follows from the semicircular density of states of the Bethe lattice under consideration [91].

¹We elucidate the framework of DMFT applied to the Hubbard model in infinite dimensions in B.

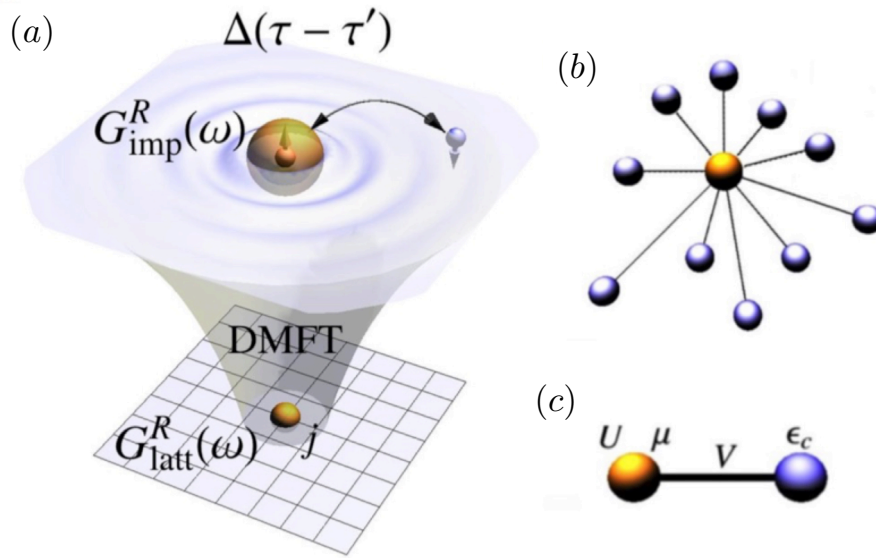


Figure 2.14: **DMFT**. (a) DMFT neglects spatial fluctuations around a single lattice site j and replaces the rest of the lattice with an effective mean-field $\Delta(\tau - \tau')$ with which the isolated site dynamically exchanges fermions, subject to the self-consistency condition $G_{\text{imp}}^R(\omega) = G_{\text{latt},jj}^R(\omega)$. Here, $G_{\text{imp}}^R(\omega)$ is the impurity Green function and $G_{\text{latt},jj}^R(\omega)$ is the local part of the lattice Green function. (b) In Hamiltonian-based DMFT methods, one considers an impurity model which describes the local part of the Hubbard model directly and represents the mean-field as a set of non-interacting bath sites that are connected to the central, interacting impurity site. (c) The minimal representation of DMFT involves the impurity site, with on-site interaction U and chemical potential μ , coupled via the hybridization energy V to only one bath site. The bath has on-site energy ϵ_c that corresponds to the mean-field $\Delta(\tau - \tau')$ and is subject to two self-consistency conditions.

2.4.2 Two-site DMFT protocol

The hybrid quantum-classical device implementing two-site DMFT consists of a few-qubit digital quantum simulator in which the impurity Green function is measured and of a classical feedback loop in which the parameters of the two-site SIAM are updated. The two-site DMFT protocol is summarized in Fig. 2.15, and proceeds as follows [87].

1. First fix U and μ to the desired values in the SIAM and set the unknown parameters ϵ_c and V equal to an initial guess.
2. Measure the interacting Green function $iG_{\text{imp}}^R(\tau)$. This can be done using, e.g., single-qubit interferometry¹.
3. After Fourier-transforming the impurity Green function, the impurity self-

¹For a detailed description see appendix C.

energy is obtained classically from the Dyson equation

$$\Sigma_{\text{imp}}(\omega) = G_{\text{imp}}^{R(0)}(\omega)^{-1} - G_{\text{imp}}^R(\omega)^{-1}. \quad (2.25)$$

Here, the non-interacting impurity Green function is given by

$$G_{\text{imp}}^{R(0)}(\omega)^{-1} = \omega + \mu - \Delta(\omega). \quad (2.26)$$

From the derivative of the self-energy one obtains the quasiparticle weight \mathcal{Z} which directly yields the updated hopping parameter V via Eq. (2.23). The update for ϵ_c is found by minimizing the difference $|n_{\text{imp}} - n|$ [87].

4. Steps 2 and 3 need to be repeated until V and ϵ_c are self-consistent, and $n_{\text{imp}} = n$.

The self-consistent Green function $G_{\text{imp}}^R(\omega)$ and self-energy $\Sigma_{\text{imp}}(\omega)$ thus obtained are used to calculate approximations to local single-particle properties of the Hubbard model¹.

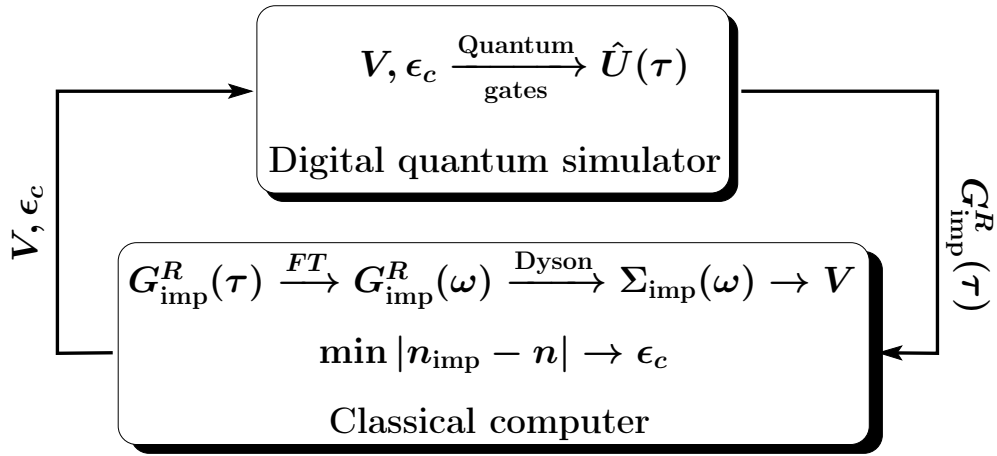


Figure 2.15: **Nonlinear hybrid quantum-classical scheme.** A digital quantum simulator works in conjunction with a classical feedback loop to perform a proof-of-principle demonstration of a two-site DMFT calculation.

¹Note that for larger systems the two-site DMFT steps need to be replaced with the general DMFT self-consistency loop outlined in appendix B.

2.4.3 Quantum algorithm for the SIAM model with superconducting circuits

Here, we consider the quantum gates of the digital quantum simulator part in Fig. 2.15, with special focus on superconducting circuits as the platform of choice [74, 58, 89].

To implement the two-site SIAM with qubits, the fermionic creation and annihilation operators need to be mapped onto tensor products of spin operators which then act on the qubits via quantum gates. In order to obtain as simple quantum gates as possible in section 2.4.4 and in the general DMFT self-consistency loop, we consider an ordering of the qubits where the first two qubits encode the spin \downarrow for both fermionic sites while the last two correspond to spin \uparrow . This is achieved via the JW transformation given explicitly as

$$\begin{aligned} c_{1\downarrow}^\dagger &= \sigma_1^- = \frac{1}{2}(\sigma_1^x - i\sigma_1^y), & c_{2\downarrow}^\dagger &= \sigma_1^z \sigma_2^- = \frac{1}{2}\sigma_1^z(\sigma_2^x - i\sigma_2^y), \\ c_{1\uparrow}^\dagger &= \sigma_1^z \sigma_2^z \sigma_3^- = \frac{1}{2}\sigma_1^z \sigma_2^z(\sigma_3^x - i\sigma_3^y), & c_{2\uparrow}^\dagger &= \sigma_1^z \sigma_2^z \sigma_3^z \sigma_4^- = \frac{1}{2}\sigma_1^z \sigma_2^z \sigma_3^z(\sigma_4^x - i\sigma_4^y), \end{aligned} \quad (2.27)$$

and $c_{j\sigma} = (c_{j\sigma}^\dagger)^\dagger$. For larger systems the use of the JW transformation, e.g., $c_{j\downarrow}^\dagger = \left(\prod_{p<2j-1} \sigma_p^z\right) \sigma_{2j-1}^-$, $c_{j\uparrow}^\dagger = \left(\prod_{p<2j} \sigma_p^z\right) \sigma_{2j}^-$, $c_{j\sigma} = (c_{j\sigma}^\dagger)^\dagger$, becomes important, as considered in Refs. [65, 40]. The hybridization terms in the SIAM, which now involve many spins, can be implemented efficiently and scalably with multiqubit MS gates, the number of which scales only linearly with the number of bath sites [44, 65, 74, 40].

With the mappings in Eq. (2.27), the hybridization terms in the SIAM described in Eq. (2.20) transform into

$$V \left(c_{1\downarrow}^\dagger c_{2\downarrow} + c_{2\downarrow}^\dagger c_{1\downarrow} \right) = \frac{V}{2} (\sigma_1^x \sigma_2^x + \sigma_1^y \sigma_2^y), \quad (2.28)$$

and

$$V \left(c_{1\uparrow}^\dagger c_{2\uparrow} + c_{2\uparrow}^\dagger c_{1\uparrow} \right) = \frac{V}{2} (\sigma_3^x \sigma_4^x + \sigma_3^y \sigma_4^y). \quad (2.29)$$

The number operators become

$$\begin{aligned} n_{1\downarrow} &= \frac{1}{2}(1 - \sigma_1^z), & n_{2\downarrow} &= \frac{1}{2}(1 - \sigma_2^z), \\ n_{1\uparrow} &= \frac{1}{2}(1 - \sigma_3^z), & n_{2\uparrow} &= \frac{1}{2}(1 - \sigma_4^z), \end{aligned} \quad (2.30)$$

and thus the interaction term can be written as

$$U n_{1\downarrow} n_{1\uparrow} = \frac{U}{4} (\sigma_1^z \sigma_3^z - \sigma_1^z - \sigma_3^z), \quad (2.31)$$

up to a constant. The total Hamiltonian then reads

$$\begin{aligned}
 H_{\text{SIAM}} = & \frac{U}{4} (\sigma_1^z \sigma_3^z - \sigma_1^z - \sigma_3^z) + \frac{\mu}{2} (\sigma_1^z + \sigma_3^z) - \frac{\epsilon_c}{2} (\sigma_2^z + \sigma_4^z) \\
 & + \frac{V}{2} (\sigma_1^x \sigma_2^x + \sigma_1^y \sigma_2^y + \sigma_3^x \sigma_4^x + \sigma_3^y \sigma_4^y), \tag{2.32}
 \end{aligned}$$

where we have dropped constant terms.

The JW transformed SIAM in Eq. (2.32) can be implemented in an experimental arrangement based on superconducting circuits by considering the entangling gates presented in section 2.1.

2.4.4 Quantum gate decomposition of the time-evolution operator

In order to use quantum gates for time-evolution, we utilize a Trotter decomposition of the time-evolution operator corresponding to H_{SIAM} in Eq. (2.32). The first order Trotter expansion is given by

$$\begin{aligned}
 U(\tau) = e^{-iH_{\text{SIAM}}\tau} \approx & \left(e^{-i\frac{V}{2}(\sigma_1^x \sigma_2^x + \sigma_1^y \sigma_2^y)\frac{\tau}{N}} e^{-i\frac{V}{2}(\sigma_3^x \sigma_4^x + \sigma_3^y \sigma_4^y)\frac{\tau}{N}} e^{-i\frac{U}{4}\sigma_1^z \sigma_3^z \frac{\tau}{N}} \right. \\
 & \left. \times e^{i\left(\frac{U}{4} - \frac{\mu}{2}\right)\sigma_1^z \frac{\tau}{N}} e^{i\left(\frac{U}{4} - \frac{\mu}{2}\right)\sigma_3^z \frac{\tau}{N}} e^{i\frac{\epsilon_c}{2}\sigma_2^z \frac{\tau}{N}} e^{i\frac{\epsilon_c}{2}\sigma_4^z \frac{\tau}{N}} \right)^N. \tag{2.33}
 \end{aligned}$$

Here, N is the number of Trotter (i.e., time) steps and $\frac{\tau}{N}$ is the size of the time step. In what follows, we use the two alternative approaches for quantum gates outlined in section 2.1 to implement Eq. (2.33). The first one is based on collective XY gates, and the second relies in the optimized CZ_ϕ gate.

As shown in section 2.1, the XY gate, given by the expression

$$XY = \exp \left[-i\frac{V}{2} (\sigma_l^x \sigma_m^x + \sigma_l^y \sigma_m^y) \frac{\tau}{n} \right],$$

naturally appears when considering the use of a superconducting resonator [56]. The quantum circuit for a single Trotter step with these gates is shown in Fig. 2.16a.

To be able to utilize the CZ_ϕ gates, we write the time-evolution operator in Eq. (2.33) in terms of $\sigma_\ell^z \sigma_m^z$ (ZZ) interactions, taking into account Eq. (2.9).

The ZZ interaction in the computational basis appears in Eq. (2.11), and thus we have the decomposition

$$\exp \left(-i\frac{\phi}{2} \sigma_1^z \sigma_2^z \right) = R_x^{(1)}(\pi) CZ_\phi R_x^{(1)}(\pi) R_x^{(2)}(\pi) CZ_\phi R_x^{(2)}(\pi), \tag{2.34}$$

where the tunable CZ_ϕ gate is given by Eq. (2.3).

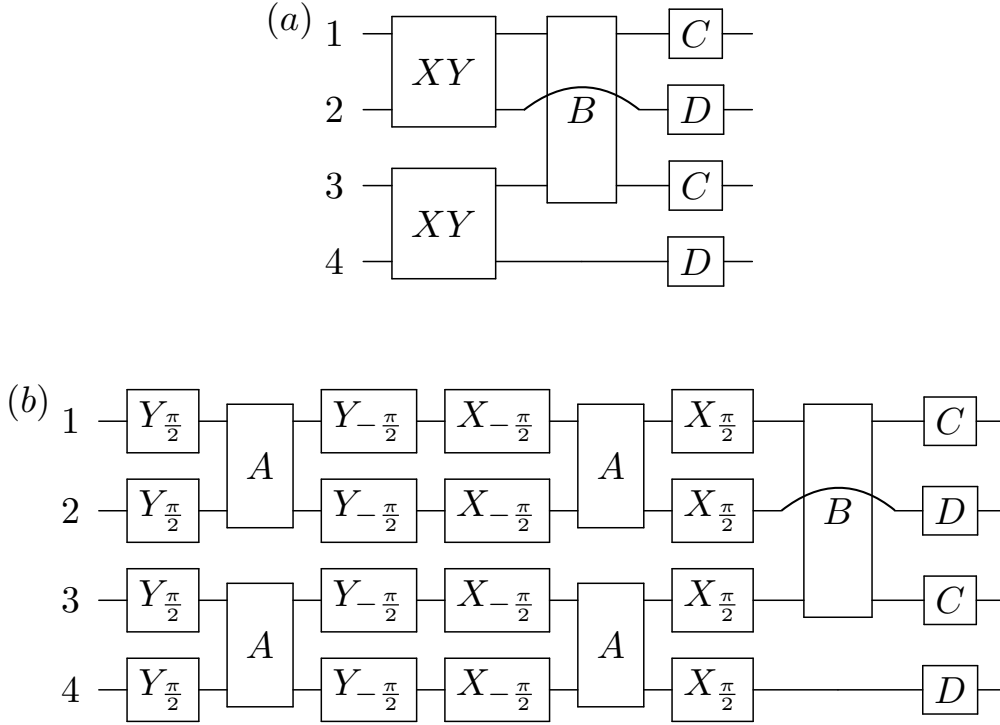


Figure 2.16: **Quantum gates for one Trotter step.** A single Trotter step is shown for (a) the XY method and (b) the CZ method. Here, B is the entangling gate $B = \exp\left(-i\frac{U}{4}\sigma_1^z\sigma_3^z\frac{\tau}{N}\right)$, A is a two-qubit gate given by $A = \exp\left(-i\frac{V}{2}\sigma_l^z\sigma_m^z\frac{\tau}{N}\right)$, acting on qubits l and m , and the quantum gates C and D are single-qubit σ^z -gates, given by $C = \exp\left[i\left(\frac{U}{4} - \frac{\mu}{2}\right)\sigma_l^z\frac{\tau}{N}\right]$ and $D = \exp\left(i\frac{\epsilon_c}{2}\sigma_l^z\frac{\tau}{N}\right)$, acting on qubit l . Finally, X_ϕ and Y_ϕ are ϕ -rotations along the x and y axis, respectively.

The time-evolution operator in Eq. (2.33) in terms of ZZ interactions is given by

$$\begin{aligned}
 U(\tau) &= e^{-iH_{\text{SIAM}}\tau} \approx \left(R_y^{(1234)}\left(\frac{\pi}{2}\right) e^{-i\frac{V}{2}\sigma_1^z\sigma_2^z\frac{\tau}{N}} e^{-i\frac{V}{2}\sigma_3^z\sigma_4^z\frac{\tau}{N}} R_y^{(1234)}\left(-\frac{\pi}{2}\right) \right. \\
 &\times R_x^{(1234)}\left(-\frac{\pi}{2}\right) e^{-i\frac{V}{2}\sigma_1^z\sigma_2^z\frac{\tau}{N}} e^{-i\frac{V}{2}\sigma_3^z\sigma_4^z\frac{\tau}{N}} R_x^{(1234)}\left(\frac{\pi}{2}\right) \\
 &\left. \times e^{-i\frac{U}{4}\sigma_1^z\sigma_3^z\frac{\tau}{N}} e^{i\left(\frac{U}{4} - \frac{\mu}{2}\right)\sigma_1^z\frac{\tau}{N}} e^{i\left(\frac{U}{4} - \frac{\mu}{2}\right)\sigma_3^z\frac{\tau}{N}} e^{i\frac{\epsilon_c}{2}\sigma_2^z\frac{\tau}{N}} e^{i\frac{\epsilon_c}{2}\sigma_4^z\frac{\tau}{N}} \right)^N. \quad (2.35)
 \end{aligned}$$

The sequence of gates for one Trotter step is depicted in Fig. 2.16b.

A single Trotter step contains 5 ZZ two-qubit gates, corresponding to the A and B gates in Fig. 2.16b, between nearest-neighbor qubits, 2 SWAP gates, for the B gate which acts on qubits 1 and 3, and 20 single-qubit rotations. We note that a SWAP gate amounts to three CZ_ϕ gates, and a ZZ gate amounts to two CZ_ϕ gates, as shown in Eq. (2.34). This number can be optimised further if we consider different orderings for odd and even Trotter steps as in Fig. 2.17, such that subsequent gates may be suppressed. This reorganisation of interactions does not in principle affect

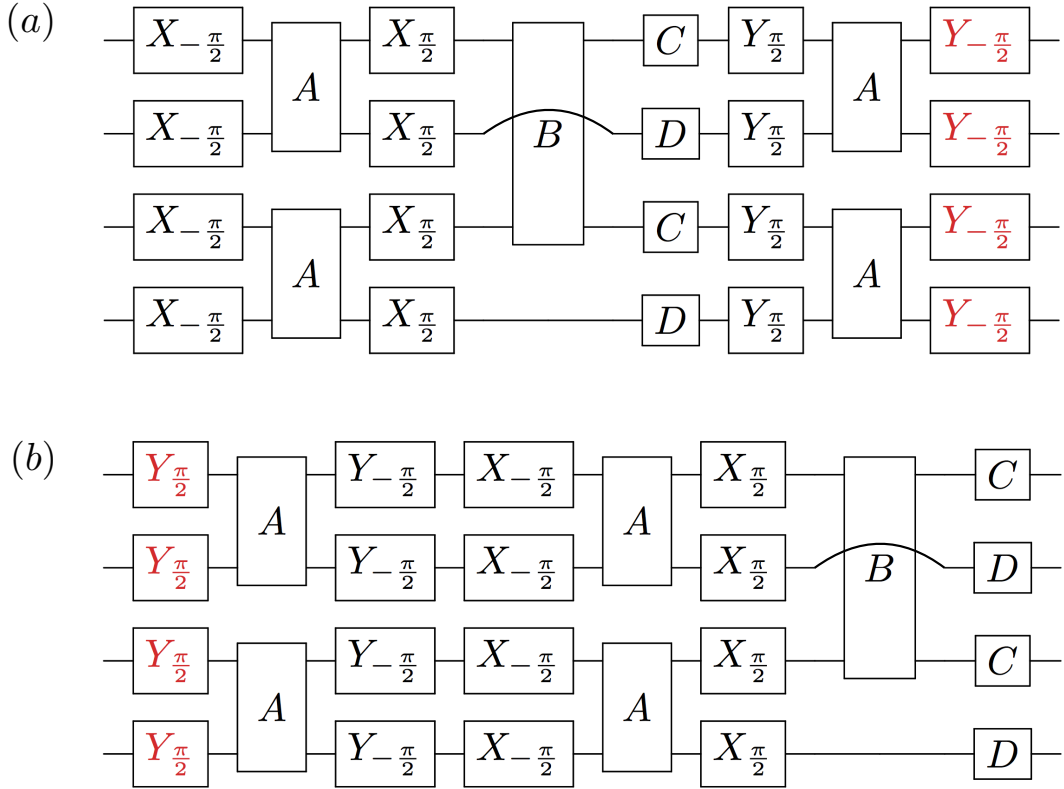


Figure 2.17: **Reordering of quantum gates.** The ordering of gates shown for (a) an odd Trotter step and (b) an even Trotter step in the CZ method. The gates depicted in red can be omitted as they cancel out during a sequence of time steps.

the Trotter error. Hence, for a pair of Trotter steps, the number of gates is reduced, and we may only consider 10 ZZ two-qubit gates between nearest-neighbor qubits, 4 SWAP gates, and 32 single-qubit rotations.

2.4.5 Results

We focus on the half-filled case, i.e., $\mu = \frac{U}{2}$ and $\epsilon_c = 0$, which requires the least amount of quantum gates, since the C and D gates in section 2.4.3 vanish. Note that since the value of ϵ_c is fixed in this case, it need not be updated in the self-consistency loop. We use t^* , the Hubbard hopping in infinite dimensions, as our unit of energy, hence time τ is measured in units of $1/t^*$. Note that τ refers here to the time in the evolution operator $U(\tau)$, not to the actual time to run the experiment.

We show in Fig. 2.18 the state fidelities $\mathcal{F} = |\langle \Psi(\tau) | \Psi_T(\tau) \rangle|^2$, where $|\Psi(\tau)\rangle$ denotes the state obtained with exact time-evolution using the full, non-Trotterized operator $U(\tau) = \exp(-i\tau H_{\text{SIAM}})$ corresponding to the two-site SIAM in Eq. (2.20), and $|\Psi_T(\tau)\rangle$ is the state evolved using either the XY or CZ_ϕ quantum gates, for various Trotter steps N up to time $\tau = 6/t^*$. Note that the number of qubits corre-

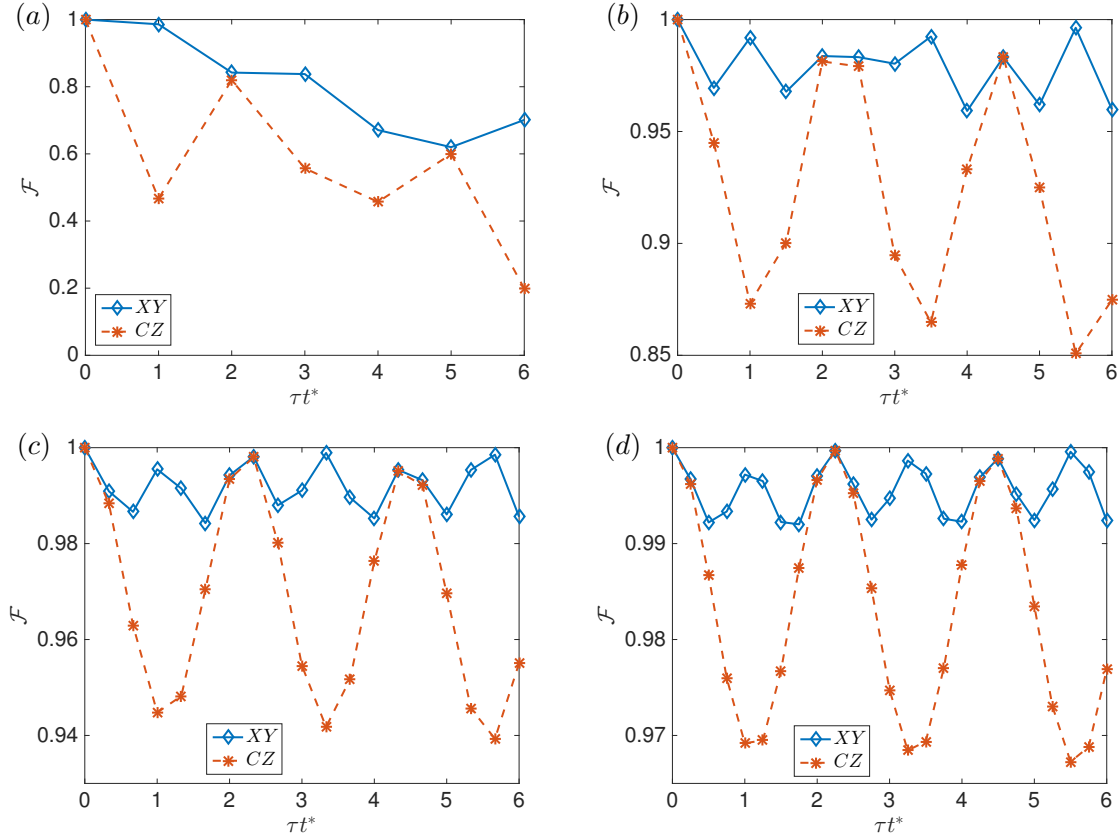


Figure 2.18: **Time-evolution of the state fidelity.** State fidelities $\mathcal{F} = |\langle \Psi(\tau) | \Psi_T(\tau) \rangle|^2$ using the XY method (blue diamonds, line is to guide the eye) and CZ gates (red stars, dashed line is to guide the eye) obtained with (a) 6, (b) 12, (c) 18, and (d) 24 Trotter steps up to time $\tau = 6/t^*$. We set $U = 4t^*$ and $V = t^*$.

sponding to the two-site SIAM is fixed, leaving only N as the parameter to be varied for increased accuracy. We use the initial state $|\Psi(\tau = 0)\rangle = c_{1\downarrow}^\dagger |GS\rangle / \|c_{1\downarrow}^\dagger |GS\rangle\|$, where $|GS\rangle$ is the ground-state of the two-site SIAM in Eq. (2.20), which is a relevant state for obtaining the impurity Green function at zero temperature defined in Eq. (B.3). As expected, using XY gates displays superior fidelities, since CZ_ϕ gates require an extra factorization of the hybridization term, as explained in section 2.4.3. For $N = 24$ steps, the state fidelity using XY gates remains over 99% throughout the evolution. In what follows, we use only XY gates for the time-evolution for concreteness.

As shown in section 2.4.1, the main object of interest is the retarded impurity Green function. One possibility to measure $iG_{\text{imp}}^R(\tau)$ is single-qubit interferometry¹, which raises the total number of qubits in the experimental arrangement to five. In Fig. 2.19, we plot the impurity Green function obtained from evolving the state with

¹See appendix C for details.

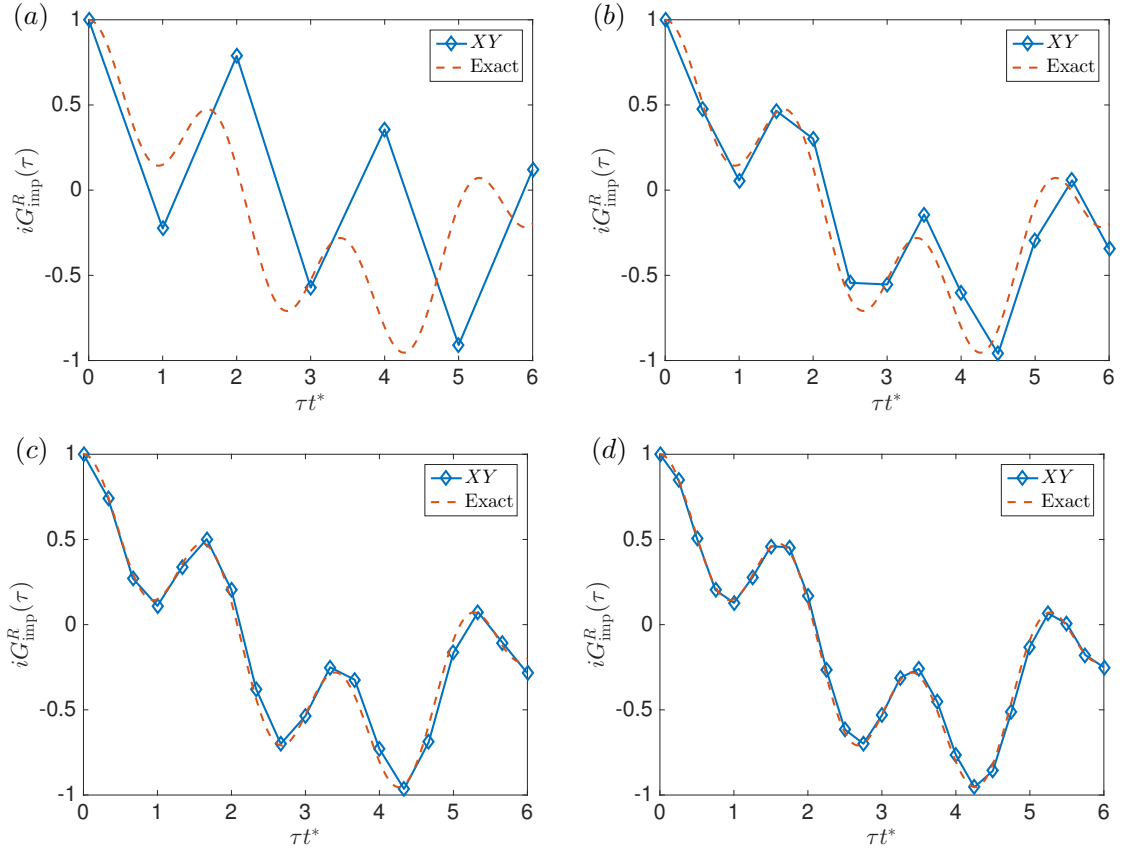


Figure 2.19: **Impurity Green function in the time domain.** The retarded impurity Green function $iG_{\text{imp}}^R(\tau)$ obtained with (a) 6, (b) 12, (c) 18, and (d) 24 Trotter steps up to time $\tau = 6/t^*$ using the XY method (blue diamonds). Comparison is given to the exact Green function (red dashed line). We set $U = 4t^*$ and $V = t^*$.

XY gates compared to exact evolution of the two-site SIAM for different N . We see that the Green function from the XY approach starts to follow the curve of the exact Green function better for increasing N . In our subsequent analysis, we use $N = 24$ up to $\tau = 6/t^*$ to study what two-site DMFT physics can be captured with the digital approach.

To obtain the impurity Green function in the frequency domain, we first consider some known and general analytic properties of the retarded Green function in Eq. (B.3). This Green function can be written as a sum of the particle and hole contributions as

$$iG_{\text{imp}}^R(\tau) = \theta(\tau) \sum_j \left(|\langle j|c_{1\sigma}^\dagger|GS\rangle|^2 e^{-i\omega_j t} + |\langle j|c_{1\sigma}|GS\rangle|^2 e^{i\omega_j t} \right), \quad (2.36)$$

where $|j\rangle$ is an eigenstate of H_{SIAM} with eigenenergy E_j , and $\omega_j = E_j - E_{GS}$. In two-site DMFT, the interacting Green function is a four-pole function [87], which limits the number of terms in the above summation to four. Moreover, in the presence of

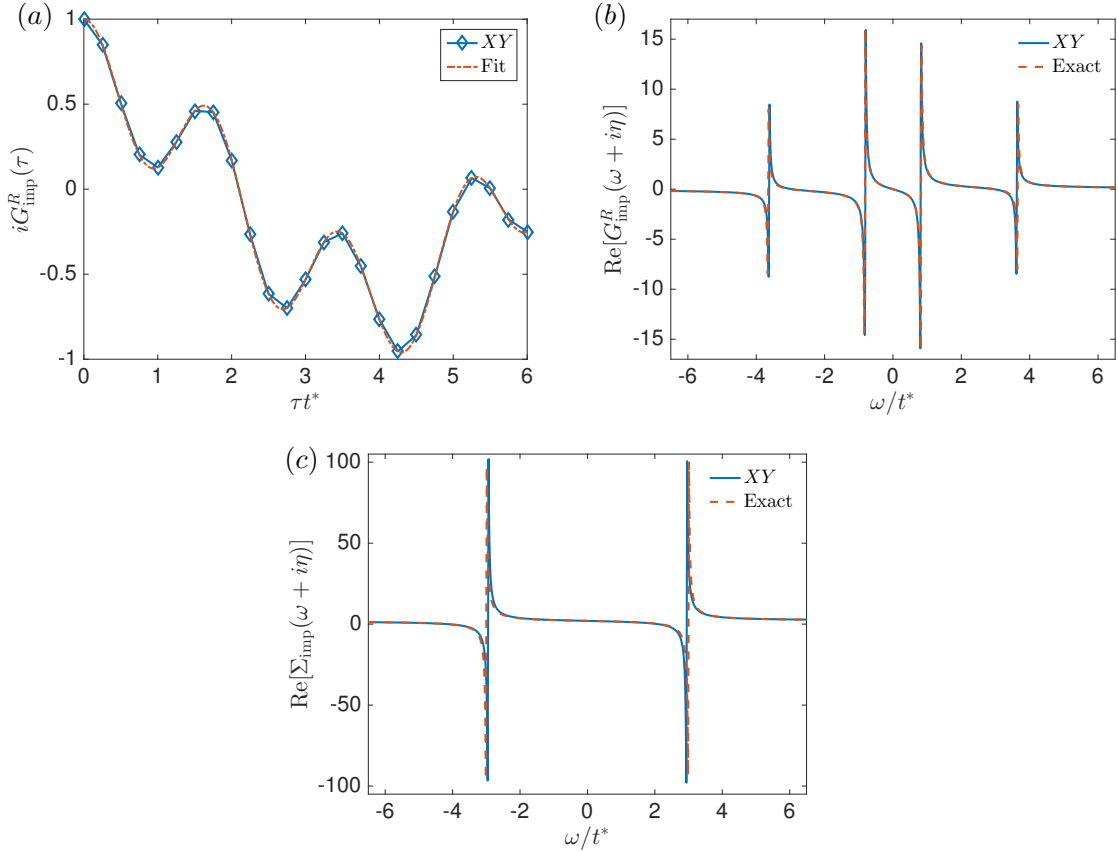


Figure 2.20: **The retarded impurity Green function and self-energy in the frequency domain.** (a) The residues and poles of the Green function can be obtained from a fit of the form in Eq. (2.37) (red dashed line) to the $G_{\text{imp}}^R(\tau)$ data from the XY method with 24 Trotter steps (blue diamonds). (b) The real part of the impurity Green function, $\text{Re}[G_{\text{imp}}^R(\omega + i\eta)]$ (blue line), with residues and poles obtained from the fit from (a), compared to the exact Green function (red dashed line). (c) Same as in (b), but for the self-energy $\text{Re}[\Sigma_{\text{imp}}(\omega + i\eta)]$. We set $U = 4t^*$ and $V = t^*$. In (b) and (c), we have broadened the peaks with $\eta = 0.01$ for clarity.

particle-hole symmetry, we have $|\langle j|c_{1\sigma}^\dagger|GS\rangle|^2 = |\langle j|c_{1\sigma}|GS\rangle|^2$, and Eq. (2.36) can be written as

$$iG_{\text{imp}}^R(\tau) = 2[\alpha_1 \cos(\omega_1\tau) + \alpha_2 \cos(\omega_2\tau)]\theta(\tau), \quad (2.37)$$

where $\alpha_j = |\langle j|c_{1\sigma}^\dagger|GS\rangle|^2$. Thus, to obtain the impurity Green function in the

frequency domain as

$$G_{\text{imp}}^R(\omega + i\eta) = \alpha_1 \left(\frac{1}{\omega + i\eta - \omega_1} + \frac{1}{\omega + i\eta + \omega_1} \right) + \alpha_2 \left(\frac{1}{\omega + i\eta - \omega_2} + \frac{1}{\omega + i\eta + \omega_2} \right), \quad (2.38)$$

we need to extract the unknown residues α_j and poles ω_j by fitting an expression of the form in Eq. (2.37) to the measurement data of $iG_{\text{imp}}^R(\tau)$, as shown in Fig. 2.20a. This method to determine α_j and ω_j is far more reliable and requires fewer time steps than numerically Fourier-transforming the $iG_{\text{imp}}^R(\tau)$ data. It can also be readily generalised to larger systems by including more terms in the sum in Eq. (2.36). Figure 2.20b shows the real part of the impurity Green function in the frequency domain, $\text{Re}[G_{\text{imp}}^R(\omega + i\eta)]$, with residues and poles obtained from the fit in Fig. 2.20a, while in Fig. 2.20c we plot the real part of the impurity self-energy, $\text{Re}[\Sigma_{\text{imp}}(\omega + i\eta)]$, obtained utilizing the Dyson equation (2.25). We clearly see the four-pole structure of the Green function, while the self-energy has two poles. The results are in excellent agreement with the exact solution of the two-site SIAM, with the poles of the self-energy using fitted α_j and ω_j differing from the exact solution by 2%.

Once we have obtained the impurity Green function, and thus the impurity self-energy, we proceed according to the two-site DMFT protocol in section 2.4.1 until self-consistency has been reached. In DMFT we are interested in the local lattice spectral function $A_{\text{latt},j}(\omega)$ which, at self-consistency, is given by the impurity spectral function $A_{\text{imp}}(\omega)$. In the paramagnetic phase of the infinite-dimensional Hubbard model, the spectral function has a three peak structure with an upper and a lower Hubbard band, corresponding to empty and doubly occupied sites, respectively, and a quasiparticle peak with integrated spectral weight \mathcal{Z} between the bands [9]. In two-site DMFT, since the self-energy has two poles, this three peak structure can be qualitatively reproduced with the spectral function [87]

$$A(\omega) = \rho_0 [\omega + \mu - \Sigma_{\text{imp}}(\omega)], \quad (2.39)$$

where ρ_0 is the non-interacting density of states of the Bethe lattice. Figure 2.21 shows the spectral function in Eq. (2.39) where the impurity self-energy has been obtained both from the XY method and from exact numerics of the two-site SIAM using the interactions $U = 5t^*$ and $U = 8t^*$. We notice that for $U = 5t^*$, the Hubbard bands from the XY method are slightly dislocated and the quasiparticle peak is slightly narrower compared with the exact solution of the two-site SIAM, but the agreement is still very good. The overall shape of the spectral function from the XY method is unchanged compared to the exact case. This underestimation of the width of the quasiparticle peak stems from the fact that the fitting procedure in Fig. 2.20a causes the negative of the derivative of the self-energy in the XY method to be a bit larger than the exact value from the two-site SIAM, i.e., $-\left. \frac{d\text{Re}[\Sigma_{\text{imp}}^{XY}(\omega + i\eta)]}{d\omega} \right|_{\omega=0} \gtrsim -\left. \frac{d\text{Re}[\Sigma_{\text{imp}}^{\text{exact}}(\omega + i\eta)]}{d\omega} \right|_{\omega=0}$, which leads to \mathcal{Z} in Eq. (2.24) from the XY method to be

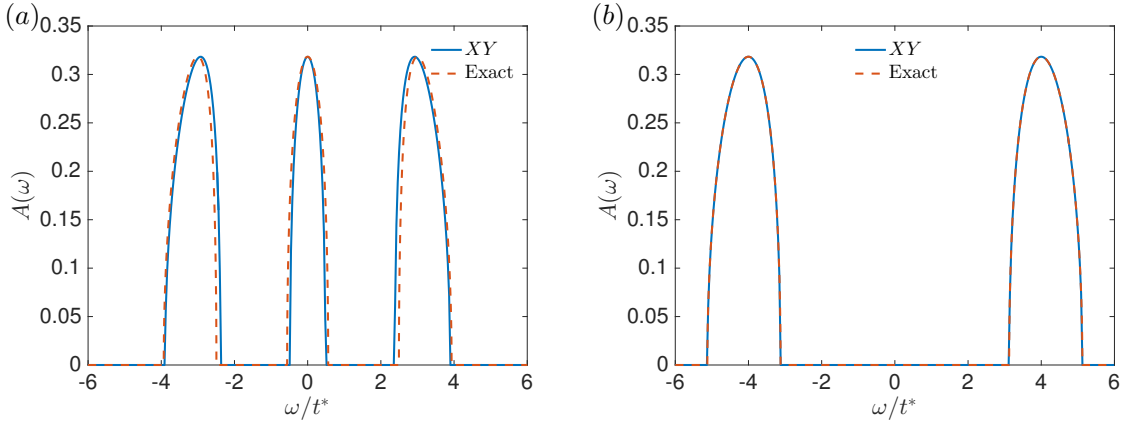


Figure 2.21: **Spectral functions in the metallic and insulating phases.** Spectral functions obtained with the XY method with 24 Trotter steps (blue line) and exact solution of the two-site SIAM (red dashed line). The parameters of the two-site SIAM are iterated to self-consistency with (a) $U = 5t^*$ and (b) $U = 8t^*$.

slightly smaller than in the exact solution of the two-site SIAM, i.e., $\mathcal{Z}^{XY} \lesssim \mathcal{Z}^{\text{exact}}$. For $U = 8t^*$, the two spectral functions agree with maximum relative error of 10^{-8} , since in this case $V = 0$ is found to be the self-consistent solution, whence the Trotterized evolution operator in Eq. (2.33) matches full evolution operator of the two-site SIAM, and thus there is no Trotter error. We observe that in Fig. 2.21 the central quasiparticle peak vanishes, which is characteristic of insulating behavior. See Ref. [87] for a discussion of the artifacts of the spectral functions in two-site DMFT compared to full DMFT.

To study the transition between the two types of spectral functions in Fig. 2.21, we plot in Fig. 2.22 the self-consistent quasiparticle weight \mathcal{Z} obtained from the XY method as a function of the interaction U for different Trotter steps N . We also show \mathcal{Z} from the exact solution of the two-site SIAM for comparison. We see that the digital approach captures the correct trend of the curve, but in the metallic side underestimates to a small degree the values of \mathcal{Z} for interactions close to $U = U_c = 6t^*$, which is the critical interaction for Mott transition in two-site DMFT at half-filling [87]. These results are consistent with the spectral functions in Fig. 2.21. The underestimation of \mathcal{Z} can be diminished by increasing N , as shown in Fig. 2.22. It is noteworthy to mention that two-site DMFT overestimates the quasiparticle weight compared to full DMFT for interactions $U < U_c$, as demonstrated in Ref. [87]. Above U_c , we find $\mathcal{Z} = 0$ to be the self-consistent solution, corresponding to the insulating phase.

On the whole, this section contains a proposal of a quantum algorithm for two-site DMFT to be run on a small digital quantum simulator with a classical feedback loop, thus providing us with the qualitative description of the infinite-dimensional Hubbard model in the thermodynamic limit. We have considered two alternative quantum gate decompositions consistent with state-of-the-art technology in super-

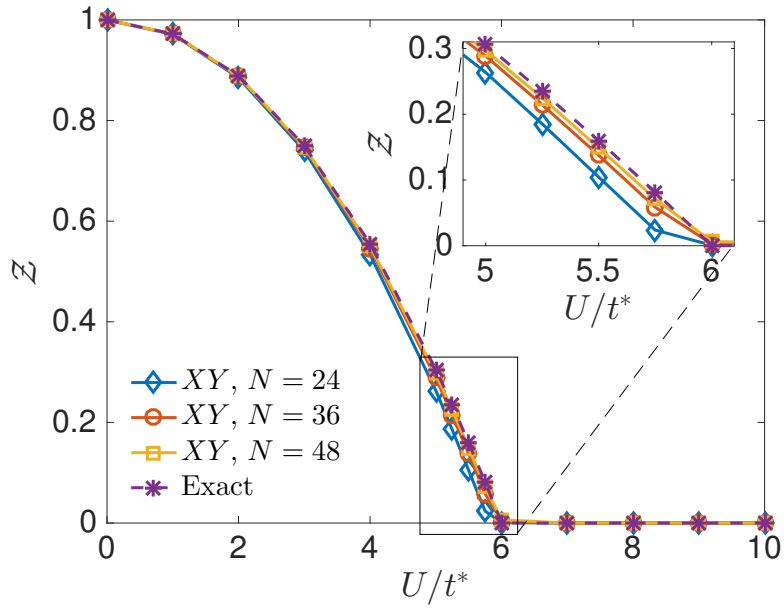


Figure 2.22: **Quasiparticle weight as a function of interaction U .** Self-consistent quasiparticle weight Z obtained from the XY method with 24 (blue diamonds), 36 (red circles), and 48 Trotter steps (yellow squares), compared to the exact solution of the two-site SIAM (purple stars). Inset: Same plot zoomed into the region around the critical interaction, $U_c = 6t^*$.

conducting circuits for the time-evolution operator. We found that an increasing number of Trotter steps improves the fidelity of our digital scheme to qualitatively describe the Mott transition. Our work therefore suggests an interesting application for small-scale quantum devices. It also paves the way for more accurate quantum simulations of strongly correlated fermions in various lattice geometries, which are relevant to novel quantum materials, when the general self-consistency condition and larger number of qubits are used.

Digital Quantum Simulation of Minimal AdS/CFT

H OLOGRAPHIC duality [92] posits the equivalence, subject to conditions, of quantum gravity and ordinary QFTs. The most celebrated such correspondence is conjectured to exist between $\mathcal{N} = 4$ supersymmetric Yang-Mills theory in four dimensions and type IIB string theory on $AdS_5 \times S^5$. Such dualities offer the exciting prospect of probing quantum gravity effects by studying the well-defined equivalent QFT. This is still hard: the semiclassical gravity regime is located at strong coupling and for large number of local degrees of freedom $N \gg 1$. Furthermore, a fully non-perturbative understanding of the dual field theory is likely necessary to resolve the most puzzling aspects of quantum black holes, such as the famous information loss paradox [93]. We may therefore opt for studying the dual field theory on the lattice, by rewriting the problem in terms of a quantum many-body system suitable for simulation on a classical computer [94, 95]. Even this powerful technique faces important challenges and limitations, such as the sign problem [12], and the inapplicability of Euclidean lattice methods for intrinsically Lorentzian physics. It is precisely the latter kind of problem one needs to understand in order to describe black hole formation [96] and evaporation.

It is essential to develop alternative avenues of dealing with strongly coupled quantum many-body systems; both for themselves, as well as with an eye on quantum

gravity. As pointed out throughout this Thesis, and in chapter 2, quantum systems are vastly more computationally efficient at solving many-body Hamiltonians than classical computer simulations. With the recent advent of quantum technologies [43, 97, 98, 35, 99], it is then natural to consider multiqubit systems that encode a dual gravity theory via quantum simulation. Currently, four-dimensional gauge theories such as the aforementioned $\mathcal{N} = 4$ theory appear out of reach (see, however, Ref. [100] for work on QCD in this context). Instead, we start by looking elsewhere for simpler models which nevertheless have a holographic interpretation.

Another reason to look for these holographically useful models is that analog gravity simulation faces severe challenges [101, 102]: any nonlinear gravity theory emerging from some local non-gravitational “substrate” will necessarily have its bulk dynamics entirely frozen. As a result, its bulk degrees of freedom may be entirely disregarded. The restrictions of Refs. [101, 102] are avoided in holographically emergent gravity.

In this chapter, as a first step in this direction, we propose the digital quantum simulation of a QFT with holographic dual, namely the SYK model [103, 104, 105]. We consider different variants of the model, two in terms of Majorana fermions, and two with complex fermions. We then propose digital quantum algorithms for simulating the SYK quantum dynamics, and protocols to test non-equilibrium aspects such as scrambling. Scrambling refers to the spreading of quantum information across a system under unitary evolution. More precisely, one defines the scrambling time t_* to be the minimum time necessary for information, initially localized to a subsystem, to spread evenly across the entire system [28, 29]. Scrambling appears as a crucial notion in holography, owing to the fact that black holes are particularly efficient scramblers of information [30]. In the context of this work the scrambling time appears as the characteristic time after which certain Out-of-Time-Order-Correlators (OTOC) of suitable operators (denoted $W(t), V(0)$, as defined in the main text) decay to zero. This effect can be traced back to the behavior of expectation values of the form $\langle [W(t), V(0)]^2 \rangle$ of two initially commuting operators. For an arbitrary choice of operators this commutator becomes appreciable once $W(t)$ has support on the entire system, in other words at the scrambling time t_* . Subsequently, we discuss the feasibility and implementation of our proposal in suitable quantum platforms such as trapped ions and superconducting circuits.

3.1 The holographic model

The SYK model, in its simplest form, is governed by the quenched-disorder Hamiltonian

$$H = \frac{1}{4 \cdot 4!} \sum_{i,j,k,l=1}^N J_{ijkl} \chi_i \chi_j \chi_k \chi_l, \quad (3.1)$$

where χ_i are Majorana fermions with $\{\chi_i, \chi_j\} = 2\delta_{ij}$, located on a lattice of N sites and interacting via all-to-all couplings J_{ijkl} , sampled from a random distribution that is usually taken to be Gaussian with variance $\frac{3!J^2}{N^3}$. While similar models are common in the study of spin glasses [106], Hamiltonian in Eq. (3.1) lacks a spin-glass phase at low temperatures, making possible its holographic interpretation [107]. Moreover, it has a number of striking features [103, 104, 107, 108], beginning with its solvability in the limit of large N and at strong coupling $\beta J \gg 1$, characterized by an approximate conformal symmetry. Here β denotes inverse temperature. Furthermore, it exhibits maximally chaotic behavior [103], in the sense that the Lyapunov exponent λ , as extracted from a certain OTO four-point function, saturates the bound $\lambda \leq 2\pi/\beta$ [109]. These features strongly suggest that the SYK model is related to an $NAdS2$ (near- $AdS2$) theory of gravity, albeit possibly one with unconventional features [103, 108, 110, 111, 112, 113, 114, 115].

3.1.1 SYK models

The SYK model described by Eq. (3.1) blends quantum gravity in a tractable fermionic Hamiltonian. One can also consider an alternative variant model in terms of complex spinless fermions capturing the same physics in the large N limit, but in principle behaving differently for finite size N . To relate both models, we take $N = 2n$, since two Majorana fermions provide us with one complex spinless fermion, and consider the Hamiltonian

$$H_c = \sum_{i,j,k,\ell=1}^n J_{ij;k\ell} c_i^\dagger c_j^\dagger c_k c_\ell - \mu \sum_i c_i^\dagger c_i, \quad (3.2)$$

with $\{c_i, c_j\} = 0$, $\{c_i, c_j^\dagger\} = \delta_{ij}$, and μ a chemical potential, while independent Gaussian random couplings $J_{ij;k\ell}$, are complex, with zero mean and such that

$$\begin{aligned} J_{ji;k\ell} &= -J_{ij;k\ell}, & J_{ij;\ell k} &= -J_{ij;k\ell}, \\ J_{k\ell;ij} &= J_{ij;k\ell}^*, & \overline{|J_{ij;k\ell}|^2} &= \frac{J^2}{(2n)^3}. \end{aligned} \quad (3.3)$$

We analyze the interaction terms appearing in both previous models for a subsequent treatment in a digital quantum simulation. In the model of Eq. (3.1), with Majorana fermions, we identify two kinds of interaction terms: (i) $\chi_i \chi_j \chi_k \chi_l$ if all

indices are distinct, and (ii) $\chi_i\chi_j$ if two or three subindices coincide. The case of all subindices being equal leads to a global phase in the evolution, which does not affect the simulation. Without loss of generality, we arrange terms such that $i > j > k > l$, where we have grouped instances with the same subindices by redefining the coupling constants¹. Then, the fermionic interaction term count reads

$$\begin{aligned} \text{(i)} \quad & \chi_i\chi_j\chi_k\chi_l : \frac{2}{3}n^4 - 2n^3 + \frac{11}{6}n^2 - \frac{1}{2}n, \\ \text{(ii)} \quad & \chi_i\chi_j : 2n^2 - n. \end{aligned}$$

Interaction terms of type (ii) gather all Majorana fermionic terms with two or three matching subindices².

Because of this separation, we also consider a model with only type (i) terms, with the same large N behavior [108]. Its implementation is straightforward given that of Eq. (3.1), by restricting us to the simulation of the terms in case.

Secondly, the model formulated in terms of spinless complex fermions deals in principle with $(n^4 - 2n^3 + n^2)/4$ summands, which are classified in different kinds of interactions as follows, where the indices are all distinct in each class of term, together with the number of terms to be simulated for each type of interaction:

$$\begin{aligned} \text{(i)} \quad & c_i^\dagger c_j^\dagger c_k c_\ell : \frac{1}{4}n^4 - \frac{3}{2}n^3 + \frac{11}{4}n^2 - \frac{3}{2}n, \\ \text{(ii)} \quad & c_i^\dagger c_j^\dagger c_j c_\ell : n^3 - 3n^2 + 2n, \\ \text{(iii)} \quad & c_i^\dagger c_j^\dagger c_j c_i : \frac{1}{2}n^2 - \frac{1}{2}n, \\ \text{(iv)} \quad & c_i^\dagger c_i : n. \end{aligned}$$

The indices in type (i) have been restricted to $i > j$ and $k > l$, thus reducing the number of terms to be simulated.

There is a straightforward variation of the model with the same holographic interpretation at large N : consider couplings $J_{ij;kl}$ as purely real numbers.

3.2 Algorithm for quantum simulation of SYK models

The digital quantum simulation of the dynamics of the SYK models involves fermionic operators, either Majorana or complex. In current technologies, such a quantum algorithm requires encoding fermionic operators into spin-1/2 operators. This is achieved via the JW transformation, as presented in section 2.1, from spinless complex fermion

¹See a detailed derivation in appendix D.1.

²See appendix D.1.

operators to spin-1/2 operators, $c_i^\dagger = (\prod_{j=1}^{i-1} \sigma_j^z) \sigma_i^+$. We consider the relations between n complex fermions and $N = 2n$ Majorana fermions, $c_j = \chi_{2j-1} + i\chi_{2j}/2$ and $c_j^\dagger = \chi_{2j-1} - i\chi_{2j}/2$. Thus, the corresponding Majorana fermionic operators are codified as $\chi_{2n-1} = (\prod_{j=1}^{n-1} \sigma_j^z) \sigma_n^x$ and $\chi_{2n} = (\prod_{j=1}^{n-1} \sigma_j^z) \sigma_n^y$, with $\{\chi_i, \chi_j\} = 2\delta_{ij}$.

Majorana interaction terms appear in terms of spin degrees of freedom as

$$\chi_i \chi_j \chi_k \chi_l = \sigma_i^{\alpha_i} \left(\prod_{m=\tilde{j}}^{\tilde{i}-1} \sigma_m^z \right) \sigma_j^{\alpha_j} \sigma_k^{\alpha_k} \left(\prod_{m=\tilde{l}}^{\tilde{k}-1} \sigma_m^z \right) \sigma_l^{\alpha_l}, \quad (3.4)$$

and

$$\chi_i \chi_j = \sigma_i^{\alpha_i} \left(\prod_{m=\tilde{j}}^{\tilde{i}-1} \sigma_m^z \right) \sigma_j^{\alpha_j}, \quad (3.5)$$

where $i > j > k > l$. Here, the tilded variables are

$$\tilde{x} = \left\lfloor \frac{x+1}{2} \right\rfloor = \max \left\{ m \in \mathbb{Z} \mid m \leq \frac{x+1}{2} \right\}, \quad (3.6)$$

and the α_n labels correspond to x if n is odd and y if even. Among the resulting spin interaction terms, the most general and complex form corresponds to that shown in Eq. (3.4). In some specific cases of combination of indices the expression is simplified¹.

Let us now consider the model with complex spinless fermions. The interaction terms can be mapped as above to spin interactions via the JW transformation. Thus, the interaction terms of type (i) of this model are expressed as

$$c_i^\dagger c_j^\dagger c_k c_\ell = \kappa \left(\prod_{\xi=\zeta_1+1}^{\zeta_2-1} \sigma_\xi^z \right) \left(\prod_{\xi=\zeta_3+1}^{\zeta_4-1} \sigma_\xi^z \right) \sigma_i^+ \sigma_j^+ \sigma_k^- \sigma_\ell^-, \quad (3.7)$$

where $\{\zeta_1, \zeta_2, \zeta_3, \zeta_4\} = \{i, j, k, \ell\}$ as sets, $\zeta_1 < \zeta_2 < \zeta_3 < \zeta_4$, and $\kappa = \text{sign}(i-j)\text{sign}(\ell-k)$. For the sake of simplicity in the quantum simulation, we have only taken into account the terms such that $i > j$ and $k > l$, wherefore $\kappa = -1$.

The interaction terms of type (ii), (iii) and (iv) can also be mapped to spin interactions as

$$(ii) \quad c_i^\dagger n_j c_k = -\frac{1}{2} \left(\prod_{\xi=\zeta_1+1}^{\zeta_2-1} \sigma_\xi^z \right) (\sigma_j^z + 1) \sigma_i^+ \sigma_k^-, \quad (3.8)$$

$$(iii) \quad n_i n_j = \frac{1}{4} (1 + \sigma_i^z + \sigma_j^z + \sigma_i^z \sigma_j^z), \quad (3.9)$$

$$(iv) \quad n_i = \frac{1}{2} (1 + \sigma_i^z), \quad (3.10)$$

¹See appendix E.1 for further details.

where $\{\zeta_1, \zeta_2\} = \{i, k\}$, again as sets, and $\zeta_1 < \zeta_2$. It is still possible to reduce the number of interaction terms by considering the properties of coefficients $J_{ij;kl}$ ¹.

These spin Hamiltonians are a sum $H = \sum_i^m H_i$, with H_i a many-body spin interaction. A purely analog quantum simulation for the exact evolution is a difficult problem in any quantum platform. On the other hand, each spin interaction term can be handled individually in digital quantum simulations [22]. We recall the theory presented in section 2.1, and decompose the evolution operator in a Trotter–Suzuki product formula with s number of steps,

$$e^{-iHt} = \left(\prod_{j=1}^m e^{-iH_j t/s} \right)^s + \sum_{i < j} \frac{[H_i, H_j] t^2}{2s} + O(J^3 t^3 / s^2). \quad (3.11)$$

This expression approximates the dynamics for time t to an accuracy ϵ of the order of $J^2 t^2 / s$. We note that for each non-zero commutator, $[H_i, H_j] \neq 0$, there is a decrease in accuracy. In the worst case scenario, where all the commutators differ from zero, there will be a reduction of accuracy given by the factor $\binom{m}{2}$, with m the number of interaction terms H_i in the Hamiltonian.

The complexity of the algorithm, i.e., the number of gates required for the dynamics simulation, grows polynomially with the number of fermions N . The coarsest evaluation suggests that achieving an accuracy ϵ over an evolution time t will require a number of gates $m \times \binom{m}{2} \times J^2 t^2 / \epsilon$. In the case at hand, there will be $m \sim O(N^4)$ spin interactions. If each interaction is given by $O(1)$ gates, the number of gates for accuracy ϵ over a time t will be $O(N^{12})$. In fact, the number of non-zero commutators is of order $O(N^6)$, rather than $m^2 \sim O(N^8)$, thus bringing the number of gates down to $O(N^{10})$. As usual, higher order Trotter–Suzuki decompositions, as the symmetric expansion considered later in section 5.1, will improve the accuracy of our simulation with the cost of increasing the number of gates per step. Digitizing the evolution and its translation to a quantum algorithm enable the application of error correction techniques if the gates reach the fault-tolerant threshold [116, 117]. In principle, in such an error-corrected simulation the number of gates is unlimited, and thus our protocol gets to be scalable.

3.2.1 Protocol for correlation measurements

In order to probe the non-equilibrium behavior of the SYK, and more specifically, the dynamics of scrambling [109] in terms of OTO functions, we consider an efficient protocol for determining n -time correlation functions [118]. Here, an ancillary qubit Q_A encodes a correlation function by means of controlled operations. This approach is particularly effective for analog quantum simulation of the evolution, but it is also applicable to digitally synthesized quantum evolutions. This leads to the desired measurement of the four-time correlation function $\langle W_S^\dagger(t) V_S^\dagger(0) W_S(t) V_S(0) \rangle$ as $(\langle \sigma_x \rangle + i \langle \sigma_y \rangle)_A$ over the ancilla². A similar approach in this context has been

¹See appendix E.1 for a detailed derivation.

²See appendix E.2.

recently proposed [119]. Note that in order to evolve the system one requires time inversion, from $t > 0$ back to 0.

3.2.2 Protocols for time inversion

We need a time inversion operation for reversing the evolution of the system. Since the models are described by time independent Hamiltonians, reversing the sign of all the couplings gives us $U(-t)$, where $U(t)$ denotes the time-evolution operator of the system. Alternatively, time inversion can also be implemented without explicitly engineering the algorithm for $U(-t)$ ¹. We consider an additional control qubit Q_C , whose state decides the direction of the evolution in the system S as

$$U_{CS}(t)|\Psi\rangle = \alpha|e\rangle_C U(t)|\psi\rangle_S + \beta|g\rangle_C U(-t)|\psi\rangle_S, \quad (3.12)$$

for an initial state $|\Psi\rangle = (\alpha|e\rangle_C + \beta|g\rangle_C)|\psi\rangle_S$. For an analogous construction, see Ref. [121].

3.2.3 Protocol for state initialization

Scrambling depends on the Hamiltonian structure for typical initial states. It is possible to prepare thermal states on a quantum computer following existing methods in the literature [122, 123]. Moreover, it is also possible to analyze scrambling for explicitly known initial states, where a state with a certain number of excitations in localized fermionic sites can be constructed with single-qubit rotations².

3.3 Implementation in quantum platforms

In order to simulate the interactions, we consider a generic term

$$H_i = \left(\prod_{m=l}^{k-1} \sigma_m^z \right) \left(\prod_{m=j}^{i-1} \sigma_m^z \right) \sigma_i^{\alpha_i} \sigma_j^{\alpha_j} \sigma_k^{\alpha_k} \sigma_l^{\alpha_l}, \quad (3.13)$$

with any combination of $\alpha_i \alpha_j \alpha_k \alpha_l$, and two separated σ^z strings. The simulation of the remaining interactions may be inferred from this technique, since this is the most general kind of spin interactions appearing in the Hamiltonian.

Each of these spin interactions will appear with a different coupling strength $j_i J$, determined by a realization of the random couplings. The protocol will in principle run for several instantiations of the couplings. This, however, might be not necessary for large N , due to self-averaging.

¹See appendix E.2 and Ref. [120] for further explanations.

²A discussion on the correspondence between spin and fermionic states appears in appendix E.2.

The time evolution generated by this term is described by $U(t) = \exp(-ij_i J H_i t)$. Different protocols for the quantum simulation of this unitary operator are platform dependent. In particular, the coupling strength $j_i J$ will be realized by controlling phases in the gates in both the trapped ion and the superconducting circuits schemes.

3.3.1 Trapped ions

The platform of trapped ions has been a workhorse of quantum simulations for some time now [42, 90]. We focus on trapped ions as a candidate platform for our protocol due to the possibility of performing collective dynamics, the high fidelity of 0.999 of the two-qubit gates [124, 125], and the high number of gates, over 200, achieved in simulations [90]. The efficient implementation of exponentials of tensor products of Pauli matrices in trapped ions relies on the MS gate, involving M qubits and local rotations [62, 67]. We consider the standard expression $U_{\text{MS}}(\theta, \varphi) = \exp[-i\theta(\cos(\varphi)S^x + \sin(\varphi)S^y)^2/4]$, and $S^{x,y} = \sum_{j=0}^M \sigma_j^{x,y}$. In order to make contact with the literature in trapped ions, we use in this paragraph a different basis, such that $|g\rangle_z, |e\rangle_z \rightarrow |\tilde{g}\rangle_x, |\tilde{e}\rangle_x$, and the corresponding mapping $\sigma^z \rightarrow \tilde{\sigma}^x$, $\sigma^x \rightarrow \tilde{\sigma}^y$, $\sigma^y \rightarrow \tilde{\sigma}^z$. The tilded objects refer to the ion implementation, while untilded ones come from our algorithms. Having made this distinction, in fact above and in what follows we obviate the tildes.

Since our quantum algorithm requires the simulation of terms with two disjoint JW tails, we consider gates U_{MS}^A and U_{MS}^B associated with the disjoint collective operators $S_A^{x,y} = \sum_{\ell=l}^{l+M} \sigma_\ell^{x,y}$ and $S_B^{x,y} = \sum_{\ell=j}^{j+K} \sigma_\ell^{x,y}$, respectively, and the entangling gate $U_{lj}(\phi) = \exp(i\phi\sigma_l^\alpha\sigma_j^\beta)$. This entangling gate can in turn be achieved in a standard way by another MS gate and individual rotations, with no impact on the complexity studied below¹. We propose then the following step shown in Fig. 3.1, that scales with $O(1)$ in the number of fermions N ,

$$U = U_{\text{MS}}^A(-\frac{\pi}{2}, 0)U_{\text{MS}}^B(-\frac{\pi}{2}, 0)U_{lj}(\phi)U_{\text{MS}}^B(\frac{\pi}{2}, 0)U_{\text{MS}}^A(\frac{\pi}{2}, 0). \quad (3.14)$$

This results in the desired terms², since the choice of the intermediate entangling gate $U_{lj}(\phi)$ allows us to modify the resulting interaction term

$$U = \begin{cases} \exp\left[i\phi\left(a(M)\prod_{i=l+1}^{l+M}\sigma_i^x\right)\left(a(K)\prod_{k=j+1}^{j+K}\sigma_k^x\right)\sigma_l^\alpha\sigma_j^\beta\right], \\ \exp\left[i\phi\left(b(M)\prod_{i=l+1}^{l+M}\sigma_i^x\right)\left(b(K)\prod_{k=j+1}^{j+K}\sigma_k^x\right)\epsilon_{x\beta\delta}\epsilon_{x\alpha\gamma}\sigma_l^\gamma\sigma_j^\delta\right], \\ \exp\left[i\phi\left(a(M)\prod_{i=l+1}^{l+M}\sigma_i^x\right)\left(b(K)\prod_{k=j+1}^{j+K}\sigma_k^x\right)\epsilon_{x\delta\beta}\sigma_l^\alpha\sigma_j^\delta\right], \\ \exp\left[i\phi\left(b(M)\prod_{i=l+1}^{l+M}\sigma_i^x\right)\left(a(K)\prod_{k=j+1}^{j+K}\sigma_k^x\right)\epsilon_{x\gamma\alpha}\sigma_l^\gamma\sigma_j^\beta\right], \end{cases} \quad (3.15)$$

for the cases M and K even, M and K odd, M even and K odd, and M odd and K

¹See appendix E.2 for an extended explanation of MS gates.

²See appendix E.2 for details on the derivation.

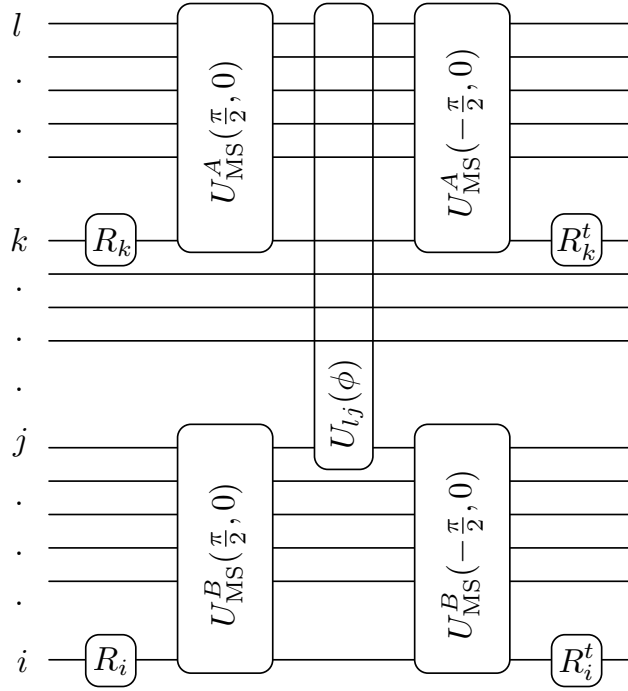


Figure 3.1: **Engineering many-body interactions in trapped-ion qubits.** Operation sequence of single-qubit and multiqubit gates, inside a Trotter step, acting on trapped-ion qubits to generate a generic interaction term (3.13). The single-qubit rotations R_i and R_k act on qubits i and k , respectively, and the phase ϕ of the two-qubit entangling gate, $U_{ij}(\phi)$, must be chosen adequately in order to produce the desired combination of $\alpha_i \alpha_j \alpha_k \alpha_l$ in the interaction.

even, respectively, and with

$$\begin{aligned}
 a(n) &= \begin{cases} -1 & \text{for } n = 4k - 2, k \in \mathbb{N}, \\ 1 & \text{for } n = 4k, k \in \mathbb{N}; \end{cases} \\
 b(n) &= \begin{cases} 1 & \text{for } n = 4k - 3, k \in \mathbb{N}, \\ -1 & \text{for } n = 4k - 1, k \in \mathbb{N}. \end{cases} \end{aligned} \tag{3.16}$$

and $\epsilon_{\alpha\beta\gamma}$ the Levi-Civita symbol.

We note that for the generic and most complex interaction, Eq. (3.13), the JW σ^z tails begin in sites l and j , and end in sites k and i , all corresponding to the ones of the four-body interaction. Up to now, we have achieved a many-body interaction involving l and j sites and two corresponding tails starting in those sites and ending in $l + M$ and $j + K$. The desired interaction can be easily achieved by considering that $l + M$ and $j + K$ correspond to k and i , respectively, and by applying the corresponding rotations in the k -th and i -th qubits to obtain the desired Pauli matrices, as depicted in Fig. 3.1.

3.3.2 Superconducting circuits

The general framework of superconducting quantum processors is an extremely active area of research [126, 58, 59, 89, 88], as stated before. The number of gates achieved in this quantum platform, bounded by system decoherence and gate fidelities, is constantly improving and now reaches up to 1000 quantum logic gates [89]. Moreover, single- and two-qubit gates have been experimentally demonstrated with fidelities at the fault-tolerant threshold for the surface code [60]. The previous protocol for a generic interaction can be taken directly for superconducting circuits if we consider the application of the multiqubit MS gate via a superconducting resonator, studied only theoretically [63], as considered in section 2.1. As they are not yet available, we decompose the basic step in Eq. (3.14) by breaking the MS gate into, in principle, $\binom{n}{2}$ single-qubit and two-qubit gates. These have been demonstrated experimentally in superconducting devices with high fidelities [60]. We consider for the sake of simplicity, and without loss of generality, a single MS gate associated with a collective operator S^x of n qubits, and the sequence of $U_{\text{MS}}(\frac{\pi}{2}, 0)U_i(\phi)U_{\text{MS}}(-\frac{\pi}{2}, 0)$, with $U_i(\phi) = \exp(i\phi\sigma_i^x)$ an intermediate single-qubit gate. In this protocol, shown in Fig. 3.2, by decomposing $U_{\text{MS}}(\frac{\pi}{2}, 0)$ and its inverse into two-qubit gates, we realize that the only operations that do not cancel out are those involving the i -th qubit, in which $U_i(\phi)$ is applied. This implies that instead of $\binom{n}{2}$ two-qubit gates per collective gate, we reduce the number of entangling gates to n in the simulation of each Hamiltonian H_i , i.e., we have a scaling of $O(N)$ gates per interaction.

We may consider not only linear arrays of qubits, but also bidimensional lattices [72, 127] in which the qubit connectivity increases with a qubit having four nearest neighbors. Thus, one can implement the JW transformation as above while reducing the number of SWAP gates needed in the protocol. Another extension, which may be needed for the case of QFTs, is to consider digital-analog quantum simulations [128, 77, 129]. In this manner, we can exploit the concept of complexity-simulating-complexity while merging digital and analog techniques in a complementary fashion.

3.4 Gate count comparison per Trotter step

We compare the number of resulting spin interactions for all models. Here, we denote as first Majorana model that with only quartic interaction terms; as second Majorana model, that which also includes quadratic terms; as first complex model, that with complex coupling constants for complex fermionic interactions; and as second complex model, the restriction of the previous one to only real coupling constants.

The number of spin interactions after the JW mapping is directly related with the number of gates needed for the quantum simulation. For trapped ions, one needs

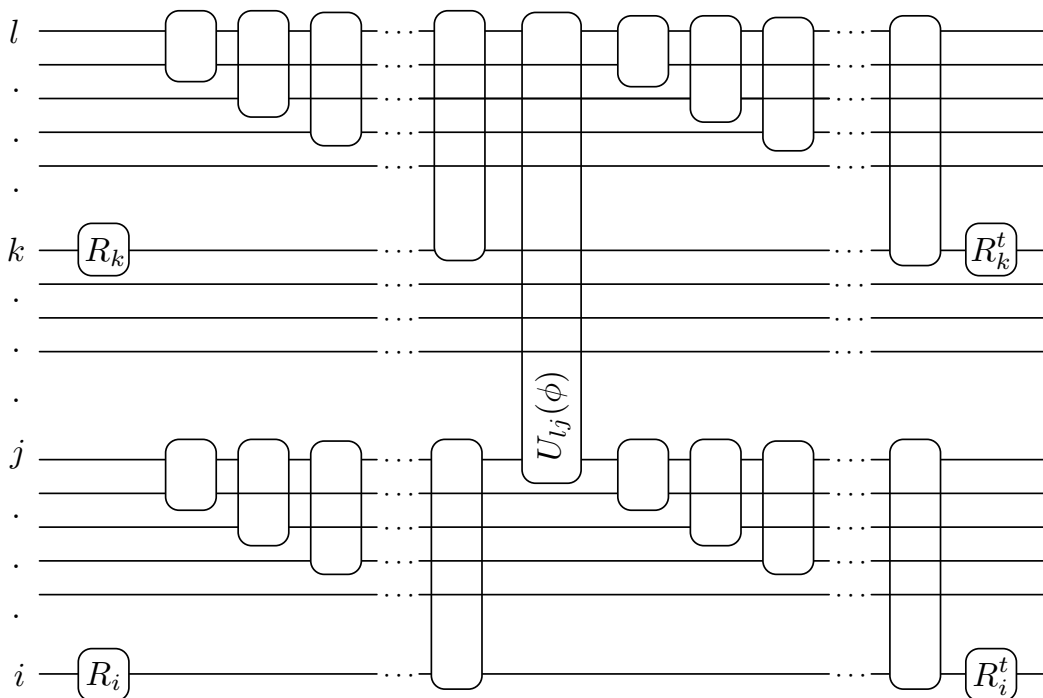


Figure 3.2: **Engineering many-body interactions in superconducting circuits.** We consider sets of two-qubit gates and their inverses, which involve qubits l and j with the rest of the qubits included in the σ^z strings of the interaction. Thus, a set of n two-qubit gates takes on the role of the MS gate in the trapped-ion protocol. Note that two-qubit gates between distant qubits may be performed by a set of SWAP gates and an entangling gate between nearest-neighbor qubits.

$O(1)$ gates per interaction term, whereas it scales with $O(N)$ per interaction for the decomposition of the algorithm in single- and two-qubit gates in superconducting circuits.

In principle, we have found that the second complex model is more suitable to be simulated with our method due to the total amount of gates required. We have not taken into account the length of the JW strings, $\prod_{\xi} \sigma_{\xi}^z$, but only treated them as an element of multiqubit gates.

We analyze deeper these contributions, by decomposing all kinds of multiqubit gates into two-qubit and single-qubit gates for all the models that we have considered, and show the counting in Tables 3.1 and 3.2.

3.5 Criteria for simulated time

Table 3.1: Independent spin interactions for the Majorana models.

Gates	First Majorana model	Second Majorana model
$\left(\prod_{\xi} \sigma_{\xi}^z\right) \left(\prod_{\xi} \sigma_{\xi}^z\right) \sigma_i^{\alpha_i} \sigma_j^{\alpha_j} \sigma_k^{\alpha_k} \sigma_l^{\alpha_l}$	$\frac{2}{3}n^4 - 4n^3 + \frac{22}{3}n^2 - 4n$	$\frac{2}{3}n^4 - 4n^3 + \frac{22}{3}n^2 - 4n$
$\left(\prod_{\xi} \sigma_{\xi}^z\right) \left(\prod_{\xi} \sigma_{\xi}^z\right) \sigma_i^{\alpha_i} \sigma_j^{\alpha_j} \sigma_k^z$	$\frac{2}{3}n^3 - 2n^2 + \frac{4}{3}n$	$\frac{2}{3}n^3 - 2n^2 + \frac{4}{3}n$
$\left(\prod_{\xi} \sigma_{\xi}^z\right) \sigma_i^{\alpha_i} \sigma_j^{\alpha_j} \sigma_k^z$	$\frac{4}{3}n^3 - 4n^2 + \frac{8}{3}n$	$\frac{4}{3}n^3 - 4n^2 + \frac{8}{3}n$
$\left(\prod_{\xi} \sigma_{\xi}^z\right) \sigma_i^{\alpha_i} \sigma_k^{\alpha_k}$	None	$2n^2 - 2n$
$\sigma_i^z \sigma_j^z$	$\frac{1}{2}n^2 - \frac{1}{2}n$	$\frac{1}{2}n^2 - \frac{1}{2}n$
σ_i^z	None	n

Table 3.2: Independent spin interactions for the spinless complex fermion models.

Gates	First complex model	Second complex model
$\left(\prod_{\xi} \sigma_{\xi}^z\right) \left(\prod_{\xi} \sigma_{\xi}^z\right) \sigma_i^{\alpha_i} \sigma_j^{\alpha_j} \sigma_k^{\alpha_k} \sigma_l^{\alpha_l}$	$\frac{2}{3}n^4 - 4n^3 + \frac{22}{3}n^2 - 4n$	$\frac{1}{3}n^4 - 2n^3 + \frac{11}{3}n^2 - 2n$
$\left(\prod_{\xi} \sigma_{\xi}^z\right) \left(\prod_{\xi} \sigma_{\xi}^z\right) \sigma_i^{\alpha_i} \sigma_j^{\alpha_j} \sigma_k^z$	None	None
$\left(\prod_{\xi} \sigma_{\xi}^z\right) \sigma_i^{\alpha_i} \sigma_j^{\alpha_j} \sigma_k^z$	$2n^3 - 6n^2 + 4n$	$n^3 - 3n^2 + 2n$
$\left(\prod_{\xi} \sigma_{\xi}^z\right) \sigma_i^{\alpha_i} \sigma_k^{\alpha_k}$	$2n^2 - 2n$	$n^2 - n$
$\sigma_i^z \sigma_j^z$	$\frac{1}{2}n^2 - \frac{1}{2}n$	$\frac{1}{2}n^2 - \frac{1}{2}n$
σ_i^z	n	n

3.5 Criteria for simulated time

We identify the suitable simulated time for which the system has followed a non-trivial evolution by considering the survival probability of the initial state $P(t) = |\langle \Psi(t) | \Psi(0) \rangle|^2$, and the Bhattacharyya bound [130] given by

$$P(t) \geq \exp(-2\Delta E t) \quad (3.17)$$

as long as $P(t) \geq 1/2$. ΔE is the energy dispersion in the state $|\psi(0)\rangle$. This quantity describes the change of a given initial state $|\Psi(0)\rangle$ for early stages of evolution. We take this state dependent quantity as an inspiration for a general state independent estimate for the time needed for non-trivial evolution. We notice that the largest ΔE , which corresponds to the fastest evolution, would be given in a state with only two components, one associated to the largest eigenvalue and another corresponding

to the smallest one [131], namely with

$$\Delta E_{\text{extr}}^2 = \frac{1}{4} \|H\|^2, \quad (3.18)$$

where $\|H\|$ denotes the spectral spread seminorm, $\|H\| = \lambda_{\max} - \lambda_{\min}$. The fastest evolution would not be typical, though, thus we propose a criterion based on a different spectral invariant, namely

$$\Delta H^2 \equiv \frac{1}{2(\mathcal{N} - 1)} \left[\text{Tr}(H^2) - \frac{1}{\mathcal{N}} \text{Tr}(H)^2 \right], \quad (3.19)$$

where \mathcal{N} is the dimension of the Hilbert space at hand. This quantity is computed to be

$$\Delta H^2 = \frac{1}{2\mathcal{N}(\mathcal{N} - 1)} \sum_{n < m}^{\mathcal{N}} (\lambda_n - \lambda_m)^2, \quad (3.20)$$

where λ_n are the eigenvalues of H . Since the difference square among any pair of eigenvalues is bounded by $\|H\|^2$, we obtain, as expected,

$$\Delta H^2 \leq \frac{1}{2\mathcal{N}(\mathcal{N} - 1)} \sum_{n < m}^{\mathcal{N}} \|H\|^2 = \frac{1}{4} \|H\|^2 = \Delta E_{\text{extr}}^2. \quad (3.21)$$

Let us consider the SYK model with Majorana fermions, keeping only terms of type (i), i.e., with no repeated indices,

$$H = \sum_{i < j < k < l = 1}^N J_{ijkl} \chi_i \chi_j \chi_k \chi_l, \quad (3.22)$$

in which the statistical average with the normalization condition is given by $\overline{|J_{ijkl}^2|} = 3!J^2/N^3$. In this case, we firstly note that $\text{Tr}(H) = 0$ since $\text{Tr}(\chi_i \chi_j \chi_k \chi_l) = 0$ if all indices are distinct. Secondly, we calculate $\text{Tr}(H^2)$, which corresponds to

$$\begin{aligned} \text{Tr}(H^2) &= \sum_{i > j > k > l = 1}^N \sum_{\alpha > \beta > \gamma > \delta = 1}^N J_{ijkl} J_{\alpha\beta\gamma\delta} \text{Tr}(\chi_i \chi_j \chi_k \chi_l \chi_\alpha \chi_\beta \chi_\gamma \chi_\delta) \\ &= \sum_{i > j > k > l = 1}^N J_{ijkl}^2 \mathcal{N}. \end{aligned} \quad (3.23)$$

We have used that under the conditions $i > j > k > l$ and $\alpha > \beta > \gamma > \delta$,

$$\text{Tr}(\chi_i \chi_j \chi_k \chi_l \chi_\alpha \chi_\beta \chi_\gamma \chi_\delta) = \delta_{i\alpha} \delta_{j\beta} \delta_{k\gamma} \delta_{l\delta} \text{Tr}(1) = \mathcal{N} \delta_{i\alpha} \delta_{j\beta} \delta_{k\gamma} \delta_{l\delta}. \quad (3.24)$$

Assuming $N = 2n$, we have $\mathcal{N} = 2^n$, and

$$\Delta H^2 = \frac{\mathcal{N}}{2(\mathcal{N} - 1)} \sum_{i > j > k > l = 1}^N J_{ijkl}^2. \quad (3.25)$$

Averaging these coefficients, which for type (i) interactions are real, we obtain

$$\overline{\Delta H^2} = \frac{\mathcal{N}}{2(\mathcal{N}-1)} \frac{3!J^2}{N^3} \sum_{i>j>k>l=1}^N 1 = \frac{\mathcal{N}}{2(\mathcal{N}-1)} \frac{3!J^2}{N^3} \frac{1}{4!} N(N-1)(N-2)(N-3). \quad (3.26)$$

Taking into account this expression and Eqs. (3.17) and (3.21), we consider as an orientation for non-trivial dynamics the bound

$$Jt = \sqrt{\frac{2(\mathcal{N}-1)}{\mathcal{N}}} \sqrt{\frac{N^3(N-4)!}{N!}} \ln 2, \quad (3.27)$$

which scales with $N^{-1/2}$. We extend this generic expression, independent of the initial state and computed for one of the models, as a guide for obtaining the correct order of magnitude of Jt for the simulations of all the similar models considered.

3.6 Implementation details for $n = 4$ complex fermions

We consider the particular case of four qubits, and the model with complex fermions for $n = 4$, extensible to $N = 8$ in the case of the model with Majorana fermions.

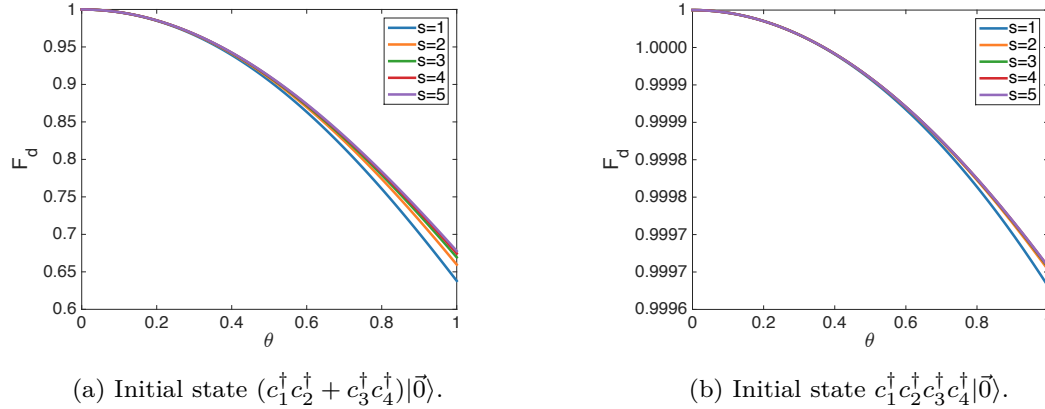


Figure 3.3: **Digital fidelities of the quantum algorithm.** Fidelity $F_d(\theta) = |\langle \Psi_d(\theta) | \Psi(\theta) \rangle|$ of the digitized evolution as a function of $\theta = Jt$, with $J = 4$. We consider a digital protocol with $s = 1, 2, 3, 4, 5$ Trotter steps, and initial states (a) $(c_1^\dagger c_2^\dagger + c_3^\dagger c_4^\dagger)|\vec{0}\rangle = (\sigma_1^+ \sigma_1^z \sigma_2^+ + \sigma_3^+ \sigma_3^z \sigma_4^+)|\vec{0}\rangle$, and (b) $c_1^\dagger c_2^\dagger c_3^\dagger c_4^\dagger|\vec{0}\rangle = \sigma_1^+ \sigma_1^z \sigma_2^+ \sigma_3^z \sigma_4^+|\vec{0}\rangle$.

The SYK model in terms of $n = 4$ complex spinless fermions is characterized by

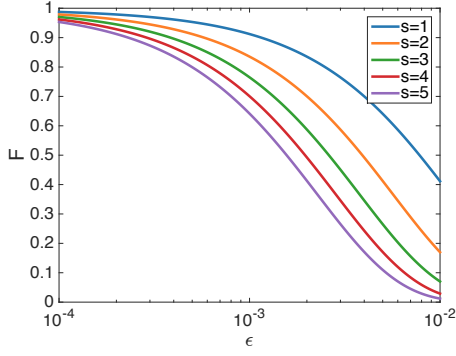
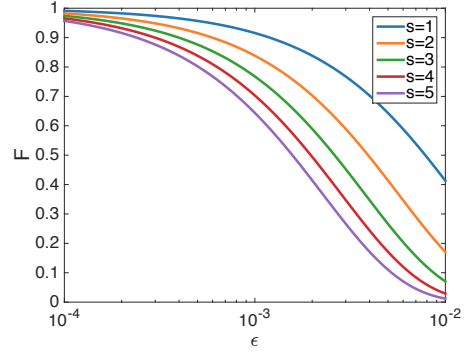
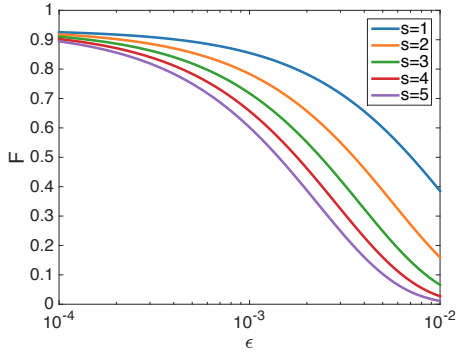
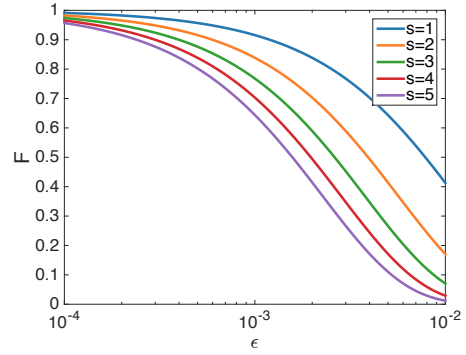
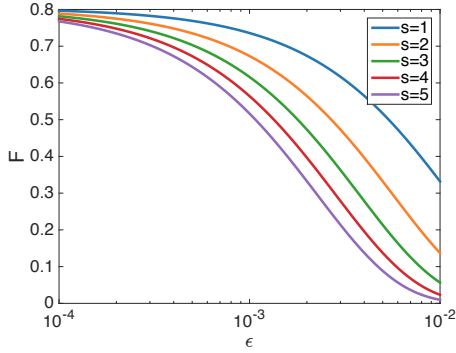
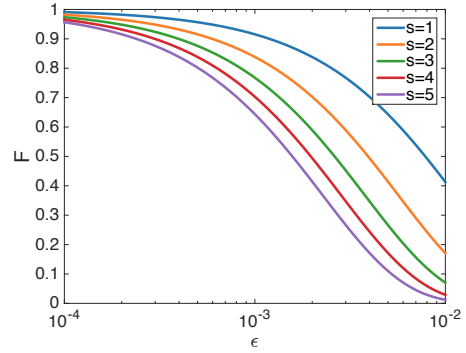
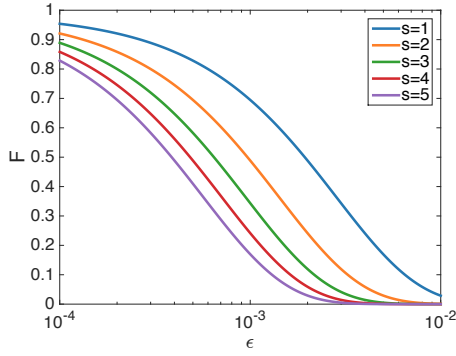
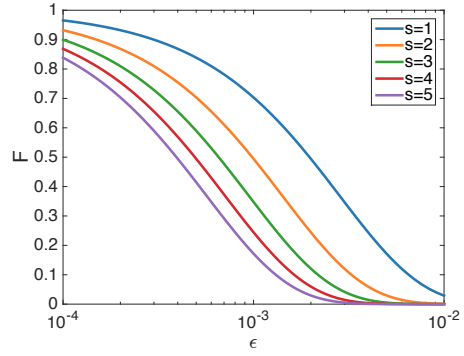

 (a) Initial state $(c_1^\dagger c_2^\dagger + c_3^\dagger c_4^\dagger)|\vec{0}\rangle$ and $\theta = 0.15$.

 (b) Initial state $c_1^\dagger c_2^\dagger c_3^\dagger c_4^\dagger|\vec{0}\rangle$ and $\theta = 0.15$.

 (c) Initial state $(c_1^\dagger c_2^\dagger + c_3^\dagger c_4^\dagger)|\vec{0}\rangle$ and $\theta = 0.30$.

 (d) Initial state $c_1^\dagger c_2^\dagger c_3^\dagger c_4^\dagger|\vec{0}\rangle$ and $\theta = 0.30$.

 (e) Initial state $(c_1^\dagger c_2^\dagger + c_3^\dagger c_4^\dagger)|\vec{0}\rangle$ and $\theta = 1$.

 (f) Initial state $c_1^\dagger c_2^\dagger c_3^\dagger c_4^\dagger|\vec{0}\rangle$ and $\theta = 1$.

Figure 3.4: **Total lower bound of the state fidelity F of the quantum simulation for trapped ions** as a function of the multiqubit gate error ϵ . We consider cases of $s = 1, 2, 3, 4, 5$ Trotter steps, and initial states (a) $(c_1^\dagger c_2^\dagger + c_3^\dagger c_4^\dagger)|\vec{0}\rangle = (\sigma_1^+ \sigma_1^z \sigma_2^+ + \sigma_3^+ \sigma_3^z \sigma_4^+)|\vec{0}\rangle$ with a simulated phase of $\theta = Jt = 0.15$, (b) $c_1^\dagger c_2^\dagger c_3^\dagger c_4^\dagger|\vec{0}\rangle = \sigma_1^+ \sigma_1^z \sigma_2^+ \sigma_3^+ \sigma_3^z \sigma_4^+|\vec{0}\rangle$ with $\theta = 0.15$, (c) $(c_1^\dagger c_2^\dagger + c_3^\dagger c_4^\dagger)|\vec{0}\rangle$ with $\theta = 0.30$, (d) $c_1^\dagger c_2^\dagger c_3^\dagger c_4^\dagger|\vec{0}\rangle$ with $\theta = 0.30$, (e) $(c_1^\dagger c_2^\dagger + c_3^\dagger c_4^\dagger)|\vec{0}\rangle$ with $\theta = 1$, and (f) $c_1^\dagger c_2^\dagger c_3^\dagger c_4^\dagger|\vec{0}\rangle$ with $\theta = 1$.

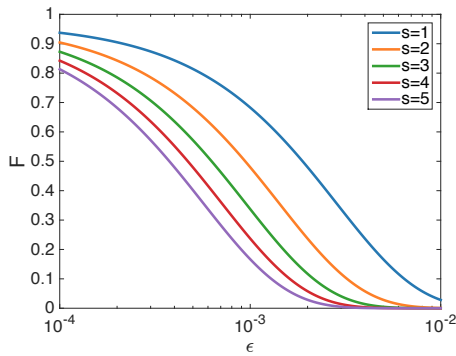
3.6 Implementation details for $n = 4$ complex fermions



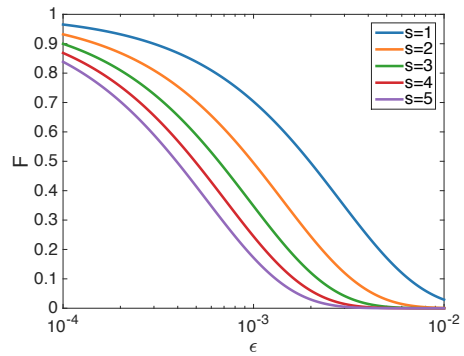
(a) Initial state $(c_1^\dagger c_2^\dagger + c_3^\dagger c_4^\dagger)|\vec{0}\rangle$ and $\theta = 0.15$.



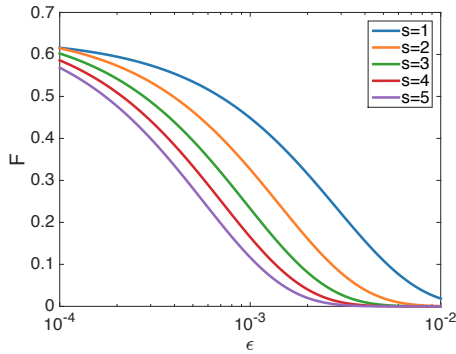
(b) Initial state $c_1^\dagger c_2^\dagger c_3^\dagger c_4^\dagger|\vec{0}\rangle$ and $\theta = 0.15$.



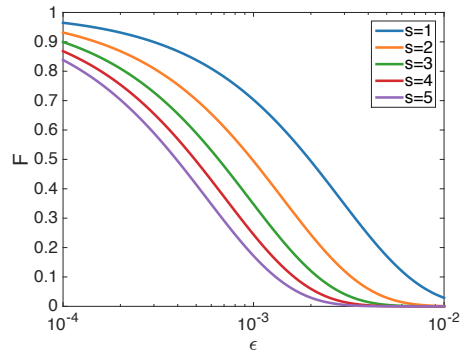
(c) Initial state $(c_1^\dagger c_2^\dagger + c_3^\dagger c_4^\dagger)|\vec{0}\rangle$ and $\theta = 0.30$.



(d) Initial state $c_1^\dagger c_2^\dagger c_3^\dagger c_4^\dagger|\vec{0}\rangle$ and $\theta = 0.30$.



(e) Initial state $(c_1^\dagger c_2^\dagger + c_3^\dagger c_4^\dagger)|\vec{0}\rangle$ and $\theta = 1$.



(f) Initial state $c_1^\dagger c_2^\dagger c_3^\dagger c_4^\dagger|\vec{0}\rangle$ and $\theta = 1$.

Figure 3.5: **Total lower bound of the state fidelity F of the quantum simulation for superconducting circuits** as a function of the two-qubit gate error ϵ . We consider cases of $s = 1, 2, 3, 4, 5$ Trotter steps, and initial states (a) $(c_1^\dagger c_2^\dagger + c_3^\dagger c_4^\dagger)|\vec{0}\rangle = (\sigma_1^+ \sigma_1^z \sigma_2^+ + \sigma_3^+ \sigma_3^z \sigma_4^+)|\vec{0}\rangle$ with a simulated phase of $\theta = Jt = 0.15$, (b) $c_1^\dagger c_2^\dagger c_3^\dagger c_4^\dagger|\vec{0}\rangle = \sigma_1^+ \sigma_1^z \sigma_2^+ \sigma_3^+ \sigma_3^z \sigma_4^+|\vec{0}\rangle$ with $\theta = 0.15$, (c) $(c_1^\dagger c_2^\dagger + c_3^\dagger c_4^\dagger)|\vec{0}\rangle$ with $\theta = 0.30$, (d) $c_1^\dagger c_2^\dagger c_3^\dagger c_4^\dagger|\vec{0}\rangle$ with $\theta = 0.30$, (e) $(c_1^\dagger c_2^\dagger + c_3^\dagger c_4^\dagger)|\vec{0}\rangle$ with $\theta = 1$, and (f) $c_1^\dagger c_2^\dagger c_3^\dagger c_4^\dagger|\vec{0}\rangle$ with $\theta = 1$.

the Hamiltonian

$$H_c = \sum_{i,j,k,\ell=1}^4 J_{ij;k\ell} c_i^\dagger c_j^\dagger c_k c_\ell - \mu \sum_i c_i^\dagger c_i, \quad (3.28)$$

with in principle complex coefficients $J_{ij;k\ell}$ sampled from a Gaussian random distribution with variance $3!J^2/(2n)^3$. This first complex model can be simplified to the second complex model by restricting ourselves to real coupling coefficients $J_{ij;k\ell}$. Both models encapsulate holographic features in the limit of large n and strong coupling, but, as shown in section 3.4, the number of gates per Trotter step is smaller for the second model.

We consider explicitly the terms for the first complex model, which is easily reduced to the second one. The Hamiltonian in terms of spin interactions can be organized as

$$H = H_1 + H_2 + H_3 + H_4, \quad (3.29)$$

with H_1 involving terms of type (iii) in section 3.1.1, that is, with the form $n_i n_j$; H_2 terms of type (i), with the form $c_i^\dagger c_j^\dagger c_k c_\ell$ and different indices; H_3 those of type (ii), $c_i^\dagger n_j c_k$, with $i - k = 1$; and H_4 those of type (ii) with $i - k \neq 1$.

The gate decomposition of H_1 in full detail is the following

$$\begin{aligned} H_1 = & (J_{12;12} + J_{13;13} + J_{14;14} + \frac{\mu}{2})\sigma_1^z + (J_{12;12} + J_{23;23} + J_{24;24} + \frac{\mu}{2})\sigma_2^z \\ & + (J_{13;13} + J_{23;23} + J_{34;34} + \frac{\mu}{2})\sigma_3^z + (J_{14;14} + J_{24;24} + J_{34;34} + \frac{\mu}{2})\sigma_4^z \\ & + J_{12;12}\sigma_1^z\sigma_2^z + J_{13;13}\sigma_1^z\sigma_3^z + J_{14;14}\sigma_1^z\sigma_4^z \\ & + J_{23;23}\sigma_2^z\sigma_3^z + J_{24;24}\sigma_2^z\sigma_4^z + J_{34;34}\sigma_3^z\sigma_4^z, \end{aligned} \quad (3.30)$$

in which we have taken into account all the interaction terms with permuted indices that can be related among them. Those can be expressed with a single coefficient of a fixed subindex order.

The Hamiltonian terms with non coincident subindices are

$$\begin{aligned} -2H_2 = & \text{Re}(J_{12;34}^1)(\sigma_1^x\sigma_2^x\sigma_3^x\sigma_4^x + \sigma_1^y\sigma_2^y\sigma_3^y\sigma_4^y) + \text{Re}(J_{12;34}^2)(\sigma_1^y\sigma_2^x\sigma_3^y\sigma_4^x + \sigma_1^x\sigma_2^y\sigma_3^x\sigma_4^y) \\ & + \text{Re}(J_{12;34}^3)(\sigma_1^y\sigma_2^x\sigma_3^x\sigma_4^y + \sigma_1^x\sigma_2^y\sigma_3^y\sigma_4^x) + \text{Re}(J_{12;34}^4)(\sigma_1^x\sigma_2^x\sigma_3^y\sigma_4^y + \sigma_1^y\sigma_2^y\sigma_3^x\sigma_4^x) \\ & + \text{Im}(J_{12;34}^1)(\sigma_1^y\sigma_2^x\sigma_3^x\sigma_4^x - \sigma_1^x\sigma_2^y\sigma_3^y\sigma_4^y) + \text{Im}(J_{12;34}^2)(\sigma_1^y\sigma_2^y\sigma_3^x\sigma_4^y - \sigma_1^x\sigma_2^x\sigma_3^y\sigma_4^x) \\ & + \text{Im}(J_{12;34}^3)(\sigma_1^y\sigma_2^y\sigma_3^y\sigma_4^x - \sigma_1^x\sigma_2^x\sigma_3^x\sigma_4^y) + \text{Im}(J_{12;34}^4)(\sigma_1^y\sigma_2^x\sigma_3^y\sigma_4^y - \sigma_1^x\sigma_2^y\sigma_3^x\sigma_4^x), \end{aligned} \quad (3.31)$$

with

$$\begin{aligned} J_{12;34}^1 &= J_{12;34}^* + J_{13;24}^* + J_{14;23}, \\ J_{12;34}^2 &= J_{12;34}^* - J_{13;24}^* + J_{14;23}, \\ J_{12;34}^3 &= J_{12;34}^* + J_{13;24}^* - J_{14;23}, \\ J_{12;34}^4 &= -J_{12;34}^* + J_{13;24}^* + J_{14;23}, \end{aligned}$$

linear dependent coefficients, since $J_{12;34}^1 = J_{12;34}^2 + J_{12;34}^3 + J_{12;34}^4$.

The spin terms grouped in H_3 are inferred from Eq. (E.6). Since we consider that $i - k = 1$, the JW tail $\prod \sigma_\xi^z$ does not appear, yielding

$$\begin{aligned}
 -H_3 = & (\sigma_1^z + 1) [\text{Re}(J_{21;13})(\sigma_2^x \sigma_3^x + \sigma_2^y \sigma_3^y) + \text{Im}(J_{21;13})(\sigma_2^x \sigma_3^y - \sigma_2^y \sigma_3^x)] \\
 & + (\sigma_1^z + 1) [\text{Re}(J_{31;14})(\sigma_3^x \sigma_4^x + \sigma_3^y \sigma_4^y) + \text{Im}(J_{31;14})(\sigma_3^x \sigma_4^y - \sigma_3^y \sigma_4^x)] \\
 & + (\sigma_3^z + 1) [\text{Re}(J_{13;32})(\sigma_1^x \sigma_2^x + \sigma_1^y \sigma_2^y) + \text{Im}(J_{13;32})(\sigma_1^x \sigma_2^y - \sigma_1^y \sigma_2^x)] \\
 & + (\sigma_4^z + 1) [\text{Re}(J_{14;42})(\sigma_1^x \sigma_2^x + \sigma_1^y \sigma_2^y) + \text{Im}(J_{14;42})(\sigma_1^x \sigma_2^y - \sigma_1^y \sigma_2^x)] \\
 & + (\sigma_2^z + 1) [\text{Re}(J_{32;24})(\sigma_3^x \sigma_4^x + \sigma_3^y \sigma_4^y) + \text{Im}(J_{32;24})(\sigma_3^x \sigma_4^y - \sigma_3^y \sigma_4^x)] \\
 & + (\sigma_4^z + 1) [\text{Re}(J_{24;43})(\sigma_2^x \sigma_3^x + \sigma_2^y \sigma_3^y) + \text{Im}(J_{24;43})(\sigma_2^x \sigma_3^y - \sigma_2^y \sigma_3^x)], \quad (3.32)
 \end{aligned}$$

in which we have taken into account a factor 4 introduced with all the variations of the coefficients $J_{ij;jk}$ with permuted indices.

In H_4 , we consider those spin terms described in Eq. (E.6) with $i - k \neq 1$. In this case, it is necessary to consider JW tails $\prod \sigma_\xi^z$, which results in

$$\begin{aligned}
 -H_4 = & (\sigma_1^z \sigma_3^z + \sigma_3^z) [\text{Re}(J_{21;14})(\sigma_2^x \sigma_4^x + \sigma_2^y \sigma_4^y) + \text{Im}(J_{21;13})(\sigma_2^x \sigma_4^y - \sigma_2^y \sigma_4^x)] \\
 & + (\sigma_2^z + 1) [\text{Re}(J_{12;23})(\sigma_1^x \sigma_3^x + \sigma_1^y \sigma_3^y) + \text{Im}(J_{12;23})(\sigma_1^x \sigma_3^y - \sigma_1^y \sigma_3^x)] \\
 & + (\sigma_2^z \sigma_3^z + \sigma_3^z) [\text{Re}(J_{12;24})(\sigma_1^x \sigma_4^x + \sigma_1^y \sigma_4^y) + \text{Im}(J_{12;24})(\sigma_1^x \sigma_4^y - \sigma_1^y \sigma_4^x)] \\
 & + (\sigma_2^z \sigma_3^z + \sigma_2^z) [\text{Re}(J_{13;34})(\sigma_1^x \sigma_4^x + \sigma_1^y \sigma_4^y) + \text{Im}(J_{13;34})(\sigma_1^x \sigma_4^y - \sigma_1^y \sigma_4^x)] \\
 & + (\sigma_2^z \sigma_4^z + \sigma_2^z) [\text{Re}(J_{14;43})(\sigma_1^x \sigma_3^x + \sigma_1^y \sigma_3^y) + \text{Im}(J_{14;43})(\sigma_1^x \sigma_3^y - \sigma_1^y \sigma_3^x)] \\
 & + (\sigma_3^z + 1) [\text{Re}(J_{23;34})(\sigma_2^x \sigma_4^x + \sigma_2^y \sigma_4^y) + \text{Im}(J_{23;34})(\sigma_2^x \sigma_4^y - \sigma_2^y \sigma_4^x)]. \quad (3.33)
 \end{aligned}$$

We consider random values for the coefficients $J_{ij;k\ell}$ such that they satisfy the constraints of the model for an arbitrary time unit. We consider several realizations of time evolution as an example for estimating the efficiency, without finally averaging. The protocol gives similar results for diverse samples of the couplings. The value of the chemical potential is $\mu = 0.75$, and the numerically random generated values for this proof-of principle example are taken from a Gaussian distribution with mean value 0 and variance $J^2/(2n)^3$, with $J = 4$ in an arbitrary unit of time. The values for the coefficients in the simulations shown in Figs. 3.3, 3.4, and 3.5 do not influence the outcome. Similar final results appear for several tests.

We analyze the efficiency of the quantum algorithm designed for computing the evolved quantum state. We consider two sources of error for this quantum simulation, the first is the digital error inherent to the proposed algorithm, and the second involves the experimental error, such as decoherence times and gate errors. The digital error ϵ_d is proportional to

$$\epsilon_d \approx \sum_{i < j} \frac{[H_i, H_j] t^2}{2s}, \quad (3.34)$$

with H_i representing each of the different summands in the simulated Hamiltonian of Eq. (3.29), t the simulated final time of the evolution, and s the number of Trotter

steps considered in the protocol. In order to take this error contribution into account, we compute the state fidelity $F_d(\theta) = |\langle \Psi_d(\theta) | \Psi(\theta) \rangle|$ of the digitized evolution, with $|\Psi_d(\theta)\rangle$ and $|\Psi(\theta)\rangle$ the quantum states associated with the digital evolution and the exact unitary evolution, respectively. Here, θ is a dimensionless parameter defined as $\theta = Jt$, which indicates the dependence of the fidelity with t .

In Fig. 3.3, we show the state fidelity F_d of the digitized evolution for different Trotter steps, ranging from $s = 1$ to $s = 5$. As expected, the higher the number of Trotter steps in the protocol and the lower the simulated time, the higher the state fidelity. For the few number of Trotter steps considered we appreciate fidelities above 0.95 for $\theta \leq 0.2$ for different cases of initial states.

In order to choose a phase θ such that the simulated final time is associated with non trivial dynamics, we take as a guide the state survival probability bound estimated in section 3.5. We consider the state survival probability $P(t)$ in terms of θ , and consider $P(\theta) = \frac{1}{2}$ as the adequate limit value for nontrivial dynamics in short times.

For $n = 4$, we consider Eq. (3.27), and obtain that the required running time scaled with J is

$$\theta = Jt = \frac{4 \cdot \ln 2}{2 \cdot \sqrt{7}} = 0.6. \quad (3.35)$$

Therefore, we select different values of θ of that order of magnitude. Notice that for higher values of θ revivals may occur following the decay at earlier stages of evolution.

The fidelity of the gates in different quantum technologies is constantly improving, reaching values of 99.4% for two-qubit gates in superconducting circuits [60], and values of 99.9% in trapped ions [124, 125]. In addition, in trapped ions it is possible to realize MS-type gate operations with fidelities of 99.3% [41]. In this quantum technology, experiments entangling 14 qubits with this kind of gate have been performed [132]. Different experimental errors contribute to the final fidelity in a quantum gate. For the sake of simplicity and generality, we consider a fixed fidelity per two-qubit gate between nearest-neighbor qubits in the case of superconducting qubits, and a fixed fidelity per MS gate in the case of trapped ions. This approach enables us to encompass different sources of experimental error in the final fidelity estimation.

In Figs. 3.4 and 3.5, we show the total lower bound of the state fidelity for the digital quantum simulation in trapped ions and superconducting circuits, respectively. This total state fidelity F is calculated as the product of the entangling gate fidelities F_g and the fidelity F_d of the digital protocol, $F = F_d(F_g)^{sm}$, with s the number of Trotter steps, and m the number of gates per step required. In trapped ions, m is identified with the number of MS gates in the protocol. The computations are performed for a phase $\theta = Jt = 0.5$ and for $s = 1, 2, 3, 4, 5$ Trotter steps. For superconducting circuits, we identify m with the number of two-qubit gates between nearest-neighbor qubits demanded.

The number of gates for this first complex model is computed in Table 3.2, with $\frac{2}{3}n^4 - 2n^3 + \frac{10}{3}n^2 - 2n$ multiqubit gates required in the first complex model. In trapped ions, MS gate operations provide these multiqubit gates, therefore we consider that

$m = \frac{2}{3}n^4 - 2n^3 + \frac{10}{3}n^2 - 2n$, that is, $m = 88$ in our case of $n = 4$. In superconducting circuits, we decompose the multiqubit interactions in two-qubit gates, which increases the number of total gates as $m = n \left(\frac{2}{3}n^4 - 2n^3 + \frac{10}{3}n^2 - 2n \right)$, leading to $m = 352$ in our case.

In both quantum platforms, we observe that for the range of gate error ϵ we explore, the protocol with fewer gates, i.e., with fewer Trotter steps, shows better performance. In general, one expects that the results improve with the number of Trotter steps, since the digital error decreases. Nonetheless, here the digital fidelity F_d is above 0.95 for all cases considered in Figs. 3.4 and 3.5, and does not affect dramatically the final result. The influence of the chosen initial state in the fidelity of a digital quantum simulation for low n is significant, as shown in the figures. One expects that for higher n the impact of the initial state diminishes, due to the scaling of the number of interactions involved in the dynamics.

In this chapter, we have proposed the digital quantum simulation of SYK models. We encode the SYK nonlocal fermionic model onto a multiqubit system, and show how to efficiently simulate its dynamics with digital techniques and polynomial resources. We also provide a protocol for studying the non-equilibrium behavior, including the scrambling of information. Our proposal could be implemented with state-of-the-art trapped ions and superconducting circuits, paving the way towards the realization in the laboratory of models that can illuminate low-dimensional theories with holographic duals.

Digital–Analog Quantum Simulations of Quantum Field Theory

QUANTUM field theories [133] are among the deepest descriptions of nature. Therefore, they deserve special attention, and different computing approaches have been developed, as Feynman diagrams [133] or lattice gauge theories [134, 135]. In general, the numerical simulations of QFTs are computationally hard, with the processing time growing exponentially with system size. Nevertheless, a quantum simulator [18, 22, 136] could provide an efficient way to emulate these theories [137, 138, 139, 140, 44, 141, 142] in polynomial time. Here, we propose the quantum simulation of fermionic field modes interacting via a continuum of bosonic modes with superconducting circuits [69, 52, 143, 144, 145, 126, 146, 147, 148], which are among the most advanced quantum technologies in terms of quantum control and scalability, as presented in section 2.3. An important feature of superconducting devices is that, unlike other quantum platforms, they offer naturally a strong coupling of qubits to a continuum of bosonic modes. Therefore, this system is a specially suited platform to realize quantum simulations of scattering processes involving interacting fermionic and bosonic QFTs, where access to the continuum of modes is required.

4.1 Quantum field theory model

Our current understanding of the most basic processes in nature is based on interacting QFTs [133]. In the same vein, models involving interaction of fermions and bosons play a key role. In this kind of systems, one is able to describe fermion-fermion scattering mediated by bosonic fields, fermionic self-energies, and bosonic polarization. In particular, we will consider a QFT model under the following assumptions: (i) 1+1 dimensions, (ii) scalar fermions and bosons, and is described by the Hamiltonian

$$H = \int dp \omega_p (b_p^\dagger b_p + d_p^\dagger d_p) + \int dk \omega_k a_k^\dagger a_k + \int dx \psi^\dagger(x) \psi(x) A(x). \quad (4.1)$$

Here, $A(x) = i \int dk \lambda_k \sqrt{\omega_k} (a_k^\dagger e^{-ikx} - a_k e^{ikx}) / \sqrt{4\pi}$ is a bosonic field, with coupling constants λ_k , and $\psi(x)$ is the fermionic field, $b_p^\dagger(b_p)$ and $d_p^\dagger(d_p)$ are its corresponding fermionic and antifermionic creation(annihilation) operators for mode frequency ω_p , while $a_k^\dagger(a_k)$ is the creation(annihilation) bosonic operator associated with frequency ω_k ¹. In this Thesis, we introduce a method for the scalable digital-analog quantum simulation of interacting fermions, based on Eq. (4.1), exploiting state-of-the-art superconducting circuits. In this quantum technology, we enjoy the possibility of a strong coupling of matter qubits with a one-dimensional continuum of bosonic field modes.

4.2 Encoding of fermions in qubits

In order to adapt the simulated model to the simulating setup, we consider a further simplification in Eq. (4.1): (iii) one fermionic and one antifermionic field comoving modes [44] interacting via a continuum of bosons. In this case, the interaction Hamiltonian reads²

$$\begin{aligned} H_{\text{int}} = & i \int dx dk \lambda_k \sqrt{\frac{\omega_k}{2}} \left(|\Lambda_1(p_f, x, t)|^2 b_{\text{in}}^\dagger b_{\text{in}} \right. \\ & + \Lambda_1^*(p_f, x, t) \Lambda_2(p_{\bar{f}}, x, t) b_{\text{in}}^\dagger d_{\text{in}}^\dagger + \Lambda_2^*(p_{\bar{f}}, x, t) \Lambda_1(p_f, x, t) d_{\text{in}} b_{\text{in}} \\ & \left. + |\Lambda_2(p_{\bar{f}}, x, t)|^2 d_{\text{in}} d_{\text{in}}^\dagger \right) \left(a_k^\dagger e^{-ikx} - a_k e^{ikx} \right). \end{aligned} \quad (4.2)$$

¹For a complete derivation of the QFT model see appendix F.

²A discussion on the field comoving modes appears in appendix F.1.

The fermionic and antifermionic operators obey anticommutation relations $\{b_{\text{in}}, b_{\text{in}}^\dagger\} = \{d_{\text{in}}, d_{\text{in}}^\dagger\} = 1$, and the bosonic operators satisfy commutation relations $[a_k, a_{k'}^\dagger] = \delta(k - k')$. Therefore, we expect that reproducing the physics of a discrete number of fermionic field modes coupled to a continuum of bosonic field modes will boost full-fledged quantum simulations of QFTs.

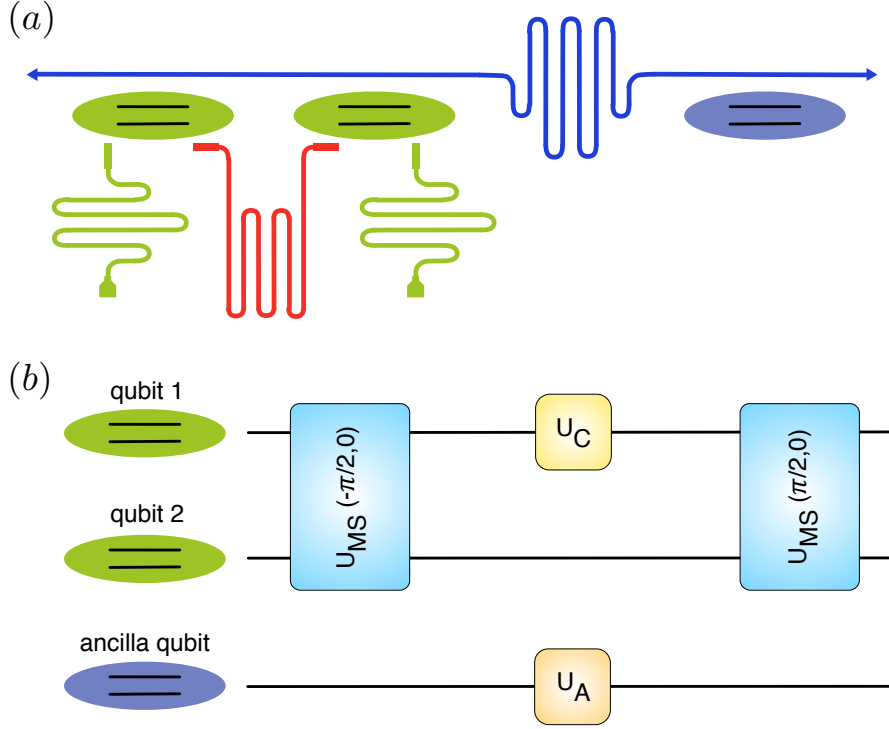


Figure 4.1: **Circuit QED schematic representation and operation sequence for simulating two-qubit gates coupled to the continuum of bosonic modes in a single Trotter step.** (a) Schematic representation of our proposal for simulating fermion-fermion scattering in QFTs. An open transmission line supporting the continuum of bosonic modes interacts with three superconducting qubits. The second one-dimensional waveguide, forming a resonator due to the capacitors at each edge, supports a single mode of the microwave field and interacts with two superconducting qubits. Each qubit can be individually addressed through on-chip flux lines producing fluxes Φ_{ext}^j and $\bar{\Phi}_{\text{ext}}^j$ to tune the coupling strength and its corresponding energies. (b) Sequence of multiple and single qubit gates, inside a Trotter step, acting on superconducting qubits to generate two-qubit interactions coupled to the continuum.

Let us now consider again the JW transformation introduced in section 2.1. It relates fermionic operators with tensor products of Pauli operators: $b_l^\dagger = \prod_{r=1}^{l-1} \sigma_l^- \sigma_r^z$, and $d_m^\dagger = \prod_{r=1}^{m-1} \sigma_m^- \sigma_r^z$, where $l = 1, 2, \dots, N/2$, $m = N/2 + 1, \dots, N$, with N the total number of fermionic plus antifermionic modes. In this case, the Hamiltonian in Eq. (4.2) presents three kinds of interactions: single and two-qubit gates coupled to

the continuum,

$$\begin{aligned}
 H_1 &= i\sigma_i^j \int dx dk g_k (a_k^\dagger e^{-ikx} - a_k e^{ikx}), \\
 H_2 &= i(\sigma_1^j \sigma_2^\ell) \int dx dk g_k (a_k^\dagger e^{-ikx} - a_k e^{ikx}),
 \end{aligned}$$

with $\sigma^q = \{\sigma^x, \sigma^y, \sigma^z\}$ for $q = 1, 2, 3$, and interactions involving only bosonic modes,

$$H_3 = i \int dx dk g_k (a_k^\dagger e^{-ikx} - a_k e^{ikx}).$$

Thus, the simulator should provide a mechanism for generating multiqubit gates and coupling spin operators to a continuum of bosons in an digital-analog approach [44].

We analyze the generation of interaction terms in the general case of N fermionic modes. In this generic case, each Hamiltonian term involves a product of fermionic operators coupled to a continuum of bosonic modes. For example, a possible interaction term reads $\mathcal{H} = i(b_i d_j^\dagger + d_j b_i^\dagger) \int dk g_k (a_k^\dagger e^{-ikx} - a_k e^{ikx})$. The JW transformation allows us to write the above interaction as the exponential of a tensor product of Pauli matrices with a band of bosonic modes. To compute this exponential, we propose the implementation of the following sequence of quantum gates [44]

$$\begin{aligned}
 U &= U_{\text{MS}}(-\pi/2, 0) U_{\sigma_1^z}(\phi) U_{\text{MS}}(\pi/2, 0) \\
 &= \exp[\phi(\sigma_1^z \sigma_2^x \sigma_3^x \dots)] \int dk g_k (a_k^\dagger e^{-ikx} - a_k e^{ikx}), \tag{4.3}
 \end{aligned}$$

where U_{MS} is the MS gate already presented in section 3.3. It can be parametrized as $U_{\text{MS}}(\theta, \phi) = \exp[-i\theta(\cos \phi S_x + \sin \phi S_y)^2/4]$, where $S_{x,y} = \sum_i \sigma_i^{x,y}$ is extended to as many qubits as fermionic modes are involved, and the central gate $U_{\sigma_1^z}(\phi)$ is $\exp[-\phi \sigma_1^z \int dk g_k (a_k^\dagger e^{-ikx} - a_k e^{ikx})]$.

4.3 Superconducting circuit model

Circuit QED architectures including the interaction between on-chip coplanar waveguides (CPWs) and transmon qubits [149, 150, 151] are an appropriate platform to fulfill the requirements of the digital-analog simulator. We consider the setup depicted in Fig. 4.1a, which consists of a microwave transmission line supporting a continuum of electromagnetic modes (open line) interacting with three transmon qubits. In addition, there is a microwave resonator with a single bosonic mode coupled only with two transmons. Notice that two superconducting qubits may interact simultaneously with both CPWs, while the ancilla qubit interacts only with the open line.

In this setup, we consider tunable couplings between each qubit and the CPWs, and also tunable superconducting qubit energies via external magnetic fluxes. In particular, the protocol for simulating fermion-fermion scattering will require the ability to switch on/off each CPW-qubit interaction with control parameters. The latter may be realized by combining tunable coupling transmon qubits, [149, 150] and standard techniques of band-stop filters [152] applied to the open transmission line, such that a finite bandwidth of bosonic modes plays a key role in the dynamics. In the same way, the decoupling of a transmon qubit from the open line may be accomplished by tuning the qubit energy out of the bandwidth. In addition, our protocol may be extended to several fermionic modes by adding more transmon qubits as depicted in Fig. 4.2.

In our protocol, the continuum-transmon and the resonator-transmon interactions can be described by the Hamiltonian

$$\begin{aligned}
 H_{\text{int}} = & i \sum_{j=1}^3 \sigma_j^y \int dk \beta(\Phi_{\text{ext}}^j, \bar{\Phi}_{\text{ext}}^j) g_k (a_k^\dagger e^{-ikx_j} - a_k e^{ikx_j}) \\
 & + i \sum_{j=1}^2 \alpha(\Phi_{\text{ext}}^j, \bar{\Phi}_{\text{ext}}^j) g_j \sigma_j^y (b^\dagger - b),
 \end{aligned} \tag{4.4}$$

where σ^y is the Pauli operator, $a_k^\dagger(a_k)$ and ω_k stand for the creation(annihilation) operator and the frequency associated with the k th continuum mode, respectively, whereas the operator $b^\dagger(b)$ creates(annihilates) excitations in the microwave resonator. The coupling strengths g_k and g_j depend on intrinsic properties of the CPW such as its impedance and the photon frequencies. In addition, x_j stands for the j th qubit position, and the coefficient $\beta(\alpha)$ can be tuned over the range $[0, \beta_{\text{max}}]$ ($[0, \alpha_{\text{max}}]$) via external magnetic fluxes Φ_{ext}^j and $\bar{\Phi}_{\text{ext}}^j$, which act on the j th transmon qubit. Note that the same magnetic fluxes also allow us to tune the qubit energy.

4.4 Simulation of spatial degrees of freedom

Let us discuss how the Hamiltonian in Eq. (4.4) is able to simulate the dynamics governed by the Hamiltonian in Eq. (4.2). The spatial dependence of the model is given by spatial integrals $\int dx (a_k^\dagger e^{-ikx} - a_k e^{ikx}) f(x, t)$, where $f(x, t)$ stands for the different space-dependent coefficients appearing in the Hamiltonian of Eq. (4.2).

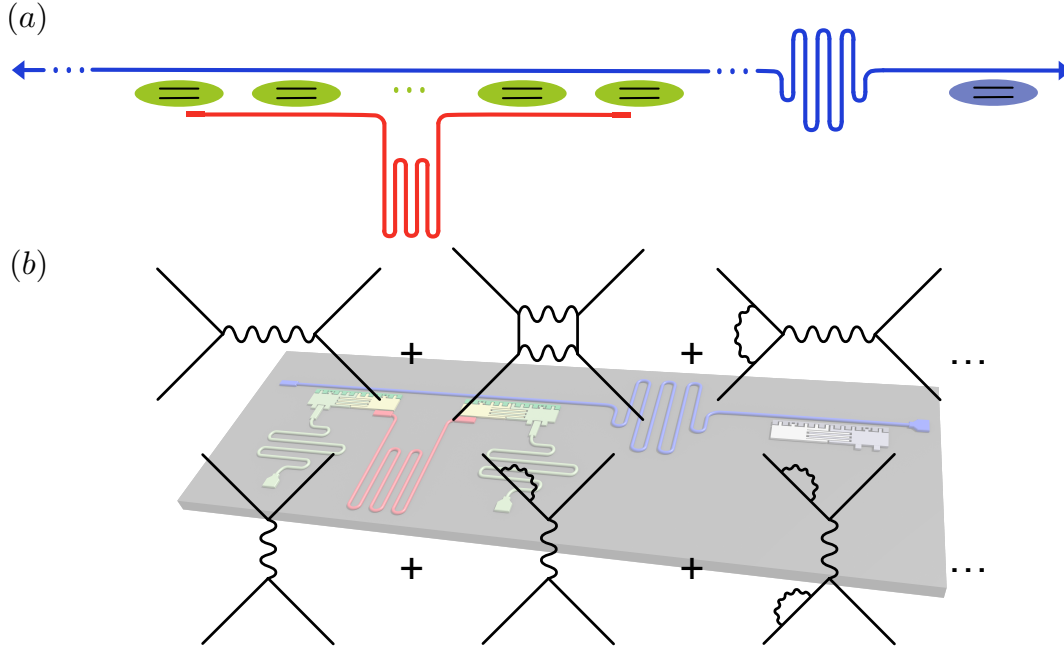


Figure 4.2: **Extension to N fermionic modes.** (a) Scheme for the implementation of a set of N fermionic modes coupled to a continuum of bosonic modes. Each fermionic mode is encoded in a nonlocal spin operator distributed among N superconducting qubits. (b) Feynman diagrams associated with the quantum simulation of two fermionic modes coupled to a continuum of bosonic modes in a superconducting circuit setup, as explained in the text.

These integrals can be rewritten as follows

$$\begin{aligned} \mathcal{I}(k, t) = & \int dx [a_k^\dagger e^{-ikx_j} (\cos k(x - x_j) - i \sin k(x - x_j)) \\ & - a_k e^{ikx_j} (\cos k(x - x_j) + i \sin k(x - x_j))] f(x, t). \end{aligned} \quad (4.5)$$

If $f(x, t)$ satisfies the condition $f(x - x_j, t) = f(-x + x_j, t)$, then we can simplify the integrals such that

$$\mathcal{I}(k, t) = (a_k^\dagger e^{-ikx_j} - a_k e^{ikx_j}) \int dx \cos k(x - x_j) f(x, t). \quad (4.6)$$

We can identify the controllable quantity of the circuit $\beta(\Phi_{\text{ext}}^j, \bar{\Phi}_{\text{ext}}^j)g_k$ with the spatial-dependent terms times the k -dependent coupling of the field theory model, i.e., $\lambda_k \sqrt{\omega_k} \int dx \cos k(x - x_j) f(x, t)$. If we consider an implementation that uses transmon qubits, their capacitive coupling to the open line leads naturally to a coupling $g_k = \sqrt{\omega_k}$, allowing us to simulate models where $\lambda_k \int dx \cos k(x - x_j) f(x, t)$ is constant or weakly dependent on k . Other kinds of couplings may be simulated by considering a different superconducting circuit such as the flux qubit, leading to the implementation of couplings depending on $1/\sqrt{\omega_k}$.

4.5 Sequence of quantum operations

In Fig. 4.1b, we show the set of quantum operations for simulating two-qubit gates coupled to the continuum in a single Trotter step [22, 44] to be realized by the proposed digital-analog simulator. In this cQED framework, each gate will correspond to the evolution under the Hamiltonian of Eq. (4.4) for specific values of parameters Φ_{ext}^j and $\bar{\Phi}_{\text{ext}}^j$. Specifically, the gates that act on the first two qubits are, from right to left, one MS [62] interaction $U_{\text{MS}}(\pi/2, 0)$ which is mediated by the resonator [63], one local gate $U_C = \exp[-\phi\sigma_1^y \int dk g_k (a_k^\dagger e^{-ikx} - a_k e^{ikx})]$ that will couple the spin operators to the bosonic continuum, and an inverse MS interaction $U_{\text{MS}}(-\pi/2, 0)$. The application of these three operations will generate the two-qubit gate coupled with a continuous band of bosonic modes, $H_2 = i(\sigma_1^j \sigma_2^\ell) \int dk g_k (a_k^\dagger e^{-ikx} - a_k e^{ikx})$.

The gate U_c will be used independently on each qubit to generate single-qubit gates coupled to the bosonic continuum. Besides, the ancilla qubit provides us with the means to generate the gates that involve only the bosonic modes by means of an interaction $U_A = \exp[-\phi\sigma_A^z \int dk g_k (a_k^\dagger e^{-ikx} - a_k e^{ikx})]$, where σ_A^z is the Pauli operator. The required gate is obtained by preparing the ancilla in an eigenstate of σ_A^z . The same scheme of gates can be applied on more qubits in order to scale the system for simulating interactions that involve a larger number of fermionic modes.

The way of scaling¹ this formalism to a larger number of fermionic modes is to consider more superconducting elements coupled both to the cavity and to the open transmission line, as depicted in Fig. 4.2. If we consider $N + 1$ transmon qubits, then, N fermionic modes can be also encoded. Accordingly, our proposal can implement a large set of fermionic modes interacting with the bosonic continuum. This effort would represent a significant advance towards full-fledged quantum simulation of QFTs in controllable superconducting circuits.

4.6 Encoding of information

By means of the proposed techniques, one could measure specific features of QFTs, such as self-interaction and pair creation and annihilation of fermions mediated via a continuum of bosonic modes.

The fermionic states will be encoded in the two levels of each qubit. This is done via the mapping of fermionic and antifermionic creation and annihilation operators onto nonlocal spin operators acting on the qubits.

¹See appendix G.2 for further considerations regarding scalability and higher dimensions of the model.

We recall the JW mapping performed previously, $b_{\text{in}}^\dagger = \sigma_1^-$, $d_{\text{in}}^\dagger = \sigma_2^- \sigma_1^z$, and we associate the fermionic operators to the following ones acting on the qubit states,

$$\begin{aligned} b_{\text{in}}^\dagger &= |\uparrow\downarrow\rangle\langle\uparrow\uparrow| + |\downarrow\downarrow\rangle\langle\downarrow\uparrow|, & b_{\text{in}} &= |\uparrow\uparrow\rangle\langle\uparrow\downarrow| + |\downarrow\uparrow\rangle\langle\downarrow\downarrow|, \\ d_{\text{in}}^\dagger &= |\downarrow\uparrow\rangle\langle\uparrow\uparrow| - |\downarrow\downarrow\rangle\langle\uparrow\downarrow|, & d_{\text{in}} &= |\uparrow\uparrow\rangle\langle\downarrow\uparrow| - |\uparrow\downarrow\rangle\langle\downarrow\downarrow|, \end{aligned} \quad (4.7)$$

where the states $|\uparrow\rangle$ and $|\downarrow\rangle$ are the levels of a qubit. With this mapping, the vacuum state corresponds to the state $|0\rangle = |\uparrow\uparrow\rangle$, the state with one fermion is $|f\rangle = |\uparrow\downarrow\rangle$, and the state with one antifermion is $|\bar{f}\rangle = |\downarrow\uparrow\rangle$. Fermion self-interaction may be computed by the probability $|\langle f, 0, 0|U(t)|f, 0, 0\rangle|^2$ at time t , and pair creation and annihilation may be simulated by the transition probabilities between a state with no fermions into a state with a fermion and an antifermion. The state of the qubits can be detected via standard quantum non demolition measurements. Additionally, the average boson population and higher order moments may be measured in the open transmission line via the dual-path technique [153].

The quantum computation resulting from this quantum simulation is based on unitary evolutions associated with the Hamiltonian in Eq. (4.2). This means that, at variance with perturbative methods in QFTs, the implementation of our protocol will involve an infinite number of perturbative Feynman diagrams with a finite number of fermionic modes. Consequently, this approach towards full-fledged QFTs is significantly different from standard procedures, since it requires adding more fermionic modes instead of more Feynman diagrams. Nevertheless, the natural presence of the continuum of bosonic modes in superconducting circuits approaches our proposal to the targeted model.

Summarizing, this chapter contains our proposal of a digital-analog quantum simulation of fermion-fermion scattering in the context of QFTs with superconducting circuits. This quantum technology provides strong coupling between superconducting qubits with a microwave resonator and a continuum of bosonic modes. Our approach represents a significant step towards scalable quantum simulations of QFTs in perturbative and nonperturbative regimes.

Digital-Analog Quantum Simulation of Quantum Chemistry and Biology

THE field of quantum chemistry arises from the application of quantum mechanics in physical models to explain the properties of chemical and biological systems [154, 155]. The study of complex electronic structures in atoms and molecules encounters the difficulty of the exponential growth of the Hilbert space dimensions with system size [156, 157]. This fact limits the results reachable with current computers and classical algorithms, and strongly suggests that we should explore the possibilities of new quantum-based tools [158, 159].

Quantum simulations are a powerful approach based on the imitation of the dynamics of a quantum system in a controllable quantum platform, as stated repeatedly in this Thesis. Theoretical and experimental efforts for solving problems in physical chemistry have been performed in technologies such as NMR [160], trapped ions [65, 66, 161], photonic systems [162, 163, 164], and superconducting circuits [165], among others. Quantum algorithms for the simulation of electronic structures with fermionic degrees of freedom and its optimisation have been widely studied [166, 167, 168, 169, 170, 171, 172, 173]. Environmental effects also play a crucial role in quantum physics, chemistry and biology [174, 175]. Fundamental phenomena such as electronic transport and electron transfer are described through the correlated dynamics of electrons and phonons, involving bosonic and fermionic modes.

Circuit quantum electrodynamics is a cutting-edge technology in terms of design versatility, coherent control, and scalability, as indicated in previous chapters. Indeed, remarkable experimental progress in cQED has enabled the realisation of digital quantum simulations of fermions [58], spin systems [59], and AQC [89]. These aspects, along with the possibility of encoding both fermions and bosons in this platform via digital [56, 57, 74, 176] and digital-analog techniques [77], make cQED a suitable platform for simulating electronic Hamiltonians [177] and dissipative processes.

In this chapter, we combine efficient digital quantum simulation techniques for electronic Hamiltonians with existing algorithms in quantum chemistry, and we analyze the scalability and feasibility according to the state-of-the-art cQED [23]. In particular, we study the gate fidelities required for the proposed tasks and the error propagation. We extend these procedures by exploiting the possibility of mimicking bosons in superconducting circuits taking full advantage of the multimode spectrum of superconducting transmission lines [178, 179, 180, 181, 182], and propose digital-analog quantum simulations of electron transfer and electronic transport in biomolecules [183, 184, 185].

5.1 Simulation of electronic Hamiltonians

The electronic structure is a quantum chemistry many-body problem that is usually difficult to solve due to the exponential growth of the Hilbert space with the size of the system. Typically, the aim is to compute ground-state energies and their associated eigenvectors of these interacting electron systems in a fixed nuclear potential.

Among the variety of possible methods for simulating fermionic models with quantum technologies, one of the most studied approaches considers quantum algorithms using the second quantized formalism of electronic systems [166, 167, 169, 170, 171, 172, 173]. The associated Hamiltonian may be represented in different bases, leading to different methods of encoding and scaling improvements in the number of qubits and gates required [169, 173]. Furthermore, other approaches related to the Configuration Interaction (CI) matrix have been recently studied [168].

The generic Hamiltonian describing a molecular electronic structure consists of the electron kinetic energy term, two-electron Coulomb interactions, and the electron-nuclei potential energy representing the electronic environment [154, 155]. This Hamiltonian in second quantization may be written as

$$H_e = \sum_{i,j} h_{ij} c_i^\dagger c_j + \frac{1}{2} \sum_{i,j,k,l} h_{ijkl} c_i^\dagger c_j^\dagger c_k c_l, \quad (5.1)$$

where the operators c_i^\dagger and c_i stand for the electrons and obey the fermionic an-

ticommutation relations. Coefficients h_{ij} come from the single-electron integrals of the electron kinetic terms and electron-nuclei interactions, and h_{ijkl} correspond to the two-electron integrals associated with the electron-electron Coulomb interaction. That is, it is expressed in atomic units as

$$h_{ij} \equiv \int d\mathbf{r} \varphi_i^*(\mathbf{r}) \left(-\frac{1}{2} \nabla_r^2 - \sum_k \frac{Z_k}{|r - R_k|} \right) \varphi_j(\mathbf{r}), \quad (5.2)$$

$$h_{ijkl} \equiv \int d\mathbf{r}_1 d\mathbf{r}_2 \frac{\varphi_i^*(\mathbf{r}_1) \varphi_j^*(\mathbf{r}_2) \varphi_k(\mathbf{r}_2) \varphi_l(\mathbf{r}_1)}{|r_1 - r_2|}, \quad (5.3)$$

where R_k are nuclear coordinates, r electronic coordinates, and Z the atomic number representing the nuclear charge. Here, $\{\varphi_i(\mathbf{r})\}$ defines a set of spin orbitals, and $\mathbf{r} = (r, \sigma)$ denotes the pair of spatial and spin parameters.

Optimal strategies of computation for quantum chemistry merge quantum simulation and classical numerical techniques. We have already demonstrated the power of this strategy in section 2.4, in the context of strongly correlated fermions. These methods, that we name as algorithmic quantum simulation [186], employ quantum simulators for the computationally hard tasks, such as time evolution, on top of the classical algorithm, which provides flexibility for computing relevant observables. In the context of quantum chemistry, we have the example of ground state finding via a variational eigensolver [163, 66, 187, 39, 188].

The simulation of the dynamics associated with the electronic Hamiltonian in Eq. (5.1) involves fermionic operators. Computations with fermionic degrees of freedom in superconducting circuits require the encoding of fermionic operators and their anticommutative algebra in the natural variables of this quantum platform. The JW transformation introduced in section 2.1 maps the fermionic operators into spin-1/2 operators, which gives us the qubit representation of the Hamiltonian. In the case of a hydrogen molecule, considering four electronic orbitals, the relations can be written as

$$\begin{aligned} c_1^\dagger &= \sigma_1^+, & c_2^\dagger &= \sigma_1^z \sigma_2^+, \\ c_3^\dagger &= \sigma_1^z \sigma_2^z \sigma_3^+, & c_4^\dagger &= \sigma_1^z \sigma_2^z \sigma_3^z \sigma_4^+. \end{aligned} \quad (5.4)$$

After this mapping, the Hamiltonian of Eq. (5.1) for the H_2 molecule is rewritten in terms of spin-1/2 operators considering only the nonzero coefficients h_{ij} and h_{ijkl} , which are computed classically with polynomial resources [167],

$$\begin{aligned} H &= \frac{1}{8} [(4h_{11} + 2h_A + 4h_C - h_D) \sigma_1^z + (4h_{22} + 2h_A + 4h_C - h_D) \sigma_2^z + \\ &\quad (4h_{33} + 2h_B + 4h_C - h_D) \sigma_3^z + (4h_{44} + 2h_B + 4h_C - h_D) \sigma_4^z + \\ &\quad 2h_A \sigma_1^z \sigma_2^z + (2h_C - h_D) \sigma_1^z \sigma_3^z + 2h_C \sigma_1^z \sigma_4^z + \\ &\quad 2h_C \sigma_2^z \sigma_3^z + (2h_C - h_D) \sigma_2^z \sigma_4^z + 2h_B \sigma_3^z \sigma_4^z + \\ &\quad 2h_D (\sigma_1^x \sigma_2^y \sigma_3^y \sigma_4^x + \sigma_1^y \sigma_2^x \sigma_3^x \sigma_4^y - \sigma_1^x \sigma_2^x \sigma_3^y \sigma_4^y - \sigma_1^y \sigma_2^y \sigma_3^x \sigma_4^x)], \end{aligned} \quad (5.5)$$

where

$$\begin{aligned}
 h_A &= h_{1221} = h_{2112}, \\
 h_B &= h_{3443} = h_{4334}, \\
 h_C &= h_{1331} = h_{3113} = h_{1441} = h_{4114} = h_{2332} \\
 &= h_{3223} = h_{2442} = h_{4224}, \\
 h_D &= h_{1243} = h_{2134} = h_{1423} = h_{4132} = h_{2314} \\
 &= h_{3241} = h_{3421} = h_{4312} = h_{1313} = h_{2424}.
 \end{aligned} \tag{5.6}$$

In general, an analog quantum simulation of an arbitrary Hamiltonian evolution is a difficult problem [189, 190], since one cannot straightforwardly map the dynamics of a given simulated system onto a given quantum platform. The flexibility and universality of digital quantum simulations allows us to reproduce models that do not appear naturally in a quantum platform. This is done via an expansion of the quantum evolution into discrete steps of quantum gates [31]. An additional advantage of such digital quantum simulations, in the spirit of gate-based quantum algorithms, is their possible improvement with quantum error correction techniques [191, 60].

We consider the digital quantum simulation of the H_2 molecule via the Trotter expansion in section 2.1, which consists in dividing the evolution time t into l time intervals of length t/l , and applying sequentially the evolution operator of each term of the Hamiltonian for each time interval [22, 31, 74]. The expression of this expansion for a Hamiltonian of the form $H = \sum_j H_j$ reads

$$e^{-iHt} \approx \left(\prod_j e^{-iH_j t/l} \right)^l, \tag{5.7}$$

for large l , where the dominating error component is $\sum_{i>j} [H_i, H_j] t^2/2l$, which depends on the value of the commutators and scales with t^2/l .

In our case, we consider the evolution operators associated with the different summands of the Hamiltonian in Eq. (5.5), which corresponds to the sequence of gates in Fig. 5.1. We propose an algorithm based on the optimized tunable CZ_ϕ gate, which allows one to perform efficiently ZZ interactions, or XX interactions in our basis [58]. In order to achieve this goal, we arrange the gates and the simulated interactions such that it allows us to simplify the algorithm by eliminating some entangling gates and their inverses, as shown in Fig. 5.1. The single Trotter step depicted in this figure represents the approximated evolution for a time t/l of the complete Hamiltonian. Note that the third and fourth logical qubits correspond to the fourth and third physical qubits, respectively. We choose this notation due to the reduction of SWAP gates needed for the performance of the protocol. The optimized Trotter step contains 24 XX two-qubit gates between nearest-neighbor qubits, 24 SWAP gates and 20 single-qubit rotations. In Fig. 5.2, we show the efficiency of the digital protocol for different number of Trotter steps. Here, we analyze the loss of the state fidelity and the expected value of some operators performed in the simulation, considering

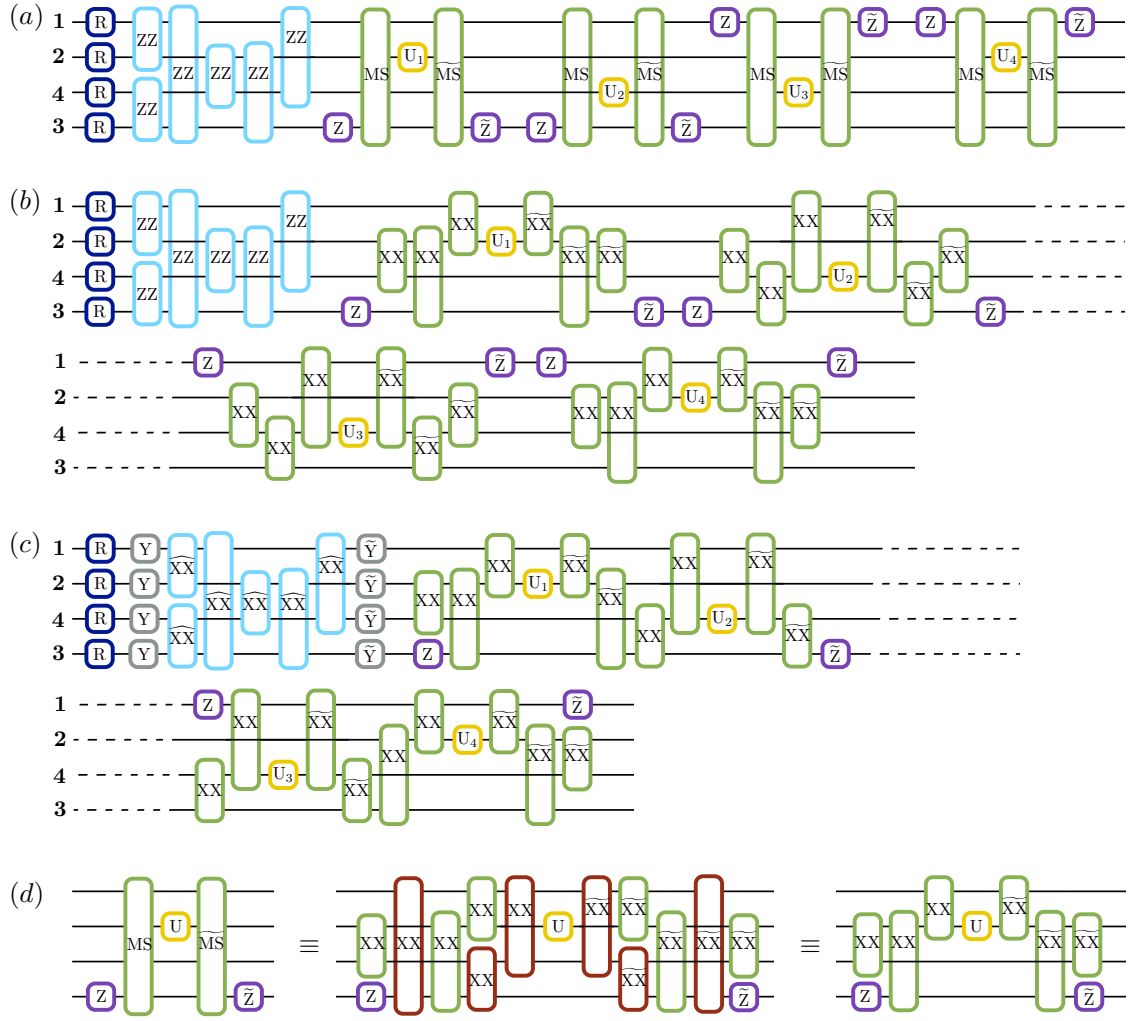


Figure 5.1: **Sequence of gates in a single Trotter step of the digital quantum simulation** of the Hamiltonian in Eq. (5.5) describing the H₂ molecule. Notice that, for the sake of optimizing the number of gates, we swap the logic label of the third and fourth physical qubits. (a) Original protocol including MS multiqubit gates (light green), $MS = \exp(i\frac{\pi}{8}S_x^2)$, $\bar{MS} = \exp(-i\frac{\pi}{8}S_x^2)$, where $S_x = \sum_i \sigma_i^x$, and intermediate unitaries (yellow) $U_1 = U_3 = \exp(-i2h_D t \sigma_j^z)$, $U_2 = U_4 = \exp(i2h_D t \sigma_j^z)$, where the subindex j means that it is applied to the j -th qubit. The Trotter step also contains $Z_{\pi/2}$ -rotations (purple) $Z = \exp(-i\frac{\pi}{4}\sigma_j^z)$ and $\tilde{Z} = \exp(i\frac{\pi}{4}\sigma_j^z)$, single-qubit gates (dark blue) $R = \exp(-i\phi_j t \sigma_j^z)$, with $\phi_1 = 4h_{11} + 2h_A + 4h_C - h_D$, $\phi_2 = 4h_{22} + 2h_A + 4h_C - h_D$, $\phi_3 = 4h_{33} + 2h_B + 4h_C - h_D$, and $\phi_4 = 4h_{44} + 2h_B + 4h_C - h_D$, and two-qubit gates (dark green) $ZZ = \exp(-i\theta_{ij} t \sigma_i^z \sigma_j^z)$, with the phase θ_{ij} depending on the qubits involved, such that $\theta_{12} = 2h_A$, $\theta_{13} = \theta_{24} = 2h_C - h_D$, $\theta_{14} = \theta_{23} = 2h_C$, and $\theta_{34} = 2h_B$. (b) Trotter step with MS multiqubit gates decomposed into two-qubit gates (dark green). Here, $XX = \exp(-i\frac{\pi}{4}\sigma_i^x \sigma_j^x)$, and $\bar{X}\bar{X} = \exp(i\frac{\pi}{4}\sigma_i^x \sigma_j^x)$. (c) Optimized Trotter step, in which we have expressed the algorithm in terms of XX gates via the $Y_{\pi/2}$ -rotations (grey) $Y = \exp(-i\frac{\pi}{4}\sigma_j^y)$ and $\bar{Y} = \exp(i\frac{\pi}{4}\sigma_j^y)$, and with $\bar{X}\bar{X} = \exp(-i\theta_{ij} t \sigma_i^x \sigma_j^x)$. (d) After a complete decomposition into two-qubit gates of the MS gates involved in the simulation of a multiqubit interaction, a simplification of two-qubit gates (red) cancelling each other is shown.

simulated phases up to $\theta = h_{11}t = 2$. We break down the Hamiltonian terms and plot the energies of each of them to observe separately the Trotter error associated with the different kinds of interactions appearing in the algorithm. We observe that, for a single Trotter step, the energies related to single-qubit gates are similar to the exact evolution, while in the case of the four body terms the deviation is higher.

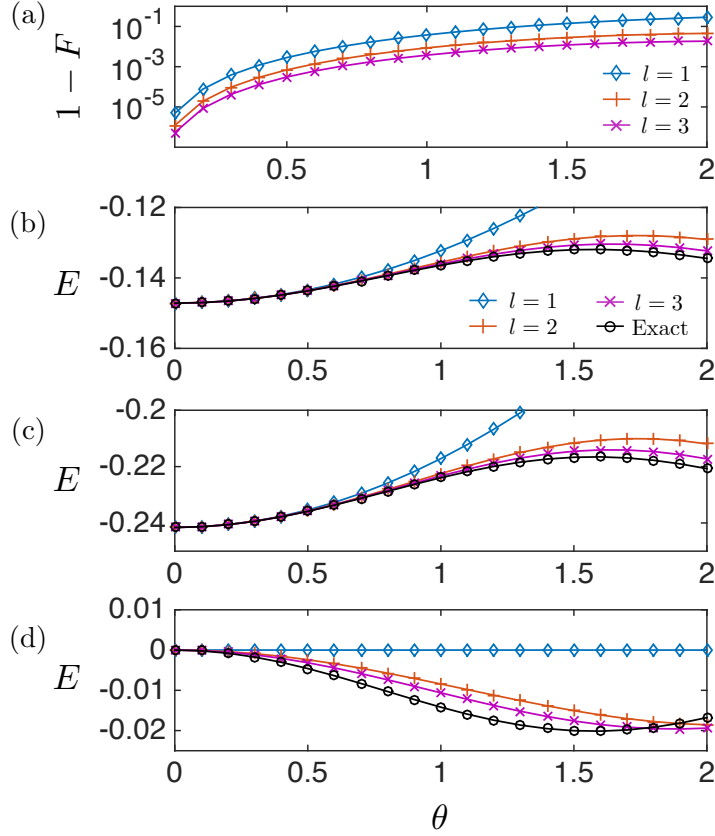


Figure 5.2: **Digital quantum simulation of the H_2 molecule Hamiltonian** for a phase of $\theta = h_{11}t$. Here, digital evolutions up to 3 Trotter steps are compared with the exact evolution for initial state $|\psi\rangle = c_1^\dagger c_2^\dagger |\text{vac}\rangle = |1100\rangle$. (a) Fidelity loss of the digitally evolved states, with $F = |\langle \Psi(t) | \Psi_l(t) \rangle|^2$. Expectation values of the separated Hamiltonians, in atomic units, proportional to (b) σ_1^z and σ_2^z , (c) σ_3^z and σ_4^z , and (d) $\sigma_1^x \sigma_2^y \sigma_3^y \sigma_4^x$, $\sigma_1^y \sigma_2^x \sigma_3^x \sigma_4^y$, $\sigma_1^x \sigma_2^x \sigma_3^y \sigma_4^y$ and $\sigma_1^y \sigma_2^y \sigma_3^x \sigma_4^x$.

Symmetric Trotter expansions provide the improvement of the digital error at the expense of more gate execution. The Hamiltonian of Eq. (5.5) can be divided in two groups of interactions, H_1 , the sum of the first 10 terms that commute among them, and H_2 , the sum of the last 4 terms that also commute among them. As commuting interactions do not generate digital error, the evolution of a symmetric Trotter step can be written as follows [31],

$$e^{-iH_1 t/2l} e^{-iH_2 t/l} e^{-iH_1 t/2l}. \quad (5.8)$$

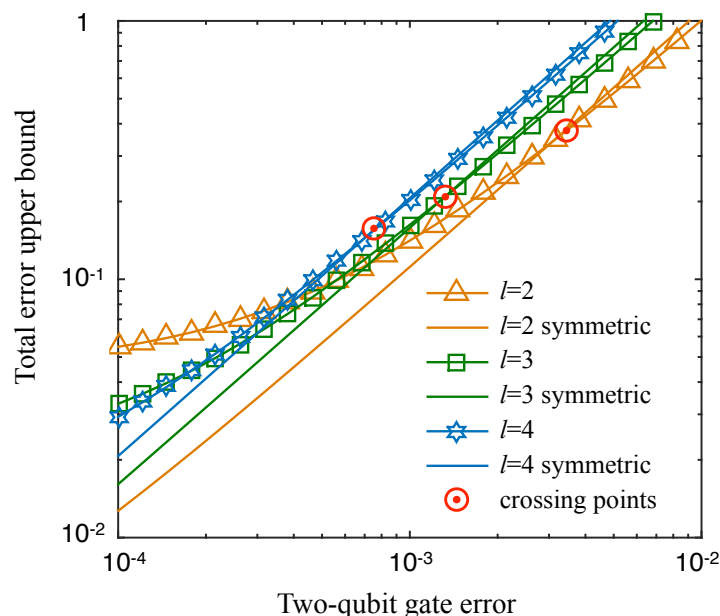


Figure 5.3: **Total upper bound of errors in digital quantum simulation of electronic Hamiltonian.** Total upper bound of symmetric and regular expansions for the digital simulation of the hydrogen molecule as a function of the error of a two-qubit gate, considering $l = 2, 3, 4$ Trotter steps and a simulated phase of $\theta = h_{11}t = 2$. The total error is calculated as the sum of the experimental error of two-qubit gates and the digital errors. This plot shows the crossing points between the symmetric and the regular protocols for the same number of Trotter steps. On the left hand side of the crossing points, the symmetric protocol provides better results than the regular one. On the right hand side, however, the considered experimental error gate is higher, and the regular protocol where a less number of gates is executed shows better performance.

This protocol requires the implementation of the interactions of H_1 one more time than in the regular digital protocol, thereby reducing the digital error. We introduce a fixed error for any two-qubit gate between nearest-neighbor qubits, without restricting ourselves to a specific setup or experimental source of error. Single-qubit gate errors are neglected due to their high fidelity with current technology. If the dominating error is the experimental one, then the aim is to reduce the number of gates and, consequently, the regular protocol gets better fidelities. In Fig. 5.3, we analyze the errors of both the regular Trotter protocol and the symmetric protocol, and we give an upper bound of the total error summing the digital and the experimental error considering a range of values for the two-qubit gate error employed. For fixed number of Trotter steps, $l = 2, 3, 4$, we observe crossing points between the errors associated with the symmetric protocol and the regular one whilst considering higher experimental gate error. On the left side of the crossing points, the experimental error is smaller and the symmetric protocol provides better results, whereas on the right side, as the experimental gate error grows, the regular protocol is more

adequate. We also notice that, as the number of Trotter steps increases, the advantages of one protocol with respect to the other lessen. It is worthy to mention that the two-qubit gate errors in current superconducting devices are on the order of 10^{-2} [60].

5.2 Simulation of environmental effects

In this section, we propose a quantum simulation in superconducting circuits of generic system-environment interactions, which have long been recognized as fundamental in the description of electron transport in biomolecules.

Biological systems are not isolated, and one can consider minimal models for characterizing the quantum baths and decoherence [174, 175], such as the spin-boson model, or the Caldeira-Leggett model. The former is a widely used model that describes the interaction between a two-level system and a bosonic bath, and the latter deals with the dynamics of a quantum particle coupled to a bosonic bath. Usually, the coupling of the quantum system to the bath degrees of freedom is completely specified by the spectral density $J(\omega)$, which may be obtained from experimental data, and allows us to explore different continuum models of the environment. Nevertheless, in certain limits of strong coupling, the evaluations are computationally hard, and the complete comprehension of the physics remains as an open problem.

In particular, we study a Hamiltonian describing the charge transfer in DNA wires [183, 184, 185], where experiments show a wide range of results, from insulator to conductor behaviours [192, 193, 194, 195, 196, 197, 198]. When describing the dynamics of electrons in these biomolecules, the influence of a dissipative medium determines substantially the transfer events. We consider a bosonic bath in which a variety of crucial factors are contained, such as the internal vibrations of the biomolecule and the environmental effects.

A generic effective charge-bath model that describes an electronic system coupled to a fluctuating environment, in this case a bosonic bath, is captured by the Hamiltonian [185]

$$\begin{aligned}
 H = & \sum_j \varepsilon_j f_j^\dagger f_j + \sum_j V_{j,j+1} \left(f_j^\dagger f_{j+1} + \text{H.c.} \right) \\
 & + \sum_i \omega_i b_i^\dagger b_i + \sum_{i,j} \lambda_{ij} f_j^\dagger f_j \left(b_i^\dagger + b_i \right), \quad (5.9)
 \end{aligned}$$

with f_j (f_j^\dagger), fermionic annihilation (creation) operators for electrons on different sites with energies ε_j . $V_{j,j+1}$ characterizes the electron hopping between nearest-neighbor sites. The bath is represented by the bosonic annihilation (creation) operators b_i (b_i^\dagger), and the coefficients λ_{ij} indicate how the system and bath are coupled.

A minimal and particular case is the two-site model with $j = A, B$, which comprises a donor (D) and an acceptor (A) site [183, 184]. This reduced model can be mapped onto the spin-boson model, which has been studied in cQED [199], for the particular case of one spinless electron in the system. We provide the patterns to treat in a cQED setup a more general situation where the spin degree-of-freedom or more electrons enter into the description. To this end, we consider Eq. (5.9) with $j = 1, 2, 3$, and $V_{j,j+1} = V$, which cannot be mapped onto the well-studied spin-boson model. For the sake of simplicity, we have chosen this truncation, but the techniques can be easily extrapolated to an arbitrary case.

As previously shown, in order to simulate fermionic operators in superconducting circuits, we replace them by Pauli matrices via the JW transformation, leading to

$$H = \frac{1}{2} \sum_{j=1}^3 \sigma_j^z - \frac{V}{2} (\sigma_1^x \sigma_2^x + \sigma_1^y \sigma_2^y + \sigma_2^x \sigma_3^x + \sigma_2^y \sigma_3^y) + \sum_i \omega_i b_i^\dagger b_i + \sum_{i,j} \frac{\lambda_{ij}}{2} (\sigma_j^z + 1) (b_i^\dagger + b_i), \quad (5.10)$$

where the first two terms correspond to the purely electronic subsystem, the third term is the free energy of the bosons in the bath, and the last term represents the interaction of the electrons with the environment.

The Hamiltonian is now suitable for a digital quantum simulation in superconducting circuits, in which the qubits are described by Pauli operators, and 3D cavities, multimode CPWs, or low-Q cavities play the role of bosonic baths. A first step in this direction, considering an open transmission line coupled to qubits in order to simulate fermionic systems interacting with a continuum of bosons was introduced in the context of QFT in chapter 4. While the basic protocol was already developed in this chapter, here we apply this formalism to the different context of electron transport in biomolecules, for a discrete set of coupled fermionic and bosonic modes. Recently, experimental realizations with a transmon qubit coupled to a multimode cavity in the strong coupling regime have been performed [181]. There, the feasibility of coupling a superconducting transmon qubit to a long coplanar resonator has been shown, achieving in this way the coupling of a qubit to a set of several bosonic modes at the same time. This multimode treatment is also needed to explain results in superconducting 3D cavities or in transmission lines [180, 182], which allows us to propose a simulation exploiting the natural complexity that superconducting circuits reveal.

By coupling three tunable superconducting qubits [150, 200] to a multimode cavity as in Fig. 5.4, the Hamiltonian of Eq. (5.10) can be reproduced by using digital-analog methods, that is, introducing the fermionic interactions digitally and the bosonic ones in analog interaction blocks. We propose the emulation of a variety of system-environment dynamics on superconducting circuit technology. To this end, we consider the interaction term describing the j th qubit coupled to a multimode

cavity,

$$H_{\text{int}} = \sum_i \beta(\phi_{\text{ext}}^j, \bar{\phi}_{\text{ext}}^j) g_j(\omega_i) \sigma_j^z (b_i^\dagger + b_i), \quad (5.11)$$

with b_i (b_i^\dagger) the i th mode annihilation (creation) operator related with the cavity frequency ω_i , couplings $g_j(\omega_i) = g_0 \sqrt{i+1}$, and g_0 the coupling strength to the fundamental cavity mode ω_0 . We profit from the tunability of the coupling between qubits and transmission lines via external magnetic fluxes ϕ_{ext}^j and $\bar{\phi}_{\text{ext}}^j$ [77, 150, 200] to address a wider range of regimes and models, since the set of couplings $\beta(\phi_{\text{ext}}^j, \bar{\phi}_{\text{ext}}^j) g_j(\omega_i)$ mimic the coefficients λ_{ij} that characterize the interaction with the environment in Eq. (5.10). Moreover, it has been shown experimentally how to engineer different shapes for the bath spectral function with a transmission line and partial reflectors [199, 201]. Additionally, it can also be proven that a simple tunable Ohmic bath, as the one provided by a transmission line, equipped with a feedback protocol, can produce highly non-Markovian dynamics [202]. Growing in electronic complexity in Eq. (5.9) implies adding more qubits coupled to the transmission line in Fig. 5.4. However, we can take full advantage of the same multimode cavity by encoding the bath in a similar fashion. Hence, the cQED setup may be easily scaled up by coupling more qubits to the same transmission line.

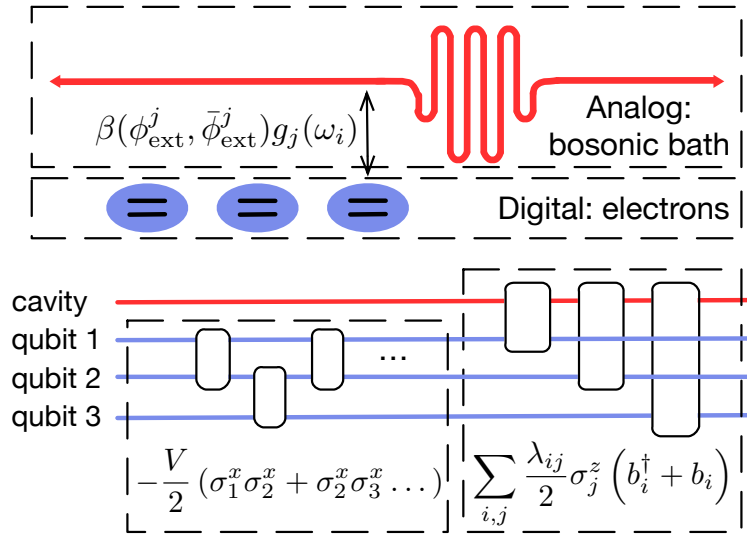


Figure 5.4: **Scheme of the cQED setup and digital-analog protocol** needed for mimicking the Hamiltonian in Eq. (5.10). We consider a multimode cavity (red), that is, either a long resonator, a 3D cavity or a transmission line, coupled to three tunable superconducting qubits (blue). The cavity simulates analogically the bosonic bath, whereas the electrons are encoded in the superconducting qubits. The coupling between the qubits and the cavity, $\beta(\phi_{\text{ext}}^j, \bar{\phi}_{\text{ext}}^j) g_j(\omega_i)$, must be tunable via external magnetic fluxes ϕ_{ext}^j and $\bar{\phi}_{\text{ext}}^j$ to enable the digital-analog quantum simulation, in which each qubit is coupled sequentially with the cavity.

Let us discuss how the Hamiltonian in Eq. (5.10) is decomposed into different digital and digital-analog blocks for the quantum simulation. As in the previous section, the purely electronic subsystem can be decomposed in Trotter steps and reproduced by single- and two-qubit gates. Since the bosonic operators do not enter in this part, we must decouple the tunable qubits from the transmission line to perform the required gates. The remaining terms are encoded in digital-analog blocks, where we divide the dynamics in different Trotter steps in which the multimode cavity enters in an analog way, providing the free energy of the bosons, and simulating the last term of Eq. (5.10). This last term is composed of purely bosonic interactions proportional to $(b_i^\dagger + b_i)$, which may be simulated through a microwave driving in the cavity. It also involves qubit-boson interactions, $\sigma_j^z(b_i^\dagger + b_i)$, which emerge from the coupling of each qubit with the multimode cavity, as in Ref. [77]. A future analysis of the error in this protocol may include not only the error of the two-qubit gates, but also the contribution of the imperfect decoupling of the qubits with the transmission line in the single-qubit gates in which we introduce the coupling with the bosonic degrees of freedom. The figure of merit in the simulation is the final state of the fermions, which may be extracted from the final state of the qubits. The quantum simulation may be performed for different final times, thereby allowing us to reconstruct the electronic dynamics, such as transfer of excitations.

With this proposal, we have provided not only a way of extracting results illustrating different charge transport regimes in biomolecules, but also a way of testing different minimal models for describing molecules embedded in a bosonic environment. Superconducting circuits are a controllable quantum platform in which we can tune couplings between spins and bosons, and manipulate external conditions to engineer different baths. We analyze models of biological systems with a certain complexity and translate them to a controllable superconducting device that enjoys a similar complexity.

In this chapter, we have proposed methods to perform feasible digital and digital-analog quantum simulations of molecular structures and biomolecules with the state-of-the-art of superconducting circuit technology. We analyze different quantum chemistry models by increasing gradually the complexity, moving from purely fermionic models of molecular structures to descriptions of charge transport in biomolecules embedded in a bosonic medium. We aim to profit from the unique features of cQED, such as the strong coupling of a two-level system to bosonic modes, in order to represent controllable scenarios in which quantum chemistry and quantum biology models may be studied. The proposal includes a purely digital quantum simulation protocol for fermionic models, for which we provide general methods of encoding and the sequence of gates needed for the particular case of simulation of the H_2 molecule. The previous formalism is partially used for simulating biomolecules affected by their bosonic surroundings, where we also add analog blocks with a multimode cavity playing the role of the bosonic bath, hence boosting the efficiency of quantum algorithms for quantum chemistry.

6

Conclusions

THIS Thesis explores the possibilities of quantum platforms, and in particular superconducting circuits, for the simulation of classically intractable models. We take into account the state-of-the-art quantum technology and analyze the resources that it provides for solving not only quantum mechanical models, but also models of QFT and quantum aspects in biology. The methods proposed in this Thesis involve in a first step the usual digital encoding of information into qubits, proper to universal quantum computing, to then shift the paradigm towards hybrid techniques in which we consider not only the qubits as the carriers of information, but also other elements in the quantum platforms whose degrees of freedom are potential resources for storage and computation. These mixed approaches enhance the possibilities of quantum technologies as information processors while setting aside the universality and complete digitalization of quantum computation. Instead, we propose narrower purpose simulators, with analog information encoding, both for the sake of feasibility in realistic current devices, and as promising forerunners in quantum analog computation, and hybrid quantum digital-analog computation.

Many-body fermionic systems in 1D and 2D containing couplings with nearest and next-nearest neighbors can be quantum simulated with polynomial resources and adequate techniques. We study the specific case of the Fermi-Hubbard model in 1D and 2D with a quantum platform in which nearest-neighbor qubits can perform

entangling gates. Our purely digital approach has the advantage of being expressed in the language of quantum algorithms, hence being implementable in any quantum platform optimized towards quantum computation. The possibility of a future implementation of quantum error correction in combination with these techniques will enable the efficient and scalable digital quantum simulation of fermionic models. Our method has been demonstrated in a quantum simulation of up to four fermionic modes with a superconducting quantum circuit, employing in excess of 300 quantum logic gates, which constituted the most advanced digital quantum simulation at that moment. The fidelities we have obtained suggest that there is, in principle, scalability to a larger number of modes, and arbitrary spatial dimensions. Consequently, the road for the construction of larger testbeds for fermionic systems reveals itself viable along with the further development of quantum technologies.

We conclude that the introduction of classical techniques as subroutines in the quantum simulation of fermionic models allows computations working directly in the thermodynamic limit, and thus unencumbered by finite-number boundary effects. We propose such an application for a few-qubit quantum device that allows the simulation of strongly correlated fermions described by the Fermi-Hubbard model and is capable of qualitatively describing the Mott metal-insulator transition. The combination of the DMFT approach with a digital quantum simulation of the reduced fermionic model in a five-qubit processor is in principle feasible with the state-of-the-art technology. This classical-quantum symbiosis in the simulation of strongly correlated fermion models constitutes a different approach in which the number of fermions encoded is not limited by the number of qubits. This hybrid procedure combines one of the best classical approaches with previous methods for the digital simulation of fermions, enriching and broadening the scope of fermionic simulation techniques. In particular, it is oriented to find applications for small quantum devices in the near future.

Fermionic models with all-to-all couplings constitute a higher step in complexity in what regards the simulation of fermionic systems. We consider the SYK model connecting quantum gravity to ordinary QFT via a holographic duality, and originally related to quantum spin glasses in condensed matter. This minimal AdS/CFT model describes interacting fermions with randomly distributed all-to-all couplings for which a non-perturbative understanding can enlighten aspects of quantum gravity, such as bewildering features of quantum black holes, e.g., the information loss paradox. The computation of such non-equilibrium aspects compel quantum platforms to cross the barrier of their observable magnitudes, and demand a method for extracting correlation functions besides simulating the non-trivial system dynamics. We give a protocol that requires polynomial resources for a digital quantum simulation of this model, and for probing non-equilibrium dynamics and the scrambling of information. The combination of proposed techniques is suitable for current technology and is posed to benefit from the rapid advances of quantum technology in the near future. It is likely that more examples of SYK-like models of holography exist, waiting to be uncovered in the near future. Our work therefore provides a foundational proposal opening a route towards the simulation of a variety of theories that span the bridge

between condensed matter and quantum gravity.

A different and distinct paradigm for quantum simulation implies analog storage and processing of information in controllable quantum platforms. In the analog treatment, we deal with continuous variables instead of discrete ones. This is the case of QFT, which was created originally to reconcile quantum mechanics and special relativity, and which is formulated in terms of infinite and continuum number of degrees of freedom. Current efforts for the simulation of these kind of theories consist on quantum algorithms and quantum simulations that reduce these complex models to a large number of controllable qubits. Such realization with controllable quantum platforms is highly demanding and has not yet been achieved in a conclusive manner. We conclude that our novel quantum simulation method involving analog and digital techniques with superconducting circuits establishes a new path to perform truly complex and efficient quantum simulations of QFT. We harness distinctive features of superconducting circuits in order to apply the complexity-simulating-complexity concept, and to avoid complete digital encoding into qubits. This quantum technology provides strong and ultrastrong coupling between superconducting qubits with microwave resonators and open transmission lines. Thus, we propose qubits to efficiently simulate fermionic modes via digital techniques, while we consider the continuum complexity of an open transmission line to capture the continuum complexity of bosonic modes in quantum fields. We consider our digital-analog approach as the most efficient path towards the scalable quantum simulation of full-fledged QFTs in perturbative and non-perturbative regimes. A consequence of this computational paradigm is the technological development of quantum platforms not only pursuing the qubit controllability and scalability, but also exploiting singular characteristics of each of them.

We state that the digital-analog approach for quantum simulations boost the efficiency of the computations while allowing flexibility in the simulated dynamics. The analog encoding of information in the bosonic fields of the superconducting devices can be applied generally in other models with analogous bosonic degrees of freedom, and particular interactions can be designed in each digital step of the discretized evolution. We thus combine two kinds of building blocks for quantum simulations. On one hand, we use purely quantum digital simulation for encoding interactions, and quantum operators which do not appear naturally in the quantum platform under consideration, as fermionic degrees of freedom in superconducting circuits. On the other hand, we propose superconducting resonators and open transmission lines, described with bosonic degrees of freedom, as analog carriers and processors of quantum information. The merger of both techniques with classical feedback simulations allows us to tackle efficiently the study of environmental effects in quantum chemistry and quantum biology. Along these lines, we propose an efficient protocol for simulating fermionic models of molecular structure with hybrid quantum-classical digital techniques. Furthermore, we address the modeling of system-environment interactions of biomolecules involving bosonic degrees of freedom with a digital-analog approach.

On the whole, this Thesis encloses increasingly sophisticated techniques for quan-

tum simulations of a variety of complex models. The treatment of fermionic models, holographic models, QFTs, quantum chemistry models, and quantum biology effects in quantum technologies establishes a dialogue between quantum information theory and condensed matter, quantum gravity, high energy physics, biology and chemistry. Our efforts are meant to influence the way we harness quantum platforms, as unique devices which possess higher capabilities as information processors beyond the purely digital quantum computation paradigm.

Appendices

A Details of the experiment in superconducting circuits

In this appendix we give more details of the experiments presented in section 2.3, and the techniques we have used.

A.1 Experimental details and state fidelity

Experiments are performed in a wet dilution refrigerator with a base temperature of 20 mK. Qubit frequencies are chosen in a staggered pattern to minimize unwanted interaction. Typical qubit frequencies are 5.5 and 4.8 GHz. Exact frequencies are optimized based on the qubits' $|e\rangle$ and $|f\rangle$ state spectra along the fully tunable trajectory of the CZ_ϕ gate, as well as on minimizing the interactions between next-nearest neighboring qubits. The qubits being used are Q1-Q4 in Ref. [80]. Data are corrected for measurement fidelity, typical measurement errors are 0.01 for qubits Q1 and Q3, and 0.04 for Q2 and Q4 [80, 203].

The state fidelity is computed using the expression $|\sum_k \sqrt{P_{k,\text{ideal}} P_k}|^2$, which is

equal to $|\langle \Psi_{\text{ideal}} | \Psi \rangle|^2$ to first order. Here, $P_{k,\text{ideal}}$ and P_k are mode occupations and k runs over the computational basis. The consistency with measured process fidelities, and the scaling of the simulation fidelity with simulation steps justify this approach.

A.2 Trotter step pulse sequences

A.2.1 Pulse sequences and gate counts

The two-, three- and four-mode Trotter step pulse sequences are shown in Fig. A.1. The gate counts are determined using Fig. A.1 and can be found in Table 2.4 in section 2.3.4.

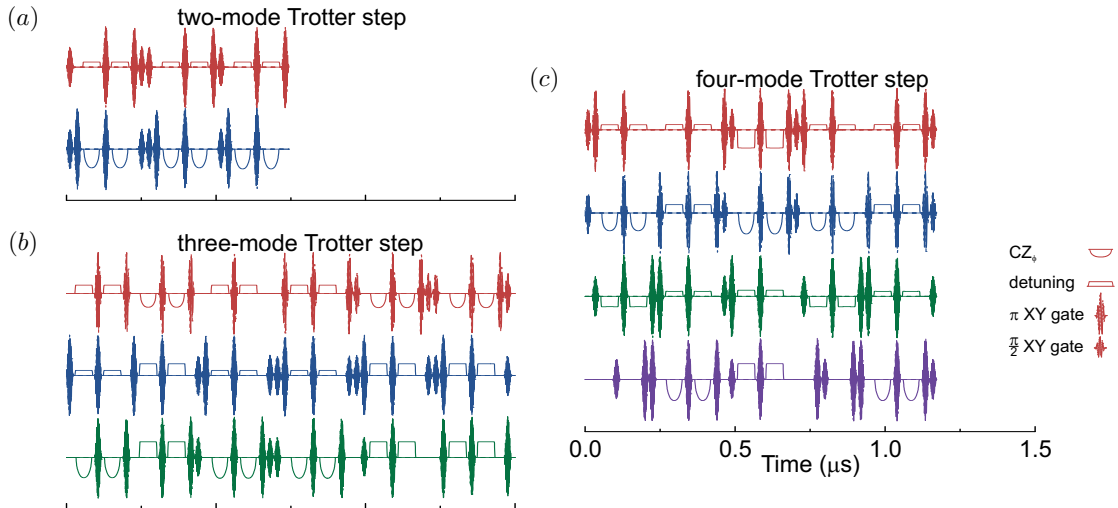


Figure A.1: Pulse sequences in the experiment. Pulse sequences for a single two-mode (a), three-mode (b), and four-mode (c) Trotter step. Used gates are entangling gates as well as single-qubit microwave, idle and detuning gates. The legend is in the bottom right.

A.2.2 Initialization

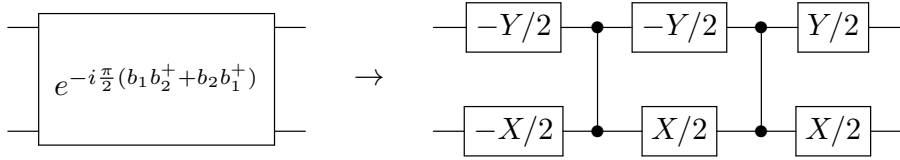
The gate sequences for the initialization of the three- and four-mode simulation are shown in Fig. A.2. For the two-mode simulation the input state is $(|01\rangle + |11\rangle)/\sqrt{2}$, for three modes, $(|101\rangle + |110\rangle)/\sqrt{2}$, and for four modes, $(|0101\rangle + |1001\rangle + |0110\rangle + |1010\rangle)/2$.

A.3 Quantum process tomography

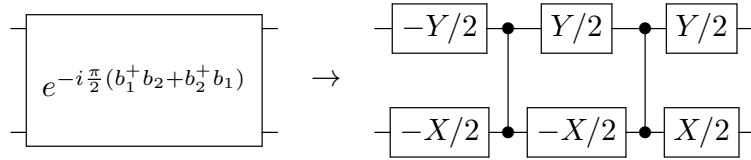
We use QPT to determine the χ matrix. We start by initializing the qubits into the ground state, and prepare input states by applying gates from $\{I, X/2, Y/2, X\}^{\otimes 2}$. The process output is reconstructed by applying gates from the same group, essentially obtaining the 16 output density matrices. The χ matrix is then determined using quadratic maximum likelihood estimation, using the MATLAB packages SeDuMi and YALMIP, while constraining it to be Hermitian, trace-preserving, and positive semidefinite; the estimation is overconstrained. Non-idealities in measurement and state preparation are suppressed by performing tomography on a zero-time idle.

The χ matrices for processes $U_1 = \exp(-i\frac{\pi}{2}(b_1 b_2^\dagger + b_2 b_1^\dagger))$ and $U_2 = \exp(-i\frac{\pi}{2}(b_1^\dagger b_2 + b_2^\dagger b_1))$ are determined experimentally, and the matrix of process $U_2 U_1$ is computed from the experimentally obtained matrices following Ref. [204].

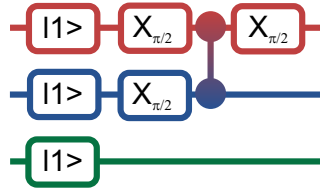
The used quantum circuits are



and



(a) three-mode init.



(b) four-mode init.

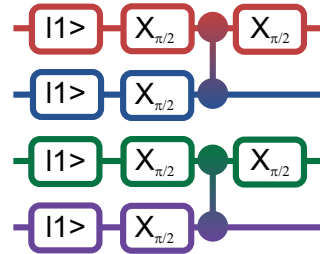


Figure A.2: **Initialization gate sequence.** (a) Three-mode initialization. (b) Four-mode initialization.

A.4 Randomized benchmarking and the two-mode Trotter step

The process fidelity of the $\exp(-i\frac{\phi}{2}\sigma_\ell^z\sigma_m^z)$ gate and the two-mode Trotter step are determined using interleaved Clifford-based randomized benchmarking [205, 206, 75]. This technique is insensitive to measurement and state preparation error, and determines the fidelity properly averaged over all input states, but it restricts the gates to have a unitary which lies within the Clifford group. As representative angles we have therefore used $\phi = \pi/2$, and $\phi_{xx} = \phi_{yy} = \phi_{zz} = \pi/2$ for the Trotter step.

The data are shown in Fig. A.3. We start by measuring the decay in sequence fidelity of sequences of random, two-qubit Clifford elements (black symbols). When interleaving we see an extra decrease of sequence fidelity, which can be linked to the process fidelity of the interleaved gate. We find that the $\exp(-i\frac{\pi}{4}\sigma_\ell^z\sigma_m^z)$ gate and the Trotter step have errors of 0.020 and 0.074, respectively. We note that these values are consistent with estimation by adding individual gate errors as shown in section 2.3.

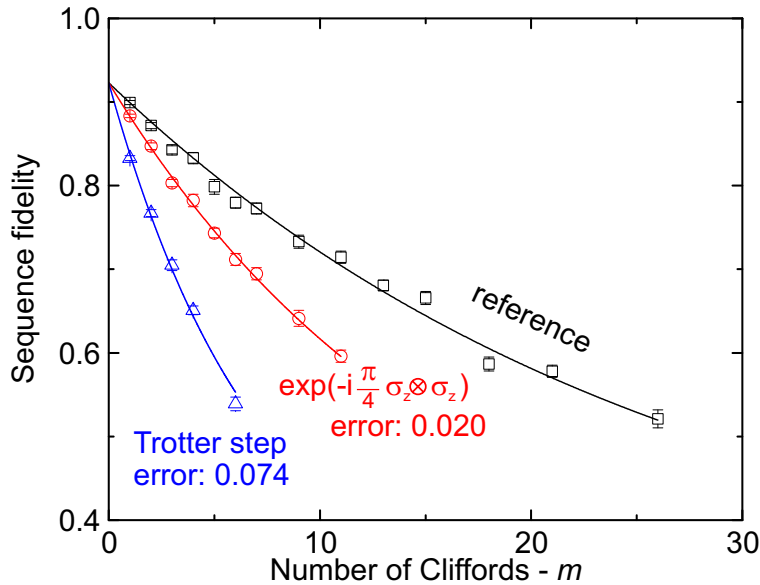


Figure A.3: **Randomized benchmarking.** Clifford-based randomized benchmarking of $\exp(-i\frac{\pi}{4}\sigma_\ell^z\sigma_m^z)$ and the two-mode Trotter step. Sequence fidelity versus number of Clifford elements. Black: reference, color: interleaved.

A.5 Digital error

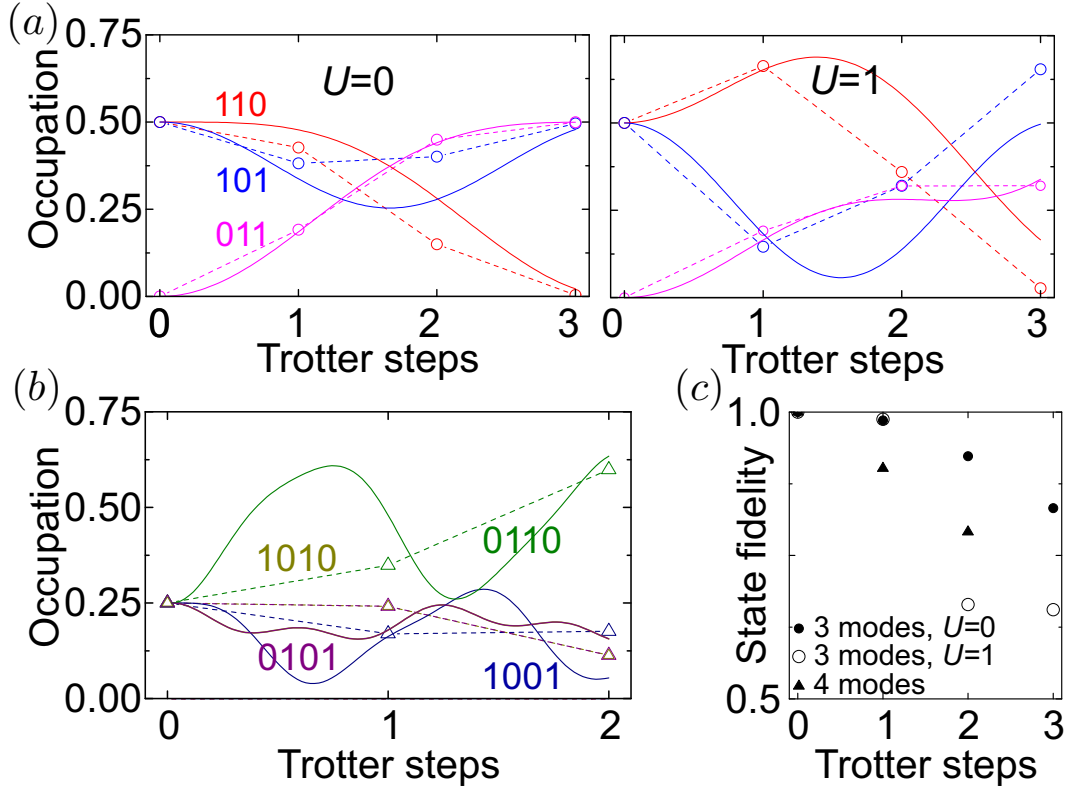


Figure A.4: **Digital error for the time-independent simulation.** (a) Three mode simulation ($U = 0$, $U = 1$, $V = 1$). (b) Four mode simulation ($U_{23} = 1$, $U_{14} = 0$, $V = 1$). (c) Fidelity. Ideal evolution (solid lines) and exact digital solution (open symbols connected by dashed lines).

The Trotter expansion introduces digital errors due to discretization. A full analysis of the digital error for the model being used can be found in section 2.2.2. For the time-independent model, the two-mode simulation has zero digital error. For the three- and four-mode simulation the full evolution (solid lines), exact digital solution (open symbols connected by dashed lines), and fidelities due to digital error are shown in Fig. A.4.

For the time-dependent model we find a negligible digital error for two modes, and a significant error for three, see Fig. A.5. The large error for three modes arises from having to approximate a larger Hamiltonian, as well as using only a single step.

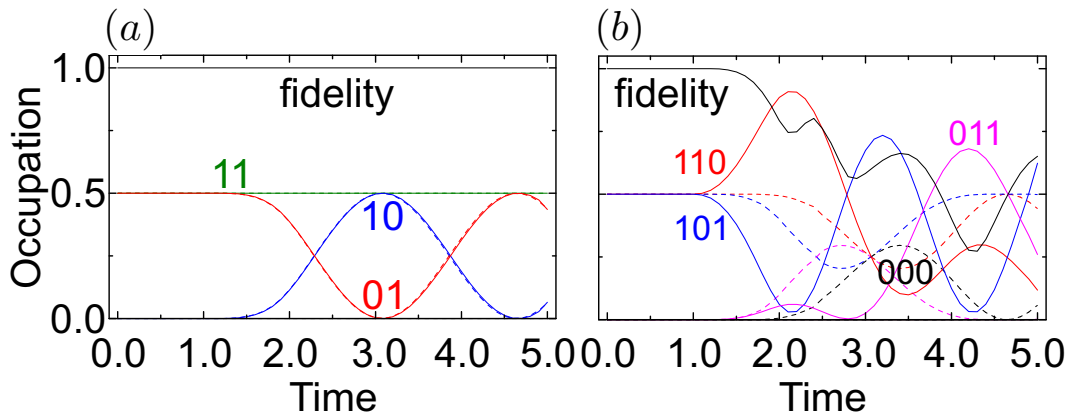


Figure A.5: **Digital error for the time-dependent simulation** for two modes, using two Trotter steps (a) and three modes, using one Trotter step (b). Ideal evolution (solid lines), exact digital solution (dashed lines), and fidelity (solid black).

A.6 Minimizing leakage of the CZ_ϕ gate

The tunable CZ_ϕ gate works by tuning the frequency of one of the qubits to approach the avoided level crossing of the $|ee\rangle$ and $|gf\rangle$ states, using an adiabatic trajectory [83]. For large phases we need to approach closely the avoided level crossing, inducing state leakage.

To minimize such leakage we have chosen to increase the length of the CZ_ϕ gate from a typical 40 ns [60] to 55 ns. However, for large phases (> 4.0 rads), see Fig. A.6a, we still see a considerable amount of leakage, see the Fig. A.6b. By choosing the leaked state population as a fitness metric, and using Nelder-Mead optimization in a similar approach to Ref. [207] to tune waveform parameters, see Figs. A.6c-d, we can significantly suppress leakage. We note that this optimization took approximately one minute in real time.

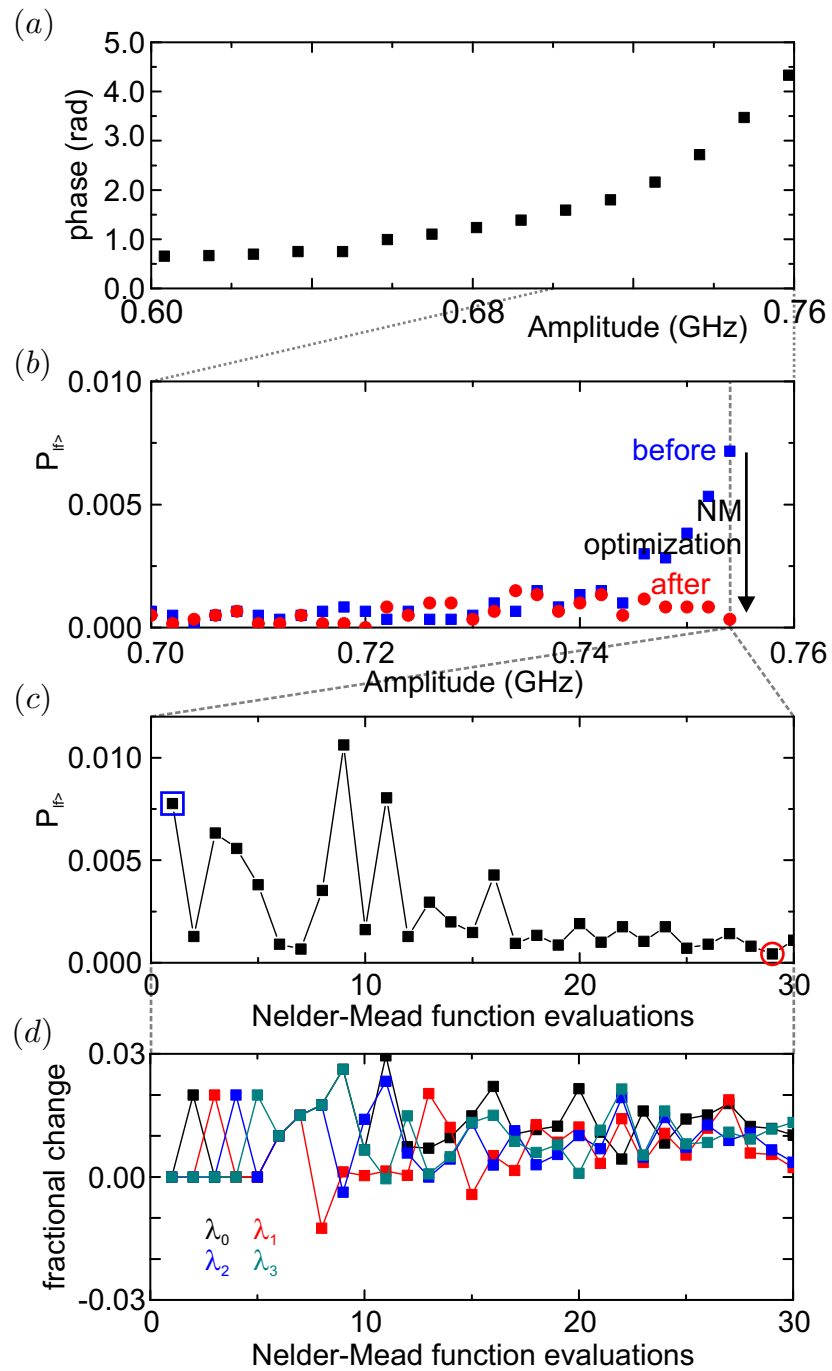


Figure A.6: **Minimizing leakage of the CZ_ϕ gate.** (a) Tunable phase versus pulse amplitude, determined with quantum state tomography. (b) Zoom-in of the amplitude region for large phases, showing the $|f\rangle$ -state population before (blue) and after (red) Nelder-Mead optimization. (c) Population of $|f\rangle$ versus Nelder-Mead function evaluation, showing a downwards trend. (d) Optimization of the waveform parameters with Nelder-Mead function evaluation, see Ref. [83] for the definition of these parameters.

B Hubbard model in infinite dimensions and DMFT

A standard model to describe strongly correlated electron systems in thermodynamic equilibrium is the Hubbard Hamiltonian

$$H = -t \sum_{\langle j,k \rangle \sigma} \left(c_{j,\sigma}^\dagger c_{k,\sigma} + c_{k,\sigma}^\dagger c_{j,\sigma} \right) + U \sum_j n_{j,\downarrow} n_{j,\uparrow}. \quad (\text{B.1})$$

In this model, electrons with spin projections $\sigma = \downarrow, \uparrow$ ‘hop’ between adjacent lattice sites with tunnelling energy t . This process is described in the first term, where $\langle j, k \rangle$ denotes the sum over all nearest-neighbor sites j and k , and $c_{j,\sigma}^\dagger$ and $c_{k,\sigma}$ denote the fermionic creation and annihilation operators, respectively. The electrons interact with on-site Coulomb repulsion $U > 0$, described in the latter term by the product of the local number operators $n_{j,\downarrow} = c_{j,\downarrow}^\dagger c_{j,\downarrow}$ and $n_{j,\uparrow} = c_{j,\uparrow}^\dagger c_{j,\uparrow}$.

Here, we consider the paramagnetic Hubbard model in an infinite-dimensional Bethe lattice [91] in the thermodynamic limit at zero temperature. This setup has very simple self-consistency relations, which makes it an ideal test-bed for a proof-of-principle demonstration of a hybrid quantum-classical scheme.

The DMFT approach [9] to solving this model consists in neglecting spatial fluctuations around a single lattice site and replacing the rest of the many-body lattice in the thermodynamic limit by a time-translation-invariant, self-consistent mean-field

$\Delta(\tau - \tau')$ (or $\Delta(\omega)$ in the frequency domain), as illustrated in Fig. 2.14a. The isolated lattice site can dynamically exchange fermions with the mean-field at time instants τ' and τ . This allows one to include retardation effects that are important in the presence of strong correlations. In short, the dynamical mean-field approach reduces the complexity of the full Hubbard model to an effective single-site system which is a slightly more benign many-body problem to solve. In infinite dimensions, DMFT becomes exact as the irreducible self-energy of the lattice model becomes strictly local in space, $\Sigma_{\text{latt},jk}(\omega) = \delta_{jk}\Sigma_{\text{latt},jj}(\omega)$, and its skeleton diagrams agree with those of a single-site, or impurity, model [9].

The solution of the effective single-site, or impurity, problem also yields the solution of the infinite-dimensional Hubbard model due to the self-consistency condition. This leads to the retarded single-particle impurity Green function in the frequency domain being given by

$$G_{\text{imp}}^R(\omega) = \frac{1}{\omega + \mu - \Delta(\omega) - \Sigma_{\text{imp}}(\omega)}, \quad (\text{B.2})$$

where μ is the chemical potential, and $\Sigma_{\text{imp}}(\omega)$ denotes the impurity self-energy. The impurity Green function describes the response of the many-body system after a localized removal or addition of a particle on the impurity site and is defined in the time domain and at zero temperature as

$$iG_{\text{imp}}^R(\tau) = \theta(\tau)\langle\{c_\sigma(\tau), c_\sigma^\dagger(0)\}\rangle, \quad (\text{B.3})$$

where i is the imaginary unit, τ is real time, $\{\cdot, \cdot\}$ denotes the anticommutator, $\theta(\tau)$ is the Heaviside step function, and the average is computed in the ground-state $|GS\rangle$ of the impurity model. The fermionic creation and annihilation operators are given in the Heisenberg picture. In the paramagnetic phase the Green function is spin symmetric and we therefore only need to work out $G_{\text{imp}}^R(\omega)$ for one spin configuration.

The initially unknown mean-field $\Delta(\omega)$ has to be chosen such that $G_{\text{imp}}^R(\omega)$ matches the local part of the retarded lattice Green function $G_{\text{latt},jj}^R(\omega)$, i.e.,

$$G_{\text{imp}}^R(\omega) = G_{\text{latt},jj}^R(\omega), \quad (\text{B.4})$$

where j is the (randomly chosen) lattice site from which the removal or addition of a particle occurs in the translationally invariant lattice model. The DMFT self-consistency condition Eq. (B.4) implies

$$\Sigma_{\text{imp}}(\omega) = \Sigma_{\text{latt},jj}(\omega), \quad (\text{B.5})$$

i.e., the impurity self-energy matches the local self-energy of the Hubbard model in the infinite-dimensional Bethe lattice.

In the general case, the DMFT self-consistency loop is iterated as follows (see also Ref. [9]). (i) First, guess the local self-energy $\Sigma_{\text{latt},jj}(\omega)$. (ii) The local lattice Green function can be computed as $G_{\text{latt},jj}^R(\omega) = \int_{-\infty}^{\infty} d\epsilon \rho_0(\epsilon) / [\omega + \mu - \epsilon - \Sigma_{\text{latt},jj}(\omega)]$, where $\rho_0(\epsilon) = \sqrt{4t^{*2} - \epsilon^2} / 2\pi t^{*2}$ is the non-interacting density of states of a Bethe

lattice. The constant t^* emerges from the requirement that the Hubbard hopping needs to be scaled as $t \sim t^*/\sqrt{z}$ to avoid a diverging kinetic energy per lattice site in the limit of infinite coordination, $z \rightarrow \infty$ [9]. (iii) With Eqs. (B.4) and (B.5), we obtain $\Delta(\omega)$ from Eq. (B.2) and the impurity model is then defined. (iv) Compute the impurity Green function and obtain the impurity self-energy $\Sigma_{\text{imp}}(\omega)$. There are several means to do this [9]. (v) Set $\Sigma_{\text{latt},jj}^{\text{new}}(\omega) = \Sigma_{\text{imp}}(\omega)$. (vi) Check if the self-energy has converged. If not, go to step (ii) and repeat.

Once self-consistent, the solution of the impurity problem then gives access to local single-particle properties of the original lattice model. For example, the local lattice spectral function is given by

$$A_{\text{latt},jj}(\omega) = -\text{Im}[G_{\text{latt},jj}^R(\omega + i\eta)]/\pi = -\text{Im}[G_{\text{imp}}^R(\omega + i\eta)]/\pi, \quad (\text{B.6})$$

where η is a positive infinitesimal.

In Hamiltonian-based impurity solvers, one parameterizes $\Delta(\omega)$ by a set of bath sites (see Fig. 2.14b). For any finite number of bath sites, the self-consistency condition (B.4) can only be approximately satisfied and in the extreme “two-site” DMFT it turns out to be more suitable to reformulate Eq. (B.4) in a manner specially focused on this minimal representation [87] (see section 2.4.1). Note that two-site DMFT is only able to provide a qualitatively correct description of the Hubbard model even in infinite dimensions [87].

C Interferometry for the impurity Green function

In this appendix, we present in detail a measurement scheme for the retarded impurity Green function.

C.1 Definitions

The retarded zero temperature impurity Green function in the time domain can be written as

$$G_{\text{imp}}^R(\tau) = \theta(\tau) [G_{\text{imp}}^>(\tau) - G_{\text{imp}}^<(\tau)], \quad (\text{C.1})$$

where the “greater” and “lesser” Green functions are given by

$$G_{\text{imp}}^>(\tau) = -i\langle c_{1\sigma}(\tau)c_{1\sigma}^\dagger(0) \rangle, \quad (\text{C.2})$$

$$G_{\text{imp}}^<(\tau) = i\langle c_{1\sigma}^\dagger(0)c_{1\sigma}(\tau) \rangle, \quad (\text{C.3})$$

respectively. The average is computed in the ground-state $|GS\rangle$ of the two-site SIAM in Eq. (2.20). Here, σ can be either \downarrow or \uparrow since we are considering a spin-symmetric case (i.e., $G_{\downarrow}^R = G_{\uparrow}^R$), and the c operators are given in the Heisenberg picture with respect to \hat{H}_{SIAM} , i.e.,

$$c_{1\sigma}(\tau) = U^\dagger(\tau)c_{1\sigma}U(\tau) = e^{i\tau H_{\text{SIAM}}}c_{1\sigma}e^{-i\tau H_{\text{SIAM}}}. \quad (\text{C.4})$$

One possibility to measure the impurity Green function $G_{\text{imp}}^R(\tau)$ is to use a single-qubit Ramsey interferometer [208] which was used in Ref. [40] in the more general non-equilibrium case. To this end, we introduce an ancilla qubit in addition to the ‘system’ qubits, raising the total number of qubits needed to implement the two-site DMFT scheme to five.

C.2 Jordan–Wigner transformation

The greater and lesser components, $G_{\text{imp}}^>(\tau)$ and $G_{\text{imp}}^<(\tau)$, must be written in terms of spin operators by again mapping the $c_{1\sigma}$ and $c_{1\sigma}^\dagger$ operators onto Pauli operators via the JW transformation. For concreteness, we focus on the case $\sigma = \downarrow$. We obtain

$$G_{\text{imp}}^>(\tau) = -\frac{i}{4} \left(\langle U^\dagger(\tau)\sigma_1^x U(\tau)\sigma_1^x \rangle + i\langle U^\dagger(\tau)\sigma_1^x U(\tau)\sigma_1^y \rangle - i\langle U^\dagger(\tau)\sigma_1^y U(\tau)\sigma_1^x \rangle + \langle U^\dagger(\tau)\sigma_1^y U(\tau)\sigma_1^y \rangle \right), \quad (\text{C.5})$$

and

$$G_{\text{imp}}^<(\tau) = \frac{i}{4} \left(\langle \sigma_1^x U^\dagger(\tau)\sigma_1^x U(\tau) \rangle - i\langle \sigma_1^x U^\dagger(\tau)\sigma_1^y U(\tau) \rangle + i\langle \sigma_1^y U^\dagger(\tau)\sigma_1^x U(\tau) \rangle + \langle \sigma_1^y U^\dagger(\tau)\sigma_1^y U(\tau) \rangle \right). \quad (\text{C.6})$$

C.3 Measurement protocol

Each of the terms of the form $\langle U^\dagger(\tau)\sigma_1^\alpha U(\tau)\sigma_1^\beta \rangle$, where $\alpha, \beta \in \{x, y\}$, can be measured in the interferometer. This can be seen as follows. We denote the state of the system qubits by $\rho_{\text{sys}} = |GS\rangle\langle GS|$, where $|GS\rangle$ is the ground-state of the system. We initialize the ancilla qubit in the state $|0\rangle$, yielding the total density operator $\rho_{\text{tot}} = |0\rangle\langle 0| \otimes \rho_{\text{sys}}$. The total system then undergoes the following evolution:

1. At time $t = 0$, a Hadamard gate $\sigma_H = \frac{1}{\sqrt{2}}(\sigma^z + \sigma^x)$ is applied on the ancilla qubit, creating the superposition $|0\rangle_{\text{ancilla}} \rightarrow (|0\rangle_{\text{ancilla}} + |1\rangle_{\text{ancilla}})/\sqrt{2}$.
2. A Controlled-Pauli gate σ_1^α is applied on the impurity qubit 1 if the ancilla qubit has state $|0\rangle$.
3. The system qubits undergo time evolution according to the unitary $U(\tau)$ which is decomposed into quantum gates.
4. Another Controlled-Pauli gate σ_1^β is applied on the impurity qubit 1 if the ancilla qubit has state $|1\rangle$.
5. Another Hadamard gate is applied on the ancilla qubit.

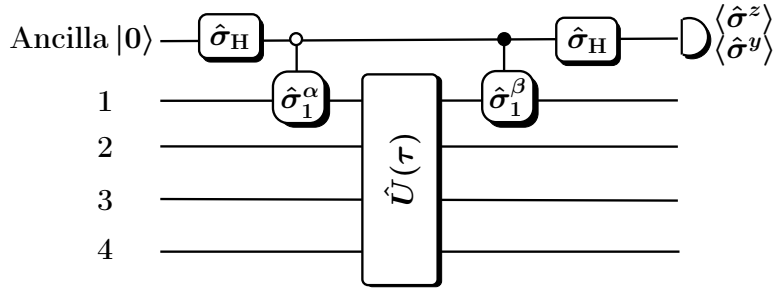


Figure C.1: **Quantum network to measure contributions to the Green function.** Quantum network to measure the $\langle GS|U^\dagger(\tau)\sigma_1^\alpha U(\tau)\sigma_1^\beta|GS\rangle$ contribution to the Green function $G_{\text{imp}}^R(\tau)$. The time-evolution operator $U(\tau)$ is composed of a set of quantum gates according to section 2.4.

Denoting the total unitary in steps 2-4 by T , the state of the ancilla qubit after this evolution is given by

$$\begin{aligned}
 \rho_{\text{ancilla}} &= \text{Tr}_{\text{sys}} [\sigma_H T \sigma_H \rho_{\text{tot}} \sigma_H T^\dagger \sigma_H] \\
 &= \frac{1 + \text{Re}[F(\tau)]}{2} |0\rangle\langle 0| - i \frac{\text{Im}[F(\tau)]}{2} |0\rangle\langle 1| + i \frac{\text{Im}[F(\tau)]}{2} |1\rangle\langle 0| \\
 &\quad + \frac{1 - \text{Re}[F(\tau)]}{2} |1\rangle\langle 1|,
 \end{aligned} \tag{C.7}$$

where $F(\tau) = \text{Tr}_{\text{sys}} [T_1^\dagger(\tau) T_0(\tau) \rho_{\text{sys}}]$. We have denoted the controlled unitaries as $T_1(\tau) = \sigma_1^\alpha U(\tau)$ and $T_0(\tau) = U(\tau) \sigma_1^\beta$. Note that since the same $U(\tau)$ appears in both unitaries, only the Pauli gates $\sigma_1^{\alpha/\beta}$ need to be controlled, as described above. Note also that $F(\tau) = \langle U^\dagger(\tau) \sigma_1^\alpha U(\tau) \sigma_1^\beta \rangle$. We can rewrite the state of the ancilla qubit as

$$\rho_{\text{ancilla}} = \frac{1}{2} (1 + \text{Re}[F(\tau)] \sigma_z + \text{Im}[F(\tau)] \sigma_y), \tag{C.8}$$

whence $\text{Tr}_{\text{ancilla}}[\rho_{\text{ancilla}}\sigma^z] = \text{Re}[F(\tau)]$, and $\text{Tr}_{\text{ancilla}}[\rho_{\text{ancilla}}\sigma^y] = \text{Im}[F(\tau)]$. Thus, repeated measurements of the σ^z and σ^y components of the ancilla qubit yield the real and imaginary parts of the term $\langle U^\dagger(\tau)\sigma_1^\alpha U(\tau)\sigma_1^\beta \rangle$. See Fig. C.1 for the quantum network of the scheme.

D Details on the holographic models

This appendix contains further details on the models and theoretical derivations we have considered in chapter 3.

D.1 SYK models

We have optimized the number of terms to simulate in all models, i.e., with Majorana and complex fermions, by grouping interaction terms via the anticommutation relations of fermionic operators. These simplifications lead to new coupling coefficients resulting from linear combinations of the original coefficients of fermionic models, $J_{ij;kl}$ and J_{ijkl} . These new groupings of coefficients will need to be generated for the simulation, and implemented as phases in the quantum gates. Thus, we analyze which are independent random variables and their distribution in relation to those of the initial models.

D.1.1 Details on Majorana models

For the Majorana models, we start with the case $i > j > k > l$ (type (i) interaction terms) and group the interaction coupling constants as follows

$$\tilde{J}_{\alpha_4\alpha_3\alpha_2\alpha_1} = \sum_{\sigma(\alpha_4\alpha_3\alpha_2\alpha_1)} \text{sgn}(\sigma) J_{\sigma(\alpha_4\alpha_3\alpha_2\alpha_1)} = 4! J_{\alpha_4\alpha_3\alpha_2\alpha_1}, \quad (\text{D.1})$$

where we have taken into account that, in this case, $J_{jklm} = \text{sgn}(\sigma) J_{\sigma(jklm)}$. A linear transformation of a stochastic variable, $\eta = a\xi + b$, induces a transformation of the probability density $p_\eta(y) = (1/|a|)p_\xi[(y-b)/a]$, and this keeps us in the Gaussian family: if $\xi \sim N(\mu, \sigma)$, then $\eta \sim N(a\mu + b, |a|\sigma)$. In our case, since $J_{jklm} \sim N(0, \sqrt{6}JN^{-3/2})$, we have $\tilde{J}_{jklm} \sim N(0, 4!\sqrt{6}JN^{-3/2})$. Defining $\tilde{J} = 4!J$, we note that the new coefficients \tilde{J}_{jklm} present the same structure as the initial ones, with a rescaled variance.

The purpose of this simplification is to identify independent stochastic variables; clearly the constraints $J_{\alpha_4\alpha_3\alpha_2\alpha_1} = \text{sign}(\sigma) J_{\sigma(\alpha_4\alpha_3\alpha_2\alpha_1)}$ signify that these are not independent. The \tilde{J} variables are symmetrized versions, and are independent.

Our first Majorana model under consideration includes only the four-body interactions above (type (i)), i.e., those with no repeated indices, that can be expressed in terms of $\chi_i\chi_j\chi_k\chi_l$ with $i > j > k > l$.

Let us now focus on terms with repeated indices, which give rise to type (ii) interaction terms. Taking them into account as well as the previous ones provides us with a second Majorana model. Notice however that the physical properties in the limit of large N would not change. Whenever present, the coefficients J_{ijkl} with repeated indices would no longer possess the symmetry described above. For instance, coefficients of $\chi_i\chi_j$ terms (to which the four fermion operators with repeated indices reduce) should be purely imaginary: let the two fermion terms be written as the operator $\mathcal{M}_2 = \chi^T A \chi$, with χ a column vector with entries the Majorana operators. The non-trivial elements correspond to the antisymmetric part of the matrix A , so this is taken as antisymmetric. In order for this operator \mathcal{M}_2 to be hermitian one additional constraint is required: A must be hermitian. It follows that A must be purely imaginary. If we consider a model in which these terms are present, the coefficients A_{ij} with $i > j$ will be taken from a Gaussian ensemble, $A_{ij} \sim N(0, \sigma_A)$. These coefficients will be independent of the previously introduced \tilde{J}_{jklm} . We give the variance as $\sigma_A = J_A/(2\sqrt{N})$. Notice however that if we were to start from the complex fermion model, with or without chemical potential μ , and rewrite it in terms of Majorana fermions, the coefficients of the two Majorana fermionic terms will not be independent of the four-point ones in that translated model.

The previous presentation can be summarized as follows: we identify independent interaction terms. Those correspond to $i > j > k > l$, four-point interactions, and $i > j$, two point interactions. The coupling constants corresponding to these independent interaction terms have been presented above. The number of independent terms of each kind, four-point or two point, is given by $\binom{N}{4}$ and $\binom{N}{2}$, respectively.

D.1.2 Details on spinless complex fermion models

We now identify the number of independent interaction terms for the spinless complex fermion models, and the corresponding coefficients and their probability distribution. They are firstly rearranged as follows

$$\tilde{J}_{\alpha_2\alpha_1;\beta_2\beta_1} = \sum_{\sigma_1(\alpha_2\alpha_1);\sigma_2(\beta_2\beta_1)} \text{sgn}(\sigma_1)\text{sgn}(\sigma_2)J_{\sigma_1(\alpha_2\alpha_1);\sigma_2(\beta_2\beta_1)} = 4J_{\alpha_2\alpha_1;\beta_2\beta_1}, \quad (\text{D.2})$$

with $\alpha_2 > \alpha_1$ and $\beta_2 > \beta_1$. Otherwise the tilded coefficients are defined to be zero. This takes into account the fermionic symmetries of the creation and annihilation operators separately, and allows us to concentrate on the case $\alpha_2 > \alpha_1$ and $\beta_2 > \beta_1$, which will be useful for the quantum simulation of interaction terms of type (i), as we will see.

Altogether there are, for n spinless fermions, $\binom{n}{2}^2$ terms of the form $c_i^\dagger c_j^\dagger c_k c_l$ that satisfy the constraints $i > j$ and $k > l$.

Now, let us connect with the four types presented in section 3.1.1. We identify first terms of type (i), for which there is no coincidence of indices, i.e., such that the additional constraints $i \neq k$, $i \neq l$, $j \neq k$ and $j \neq l$ hold, as separate from those cases in which there is coincidence.

Interaction terms of type (ii) have a coincidence of two indices with the other two distinct from each other and from the repeated one, that is, a generic interaction $c_i^\dagger n_j c_k$, with no ordering of indices imposed on them. The counting of combinations of three different indices taken from a set of n is $\frac{n!}{(n-3)!} = n^3 - 3n^2 + 2n$. Let us connect this point of view with the symmetry perspective above. We reintroduce the restriction $i > j$ and $k > l$ for $c_i^\dagger c_j^\dagger c_k c_l$. There are four separate cases of coincidence of two indices with the other two distinct from each other: a) $k = i$, and $j \neq l$; b) $l = i$, which implies $k > i > j$; c) $k = j$, leading to $i > j > l$; and d) $j = l$, with $i \neq k$. There are $\binom{n}{3}$ cases of types b) and c), and $2 \times \binom{n}{3}$ each for cases a) and d). All these cases can be unified in terms of the form $c_i^\dagger c_j^\dagger c_j c_l$ (type (ii)) by relaxing the ordering condition. There are altogether, as before, $6 \times \binom{n}{3} = n^3 - 3n^2 + 2n$ terms of this kind.

There is only one type of coincidence of two pairs, given by $k = i$ and $j = l$, with $i > j$ (type (iii)), and there are $\binom{n}{2}$ of these terms.

Altogether we see that there are $\binom{n}{2}^2 - 6\binom{n}{3} - \binom{n}{2} = 6\binom{n}{4}$ independent terms of type (i). This does not yet mean that their coefficients are independent stochastic variables. We have not imposed as yet hermiticity of the Hamiltonian.

There is a further simplification for interactions of type (i), in which the terms are grouped as

$$\begin{aligned} J_{ij;kl}^1 &= \tilde{J}_{ij;kl} + \tilde{J}_{ik;jl} + \tilde{J}_{il;jk}, \\ J_{ij;kl}^2 &= \tilde{J}_{ij;kl} - \tilde{J}_{ik;jl} + \tilde{J}_{il;jk}, \\ J_{ij;kl}^3 &= \tilde{J}_{ij;kl} + \tilde{J}_{ik;jl} - \tilde{J}_{il;jk}, \\ J_{ij;kl}^4 &= -\tilde{J}_{ij;kl} + \tilde{J}_{ik;jl} + \tilde{J}_{il;jk}, \end{aligned} \quad (\text{D.3})$$

which we notice are related as $J_{ij;kl}^1 = J_{ij;kl}^2 + J_{ij;kl}^3 + J_{ij;kl}^4$. We consider a larger number of dependent parameters in order to minimize spin interactions, as shown in Eq. (E.5). The real coefficients appearing in the spin Hamiltonian are $\text{Re}(J_{ij;kl}^a)$ and $\text{Im}(J_{ij;kl}^a)$, with $a = 1, 2, 3, 4$.

As we must emphasize, the fermionic symmetries of these models entail that not all coefficients are independent. In fact, a choice of indices $i > j > k > l$ determines all the possible six orderings of those distinct numbers that maintain the property that both the first and the second pair are ordered, i.e., for type (i). This will give rise to the combinations above, in Eq. (D.3). The complex coefficients $J_{ij;kl}$ in the fermionic model satisfy a Gaussian random distribution with zero mean. If we consider that the real and imaginary parts are independently Gaussian distributed and have zero mean, then $\text{Re}(J_{ij;kl}^a)$ and $\text{Im}(J_{ij;kl}^a)$ with $a = 2, 3, 4$, which are a linear combination of Gaussian stochastic variables are themselves Gaussian distributed. Assuming that in the initial definition of the complex coefficients the real and imaginary parts are identically distributed, so are $\text{Re}(J_{ij;kl}^a)$ and $\text{Im}(J_{ij;kl}^a)$, more concretely $\sim N(0, 3J/n^{3/2})$. Furthermore, they are independent when we set $i > j > k > l$, and identically distributed. We note that $J_{ij;kl}^1$ is obtained from the sum of $J_{ij;kl}^2$, $J_{ij;kl}^3$ and $J_{ij;kl}^4$. Summarizing, for the case of distinct indices we have six independent identically distributed (i.i.d.) real Gaussian random variables for the $\binom{n}{4}$ alternatives $i > j > k > l$, starting from complex coefficients. If we were to restrict ourselves to real coefficients, there would be just three i.i.d. real Gaussian random variables for those alternatives, $\sim N(0, 3\sqrt{2}J/n^{3/2})$.

E Details on the quantum algorithm for SYK

E.1 Construction of spin interaction terms for the quantum algorithm

E.1.1 Details on Majorana models

As stated in section 3.2, the JW construction for Majorana fermions is given by

$$\chi_l \rightarrow \left(\prod_{j=1}^{\tilde{l}-1} \sigma_j^z \right) \sigma_{\tilde{l}}^{\alpha_l}, \quad (\text{E.1})$$

where $\tilde{l} = \lfloor (l+1)/2 \rfloor$ and α_l is x for even l and y for odd l .

The Majorana interaction terms of type (i), $\chi_i \chi_j \chi_k \chi_l$ with $i > j > k > l$, correspond to spin interaction terms of the form $\left(\prod_{m=\tilde{l}}^{\tilde{k}-1} \sigma_m^z \right) \left(\prod_{m=\tilde{j}}^{\tilde{i}-1} \sigma_m^z \right) \sigma_{\tilde{i}}^{\alpha_i} \sigma_{\tilde{j}}^{\alpha_j} \sigma_{\tilde{k}}^{\alpha_k} \sigma_{\tilde{l}}^{\alpha_l}$. Note that each fermionic interaction term is translated into just a single kind of spin interaction, with a definite combination of α spin indices. This general expression

can be reduced by the following observation: a pair of ordered indices s and t , with $s > t$, give identical reduced indices $\tilde{s} = \tilde{t}$ only if both a) $s = t + 1$ and b) t is odd (s is even) are fulfilled. Therefore, there are four possibilities of a simplification in the spin presentation: A) $\tilde{i} = \tilde{j} > \tilde{k} \geq \tilde{l}$; B) $\tilde{i} \geq \tilde{j} > \tilde{k} = \tilde{l}$; C) $\tilde{i} > \tilde{j} = \tilde{k} > \tilde{l}$. The possibility does exist that $\tilde{i} = \tilde{j} > \tilde{k} = \tilde{l}$, which has been included in both A and B. We present these cases and the number of combinations corresponding to each in Table E.1 in terms of Majorana terms.

 Table E.1: Majorana quartic fermionic interaction terms when $i > j > k > l$.

Set	Fermionic interaction	Number of terms
U	$\chi_i \chi_j \chi_k \chi_l$	$ U = \binom{2n}{4} = \frac{2}{3}n^4 - 2n^3 + \frac{11}{6}n^2 - \frac{1}{2}n$
A	$\chi_i \chi_{i-1} \chi_k \chi_l \quad \forall i \text{ even}$	$ A = \sum_{m=2}^n \sum_{k=2}^{2m-2} \sum_{l=1}^{k-1} 1 = \frac{2}{3}n^3 - \frac{3}{2}n^2 + \frac{5}{6}n$
B	$\chi_i \chi_j \chi_k \chi_{k-1} \quad \forall k \text{ even}$	$ B = \sum_{i=4}^{2n} \sum_{j=3}^{i-1} \lfloor \frac{j-1}{2} \rfloor = \frac{2}{3}n^3 - \frac{3}{2}n^2 + \frac{5}{6}n$
$A \cap B$	$\chi_i \chi_{i-1} \chi_k \chi_{k-1} \quad \forall i, k \text{ even}$	$ A \cap B = \binom{n}{2} = \frac{1}{2}n^2 - \frac{1}{2}n$
C	$\chi_i \chi_j \chi_{j-1} \chi_l \quad \forall j \text{ even}$	$ C = \sum_{i=5}^{2n} \sum_{m=2}^{\tilde{i}-1} \sum_{l=1}^{2m-2} 1 = \frac{2}{3}n^3 - 2n^2 + \frac{4}{3}n$

Now we state the simplifications in spin interaction terms as shown in Table E.2. First, the cases $A \setminus \{A \cap B\}$ and $B \setminus \{A \cap B\}$ present a similar structure. As an example, the spin interaction term for $A \setminus \{A \cap B\}$ becomes $i \left(\prod_{m=\tilde{l}}^{\tilde{k}-1} \sigma_m^z \right) \sigma_i^z \sigma_k^{\alpha_k} \sigma_l^{\alpha_l}$. Notice the presence of the i factor, which is in fact required for hermiticity, because $(\sigma_i^z \sigma_l^{\alpha_l})^\dagger = -\sigma_i^z \sigma_l^{\alpha_l}$.

The intersection set $A \cap B$ has representative $-\sigma_i^z \sigma_k^z$.

Finally, the central coincidence of the indices in terms belonging to set C produces spin interaction terms of the form $i \left(\prod_{m=\tilde{l}}^{\tilde{k}-1} \sigma_m^z \right) \left(\prod_{m=\tilde{j}}^{\tilde{i}-1} \sigma_m^z \right) \sigma_i^{\alpha_i} \sigma_j^z \sigma_l^{\alpha_l}$.

Table E.2: Spin interactions for quartic Majorana fermionic terms.

Set	Spin interaction	Number of terms
$U \setminus \{A \cup B \cup C\}$	$\left(\prod_{m=\tilde{l}}^{\tilde{k}-1} \sigma_m^z \right) \left(\prod_{m=\tilde{j}}^{\tilde{i}-1} \sigma_m^z \right) \sigma_i^{\alpha_i} \sigma_j^{\alpha_j} \sigma_k^{\alpha_k} \sigma_l^{\alpha_l}$	$\frac{2}{3}n^4 - 4n^3 + \frac{22}{3}n^2 - 4n$
$A \setminus \{A \cap B\}$	$i \left(\prod_{m=\tilde{l}}^{\tilde{k}-1} \sigma_m^z \right) \sigma_i^z \sigma_k^{\alpha_k} \sigma_l^{\alpha_l}$	$\frac{2}{3}n^3 - 2n^2 + \frac{4}{3}n$
$B \setminus \{A \cap B\}$	$i \left(\prod_{m=\tilde{j}}^{\tilde{i}-1} \sigma_m^z \right) \sigma_i^{\alpha_i} \sigma_j^{\alpha_j} \sigma_k^z$	$\frac{2}{3}n^3 - 2n^2 + \frac{4}{3}n$
$A \cap B$	$-\sigma_i^z \sigma_k^z$	$\frac{n^2}{2} - \frac{n}{2}$
C	$i \left(\prod_{m=\tilde{l}}^{\tilde{k}-1} \sigma_m^z \right) \left(\prod_{m=\tilde{j}}^{\tilde{i}-1} \sigma_m^z \right) \sigma_i^{\alpha_i} \sigma_j^z \sigma_l^{\alpha_l}$	$\frac{2}{3}n^3 - 2n^2 + \frac{4}{3}n$

Coming now to quadratic terms $\chi_i \chi_j$, with $i > j$, notice again that they are

antihermitian as such. They are generically codified as

$$i\chi_i\chi_j \rightarrow i \left(\prod_{l=\tilde{j}}^{\tilde{i}-1} \sigma_l^z \right) \sigma_{\tilde{i}}^{\alpha_i} \sigma_{\tilde{j}}^{\alpha_j}, \quad (\text{E.2})$$

and there are $\binom{2n}{2}$ of them. The special case is here when i is even and $j = i - 1$. There are n possibilities, all of which are represented by $-\sigma_{\tilde{i}}^z$.

E.1.2 Details on spinless complex fermion models

Let us now consider the model with complex spinless fermions. The interaction terms can be mapped as above to spin interactions via the JW transformation. Thus, the interaction terms of type (i) of this model are expressed as

$$c_i^\dagger c_j^\dagger c_k c_\ell = \kappa \left(\prod_{\xi=\zeta_1+1}^{\zeta_2-1} \sigma_\xi^z \right) \left(\prod_{\xi=\zeta_3+1}^{\zeta_4-1} \sigma_\xi^z \right) \sigma_i^+ \sigma_j^+ \sigma_k^- \sigma_\ell^-, \quad (\text{E.3})$$

where $\{\zeta_1, \zeta_2, \zeta_3, \zeta_4\}$ is the permutation of $\{i, j, k, \ell\}$ such that $\zeta_1 < \zeta_2 < \zeta_3 < \zeta_4$, and $\kappa = \text{sign}(i - j)\text{sign}(\ell - k)$. We remark that this general expression for distinct indices holds for any ordering of them. Now, in the quantum simulation, we focus on the terms such that $i > j$ and $k > l$, for which $\kappa = -1$ in our case for type (i).

Let us begin with the general case of complex coefficients $J_{ij;kl}$. The complex fermionic interaction terms with all indices distinct from each other, can be rearranged such that the interaction coefficients for spins are real. By means of the coefficient relation $J_{kl;ij} = J_{ij;kl}^*$, and the identity $\sigma^\pm = (\sigma^x \pm i\sigma^y)/2$, the corresponding spin interaction terms read

$$\begin{aligned} J_{ij;kl} c_i^\dagger c_j^\dagger c_k c_\ell + J_{kl;ij} c_k^\dagger c_\ell^\dagger c_i c_j &= \frac{\kappa}{8} \left(\prod_{\xi=\zeta_1+1}^{\zeta_2-1} \sigma_\xi^z \right) \left(\prod_{\xi=\zeta_3+1}^{\zeta_4-1} \sigma_\xi^z \right) \\ &\times \left[\text{Re}(J_{ij;kl}) (\sigma_i^x \sigma_j^x \sigma_k^x \sigma_\ell^x + \sigma_i^y \sigma_j^y \sigma_k^y \sigma_\ell^y + \sigma_i^y \sigma_j^x \sigma_k^y \sigma_\ell^x + \sigma_i^x \sigma_j^y \sigma_k^x \sigma_\ell^y \right. \\ &+ \sigma_i^y \sigma_j^x \sigma_k^x \sigma_\ell^y + \sigma_i^x \sigma_j^y \sigma_k^y \sigma_\ell^x - \sigma_i^x \sigma_j^x \sigma_k^y \sigma_\ell^y - \sigma_i^y \sigma_j^y \sigma_k^x \sigma_\ell^x) \\ &+ \text{Im}(J_{ij;kl}) (\sigma_i^y \sigma_j^x \sigma_k^x \sigma_\ell^x - \sigma_i^x \sigma_j^x \sigma_k^y \sigma_\ell^x + \sigma_i^x \sigma_j^y \sigma_k^x \sigma_\ell^x - \sigma_i^x \sigma_j^x \sigma_k^x \sigma_\ell^y \\ &+ \sigma_i^y \sigma_j^y \sigma_k^x \sigma_\ell^y - \sigma_i^x \sigma_j^y \sigma_k^y \sigma_\ell^y + \sigma_i^y \sigma_j^y \sigma_k^y \sigma_\ell^x - \sigma_i^y \sigma_j^x \sigma_k^y \sigma_\ell^y) \left. \right]. \quad (\text{E.4}) \end{aligned}$$

Notice that this relation is valid for all orderings of indices, and that for $\zeta_2 - \zeta_1 = 1$ and $\zeta_4 - \zeta_3 = 1$ the products are substituted by the identity operator. We will take into account the model rewritten in terms of $\tilde{J}_{\alpha_2\alpha_1;\beta_2\beta_1}$ for interaction terms with distinct indices. In this case, by definition, those coefficients are different from zero only

for $\alpha_2 > \alpha_1$ and $\beta_2 > \beta_1$, for which $\kappa = -1$. That is, it accounts for those interactions classified as type (i) in the text. We now want to identify a minimal set of spin interaction terms with real coefficients. We thus group type (i) complex fermionic terms by making use of the previous relation of conjugated interactions. Now, we choose a set of ordered indices $i > j > k > l$. This determines six orderings $\alpha_1\alpha_2; \beta_1\beta_2$ which respect $\alpha_2 > \alpha_1$ and $\beta_2 > \beta_1$, namely, $\{(ij; kl), (kl; ij), (ik; jl), (jl; ik), (il; jk), (jk; il)\}$. Then, keeping this choice $i > j > k > l$, we group

$$\begin{aligned}
 & \tilde{J}_{ij;kl} c_i^\dagger c_j^\dagger c_k c_\ell + \tilde{J}_{kl;ij} c_k^\dagger c_\ell^\dagger c_i c_j + \tilde{J}_{ik;jl} c_i^\dagger c_k^\dagger c_j c_\ell + \tilde{J}_{jl;ik} c_j^\dagger c_\ell^\dagger c_i c_k + \tilde{J}_{il;jk} c_i^\dagger c_\ell^\dagger c_j c_k \\
 & + \tilde{J}_{jk;il} c_j^\dagger c_k^\dagger c_i c_\ell = \frac{\kappa}{8} \left(\prod_{\xi=\zeta_1+1}^{\zeta_2-1} \sigma_\xi^z \right) \left(\prod_{\xi=\zeta_3+1}^{\zeta_4-1} \sigma_\xi^z \right) \\
 & \times \left[\text{Re}(\tilde{J}_{ij;kl} + \tilde{J}_{ik;jl} + \tilde{J}_{il;jk})(\sigma_i^x \sigma_j^x \sigma_k^x \sigma_\ell^x + \sigma_i^y \sigma_j^y \sigma_k^y \sigma_\ell^y) \right. \\
 & + \text{Re}(\tilde{J}_{ij;kl} - \tilde{J}_{ik;jl} + \tilde{J}_{il;jk})(\sigma_i^y \sigma_j^x \sigma_k^y \sigma_\ell^x + \sigma_i^x \sigma_j^y \sigma_k^x \sigma_\ell^y) \\
 & + \text{Re}(\tilde{J}_{ij;kl} + \tilde{J}_{ik;jl} - \tilde{J}_{il;jk})(\sigma_i^y \sigma_j^x \sigma_k^x \sigma_\ell^y + \sigma_i^x \sigma_j^y \sigma_k^y \sigma_\ell^x) \\
 & + \text{Re}(-\tilde{J}_{ij;kl} + \tilde{J}_{ik;jl} + \tilde{J}_{il;jk})(\sigma_i^x \sigma_j^x \sigma_k^y \sigma_\ell^y + \sigma_i^y \sigma_j^y \sigma_k^x \sigma_\ell^x) \\
 & + \text{Im}(\tilde{J}_{ij;kl} + \tilde{J}_{ik;jl} + \tilde{J}_{il;jk})(\sigma_i^y \sigma_j^x \sigma_k^x \sigma_\ell^x - \sigma_i^x \sigma_j^y \sigma_k^y \sigma_\ell^y) \\
 & + \text{Im}(\tilde{J}_{ij;kl} - \tilde{J}_{ik;jl} + \tilde{J}_{il;jk})(\sigma_i^y \sigma_j^y \sigma_k^x \sigma_\ell^y - \sigma_i^x \sigma_j^x \sigma_k^y \sigma_\ell^x) \\
 & + \text{Im}(\tilde{J}_{ij;kl} + \tilde{J}_{ik;jl} - \tilde{J}_{il;jk})(\sigma_i^y \sigma_j^y \sigma_k^y \sigma_\ell^x - \sigma_i^x \sigma_j^x \sigma_k^x \sigma_\ell^y) \\
 & \left. + \text{Im}(-\tilde{J}_{ij;kl} + \tilde{J}_{ik;jl} + \tilde{J}_{il;jk})(\sigma_i^y \sigma_j^x \sigma_k^y \sigma_\ell^y - \sigma_i^x \sigma_j^y \sigma_k^x \sigma_\ell^x) \right] \\
 & = \frac{\kappa}{8} \left(\prod_{\xi=\zeta_1+1}^{\zeta_2-1} \sigma_\xi^z \right) \left(\prod_{\xi=\zeta_3+1}^{\zeta_4-1} \sigma_\xi^z \right) \\
 & \times \left[\text{Re}(J_{ij;kl}^1)(\sigma_i^x \sigma_j^x \sigma_k^x \sigma_\ell^x + \sigma_i^y \sigma_j^y \sigma_k^y \sigma_\ell^y) + \text{Re}(J_{ij;kl}^2)(\sigma_i^y \sigma_j^x \sigma_k^y \sigma_\ell^x + \sigma_i^x \sigma_j^y \sigma_k^x \sigma_\ell^y) \right. \\
 & + \text{Re}(J_{ij;kl}^3)(\sigma_i^y \sigma_j^x \sigma_k^x \sigma_\ell^y + \sigma_i^x \sigma_j^y \sigma_k^y \sigma_\ell^x) + \text{Re}(J_{ij;kl}^4)(\sigma_i^x \sigma_j^x \sigma_k^y \sigma_\ell^y + \sigma_i^y \sigma_j^y \sigma_k^x \sigma_\ell^x) \\
 & + \text{Im}(J_{ij;kl}^1)(\sigma_i^y \sigma_j^x \sigma_k^x \sigma_\ell^x - \sigma_i^x \sigma_j^y \sigma_k^y \sigma_\ell^y) + \text{Im}(J_{ij;kl}^2)(\sigma_i^y \sigma_j^y \sigma_k^x \sigma_\ell^y - \sigma_i^x \sigma_j^x \sigma_k^y \sigma_\ell^x) \\
 & \left. + \text{Im}(J_{ij;kl}^3)(\sigma_i^y \sigma_j^y \sigma_k^y \sigma_\ell^x - \sigma_i^x \sigma_j^x \sigma_k^x \sigma_\ell^y) + \text{Im}(J_{ij;kl}^4)(\sigma_i^y \sigma_j^x \sigma_k^y \sigma_\ell^y - \sigma_i^x \sigma_j^y \sigma_k^x \sigma_\ell^x) \right]. \tag{E.5}
 \end{aligned}$$

In principle, we have mapped fermionic interaction terms with 6 independent real coefficients in terms of spin interaction terms with 8 real coefficients. We have preferred to minimize the number of spin interactions, even if it implies using the dependent coefficients $J_{ij;k\ell}^a$ with $a = 1, 2, 3, 4$ defined previously.

For interaction terms of type (ii), we do not impose the constraints $i > j$ and $k > l$, as can be seen in the classification. The complex interaction terms can be also reordered such that the interaction coefficients for spins are real,

$$J_{ij;jk}c_i^\dagger c_j^\dagger c_j c_k + J_{jk;ij}c_j^\dagger c_k^\dagger c_i c_j = -\frac{1}{4} \left(\prod_{\xi=\zeta_1+1}^{\zeta_2-1} \sigma_\xi^z \right) (\sigma_j^z + 1) \times \left[\text{Re}(J_{ij;jk})(\sigma_i^x \sigma_k^x + \sigma_i^y \sigma_k^y) + \text{Im}(J_{ij;jk})(\sigma_i^x \sigma_k^y - \sigma_i^y \sigma_k^x) \right]. \quad (\text{E.6})$$

We note that interactions (iii) and (iv) can be grouped as follows

$$4J_{ij;ji}n_i n_j + \frac{\mu}{n-1}n_i + \frac{\mu}{n-1}n_j = \left(J_{ij;ji} + \frac{\mu}{2(n-1)} \right) (2 + \sigma_i^z + \sigma_j^z) + J_{ij;ji}\sigma_i^z \sigma_j^z, \quad (\text{E.7})$$

so that we only take into account the interaction terms of type (iii) in the counting, where $J_{ij;ji}$ must be real because of the symmetries.

We show the counting of complex fermionic interaction terms in Table E.3, and the corresponding spin interactions in Table E.4.

Table E.3: Complex fermionic interaction terms.

Fermionic interaction	Number of terms
$J_{ij;k\ell}c_i^\dagger c_j^\dagger c_k c_\ell + J_{k\ell;ij}c_k^\dagger c_\ell^\dagger c_i c_j$	$\frac{1}{2} \binom{n}{2} \binom{n-2}{2} = \frac{1}{8}n^4 - \frac{3}{4}n^3 + \frac{11}{8}n^2 - \frac{3}{4}n$
$J_{ij;jk}c_i^\dagger n_j c_k + J_{jk;ij}c_k^\dagger n_j c_i$	$\frac{1}{2}n^3 - \frac{3}{2}n^2 + n$
$n_i n_j$	$\frac{1}{2}n^2 - \frac{1}{2}n$

Table E.4: Complex fermionic interaction terms and their corresponding spin interaction translation.

Spin interaction	Number of spin terms
$\left(\prod_{\xi=\zeta_1+1}^{\zeta_2-1} \sigma_\xi^z \right) \left(\prod_{\xi=\zeta_3+1}^{\zeta_4-1} \sigma_\xi^z \right) \sigma_i^{\alpha_i} \sigma_j^{\alpha_j} \sigma_k^{\alpha_k} \sigma_l^{\alpha_l}$	$\frac{16}{6} \binom{n}{2} \binom{n-2}{2} = \frac{2}{3}n^4 - 4n^3 + \frac{22}{3}n^2 - 4n$
$\left(\prod_{\xi=\zeta_1+1}^{\zeta_2-1} \sigma_\xi^z \right) (\sigma_j^z + 1) \sigma_i^{\alpha_i} \sigma_k^{\alpha_k}$	$\frac{4}{2} \frac{n!}{(n-3)!} = 2n^3 - 6n^2 + 4n$
$\sigma_i^z + \sigma_j^z + \sigma_i^z \sigma_j^z$	$\binom{n}{2} = \frac{1}{2}n^2 - \frac{1}{2}n$

E.2 Details on the protocols of the quantum algorithm

E.2.1 Protocol for correlation measurements

We particularize the efficient protocol for determining n -time correlation functions introduced in [118] for the case of the dynamics of scrambling. In this method, valid for both analog and digital quantum simulations, an ancillary qubit Q_A encodes a correlation function by means of controlled operations.

Let us consider a set of unitaries $\{V_i\}_{i=0}^n$ acting on the system. We aim at computing the correlation function $\langle V_n(t_n)V_{n-1}(t_{n-1}) \cdots V_1(t_1)V_0(0) \rangle$. Let us assume that we know how to implement in the laboratory the unitaries $\tilde{V}_i = |0\rangle\langle 0|_A I + |1\rangle\langle 1|_A V_i$, which act on the ancilla and the system. The ancilla Q_A and the system evolve with $I_A U(t)$, where $U(t)$ is the unitary evolution operator for the system S . We consider now the following protocol.

1. Prepare the system in the state of interest, $|\Psi\rangle$, and the ancilla in the state $(|0\rangle + |1\rangle)/\sqrt{2}$. Set counter k to 0. Define $t_0 = 0$.
2. Apply the controlled unitary \tilde{V}_k .
3. Evolve a time $t_{k+1} - t_k$.
4. If $k < n$, then advance k by 1 and go to step b). Else, measure σ_x and σ_y of the ancilla Q_A , which completes the protocol.

This leads to the desired measurement of the n -time correlation function

$$\frac{1}{2} (\langle \sigma_x \rangle + i \langle \sigma_y \rangle) = \frac{1}{2} \langle V_n(t_n) V_{n-1}(t_{n-1}) \cdots V_1(t_1) V_0(0) \rangle. \quad (\text{E.8})$$

For the particular case of the scrambling four-point correlation function

$$\langle W_S^\dagger(t) V_S^\dagger(0) W_S(t) V_S(0) \rangle,$$

the set of unitaries to be considered in the protocol is $\{W_S^\dagger, V_S^\dagger, W_S, V_S\}$, with corresponding times $t_1 = t$, $t_2 = 0$, and $t_3 = t$. Note that in order to evolve the system one requires time inversion, since $t_2 < t_1$, for which case the protocol introduced previously can be used.

E.2.2 Protocol for time inversion

Time inversion for the SYK models described in section 3.2 can be engineered by considering an additional ancilla qubit Q_C , without explicitly constructing a time-evolution operator $U(-t)$. We consider an additional ancilla qubit Q_C , which controls the direction of the SYK time evolution allowing us to implement both $U(t)$ and

$U(-t)$ time-evolution operators. The evolution for the pair controlling ancilla and system is governed by the Hamiltonian $H_{CS} = \sigma_C^z H_S$, where σ_C^z acts on the ancilla qubit, and H_S is the system Hamiltonian. The complete Hamiltonian consists in a tensor that acts on the ancilla-system product state as

$$\begin{aligned} H_{CS}(\alpha|e\rangle + \beta|g\rangle)|\psi\rangle &= \sigma_C^z(\alpha|e\rangle + \beta|g\rangle)H_S|\psi\rangle \\ &= \alpha|e\rangle H_S|\psi\rangle - \beta|g\rangle H_S|\psi\rangle, \end{aligned} \quad (\text{E.9})$$

with $\alpha|e\rangle + \beta|g\rangle$ and $|\psi\rangle$ the ancilla and system states, respectively. In general, one may consider n applications of the Hamiltonian

$$\begin{aligned} H_{CS}^n(\alpha|e\rangle + \beta|g\rangle)|\psi\rangle &= (\sigma_C^z)^n(\alpha|e\rangle + \beta|g\rangle)H_S^n|\psi\rangle \\ &= \alpha|e\rangle H_S^n|\psi\rangle + \beta|g\rangle (-1)^n H_S^n|\psi\rangle, \end{aligned} \quad (\text{E.10})$$

which leads to a time evolution for an initial product state $|\Psi\rangle = (\alpha|e\rangle + \beta|g\rangle)|\psi\rangle$ described by

$$\begin{aligned} U_{CS}(t)|\Psi\rangle &= \exp(-iH_{CS}t)|\Psi\rangle = \sum_n \frac{(-iH_{CS}t)^n}{n!} |\Psi\rangle \\ &= \alpha|e\rangle \sum_n \frac{(-iH_S t)^n}{n!} |\psi\rangle + \beta|g\rangle \sum_n \frac{(-1)^n (-iH_S t)^n}{n!} |\psi\rangle \\ &= \alpha|e\rangle U(t)|\psi\rangle + \beta|g\rangle U(-t)|\psi\rangle. \end{aligned} \quad (\text{E.11})$$

Here, the controlling ancilla qubit decides the direction of the evolution. The scrambling four-point function for operators $V_S \hat{A} \check{A}$ and W_S is thus computable by the sequence

$$\sigma_C^x U_{CS}(t) \sigma_C^x W_S^\dagger U_{CS}(t) V_S^\dagger \sigma_C^x U_{CS}(t) \sigma_C^x W_S U_{CS}(t) V_S \quad (\text{E.12})$$

and its expectation value over the state $|e\rangle \otimes |\psi\rangle$. We notice that operators labeled by S , all of them feasible in our proposed scheme, are only applied to the system S .

E.2.3 Protocol for state initialization

The initialization of the system in explicitly known initial states relies in the application of certain local operations. In order to do that, one uses again the JW transformation to encode fermionic states in qubit states. Let us now give some examples.

In the case of the spinless complex fermions, the mapping $c_i^\dagger = (\prod_{j=1}^{i-1} \sigma_j^z) \sigma_i^+$ indicates that the fermionic state with zero excitations, $|\vec{0}\rangle$, corresponds to the product state of all the qubits in their ground state, $|g_1, \dots, g_n\rangle$, since

$$c_i |\vec{0}\rangle = \sigma_i^- \left(\prod_{j=1}^{i-1} \sigma_j^z \right) |\vec{0}\rangle = 0 \quad \forall i \Leftrightarrow |\vec{0}\rangle = |g_1, \dots, g_n\rangle. \quad (\text{E.13})$$

Once this identification is known, one may consider the action of a set of creation fermionic operators on $|\vec{0}\rangle$ by acting with their spin correspondents on $|g_1, \dots, g_n\rangle$. This way, a state with a certain number of excitations in localized fermionic sites can be constructed. In particular, the zero fermion excitation state above, which is a maximal total spin one.

E.2.4 Details on Mølmer–Sørensen gates

The entangling gate $U_{lj}(\phi)$ between two distant qubits in trapped ions can be achieved via a global MS gate and individual operations. All qubits but qubits l and j can be decoupled by electronic shelving [90] or AC-Stark shifts [209], so that the entangling operation only affects the desired qubits l and j . The first method uses suitable laser pulses to transfer the population of the qubits to electronic states insensitive to the entangling operation. The second consists in modifying the qubit transition frequency with off-resonant lasers, with the same effect.

The gate proposed in section 3.3 is developed as

$$\begin{aligned}
 U &= U_{\text{MS}}^A(-\frac{\pi}{2}, 0) U_{\text{MS}}^B(-\frac{\pi}{2}, 0) U_{lj}(\phi) U_{\text{MS}}^B(\frac{\pi}{2}, 0) U_{\text{MS}}^A(\frac{\pi}{2}, 0) \\
 &= \exp \left[i\phi \left(\cos\left(\frac{\pi}{2}s_A^x\right) \cos\left(\frac{\pi}{2}s_B^x\right) \sigma_l^\alpha \sigma_j^\beta \right. \right. \\
 &\quad + \cos\left(\frac{\pi}{2}s_A^x\right) \sin\left(\frac{\pi}{2}s_B^x\right) \epsilon_{x\delta\beta} \sigma_l^\alpha \sigma_j^\delta \\
 &\quad + \sin\left(\frac{\pi}{2}s_A^x\right) \cos\left(\frac{\pi}{2}s_B^x\right) \epsilon_{x\gamma\alpha} \sigma_l^\gamma \sigma_j^\beta \\
 &\quad \left. \left. + \sin\left(\frac{\pi}{2}s_A^x\right) \sin\left(\frac{\pi}{2}s_B^x\right) \epsilon_{x\beta\delta} \epsilon_{x\alpha\gamma} \sigma_l^\gamma \sigma_j^\delta \right) \right], \tag{E.14}
 \end{aligned}$$

with $s_A^x = \sum_{i=l+1}^{l+M} \sigma_i^x$, $s_B^x = \sum_{i=j+1}^{j+K} \sigma_i^x$, and $\epsilon_{\alpha\beta\gamma}$ the Levi–Civita symbol. For a generic operator $s^x = \sum_{i=1}^n \sigma_i^x$ acting on n qubits, we now take into account the identities

$$\cos\left(\frac{\pi}{2}s^x\right) = \begin{cases} -\prod_{i=1}^n \sigma_i^x & \text{for } n = 4k - 2, k \in \mathbb{N}, \\ \prod_{i=1}^n \sigma_i^x & \text{for } n = 4k, k \in \mathbb{N}, \\ 0 & \text{for } n \text{ odd,} \end{cases} \tag{E.15}$$

and

$$\sin\left(\frac{\pi}{2}s^x\right) = \begin{cases} \prod_{i=1}^n \sigma_i^x & \text{for } n = 4k - 3, k \in \mathbb{N}, \\ -\prod_{i=1}^n \sigma_i^x & \text{for } n = 4k - 1, k \in \mathbb{N}, \\ 0 & \text{for } n \text{ even,} \end{cases} \tag{E.16}$$

leading to the result presented in section 3.3.

F Details on the QFT model

We start from the following family of interaction Hamiltonians in 1 + 1 dimensions,

$$H_{\text{int}} = \int dx \psi^\dagger(x)\psi(x) \int \frac{dk}{\sqrt{2\pi}} \frac{\tilde{\lambda}_k}{\sqrt{2\omega_k}} \left(A_k e^{ikx} + A_k^\dagger e^{-ikx} \right), \quad (\text{F.1})$$

where $A_k^\dagger (A_k)$ is a bosonic creation(annihilation) operator with the canonical commutation relation $[A_k, A_{k'}^\dagger] = \delta(k - k')$, and $\tilde{\lambda}_k$ is a k -dependent coupling constant. Note that this could be equivalently written, using the unitary transformation $A_k^\dagger \rightarrow ia_k^\dagger (A_k \rightarrow -ia_k)$ and the redefinition $\tilde{\lambda}_k/\sqrt{\omega_k} \rightarrow \lambda_k\sqrt{\omega_k}$, as a coupling with a bosonic field with the following form

$$A(x) = \frac{i}{\sqrt{2\pi}} \int dk \lambda_k \sqrt{\frac{\omega_k}{2}} \left(a_k^\dagger e^{-ikx} - a_k e^{ikx} \right). \quad (\text{F.2})$$

In our simulation, we will use this definition for the bosonic field A , which is motivated by the specific transmon implementation that we consider. This is not a restriction and we may use a model with coupling constant $\tilde{\lambda}_k/\sqrt{\omega_k}$ by considering a flux qubit instead.

In 1 + 1 dimensions, scalar fermionic fields are written as

$$\psi(x) = \frac{1}{\sqrt{2\pi}} \int \frac{dp}{\sqrt{2\omega_p}} \left(b_p e^{ipx} + d_p^\dagger e^{-ipx} \right), \quad (\text{F.3})$$

where the operator $b_p^\dagger(d_p^\dagger)$ that creates fermionic particles(antiparticles) satisfies the anticommutation rules $\{b_p, b_{p'}^\dagger\} = \delta(p - p')$ and $\{d_p, d_{p'}^\dagger\} = \delta(p - p')$.

The scalability of this simplified model will be discussed in the last section. In particular, we will consider the possibility of including spinors in the treatment of the fermionic fields in the simulation.

F.1 Discretization and comoving modes

For the purpose of analyzing an interacting theory that may describe fermion-fermion scattering, pair creation, dressed states, and non-perturbative regimes, we introduce comoving fermionic and antifermionic modes. The j th input comoving modes are defined in the Schrödinger picture as follows [139]

$$b_{\text{in}}^{\dagger(j)} = \int dp \Omega_{f_f}^{(j)}(p_f^{(j)}, p) b_p^\dagger e^{-i\omega_p t} \quad (\text{F.4})$$

$$d_{\text{in}}^{\dagger(j)} = \int dp \Omega_{f_{\bar{f}}}^{(j)}(p_{\bar{f}}^{(j)}, p) d_p^\dagger e^{-i\omega_p t}, \quad (\text{F.5})$$

where $\Omega_{f, \bar{f}}^{(j)}(p_{f, \bar{f}}^{(j)}, p)$ are the j th fermionic and antifermionic envelopes centered in the momenta p_f and $p_{\bar{f}}$, respectively. These modes create normalizable propagating wave packets when applied to the vacuum which are suitable for describing physical particles, unlike the standard momentum eigenstates which are delocalized over all space. For our purposes we restrict ourselves to orthonormal envelope functions $\Omega_{f, \bar{f}}^{(j)}(p_{f, \bar{f}}^{(j)}, p)$, such that the comoving modes satisfy, at equal times, the anti-commutation relations $\{b_{\text{in}}^{(i)}, b_{\text{in}}^{\dagger(j)}\} = \delta_{ij}$.

The implementation of the Hamiltonian in Eq. (F.1) in a superconducting circuit setup appears to be a hard problem because it contains an infinite number of both bosonic and fermionic modes. We are able to mimic the former by using the continuum of bosonic modes appearing in transmission lines or low-quality resonators. In order to deal with the latter, we consider the field (F.3) as composed of a discrete, truncated set of comoving modes. That is, we expand the field $\psi(x)$ in terms of two of these new anticommuting modes as a first order approximation, neglecting the remaining anticommuting modes. Thus, the fermionic field reads

$$\psi(x) \simeq \Lambda_1(p_f^{(1)}, x, t) b_{\text{in}}^{(1)} + \Lambda_2(p_{\bar{f}}^{(1)}, x, t) d_{\text{in}}^{\dagger(1)}, \quad (\text{F.6})$$

where the coefficients can be computed by considering the anticommutators $\{\psi(x), b_{\text{in}}^{\dagger(1)}\}$

and $\{\psi(x), d_{\text{in}}^{(1)}\}$ as follows

$$\Lambda_1(p_f^{(1)}, x, t) = \{\psi(x), b_{\text{in}}^{\dagger(1)}\} = \frac{1}{\sqrt{2\pi}} \int \frac{dp}{\sqrt{2\omega_p}} \Omega^{(1)}(p_f^{(1)}, p) e^{i(px - \omega_p t)}, \quad (\text{F.7})$$

$$\Lambda_2(p_{\bar{f}}^{(1)}, x, t) = \{\psi(x), d_{\text{in}}^{(1)}\} = \frac{1}{\sqrt{2\pi}} \int \frac{dp}{\sqrt{2\omega_p}} \Omega^{(1)}(p_{\bar{f}}^{(1)}, p) e^{-i(px - \omega_p t)}, \quad (\text{F.8})$$

where we have considered $\psi(x)$ in the Schrödinger picture. Henceforth, we shall omit the index (1) since we only consider two creation operators.

F.2 Hamiltonian in the Schrödinger picture

The Hamiltonian associated with the proposed QFT model can be rewritten in the light of the previous assumptions. Substituting the expressions for the bosonic and fermionic fields of Eqs. (F.2) and (F.6), respectively, into the interaction Hamiltonian of Eq. (F.1) yields

$$\begin{aligned} H_{\text{int}} = & i \int dx dk \lambda_k \sqrt{\frac{\omega_k}{2}} \left(|\Lambda_1(p_f, x, t)|^2 b_{\text{in}}^{\dagger} b_{\text{in}} + \Lambda_1^*(p_f, x, t) \Lambda_2(p_{\bar{f}}, x, t) b_{\text{in}}^{\dagger} d_{\text{in}}^{\dagger} \right. \\ & \left. + \Lambda_2^*(p_{\bar{f}}, x, t) \Lambda_1(p_f, x, t) d_{\text{in}} b_{\text{in}} + |\Lambda_2(p_{\bar{f}}, x, t)|^2 d_{\text{in}} d_{\text{in}}^{\dagger} \right) \left(a_k^{\dagger} e^{-ikx} - a_k e^{ikx} \right). \end{aligned} \quad (\text{F.9})$$

In order to connect eventually with the circuit simulator, it will prove convenient to use now the JW transformation, that relates the four fermionic operators with tensor products of Pauli matrices, $b_{\text{in}}^{\dagger} = \sigma_1^-$, $b_{\text{in}} = \sigma_1^+$, $d_{\text{in}}^{\dagger} = \sigma_2^- \sigma_1^z$, $d_{\text{in}} = \sigma_2^+ \sigma_1^z$, and $\sigma^{\pm} = \frac{1}{2}(\sigma^x \pm i\sigma^y)$. Thus, the interaction term of the Hamiltonian in the Schrödinger picture can be expressed as

$$\begin{aligned} H_{\text{int}} = & i \int dx dk \lambda_k \sqrt{\frac{\omega_k}{2}} \left(a_k^{\dagger} e^{-ikx} - a_k e^{ikx} \right) \\ & \times \left(\frac{|\Lambda_1(p_f, x, t)|^2 + |\Lambda_2(p_{\bar{f}}, x, t)|^2}{2} \mathbb{1} - \frac{|\Lambda_1(p_f, x, t)|^2}{2} \sigma_1^z + \frac{|\Lambda_2(p_{\bar{f}}, x, t)|^2}{2} \sigma_2^z \right. \\ & + \frac{1}{2} \text{Re}(\Lambda_1^*(p_f, x, t) \Lambda_2(p_{\bar{f}}, x, t)) (\sigma_2^x \sigma_1^x - \sigma_2^y \sigma_1^y) \\ & \left. + \frac{1}{2} \text{Im}(\Lambda_1^*(p_f, x, t) \Lambda_2(p_{\bar{f}}, x, t)) (\sigma_2^y \sigma_1^x + \sigma_2^x \sigma_1^y) \right). \end{aligned} \quad (\text{F.10})$$

G Details on the DAQS for QFT

This appendix contains further considerations on the superconducting circuit model, and the scalability of the quantum simulation protocol.

G.1 Details on the superconducting circuit model

The superconducting circuit of our proposal consists of an open transmission line coupled to three tunable coupling transmon qubits [149] and three resonators. One of the resonators couples to two transmon qubits, while the other two are used for individual addressing/readout of these transmons. The Lagrangian describing the system

of a single transmon coupled to the open transmission line and one resonator [210] is

$$\begin{aligned}
 L = & \frac{C_r}{2} \dot{\phi}_r^2 - \frac{1}{2L_r} \phi_r^2 + \int dx \left(\frac{c_{tl}}{2} \dot{\phi}_{tl}^2(x, t) - \frac{1}{2l_{tl}} \phi_{tl}^2(x, t) \right) \\
 & + \frac{C_{c1}}{2} (\dot{\phi}_r - \dot{\phi}_+)^2 + \frac{C_{g+}}{2} (\dot{\phi}_+ - V_{g+} - \dot{\phi}_-)^2 + \frac{C_{g-}}{2} (\dot{\phi}_- - V_{g-})^2 \\
 & + \frac{C_I}{2} \dot{\phi}_+^2 + \frac{C_+}{2} (\dot{\phi}_+ - \dot{\phi}_-)^2 + \frac{C_-}{2} \dot{\phi}_-^2 + \frac{C_{c2}}{2} (\dot{\phi}_{tl}(x_j, t) - \dot{\phi}_-)^2 \\
 & + E_{J+} \cos\left(\frac{\phi_+ - \phi_-}{\Phi_0}\right) + E_{J-} \cos\left(\frac{\phi_-}{\Phi_0}\right). \tag{G.1}
 \end{aligned}$$

Here, ϕ_r , ϕ_{tl} , ϕ_+ , and ϕ_- are the node variables depicted in Fig. G.1, associated with the resonator, the open transmission line, the upper island, and the center island, respectively. Additionally, Φ_0 is the flux quantum, C_r and L_r are the capacitance and inductance of the resonator, c_{tl} and l_{tl} , the capacitance and inductance per unit length of the open transmission line. Finally, C_{c1} and C_{c2} represent the capacitive coupling of the tunable qubit and the resonator and transmission line, respectively.

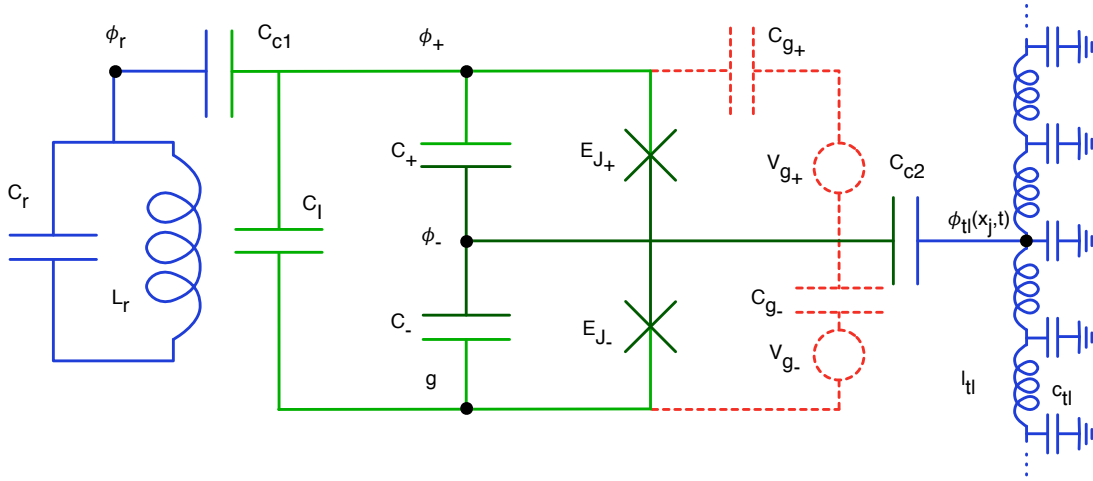


Figure G.1: **Tunable transmon qubit coupled to resonator and transmission line.** Effective circuit diagram of a tunable transmon qubit [149] coupled to a resonator and a transmission line via the upper (+) and center (-) islands, respectively.

The Hamiltonian of the system is given by $H = H_T + H_{\text{res}} + H_{\text{tl}} + H_{\text{int}}$, where the terms correspond to the transmon, the resonator, the transmission line and the interaction among them, respectively. By the following choice of variables, $\gamma_+ = \phi_+ - \phi_-$ and $\gamma_- = \phi_-$, the transmon is described as

$$H_T = 4E_{C_+} (n_+ - n_{g+})^2 + 4E_{C_-} (n_- - n_{g-})^2 + 4E_I n_+ n_-, \tag{G.2}$$

with charging energies

$$E_{C_+} = \frac{e^2}{2M} [C_{c2}C_{tl}(C_{c1} + C_r) - \alpha_-],$$

$$E_{C_-} = -\frac{e^2}{2M}\alpha_+,$$

dimensionless gate voltages

$$n_{g_+} = \frac{1}{2e} \left(C_{g_+}V_{g_+} + C_{g_-}V_{g_-} \frac{\alpha_I}{\alpha_- - C_{c2}C_{tl}(C_{c1} + C_r)} \right),$$

$$n_{g_-} = \frac{1}{2e} \left(C_{g_-}V_{g_-} + C_{g_+}V_{g_+} \frac{\alpha_I}{\alpha_+} \right),$$

and interaction energy

$$E_I = -\frac{e^2}{M}\alpha_I,$$

with

$$\alpha_{\pm} = (C_{c2} + C_{tl})(C_{c1}^2 - C_{c1}C_{\Sigma_{\pm}} - C_rC_{\Sigma_{\pm}}),$$

$$\alpha_I = (C_{c2} + C_{tl})(C_{c1}C_I + C_{c1}C_r + C_IC_r),$$

$$M = \alpha_+ \left(\frac{C_{c2}^2}{C_{c2} + C_{tl}} - C_{c2} + C_{c1} - C_{\Sigma_-} \right) - \alpha_I(C_I + C_{c1})$$

$$+ C_{c1}(C_{c2} + C_{tl})(C_rC_{\Sigma_+} + C_{c1}C_I),$$

$$C_{\Sigma_{\pm}} = C_{c1} + C_{g_{\pm}} + C_I + C_{\pm},$$

$$C_{tl} = \int c_{tl} dx.$$

The transmission line and resonator Hamiltonians may be written in terms of creation and annihilation operators as

$$H_{tl} = \int dk \omega_k a_k^{\dagger} a_k,$$

$$H_{res} = \omega_r b^{\dagger} b, \tag{G.3}$$

where $a_k^{\dagger}(a_k)$ and ω_k are the creation(annihilation) operator and the frequency associated with the k th mode of the open transmission line, respectively. In addition, b and b^{\dagger} annihilate and create excitations of frequency ω_r in the resonator. We use the same notation of a_k^{\dagger} and a_k to describe the QFT model and the superconducting circuit proposal.

The interaction Hamiltonian reads

$$H_I = 2eC_r \sqrt{\frac{\omega_r}{2C_r}} i(b^{\dagger} - b)(\beta_+ n_+ + \beta_- n_-)$$

$$+ 2eC_{tl}(\lambda_+ n_+ + \lambda_- n_-) i \int dk \sqrt{\frac{\omega_k}{4\pi c_{tl}}} (a_k^{\dagger} e^{-ikx_j} - a_k e^{ikx_j}), \tag{G.4}$$

where the coefficients are

$$\begin{aligned}\beta_+ &= -\frac{C_{c1}(C_{c2} + C_{tl})(C_{c1} + C_I - C_{\Sigma_-}) - C_{c1}C_{c2}C_{tl}}{M}, \\ \beta_- &= -\frac{C_{c1}(C_{c2} + C_{tl})(C_{c1} + C_I - C_{\Sigma_+})}{M}, \\ \lambda_+ &= -\frac{C_{c2}\alpha_I}{M(C_{c2} + C_{tl})}, \\ \lambda_- &= -\frac{C_{c2}\alpha_+}{M(C_{c2} + C_{tl})}.\end{aligned}$$

In this Hamiltonian, a coupling between the resonator and the open transmission line has been neglected due to its small value compared to the rest of the interactions.

The coupling energy between the qubit and the resonator is given by

$$2eC_r\sqrt{\frac{\omega_r}{2C_r}}\langle i|(\beta_+n_+ + \beta_-n_-)|j\rangle, \quad (\text{G.5})$$

while the coupling with the transmission line depends on the frequency and is proportional to

$$\sqrt{\omega_k}\langle i|(\lambda_+n_+ + \lambda_-n_-)|j\rangle. \quad (\text{G.6})$$

The Hamiltonian of Eq. (G.4) can be expressed in terms of Pauli matrices if we truncate the Hilbert space of the transmon to the two lowest eigenvalues. We are able to perform this approximation due to the anharmonicity of the energy distribution, in which the pair of lowest states may be discriminated from the others.

Hence, the interaction Hamiltonian in Eq. (G.4) can be written in terms of Pauli matrices in the following general form

$$\begin{aligned}H_{\text{int}} &= i\sum_{j=1}^3\sigma_j^y\int dk\beta(\Phi_{\text{ext}}^j, \bar{\Phi}_{\text{ext}}^j)g_k(a_k^\dagger e^{-ikx_j} - a_k e^{ikx_j}) \\ &\quad + i\sum_{j=1}^2\alpha(\Phi_{\text{ext}}^j, \bar{\Phi}_{\text{ext}}^j)g_j\sigma_j^y(b^\dagger - b),\end{aligned} \quad (\text{G.7})$$

where σ_0 stands for the identity operator, σ_j with $j = 1, 2, 3$ correspond to the Pauli matrices, and $g_k = \sqrt{\omega_k}$.

G.2 Higher dimensions and scalability issues

In order to access a full-fledged QFT, we need to take into account spinors in the fermionic field, polarizations in the bosonic field, and other couplings in the QFT

side, for instance, $\bar{\psi}\psi\phi$, $\bar{\psi}\gamma^\mu\psi A_\mu$, etc. To achieve this, we add more qubits between the resonator and the open transmission line. In this case, an analogous mapping between the fermionic operators and tensor products of Pauli matrices is encoded via the N -mode JW transformation

$$\begin{aligned} b_l^\dagger &= \sigma_l^- \sigma_{l-1}^z \dots \sigma_1^z, \\ d_m^\dagger &= \sigma_m^- \sigma_{m-1}^z \dots \sigma_1^z, \end{aligned} \tag{G.8}$$

where $l = 1, 2, \dots, N/2$, $m = N/2 + 1, \dots, N$, with N the total number of fermion plus antifermion modes. Since fermionic couplings will appear through bilinears, this encoding will encompass all usual cases. The consideration of bosonic fields beyond one single scalar field may be implemented by the use of multiple open transmission lines.

Bibliography

- [1] A. M. Turing, “*On Computable Numbers, with an Application to the Entscheidungsproblem*”, [Proceedings of the London Mathematical Society](#) **s2-42**, 230–265 (1937).
- [2] K. Gödel, “*Über formal unentscheidbare Sätze der Principia Mathematica und verwandter Systeme I*”, [Monatshefte für Mathematik und Physik](#) **38**, 173–198 (1931).
- [3] S. Arora and B. Barak, *Computational Complexity: A Modern Approach*. Cambridge University Press, New York, NY, USA, 1st ed., 2009.
- [4] G. Vidal, “*Efficient Classical Simulation of Slightly Entangled Quantum Computations*”, [Phys. Rev. Lett.](#) **91**, 147902 (2003).
- [5] G. Vidal, “*Efficient Simulation of One-Dimensional Quantum Many-Body Systems*”, [Phys. Rev. Lett.](#) **93**, 040502 (2004).
- [6] F. Verstraete, V. Murg, and J. Cirac, “*Matrix product states, projected entangled pair states, and variational renormalization group methods for quantum spin systems*”, [Advances in Physics](#) **57**, 143-224 (2008).

-
- [7] J. I. Cirac and F. Verstraete, “Renormalization and tensor product states in spin chains and lattices”, *Journal of Physics A: Mathematical and Theoretical* **42**, 504004 (2009).
- [8] U. Schollwöck, “The density-matrix renormalization group in the age of matrix product states”, *Annals of Physics* **326**, 96–192 (2011).
- [9] A. Georges, G. Kotliar, W. Krauth, and M. J. Rozenberg, “Dynamical mean-field theory of strongly correlated fermion systems and the limit of infinite dimensions”, *Rev. Mod. Phys.* **68**, 13–125 (1996).
- [10] W. M. C. Foulkes, L. Mitas, R. J. Needs, and G. Rajagopal, “Quantum Monte Carlo simulations of solids”, *Rev. Mod. Phys.* **73**, 33–83 (2001).
- [11] A. N. Rubtsov, V. V. Savkin, and A. I. Lichtenstein, “Continuous-time quantum Monte Carlo method for fermions”, *Phys. Rev. B* **72**, 035122 (2005).
- [12] M. Troyer and U.-J. Wiese, “Computational Complexity and Fundamental Limitations to Fermionic Quantum Monte Carlo Simulations”, *Phys. Rev. Lett.* **94**, 170201 (2005).
- [13] N. F. Mott, “Metal-insulator transition”, *Rev. Mod. Phys.* **40**, 677–683 (1968).
- [14] M. Imada, A. Fujimori, and Y. Tokura, “Metal-insulator transitions”, *Rev. Mod. Phys.* **70**, 1039–1263 (1998).
- [15] P. A. Lee, N. Nagaosa, and X.-G. Wen, “Doping a Mott insulator: Physics of high-temperature superconductivity”, *Rev. Mod. Phys.* **78**, 17–85 (2006).
- [16] J. R. Schrieffer and J. S. Brooks, eds., *Handbook of High-Temperature Superconductivity*. Springer New York, New York, 2007.
- [17] A. P. Ramirez, “Colossal magnetoresistance”, *Journal of Physics: Condensed Matter* **9**, 8171 (1997).
- [18] R. P. Feynman, “Simulating physics with computers”, *Int. J. Theor. Phys.* **21**, 467–488 (1982).
- [19] M. A. Nielsen and I. L. Chuang, *Quantum Computation and Quantum Information*. Cambridge University Press, 2000.
- [20] P. W. Shor, “Polynomial-Time Algorithms for Prime Factorization and Discrete Logarithms on a Quantum Computer”, *SIAM Journal on Computing* **26**, 1484–1509 (1997).
- [21] S. Boixo, S. V. Isakov, V. N. Smelyanskiy, R. Babbush, N. Ding, Z. Jiang, M. J. Bremner, J. M. Martinis, and H. Neven, “Characterizing Quantum Supremacy in Near-Term Devices”, [arXiv:1608.00263](https://arxiv.org/abs/1608.00263) (2016).
- [22] S. Lloyd, “Universal Quantum Simulators”, *Science* **273**, 1073–1078 (1996).

-
- [23] M. H. Devoret and R. J. Schoelkopf, “*Superconducting Circuits for Quantum Information: An Outlook*”, *Science* **339**, 1169–1174 (2013).
- [24] B. J. Copeland, ed., *The Essential Turing*. Oxford University Press, 2004.
- [25] L. Hormozi, E. W. Brown, G. Carleo, and M. Troyer, “*Nonstoquastic Hamiltonians and quantum annealing of an Ising spin glass*”, *Phys. Rev. B* **95**, 184416 (2017).
- [26] A. F. van Loo, A. Fedorov, K. Lalumière, B. C. Sanders, A. Blais, and A. Wallraff, “*Photon-Mediated Interactions Between Distant Artificial Atoms*”, *Science* **342**, 1494–1496 (2013).
- [27] S. Aaronson and A. Arkhipov, “*The Computational Complexity of Linear Optics*”, in *Proceedings of the Forty-third Annual ACM Symposium on Theory of Computing*, STOC '11, pp. 333–342. ACM, New York, NY, USA, 2011.
- [28] N. Lashkari, D. Stanford, M. Hastings, T. Osborne, and P. Hayden, “*Towards the fast scrambling conjecture*”, *Journal of High Energy Physics* **2013**, 22 (2013).
- [29] Y. Sekino and L. Susskind, “*Fast scramblers*”, *Journal of High Energy Physics* **2008**, 065 (2008).
- [30] L. Susskind, “*Addendum to Fast Scramblers*”, [arXiv:1101.6048](https://arxiv.org/abs/1101.6048) (2011).
- [31] M. Suzuki, “*Fractal decomposition of exponential operators with applications to many-body theories and Monte Carlo simulations*”, *Physics Letters A* **146**, 319 - 323 (1990).
- [32] D. W. Berry, G. Ahokas, R. Cleve, and B. C. Sanders, “*Efficient Quantum Algorithms for Simulating Sparse Hamiltonians*”, *Communications in Mathematical Physics* **270**, 359–371 (2007).
- [33] A. Altland and B. Simons, *Condensed Matter Field Theory*. Cambridge University Press, 2nd edition ed., 2010.
- [34] “*The rise of quantum materials*”, *Nature Physics* **12**, 105–105 (2016).
- [35] I. Bloch, J. Dalibard, and S. Nascimbène, “*Quantum simulations with ultracold quantum gases*”, *Nature Physics* **8**, 267–276 (2012).
- [36] U. Schneider, L. Hackermüller, J. P. Ronzheimer, S. Will, S. Braun, T. Best, I. Bloch, E. Demler, S. Mandt, D. Rasch, and A. Rosch, “*Fermionic transport and out-of-equilibrium dynamics in a homogeneous Hubbard model with ultracold atoms*”, *Nature Physics* **8**, 213–218 (2012).
- [37] D. Greif, T. Uehlinger, G. Jotzu, L. Tarruell, and T. Esslinger, “*Short-Range Quantum Magnetism of Ultracold Fermions in an Optical Lattice*”, *Science* **340**, 1307–1310 (2013).

-
- [38] P. Jordan and E. Wigner, “Über das Paulische Äquivalenzverbot”, *Zeitschrift für Physik* **47**, 631–651 (1928).
- [39] B. Bauer, D. Wecker, A. J. Millis, M. B. Hastings, and M. Troyer, “Hybrid Quantum-Classical Approach to Correlated Materials”, *Phys. Rev. X* **6**, 031045 (2016).
- [40] J. M. Kreula, S. R. Clark, and D. Jaksch, “Non-linear quantum-classical scheme to simulate non-equilibrium strongly correlated fermionic many-body dynamics”, *Scientific Reports* **6**, 32940 (2016).
- [41] J. Benhelm, G. Kirchmair, C. F. Roos, and R. Blatt, “Towards fault-tolerant quantum computing with trapped ions”, *Nature Physics* **4**, 463–466 (2008).
- [42] B. P. Lanyon, C. Hempel, D. Nigg, M. Müller, R. Gerritsma, F. Zähringer, P. Schindler, J. T. Barreiro, M. Rambach, G. Kirchmair, M. Hennrich, P. Zoller, R. Blatt, and C. F. Roos, “Universal Digital Quantum Simulation with Trapped Ions”, *Science* **334**, 57–61 (2011).
- [43] R. Blatt and C. F. Roos, “Quantum simulations with trapped ions”, *Nature Physics* **8**, 277–284 (2012).
- [44] J. Casanova, A. Mezzacapo, L. Lamata, and E. Solano, “Quantum Simulation of Interacting Fermion Lattice Models in Trapped Ions”, *Phys. Rev. Lett.* **108**, 190502 (2012).
- [45] D. I. Tsomokos, S. Ashhab, and F. Nori, “Using superconducting qubit circuits to engineer exotic lattice systems”, *Phys. Rev. A* **82**, 052311 (2010).
- [46] A. van Oudenaarden and J. E. Mooij, “One-Dimensional Mott Insulator Formed by Quantum Vortices in Josephson Junction Arrays”, *Phys. Rev. Lett.* **76**, 4947–4950 (1996).
- [47] D. I. Tsomokos, S. Ashhab, and F. Nori, “Fully connected network of superconducting qubits in a cavity”, *New Journal of Physics* **10**, 113020 (2008).
- [48] J. J. García-Ripoll, E. Solano, and M. A. Martin-Delgado, “Quantum simulation of Anderson and Kondo lattices with superconducting qubits”, *Phys. Rev. B* **77**, 024522 (2008).
- [49] A. L. Rakhmanov, A. M. Zagoskin, S. Savel’ev, and F. Nori, “Quantum metamaterials: Electromagnetic waves in a Josephson qubit line”, *Phys. Rev. B* **77**, 144507 (2008).
- [50] J. Koch, A. A. Houck, K. L. Hur, and S. M. Girvin, “Time-reversal-symmetry breaking in circuit-QED-based photon lattices”, *Phys. Rev. A* **82**, 043811 (2010).

- [51] J. Q. You, X.-F. Shi, X. Hu, and F. Nori, “Quantum emulation of a spin system with topologically protected ground states using superconducting quantum circuits”, *Phys. Rev. B* **81**, 014505 (2010).
- [52] A. Wallraff, D. I. Schuster, A. Blais, L. Frunzio, R. S. Huang, J. Majer, S. Kumar, S. M. Girvin, and R. J. Schoelkopf, “Strong coupling of a single photon to a superconducting qubit using circuit quantum electrodynamics”, *Nature* **431**, 162–167 (2004).
- [53] J. Li, M. P. Silveri, K. S. Kumar, J. M. Pirkkalainen, A. Vepsäläinen, W. C. Chien, J. Tuorila, M. A. Sillanpää, P. J. Hakonen, E. V. Thuneberg, and G. S. Paraoanu, “Motional averaging in a superconducting qubit”, *Nature Communications* **4**, 1420 (2013).
- [54] D. Marcos, P. Rabl, E. Rico, and P. Zoller, “Superconducting Circuits for Quantum Simulation of Dynamical Gauge Fields”, *Phys. Rev. Lett.* **111**, 110504 (2013).
- [55] V. M. Stojanović, M. Vanević, E. Demler, and L. Tian, “Transmon-based simulator of nonlocal electron-phonon coupling: A platform for observing sharp small-polaron transitions”, *Phys. Rev. B* **89**, 144508 (2014).
- [56] U. L. Heras, A. Mezzacapo, L. Lamata, S. Filipp, A. Wallraff, and E. Solano, “Digital Quantum Simulation of Spin Systems in Superconducting Circuits”, *Phys. Rev. Lett.* **112**, 200501 (2014).
- [57] A. Mezzacapo, U. Las Heras, J. S. Pedernales, L. DiCarlo, E. Solano, and L. Lamata, “Digital Quantum Rabi and Dicke Models in Superconducting Circuits”, *Scientific Reports* **4**, 7482 (2014).
- [58] R. Barends, L. Lamata, J. Kelly, L. García-Álvarez, A. G. Fowler, A. Megrant, E. Jeffrey, T. C. White, D. Sank, J. Y. Mutus, B. Campbell, Y. Chen, Z. Chen, B. Chiaro, A. Dunsworth, I. C. Hoi, C. Neill, P. J. J. O’Malley, C. Quintana, P. Roushan, A. Vainsencher, J. Wenner, E. Solano, and J. M. Martinis, “Digital quantum simulation of fermionic models with a superconducting circuit”, *Nature Communications* **6**, 7654 (2015).
- [59] Y. Salathé, M. Mondal, M. Oppliger, J. Heinsoo, P. Kurpiers, A. Potočnik, A. Mezzacapo, U. Las Heras, L. Lamata, E. Solano, S. Filipp, and A. Wallraff, “Digital Quantum Simulation of Spin Models with Circuit Quantum Electrodynamics”, *Phys. Rev. X* **5**, 021027 (2015).
- [60] R. Barends, J. Kelly, A. Megrant, A. Veitia, D. Sank, E. Jeffrey, T. C. White, J. Mutus, A. G. Fowler, B. Campbell, Y. Chen, Z. Chen, B. Chiaro, A. Dunsworth, C. Neill, P. O’Malley, P. Roushan, A. Vainsencher, J. Wenner, A. N. Korotkov, A. N. Cleland, and J. M. Martinis, “Superconducting quantum circuits at the surface code threshold for fault tolerance”, *Nature* **508**, 500–503 (2014).

-
- [61] L. Steffen, Y. Salathe, M. Oppliger, P. Kurpiers, M. Baur, C. Lang, C. Eichler, G. Puebla-Hellmann, A. Fedorov, and A. Wallraff, “*Deterministic quantum teleportation with feed-forward in a solid state system*”, *Nature* **500**, 319–322 (2013).
- [62] K. Mølmer and A. Sørensen, “*Multiparticle Entanglement of Hot Trapped Ions*”, *Phys. Rev. Lett.* **82**, 1835–1838 (1999).
- [63] A. Mezzacapo, L. Lamata, S. Filipp, and E. Solano, “*Many-Body Interactions with Tunable-Coupling Transmon Qubits*”, *Phys. Rev. Lett.* **113**, 050501 (2014).
- [64] A. Mezzacapo, J. Casanova, L. Lamata, and E. Solano, “*Digital Quantum Simulation of the Holstein Model in Trapped Ions*”, *Phys. Rev. Lett.* **109**, 200501 (2012).
- [65] L. Lamata, A. Mezzacapo, J. Casanova, and E. Solano, “*Efficient quantum simulation of fermionic and bosonic models in trapped ions*”, *EPJ Quantum Technology* **1**, 9 (2014).
- [66] M. H. Yung, J. Casanova, A. Mezzacapo, J. McClean, L. Lamata, A. Aspuru-Guzik, and E. Solano, “*From transistor to trapped-ion computers for quantum chemistry*”, *Scientific Reports* **4**, 3589 (2014).
- [67] M. Müller, K. Hammerer, Y. L. Zhou, C. F. Roos, and P. Zoller, “*Simulating open quantum systems: from many-body interactions to stabilizer pumping*”, *New Journal of Physics* **13**, 085007 (2011).
- [68] J. T. Barreiro, M. Müller, P. Schindler, D. Nigg, T. Monz, M. Chwalla, M. Hennrich, C. F. Roos, P. Zoller, and R. Blatt, “*An open-system quantum simulator with trapped ions*”, *Nature* **470**, 486–491 (2011).
- [69] A. Blais, R.-S. Huang, A. Wallraff, S. M. Girvin, and R. J. Schoelkopf, “*Cavity quantum electrodynamics for superconducting electrical circuits: An architecture for quantum computation*”, *Phys. Rev. A* **69**, 062320 (2004).
- [70] J. A. Mlynek, A. A. Abdumalikov, J. M. Fink, L. Steffen, M. Baur, C. Lang, A. F. van Loo, and A. Wallraff, “*Demonstrating W-type entanglement of Dicke states in resonant cavity quantum electrodynamics*”, *Phys. Rev. A* **86**, 053838 (2012).
- [71] A. Kitaev, “*Fault-tolerant quantum computation by anyons*”, *Annals of Physics* **303**, 2 - 30 (2003).
- [72] F. Helmer, M. Mariantoni, A. G. Fowler, J. von Delft, E. Solano, and F. Marquardt, “*Cavity grid for scalable quantum computation with superconducting circuits*”, *EPL (Europhysics Letters)* **85**, 50007 (2009).

-
- [73] J. Hubbard, “*Electron Correlations in Narrow Energy Bands*”, *Proceedings of the Royal Society of London A: Mathematical, Physical and Engineering Sciences* **276**, 238–257 (1963).
- [74] U. Las Heras, L. García-Álvarez, A. Mezzacapo, E. Solano, and L. Lamata, “*Fermionic models with superconducting circuits*”, *EPJ Quantum Technology* **2**, 8 (2015).
- [75] A. D. Córcoles, J. M. Gambetta, J. M. Chow, J. A. Smolin, M. Ware, J. Strand, B. L. T. Plourde, and M. Steffen, “*Process verification of two-qubit quantum gates by randomized benchmarking*”, *Phys. Rev. A* **87**, 030301 (2013).
- [76] V. Vesterinen, O.-P. Saira, A. Bruno, and L. DiCarlo, “*Mitigating information leakage in a crowded spectrum of weakly anharmonic qubits*”, [arXiv:1405.0450](https://arxiv.org/abs/1405.0450) (2014).
- [77] L. García-Álvarez, J. Casanova, A. Mezzacapo, I. L. Egusquiza, L. Lamata, G. Romero, and E. Solano, “*Fermion-Fermion Scattering in Quantum Field Theory with Superconducting Circuits*”, *Phys. Rev. Lett.* **114**, 070502 (2015).
- [78] R. Jordens, N. Strohmaier, K. Gunter, H. Moritz, and T. Esslinger, “*A Mott insulator of fermionic atoms in an optical lattice*”, *Nature* **455**, 204–207 (2008).
- [79] U. Schneider, L. Hackermüller, S. Will, T. Best, I. Bloch, T. A. Costi, R. W. Helmes, D. Rasch, and A. Rosch, “*Metallic and Insulating Phases of Repulsively Interacting Fermions in a 3D Optical Lattice*”, *Science* **322**, 1520–1525 (2008).
- [80] J. Kelly, R. Barends, A. G. Fowler, A. Megrant, E. Jeffrey, T. C. White, D. Sank, J. Y. Mutus, B. Campbell, Y. Chen, Z. Chen, B. Chiaro, A. Dunsworth, I.-C. Hoi, C. Neill, P. J. J. O’Malley, C. Quintana, P. Roushan, A. Vainsencher, J. Wenner, A. N. Cleland, and J. M. Martinis, “*State preservation by repetitive error detection in a superconducting quantum circuit*”, *Nature* **519**, 66–69 (2015).
- [81] R. Barends, J. Kelly, A. Megrant, D. Sank, E. Jeffrey, Y. Chen, Y. Yin, B. Chiaro, J. Mutus, C. Neill, P. O’Malley, P. Roushan, J. Wenner, T. C. White, A. N. Cleland, and J. M. Martinis, “*Coherent Josephson Qubit Suitable for Scalable Quantum Integrated Circuits*”, *Phys. Rev. Lett.* **111**, 080502 (2013).
- [82] R. Barends, J. Kelly, A. Veitia, A. Megrant, A. G. Fowler, B. Campbell, Y. Chen, Z. Chen, B. Chiaro, A. Dunsworth, I.-C. Hoi, E. Jeffrey, C. Neill, P. J. J. O’Malley, J. Mutus, C. Quintana, P. Roushan, D. Sank, J. Wenner, T. C. White, A. N. Korotkov, A. N. Cleland, and J. M. Martinis, “*Rolling quantum dice with a superconducting qubit*”, *Phys. Rev. A* **90**, 030303 (2014).

-
- [83] J. M. Martinis and M. R. Geller, “Fast adiabatic qubit gates using only σ_z control”, *Phys. Rev. A* **90**, 022307 (2014).
- [84] P. J. J. O’Malley, J. Kelly, R. Barends, B. Campbell, Y. Chen, Z. Chen, B. Chiaro, A. Dunsworth, A. G. Fowler, I.-C. Hoi, E. Jeffrey, A. Megrant, J. Mutus, C. Neill, C. Quintana, P. Roushan, D. Sank, A. Vainsencher, J. Wenner, T. C. White, A. N. Korotkov, A. N. Cleland, and J. M. Martinis, “Qubit Metrology of Ultralow Phase Noise Using Randomized Benchmarking”, *Phys. Rev. Applied* **3**, 044009 (2015).
- [85] O. Dutta, M. Gajda, P. Hauke, M. Lewenstein, D.-S. Lühmann, B. A. Malomed, T. Sowiński, and J. Zakrzewski, “Non-standard Hubbard models in optical lattices: a review”, *Reports on Progress in Physics* **78**, 066001 (2015).
- [86] I. de Vega, U. Schollwöck, and F. A. Wolf, “How to discretize a quantum bath for real-time evolution”, *Phys. Rev. B* **92**, 155126 (2015).
- [87] M. Potthoff, “Two-site dynamical mean-field theory”, *Phys. Rev. B* **64**, 165114 (2001).
- [88] “IBM Quantum Computing.” <https://www.research.ibm.com/quantum/>. (Retrieved 14 June, 2016).
- [89] R. Barends, A. Shabani, L. Lamata, J. Kelly, A. Mezzacapo, U. L. Heras, R. Babbush, A. G. Fowler, B. Campbell, Y. Chen, Z. Chen, B. Chiaro, A. Dunsworth, E. Jeffrey, E. Lucero, A. Megrant, J. Y. Mutus, M. Neeley, C. Neill, P. J. J. O’Malley, C. Quintana, P. Roushan, D. Sank, A. Vainsencher, J. Wenner, T. C. White, E. Solano, H. Neven, and J. M. Martinis, “Digitized adiabatic quantum computing with a superconducting circuit”, *Nature* **534**, 222–226 (2016).
- [90] E. A. Martinez, C. A. Muschik, P. Schindler, D. Nigg, A. Erhard, M. Heyl, P. Hauke, M. Dalmonte, T. Monz, P. Zoller, and R. Blatt, “Real-time dynamics of lattice gauge theories with a few-qubit quantum computer”, *Nature* **534**, 516–519 (2016).
- [91] G. D. Mahan, *Many-Particle Physics*. Springer US, 3 ed., 2000.
- [92] J. Maldacena, “The Large- N Limit of Superconformal Field Theories and Supergravity”, *International Journal of Theoretical Physics* **38**, 1113–1133 (1999).
- [93] S. W. Hawking, “Breakdown of predictability in gravitational collapse”, *Phys. Rev. D* **14**, 2460–2473 (1976).
- [94] S. Catterall and T. Wiseman, “Towards lattice simulation of the gauge theory duals to black holes and hot strings”, *Journal of High Energy Physics* **2007**, 104 (2007).

-
- [95] M. Hanada, Y. Hyakutake, G. Ishiki, and J. Nishimura, “*Holographic description of a quantum black hole on a computer*”, *Science* **344**, 882–885 (2014).
- [96] T. Anous, T. Hartman, A. Rovai, and J. Sonner, “*Black hole collapse in the $1/c$ expansion*”, *Journal of High Energy Physics* **2016**, 123 (2016).
- [97] G. S. Paraoanu, “*Recent Progress in Quantum Simulation Using Superconducting Circuits*”, *Journal of Low Temperature Physics* **175**, 633–654 (2014).
- [98] G. Romero, E. Solano, and L. Lamata, *Quantum Simulations with Photons and Polaritons*, ch. 7. Springer International Publishing, 2017.
- [99] A. Aspuru-Guzik and P. Walther, “*Photonic quantum simulators*”, *Nature Physics* **8**, 285–291 (2012).
- [100] U.-J. Wiese, “*Towards quantum simulating QCD*”, *Nuclear Physics A* **931**, 246 - 256 (2014).
- [101] S. Weinberg and E. Witten, “*Limits on massless particles*”, *Physics Letters B* **96**, 59 - 62 (1980).
- [102] D. Marolf, “*Emergent Gravity Requires Kinematic Nonlocality*”, *Phys. Rev. Lett.* **114**, 031104 (2015).
- [103] A. Kitaev, “A simple model of quantum holography.” Talks at KITP, April 7, 2015 and May 27, 2015.
- [104] S. Sachdev, “*Bekenstein-Hawking Entropy and Strange Metals*”, *Phys. Rev. X* **5**, 041025 (2015).
- [105] I. Danshita, M. Hanada, and M. Tezuka, “*Creating and probing the Sachdev-Ye-Kitaev model with ultracold gases: Towards experimental studies of quantum gravity*”, [arXiv:1606.02454](https://arxiv.org/abs/1606.02454) (2016).
- [106] A. J. Bray and M. A. Moore, “*Replica theory of quantum spin glasses*”, *Journal of Physics C: Solid State Physics* **13**, L655 (1980).
- [107] J. Polchinski and V. Rosenhaus, “*The spectrum in the Sachdev-Ye-Kitaev model*”, *Journal of High Energy Physics* **2016**, 1 (2016).
- [108] J. Maldacena and D. Stanford, “*Remarks on the Sachdev-Ye-Kitaev model*”, *Phys. Rev. D* **94**, 106002 (2016).
- [109] J. Maldacena, S. H. Shenker, and D. Stanford, “*A bound on chaos*”, *Journal of High Energy Physics* **2016**, 106 (2016).
- [110] K. Jensen, “*Chaos in AdS₂ Holography*”, *Phys. Rev. Lett.* **117**, 111601 (2016).

-
- [111] J. Maldacena, D. Stanford, and Z. Yang, “*Conformal symmetry and its breaking in two-dimensional nearly anti-de Sitter space*”, [Progress of Theoretical and Experimental Physics](#) **2016**, 12C104 (2016).
- [112] J. Engelsöy, T. G. Mertens, and H. Verlinde, “*An investigation of AdS2 backreaction and holography*”, [Journal of High Energy Physics](#) **2016**, 139 (2016).
- [113] J. S. Cotler, G. Gur-Ari, M. Hanada, J. Polchinski, P. Saad, S. H. Shenker, D. Stanford, A. Streicher, and M. Tezuka, “*Black holes and random matrices*”, [Journal of High Energy Physics](#) **2017**, 118 (2017).
- [114] Y.-Z. You, A. W. W. Ludwig, and C. Xu, “*Sachdev-Ye-Kitaev model and thermalization on the boundary of many-body localized fermionic symmetry-protected topological states*”, [Phys. Rev. B](#) **95**, 115150 (2017).
- [115] A. M. García-García and J. J. M. Verbaarschot, “*Spectral and thermodynamic properties of the Sachdev-Ye-Kitaev model*”, [Phys. Rev. D](#) **94**, 126010 (2016).
- [116] S. B. Bravyi and A. Y. Kitaev, “*Quantum codes on a lattice with boundary*”, [arXiv:quant-ph/9811052](#) (1998).
- [117] A. G. Fowler, M. Mariantoni, J. M. Martinis, and A. N. Cleland, “*Surface codes: Towards practical large-scale quantum computation*”, [Phys. Rev. A](#) **86**, 032324 (2012).
- [118] J. S. Pedernales, R. Di Candia, I. L. Egusquiza, J. Casanova, and E. Solano, “*Efficient Quantum Algorithm for Computing n-time Correlation Functions*”, [Phys. Rev. Lett.](#) **113**, 020505 (2014).
- [119] B. Swingle, G. Bentsen, M. Schleier-Smith, and P. Hayden, “*Measuring the scrambling of quantum information*”, [Phys. Rev. A](#) **94**, 040302 (2016).
- [120] J. Casanova, C. Sabín, J. León, I. L. Egusquiza, R. Gerritsma, C. F. Roos, J. J. García-Ripoll, and E. Solano, “*Quantum Simulation of the Majorana Equation and Unphysical Operations*”, [Phys. Rev. X](#) **1**, 021018 (2011).
- [121] G. Zhu, M. Hafezi, and T. Grover, “*Measurement of many-body chaos using a quantum clock*”, [Phys. Rev. A](#) **94**, 062329 (2016).
- [122] A. Riera, C. Gogolin, and J. Eisert, “*Thermalization in Nature and on a Quantum Computer*”, [Phys. Rev. Lett.](#) **108**, 080402 (2012).
- [123] P.-L. Dallaire-Demers and F. K. Wilhelm, “*Method to efficiently simulate the thermodynamic properties of the Fermi-Hubbard model on a quantum computer*”, [Phys. Rev. A](#) **93**, 032303 (2016).
- [124] C. J. Ballance, T. P. Harty, N. M. Linke, M. A. Sepiol, and D. M. Lucas, “*High-Fidelity Quantum Logic Gates Using Trapped-Ion Hyperfine Qubits*”, [Phys. Rev. Lett.](#) **117**, 060504 (2016).

-
- [125] J. P. Gaebler, T. R. Tan, Y. Lin, Y. Wan, R. Bowler, A. C. Keith, S. Glancy, K. Coakley, E. Knill, D. Leibfried, and D. J. Wineland, “*High-Fidelity Universal Gate Set for $^9\text{Be}^+$ Ion Qubits*”, *Phys. Rev. Lett.* **117**, 060505 (2016).
- [126] A. A. Houck, H. E. Türeci, and J. Koch, “*On-chip quantum simulation with superconducting circuits*”, *Nature Physics* **8**, 292–299 (2012).
- [127] E. Zohar, A. Farace, B. Reznik, and J. I. Cirac, “*Digital lattice gauge theories*”, *Phys. Rev. A* **95**, 023604 (2017).
- [128] E. Jané, G. Vidal, W. Dür, P. Zoller, and J. I. Cirac, “*Simulation of Quantum Dynamics with Quantum Optical Systems*”, *Quantum Info. Comput.* **3**, 15–37 (2003).
- [129] I. Arrazola, J. S. Pedernales, L. Lamata, and E. Solano, “*Digital-Analog Quantum Simulation of Spin Models in Trapped Ions*”, *Scientific Reports* **6**, 30534 (2016).
- [130] K. Bhattacharyya, “*Quantum decay and the Mandelstam-Tamm-energy inequality*”, *Journal of Physics A: Mathematical and General* **16**, 2993 (1983).
- [131] S. Boixo, S. T. Flammia, C. M. Caves, and J. Geremia, “*Generalized Limits for Single-Parameter Quantum Estimation*”, *Phys. Rev. Lett.* **98**, 090401 (2007).
- [132] T. Monz, P. Schindler, J. T. Barreiro, M. Chwalla, D. Nigg, W. A. Coish, M. Harlander, W. Hänsel, M. Hennrich, and R. Blatt, “*14-Qubit Entanglement: Creation and Coherence*”, *Phys. Rev. Lett.* **106**, 130506 (2011).
- [133] M. E. Peskin and D. V. Schroeder, “*Quantum field theory*”, The Advanced Book Program, Perseus Books Reading, Massachusetts (1995).
- [134] J. B. Kogut, “*An introduction to lattice gauge theory and spin systems*”, *Rev. Mod. Phys.* **51**, 659–713 (1979).
- [135] J. B. Kogut and M. A. Stephanov, *The phases of quantum chromodynamics: From confinement to extreme environments*. Cambridge University Press, 2003.
- [136] I. M. Georgescu, S. Ashhab, and F. Nori, “*Quantum simulation*”, *Rev. Mod. Phys.* **86**, 153–185 (2014).
- [137] T. Byrnes and Y. Yamamoto, “*Simulating lattice gauge theories on a quantum computer*”, *Phys. Rev. A* **73**, 022328 (2006).
- [138] J. I. Cirac, P. Maraner, and J. K. Pachos, “*Cold Atom Simulation of Interacting Relativistic Quantum Field Theories*”, *Phys. Rev. Lett.* **105**, 190403 (2010).

-
- [139] J. Casanova, L. Lamata, I. L. Egusquiza, R. Gerritsma, C. F. Roos, J. J. García-Ripoll, and E. Solano, “*Quantum Simulation of Quantum Field Theories in Trapped Ions*”, *Phys. Rev. Lett.* **107**, 260501 (2011).
- [140] L. Mazza, A. Bermudez, N. Goldman, M. Rizzi, M. A. Martin-Delgado, and M. Lewenstein, “*An optical-lattice-based quantum simulator for relativistic field theories and topological insulators*”, *New Journal of Physics* **14**, 015007 (2012).
- [141] S. P. Jordan, K. S. M. Lee, and J. Preskill, “*Quantum Algorithms for Quantum Field Theories*”, *Science* **336**, 1130–1133 (2012).
- [142] P. Hauke, D. Marcos, M. Dalmonte, and P. Zoller, “*Quantum Simulation of a Lattice Schwinger Model in a Chain of Trapped Ions*”, *Phys. Rev. X* **3**, 041018 (2013).
- [143] I. Chiorescu, P. Bertet, K. Semba, Y. Nakamura, C. J. P. M. Harmans, and J. E. Mooij, “*Coherent dynamics of a flux qubit coupled to a harmonic oscillator*”, *Nature* **431**, 159–162 (2004).
- [144] H. Paik, D. I. Schuster, L. S. Bishop, G. Kirchmair, G. Catelani, A. P. Sears, B. R. Johnson, M. J. Reagor, L. Frunzio, L. I. Glazman, S. M. Girvin, M. H. Devoret, and R. J. Schoelkopf, “*Observation of High Coherence in Josephson Junction Qubits Measured in a Three-Dimensional Circuit QED Architecture*”, *Phys. Rev. Lett.* **107**, 240501 (2011).
- [145] M. Mariantoni, H. Wang, T. Yamamoto, M. Neeley, R. C. Bialczak, Y. Chen, M. Lenander, E. Lucero, A. D. O’Connell, D. Sank, M. Weides, J. Wenner, Y. Yin, J. Zhao, A. N. Korotkov, A. N. Cleland, and J. M. Martinis, “*Implementing the Quantum von Neumann Architecture with Superconducting Circuits*”, *Science* **334**, 61–65 (2011).
- [146] D. L. Underwood, W. E. Shanks, J. Koch, and A. A. Houck, “*Low-disorder microwave cavity lattices for quantum simulation with photons*”, *Phys. Rev. A* **86**, 023837 (2012).
- [147] M. Stern, G. Catelani, Y. Kubo, C. Grezes, A. Bienfait, D. Vion, D. Esteve, and P. Bertet, “*Flux Qubits with Long Coherence Times for Hybrid Quantum Circuits*”, *Phys. Rev. Lett.* **113**, 123601 (2014).
- [148] Y. Chen, P. Roushan, D. Sank, C. Neill, E. Lucero, M. Mariantoni, R. Barends, B. Chiaro, J. Kelly, A. Megrant, J. Y. Mutus, P. J. J. O’Malley, A. Vainsencher, J. Wenner, T. C. White, Y. Yin, A. N. Cleland, and J. M. Martinis, “*Emulating weak localization using a solid-state quantum circuit*”, *Nature Communications* **5**, 5184 (2014).
- [149] J. M. Gambetta, A. A. Houck, and A. Blais, “*Superconducting Qubit with Purcell Protection and Tunable Coupling*”, *Phys. Rev. Lett.* **106**, 030502 (2011).

- [150] S. J. Srinivasan, A. J. Hoffman, J. M. Gambetta, and A. A. Houck, “*Tunable Coupling in Circuit Quantum Electrodynamics Using a Superconducting Charge Qubit with a V-Shaped Energy Level Diagram*”, *Phys. Rev. Lett.* **106**, 083601 (2011).
- [151] J. M. Chow, J. M. Gambetta, E. Magesan, D. W. Abraham, A. W. Cross, B. R. Johnson, N. A. Masluk, C. A. Ryan, J. A. Smolin, S. J. Srinivasan, and M. Steffen, “*Implementing a strand of a scalable fault-tolerant quantum computing fabric*”, *Nature Communications* **5**, 4015 (2014).
- [152] D. M. Pozar, *Microwave engineering*. John Wiley & Sons, 4th ed., 2011.
- [153] R. D. Candia, E. P. Menzel, L. Zhong, F. Deppe, A. Marx, R. Gross, and E. Solano, “*Dual-path methods for propagating quantum microwaves*”, *New Journal of Physics* **16**, 015001 (2014).
- [154] N. S. Ostlund and A. Szabo, *Modern quantum chemistry: introduction to advanced electronic structure theory*. Dover Publications, New York, 1996.
- [155] T. Helgaker, P. Jorgensen, and J. Olsen, *Molecular electronic-structure theory*. John Wiley & Sons, 2014.
- [156] C. D. Sherrill, “*Frontiers in electronic structure theory*”, *The Journal of Chemical Physics* **132**, (2010).
- [157] J. D. Whitfield, P. J. Love, and A. Aspuru-Guzik, “*Computational complexity in electronic structure*”, *Phys. Chem. Chem. Phys.* **15**, 397-411 (2013).
- [158] A. Aspuru-Guzik, A. D. Dutoi, P. J. Love, and M. Head-Gordon, “*Simulated Quantum Computation of Molecular Energies*”, *Science* **309**, 1704–1707 (2005).
- [159] I. Kassal, J. D. Whitfield, A. Perdomo-Ortiz, M.-H. Yung, and A. Aspuru-Guzik, “*Simulating chemistry using quantum computers*”, *Annual review of physical chemistry* **62**, 185–207 (2011).
- [160] J. Du, N. Xu, X. Peng, P. Wang, S. Wu, and D. Lu, “*NMR Implementation of a Molecular Hydrogen Quantum Simulation with Adiabatic State Preparation*”, *Phys. Rev. Lett.* **104**, 030502 (2010).
- [161] Y. Shen, X. Zhang, S. Zhang, J.-N. Zhang, M.-H. Yung, and K. Kim, “*Quantum implementation of the unitary coupled cluster for simulating molecular electronic structure*”, *Phys. Rev. A* **95**, 020501 (2017).
- [162] B. P. Lanyon, J. D. Whitfield, G. G. Gillett, M. E. Goggin, M. P. Almeida, I. Kassal, J. D. Biamonte, M. Mohseni, B. J. Powell, M. Barbieri, A. Aspuru-Guzik, and A. G. White, “*Towards quantum chemistry on a quantum computer*”, *Nature Chemistry* **2**, 106–111 (2010).

-
- [163] A. Peruzzo, J. McClean, P. Shadbolt, M.-H. Yung, X.-Q. Zhou, P. J. Love, A. Aspuru-Guzik, and J. L. O'Brien, "A variational eigenvalue solver on a photonic quantum processor", *Nature Communications* **5**, 4213 (2014).
- [164] J. Huh, G. G. Guerreschi, B. Peropadre, J. R. McClean, and A. Aspuru-Guzik, "Boson sampling for molecular vibronic spectra", *Nat Photon* **9**, 615–620 (2015).
- [165] S. Mostame, P. Reberntrost, A. Eisfeld, A. J. Kerman, D. I. Tsomokos, and A. Aspuru-Guzik, "Quantum simulator of an open quantum system using superconducting qubits: exciton transport in photosynthetic complexes", *New Journal of Physics* **14**, 105013 (2012).
- [166] I. Kassal, S. P. Jordan, P. J. Love, M. Mohseni, and A. Aspuru-Guzik, "Polynomial-time quantum algorithm for the simulation of chemical dynamics", *Proceedings of the National Academy of Sciences* **105**, 18681-18686 (2008).
- [167] J. D. Whitfield, J. Biamonte, and A. Aspuru-Guzik, "Simulation of electronic structure Hamiltonians using quantum computers", *Molecular Physics* **109**, 735-750 (2011).
- [168] B. Toloui and P. J. Love, "Quantum Algorithms for Quantum Chemistry based on the sparsity of the CI-matrix", [arXiv:1312.2579](https://arxiv.org/abs/1312.2579) (2013).
- [169] M. B. Hastings, D. Wecker, B. Bauer, and M. Troyer, "Improving Quantum Algorithms for Quantum Chemistry", *Quantum Inf. Comput.* **15**, 1-21 (2015).
- [170] R. Babbush, P. J. Love, and A. Aspuru-Guzik, "Adiabatic Quantum Simulation of Quantum Chemistry", *Scientific Reports* **4**, 6603 (2014).
- [171] D. Poulin, M. B. Hastings, D. Wecker, N. Wiebe, A. C. Doberty, and M. Troyer, "The Trotter Step Size Required for Accurate Quantum Simulation of Quantum Chemistry", *Quantum Info. Comput.* **15**, 361–384 (2015).
- [172] J. D. Whitfield, "Unified views of quantum simulation algorithms for chemistry", [arXiv:1502.03771](https://arxiv.org/abs/1502.03771) (2015).
- [173] R. Babbush, J. McClean, D. Wecker, A. Aspuru-Guzik, and N. Wiebe, "Chemical basis of Trotter-Suzuki errors in quantum chemistry simulation", *Phys. Rev. A* **91**, 022311 (2015).
- [174] D. Abbott, P. C. W. Davies, and A. K. Pati, *Quantum aspects of life*. Imperial College Press, 2008.
- [175] V. May and O. Kühn, *Charge and energy transfer dynamics in molecular systems*. WILEY-VCH Verlag GmbH & Co. KGaA, Weinheim, 2004.

-
- [176] A. Chiesa, P. Santini, D. Gerace, J. Raftery, A. A. Houck, and S. Carretta, “*Digital quantum simulators in a scalable architecture of hybrid spin-photon qubits*”, *Scientific Reports* **5**, 16036 (2015).
- [177] P. J. J. O’Malley, R. Babbush, I. D. Kivlichan, J. Romero, J. R. McClean, R. Barends, J. Kelly, P. Roushan, A. Tranter, N. Ding, B. Campbell, Y. Chen, Z. Chen, B. Chiaro, A. Dunsworth, A. G. Fowler, E. Jeffrey, E. Lucero, A. Megrant, J. Y. Mutus, M. Neeley, C. Neill, C. Quintana, D. Sank, A. Vainsencher, J. Wenner, T. C. White, P. V. Coveney, P. J. Love, H. Neven, A. Aspuru-Guzik, and J. M. Martinis, “*Scalable Quantum Simulation of Molecular Energies*”, *Phys. Rev. X* **6**, 031007 (2016).
- [178] D. J. Egger and F. K. Wilhelm, “*Multimode Circuit Quantum Electrodynamics with Hybrid Metamaterial Transmission Lines*”, *Phys. Rev. Lett.* **111**, 163601 (2013).
- [179] D. O. Krimer, M. Liertzer, S. Rotter, and H. E. Türeci, “*Route from spontaneous decay to complex multimode dynamics in cavity QED*”, *Phys. Rev. A* **89**, 033820 (2014).
- [180] S. E. Nigg, H. Paik, B. Vlastakis, G. Kirchmair, S. Shankar, L. Frunzio, M. H. Devoret, R. J. Schoelkopf, and S. M. Girvin, “*Black-Box Superconducting Circuit Quantization*”, *Phys. Rev. Lett.* **108**, 240502 (2012).
- [181] N. M. Sundaresan, Y. Liu, D. Sadri, L. J. Szöcs, D. L. Underwood, M. Malekakhlagh, H. E. Türeci, and A. A. Houck, “*Beyond Strong Coupling in a Multimode Cavity*”, *Phys. Rev. X* **5**, 021035 (2015).
- [182] D. C. McKay, R. Naik, P. Reinhold, L. S. Bishop, and D. I. Schuster, “*High-Contrast Qubit Interactions Using Multimode Cavity QED*”, *Phys. Rev. Lett.* **114**, 080501 (2015).
- [183] R. Bulla, R. Gutiérrez, and G. Cuniberti, *Modelling molecular conduction in DNA wires: charge transfer theories and dissipative quantum transport (Modern Methods for Theoretical Physics Chemistry of Biopolymers)*, ch. 19. Elsevier, Amsterdam, 2006.
- [184] S. Tornow, N.-H. Tong, and R. Bulla, “*Electron transfer in donor-acceptor systems: Many-particle effects and influence of electronic correlations*”, *EPL (Europhysics Letters)* **73**, 913 (2006).
- [185] R. Gutiérrez, R. A. Caetano, B. P. Woiczikowski, T. Kubar, M. Elstner, and G. Cuniberti, “*Charge Transport through Biomolecular Wires in a Solvent: Bridging Molecular Dynamics and Model Hamiltonian Approaches*”, *Phys. Rev. Lett.* **102**, 208102 (2009).
- [186] U. Alvarez-Rodriguez, R. Di Candia, J. Casanova, M. Sanz, and E. Solano, “*Algorithmic quantum simulation of memory effects*”, *Phys. Rev. A* **95**, 020301 (2017).

-
- [187] D. Wecker, M. B. Hastings, and M. Troyer, “*Progress towards practical quantum variational algorithms*”, [Phys. Rev. A **92**, 042303 \(2015\)](#).
- [188] J. R. McClean, J. Romero, R. Babbush, and A. Aspuru-Guzik, “*The theory of variational hybrid quantum-classical algorithms*”, [New Journal of Physics **18**, 023023 \(2016\)](#).
- [189] F. Mei, V. M. Stojanović, I. Siddiqi, and L. Tian, “*Analog superconducting quantum simulator for Holstein polarons*”, [Phys. Rev. B **88**, 224502 \(2013\)](#).
- [190] K. Seo and L. Tian, “*Quantum phase transition in a multiconnected superconducting Jaynes-Cummings lattice*”, [Phys. Rev. B **91**, 195439 \(2015\)](#).
- [191] C. J. Trout and K. R. Brown, “*Magic state distillation and gate compilation in quantum algorithms for quantum chemistry*”, [International Journal of Quantum Chemistry **115**, 1296–1304 \(2015\)](#).
- [192] D. Porath, A. Bezryadin, S. de Vries, and C. Dekker, “*Direct measurement of electrical transport through DNA molecules*”, [Nature **403**, 635–638 \(2000\)](#).
- [193] A. J. Storm, J. van Noort, S. de Vries, and C. Dekker, “*Insulating behavior for DNA molecules between nanoelectrodes at the 100 nm length scale*”, [Applied Physics Letters **79**, 3881–3883 \(2001\)](#).
- [194] K.-H. Yoo, D. H. Ha, J.-O. Lee, J. W. Park, J. Kim, J. J. Kim, H.-Y. Lee, T. Kawai, and H. Y. Choi, “*Electrical Conduction through Poly(dA)-Poly(dT) and Poly(dG)-Poly(dC) DNA Molecules*”, [Phys. Rev. Lett. **87**, 198102 \(2001\)](#).
- [195] G. Schuster, ed., *Long-Range Charge Transfer in DNA II*, volume 237 of *Topics in Current Chemistry*. Springer Berlin Heidelberg, 2004.
- [196] B. Xu, P. Zhang, X. Li, and N. Tao, “*Direct Conductance Measurement of Single DNA Molecules in Aqueous Solution*”, [Nano Letters **4**, 1105–1108 \(2004\)](#).
- [197] H. Cohen, C. Nogues, R. Naaman, and D. Porath, “*Direct measurement of electrical transport through single DNA molecules of complex sequence*”, [Proceedings of the National Academy of Sciences of the United States of America **102**, 11589–11593 \(2005\)](#).
- [198] C. Nogues, S. R. Cohen, S. Daube, N. Apter, and R. Naaman, “*Sequence Dependence of Charge Transport Properties of DNA*”, [The Journal of Physical Chemistry B **110**, 8910–8913 \(2006\)](#). PMID: 16671692.
- [199] M. Haeberlein, F. Deppe, A. Kurcz, J. Goetz, A. Baust, P. Eder, K. Fedorov, M. Fischer, E. P. Menzel, M. J. Schwarz, F. Wulschner, E. Xie, L. Zhong, E. Solano, A. Marx, J. J. García-Ripoll, and R. Gross, “*Spin-boson model with an engineered reservoir in circuit quantum electrodynamics*”, [arXiv:1506.09114 \(2015\)](#).

- [200] Y. Chen, C. Neill, P. Roushan, N. Leung, M. Fang, R. Barends, J. Kelly, B. Campbell, Z. Chen, B. Chiaro, A. Dunsworth, E. Jeffrey, A. Megrant, J. Y. Mutus, P. J. J. O'Malley, C. M. Quintana, D. Sank, A. Vainsencher, J. Wenner, T. C. White, M. R. Geller, A. N. Cleland, and J. M. Martinis, “*Qubit Architecture with High Coherence and Fast Tunable Coupling*”, *Phys. Rev. Lett.* **113**, 220502 (2014).
- [201] P. Forn-Díaz, J. J. García-Ripoll, B. Peropadre, J.-L. Orgiazzi, M. A. Yurtalan, R. Belyansky, C. M. Wilson, and A. Lupascu, “*Ultrastrong coupling of a single artificial atom to an electromagnetic continuum in the nonperturbative regime*”, *Nature Physics* **13**, 39–43 (2017).
- [202] P. Pfeiffer, I. L. Egusquiza, M. Di Ventura, M. Sanz, and E. Solano, “*Quantum memristors*”, *Scientific Reports* **6**, 29507 (2016).
- [203] E. Jeffrey, D. Sank, J. Y. Mutus, T. C. White, J. Kelly, R. Barends, Y. Chen, Z. Chen, B. Chiaro, A. Dunsworth, A. Megrant, P. J. J. O'Malley, C. Neill, P. Roushan, A. Vainsencher, J. Wenner, A. N. Cleland, and J. M. Martinis, “*Fast Accurate State Measurement with Superconducting Qubits*”, *Phys. Rev. Lett.* **112**, 190504 (2014).
- [204] A. N. Korotkov, “*Error matrices in quantum process tomography*”, [arXiv:1309.6405](https://arxiv.org/abs/1309.6405) (2013).
- [205] C. A. Ryan, M. Laforest, and R. Laflamme, “*Randomized benchmarking of single- and multi-qubit control in liquid-state NMR quantum information processing*”, *New Journal of Physics* **11**, 013034 (2009).
- [206] K. R. Brown, A. C. Wilson, Y. Colombe, C. Ospelkaus, A. M. Meier, E. Knill, D. Leibfried, and D. J. Wineland, “*Single-qubit-gate error below 10^{-4} in a trapped ion*”, *Phys. Rev. A* **84**, 030303 (2011).
- [207] J. Kelly, R. Barends, B. Campbell, Y. Chen, Z. Chen, B. Chiaro, A. Dunsworth, A. G. Fowler, I.-C. Hoi, E. Jeffrey, A. Megrant, J. Mutus, C. Neill, P. J. J. O'Malley, C. Quintana, P. Roushan, D. Sank, A. Vainsencher, J. Wenner, T. C. White, A. N. Cleland, and J. M. Martinis, “*Optimal Quantum Control Using Randomized Benchmarking*”, *Phys. Rev. Lett.* **112**, 240504 (2014).
- [208] R. Dorner, S. R. Clark, L. Heaney, R. Fazio, J. Goold, and V. Vedral, “*Extracting Quantum Work Statistics and Fluctuation Theorems by Single-Qubit Interferometry*”, *Phys. Rev. Lett.* **110**, 230601 (2013).
- [209] P. Schindler, D. Nigg, T. Monz, J. T. Barreiro, E. Martinez, S. X. Wang, S. Quint, M. F. Brandl, V. Nebendahl, C. F. Roos, M. Chwalla, M. Hennrich, and R. Blatt, “*A quantum information processor with trapped ions*”, *New Journal of Physics* **15**, 123012 (2013).

-
- [210] M. Devoret, *Quantum Fluctuations (Les Houches Session LXIII)*, volume Les Houches Session LXIII. Elsevier, New York, 1997.